UNIVERSITÀ DEGLI STUDI DI MILANO

Ph.D. course in Integrative Biomedical Research

XXXIII Cycle

Department of Biomedical Sciences for Health

Ph.D. Thesis

Molecular and functional characterization of the mechanotransduction signaling pathway in pancreatic endocrine cells: implications for beta cells survival, differentiation and function

Candidate:

Alessandra Galli

Tutor: Prof. Carla Perego

Co-Tutor: Prof. Romano Regazzi

Degree course coordinator: Prof. Chiarella Sforza

A.A. 2019/2020

Abstract

Abstract -English

Pancreatic β-cells, the only cells within the body able to secrete large amount of insulin, play a crucial role in the control of glucose homeostasis and alteration of their function and mass leads to diabetes pathogenesis, a group of pathologies characterized by severe hyperglycemia. Therefore, preserving the remaining β-cell function and replacing the β-cell mass represent the most promising strategies to treat diabetes. Embryonic and pluripotent stem cells hold great promise in generating β-cells for novel therapeutic discoveries in diabetes mellitus. However, their differentiation *in vitro* is still inefficient, and functional studies reveal that most of these β-like cells still fail to fully mirror the adult β-cell physiology. For their proper growth and functioning, β-cells require a very specific environment, the islet niche, which provides a myriad of chemical and physical signals. While the nature and effects of chemical stimuli have been widely characterized, less is known about the mechanical signals. Therefore, aim of the proposed research was to investigate the contribution of nanotopographical cues on β-cell differentiation and function and to characterize the molecular mechanisms involved. To mimic the nanotopography of the extracellular matrix, cluster-assembled zirconia substrates with tailored roughness were employed. We demonstrated that β-cells perceive nanoscale features and convert these stimuli into mechanotransductive processes which modulate the cellular behavior, via remodeling of the actin cytoskeleton and nuclear architecture. These changes are also paralleled by modulation of mitochondrial dynamics, morphology, and function, favoring a metabolic switch of the cells. The mitomorphosis is driven by substrate-induced reorganization of the cytoskeleton and modification of the mitochondria interplay with other organelles. In conclusion, our data suggest that β-cells sense and respond to nanoscale features by activating a mechanotransductive pathway that promotes β-cell survival and function. By engineering microenvironments mirroring the biophysical niche properties it is possible to elucidate the β-cell mechanotransductive-regulatory mechanisms and to harness them for the promotion of β-cell differentiation capacity. This hopefully will allow us to improve the efficacy of β-cell transplantation therapies and to identify a core set of signaling pathways useful for accelerating regenerative strategies for diabetes treatment.

Abstract -Italian

Le cellule β-pancreatiche svolgono un ruolo fondamentale nell'omeostasi glucidica, essendo le uniche cellule del corpo in grado di produrre e secernere insulina. Alterazioni della loro funzionalità o del loro numero determinano lo sviluppo del diabete mellito, un gruppo di patologie ad eziologia eterogenea caratterizzate da iperglicemia. L'approccio più efficace per trattare i pazienti diabetici dovrebbe consistere nel ripristinare la funzionalità o la massa β-cellulare tramite terapie rigenerative o sostitutive. Tra le terapie sostitutive particolarmente promettenti vi sono quelle che utilizzano cellule staminali embrionali o pluripotenti. Tuttavia, i protocolli ad oggi disponibili per promuovere il loro differenziamento *in vitro* non sono del tutto efficaci nel generare cellule β completamente mature. Le cellule β, infatti, per essere funzionali ed efficienti necessitano di uno specifico microambiente che fornisca molteplici stimoli chimici e fisici. Particolarmente studiati sono gli stimoli chimici, mentre poco conosciuti sono gli effetti delle proprietà fisiche della matrice extracellulare. Lo scopo del nostro studio è stato, quindi, quello di valutare l'impatto della nanotopografia sul differenziamento e la funzionalità β-cellulare e caratterizzarne i meccanismi molecolari coinvolti. Per riprodurre le proprietà nanotopografiche della matrice extracellulare sono stati utilizzati substrati di zirconio ingegnerizzati su scala nanometrica. Nel nostro lavoro abbiamo dimostrato che le cellule β percepiscono la nanotopografia della matrice e rispondono attraverso una riorganizzazione del citoscheletro di actina e dell'architettura nucleare. Tale processo, noto come meccanotrasduzione, permette il mantenimento delle isole di Langerhans per lungo tempo in cultura, preservando il differenziamento e la funzionalità delle cellule β. I nostri dati, inoltre, dimostrano che la nanostruttura induce una modifica della dinamicità, morfologia e funzionalità mitocondriale favorendo un cambiamento del metabolismo β-cellulare. Anche il processo mitomorfico sembra essere direttamente promosso dalla riorganizzazione del citoscheletro e dalla modifica delle interazioni dei mitocondri con altri organelli citoplasmatici. Nell'insieme, i nostri dati dimostrano che le cellule β percepiscono e rispondono alla nanotopografia attivando un processo meccanotransduttivo che promuove la sopravvivenza e la funzionalità β-cellulare. L'utilizzo di substrati ingegnerizzati che riproducono le proprietà biofisiche del microambiente rappresenta un ottimo strumento per approfondire le conoscenze sui meccanismi molecolari alla base della meccanotransduzione. Queste conoscenze saranno utili per potenziare le terapie rigenerative e per promuovere il differenziamento di cellule staminali in vitro, migliorando così anche l'efficacia delle terapie sostitutive.

1. Introduction

Pancreatic β-cells reside within the islets of Langerhans, small cell clusters (50-200 μm diameter) representing only 1-2% of the whole pancreas (Aamodt and Powers, 2017). In response to changes in nutrient concentrations in the blood stream, in particular glucose and amino acids, islets of Langerhans release hormones controlling whole body glucose homeostasis. Islets can be considered endocrine organs in miniature, since they contain five endocrine cells responsible for hormone synthesis and secretion: α-cells for glucagon, β-cells for insulin, δ-cells for somatostatin, ε-cells for ghrelin, and F-cells for the pancreatic polypeptide production.

In the last years, a number of studies have focused on differentiation and survival of islet cells, and on the regulation of hormone release, since it appears that the complex mechanisms underlying such a regulation are strictly related to many metabolic disorders, including diabetes mellitus, a group of pathologies characterized by severe hyperglycemia. The worldwide accepted classification of diabetes mellitus was published in 2003 by the American Diabetes Association which clustered the diabetic cases into 4 groups according to their etiopathogenesis: type 1 and type 2 diabetes mellitus, the maturity onset diabetes of the young (MODY), and the gestational diabetes (American Diabetes Association, 2014). MODY is a genetic disease characterized by a punctiform mutation in genes controlling the β-cell function and differentiation. Gestational diabetes affects about 4% of pregnant women. It is caused by the placental high production of prolactin and estradiol that antagonize the insulin effects on peripheral tissues (Solis-Herrera et al., 2018). Type 1 and type 2 diabetes represent approximately the 99% of diabetic cases. Type 1 diabetes (T1D), which accounts for 9-10% of diabetic patients, is characterized by an immune mediated-destruction of pancreatic β-cells resulting in insulin deficiency; the standard therapy for T1D patients is the administration of exogenous insulin (DiMeglio et al., 2018). Type 2 diabetes (T2D) represents the 90% of diabetic cases and its incidence is exponentially growing, so much that 700 million people will be affected by T2D in 2045 (Cho et al., 2018). During the development of T2D, insulin is not able to compensate the increased blood glucose concentration due to peripheric insulin resistance and β-cells dysfunction. Nowadays, it is not completely clear whether the insulin resistance causes the β-cell dysfunction by increasing the metabolic demand or insulin resistance and β-cell dysfunction occur simultaneously. At late stages, decreased β-cell mass due to β-cell apoptosis or de-differentiation is observed in T2D diabetic patients (Butler et al., 2003; Folli et al., 2018; Talchai et al., 2012). Current therapies aim to increase insulin secretion and improve insulin sensitivity; however, when these treatments fail, the last resource is the insulin injection therapy just as in T1D patients. Although type 1 and type 2 diabetes etiopathogenesis is different, the destruction of pancreatic β-cell mass represents the final common outcome. Therefore, despite current therapies are effective in controlling the blood glucose levels, the regeneration of β-cell mass is necessary to have remission and only regenerative or replacing therapies can resolve the problem (Peloso et al., 2018).

1.1 Strategies for β-cell replacement

The whole pancreas transplantation represents the first attempt to replace the β-cell mass and it has been carried out since 1966. Originally, this procedure was performed only in selected patients with end-stage renal failure together with a kidney transplant (Lombardo et al., 2017). However, the improvement of the surgery and of the immunosuppressive pharmacological treatments resulted in a successful whole pancreas transplantation alone with a graft survival rate of 76% and 62% at one and three years (Vaithilingam and Tuch, 2011). As a result, over the decades, the

number of transplantations has greatly increased and the International Pancreas Transplantation Registry (IPRT) reports 23043 transplantation till 2011 (Cohen et al., 2006). Despite its clinical successful, since whole pancreas transplantation is a major surgical intervention that requires life-long immunosuppressive therapy, alternative strategies such as the transplantation of pancreatic islets alone have been proposed (Peloso et al., 2018).

1.1.1 Allogeneic pancreatic islets transplantation

The first islet transplantation was performed in 1972 in chemically induced diabetic rats (Ballinger and Lacy, 1972) and only five years later, Sutherland's group proposed the first islets infusion in humans (Najarian et al., 1977). Islet transplantation has dramatically improved only in 2000 with the publication of the Edmonton protocol, achieving a 100% insulin independence in seven T1D patients treated with immunosuppressive drugs (Shapiro et al., 2000). Modification and improvement of the Edmonton protocol currently result in 5-years insulin independence in the 50–70% of patients undergoing islet transplantation (Gamble et al., 2018; Pepper et al., 2018; Shapiro et al., 2017). The islet transplantation presents many advantages compared to the whole pancreas transplant. It is a non-invasive surgical procedure mainly performed through a transhepatic portal infusion that reduces the morbidity and the use of immunosuppressive drugs. However, the islets transplantation has important drawbacks starting with the low survival of the islets graft due to the hypoxia-induced β-cell death and the immune attack from the host immune surveillance (Desai and Shea, 2017; Pellegrini et al., 2016). The most promising attempt to solve these problems consists in encapsulating the isolated islets with semipermeable bioinert membranes that prevent the penetration of immune cells, while allowing the flux of nutrient, oxygen, glucose and other metabolites (Salvatori et al., 2014). Several biomaterials carriers have been investigated including natural biomaterials such as protein or polysaccharide-based scaffolds, and synthetic biomaterials as poly-glycolic acid (PGA), poly-L-Lactic acid (PLLA), poly-Lactic-co-Glycolic Acid (PLGA) and poly-ethylene glycol (PEG) (Wheeldon et al., 2011). The encapsulation technology only partially solves the autoimmune response, since the islets remain vulnerable to the attack of chemokines and cytokines which have a molecular weight comparable to insulin (Vaithilingam and Tuch, 2011). Encapsulation is also challenging because the highly metabolic β-cells require high oxygen availability. To ensure an appropriate oxygen availability islets must be immobilized in the device at relatively low surface density (as low as about 1,000 islet equivalents for 1 cm^2) (Papas et al., 2016). Oxygen-generating devices have also been developed by including calcium peroxide within the encapsulating biomaterials, which ensure the release of oxygen for more than 40 days (Desai and Shea, 2017; Pedraza et al., 2012). Table 1.1 shows the islets encapsulation devices that are currently in clinical trials; they present a good safety profile but further studies are required to assess their functional outcomes.

Device	*Properties*	*Trial phase*	*References*
βAir	Disc-shaped device formed by 2 chambers: an alginate slab containing the islets and a gas releasing chamber	I/II	(ClinicalTrials.gov, 2016)
Theracyte™	Double membrane device that promotes subcutaneous vascularization. Islets seeding after vessel ingrowth into the pouch	I/II	(Kumagai-Braesch et al., 2013)
Sernova Cell Pouch	Promote the vascularization through a series of rods. Islets seeding, upon vessel ingrowth, in the spaces obtained by rods removal	I/II	(ClinicalTrials.gov, 2016b)
Alginate scaffolds	Isolated islets dispersed within mono or multilayers alginate scaffolds	I/II	(ClinicalTrials.gov, 2016c, 2013)

Table 1.1. *Islets encapsulation devices currently in clinical trials.*

Encapsulation technologies have dramatically improved the success of islet transplantation, but the shortage of human islets, due to the limited availability of cadaveric tissue, remains the main challenge to be solved. Indeed, for a successful transplantation the minimum requirement is 5000 islets equivalent (IEQ) per kg body weight resulting in at least 2-4 whole cadaveric pancreata for one patient (Salvatori et al., 2014; Shapiro et al., 2006). For this reason, increasing efforts have been focused on the isolation and the expansion of β-cells from xenogeneic sources.

1.1.2 Xenogeneic pancreatic islets transplantation

Porcine islets represent the best candidates for xenogeneic islets transplantation since pig insulin is similar to the human one and porcine β-cells regulate blood glucose levels in the same physiological range as human' (Klymiuk et al., 2010). The first clinical attempt was performed in 1994 (Groth et al., 1994). Interestingly, a device containing porcine islets, called Diabecell, has reached the phase II clinical trials; it consists of an alginate scaffold that is delivered in the peritoneal cavity by laparoscopic surgery (ClinicalTrials.gov, 2014). Although porcine islets can solve the shortage of islets for transplantation, the risk of hyperacute immunologic reaction and of zoonosis dramatically limits the xenogeneic islet transplantation (Pellegrini et al., 2016). Therefore, in the last few years, a great attention has been focused on β-cell expansion and differentiation from alternative sources.

1.1.3 β-cell generation from reprogramming of islet resident cells

Reprogramming of pancreatic cells, other than β-cells, into functional β-cells represents a promising strategy for β-cell generation (Guney et al., 2020). Pancreatic cells derive from a common multipotent progenitor and maintain significant plasticity during adulthood (Osipovich and Magnuson, 2018). Increasing efforts have been focused on reprogramming non-β cells into mature, functional β-cells. Acinar/ductal conversion into β-cells can be achieved by forcing their de-differentiation into a progenitor-like state and inducing, by viral transfection, the expression of Pdx1 (pancreatic and duodenal homeobox 1), Ngn3 (neurogenin 3) and MafA, three transcription factors that promote β-cell commitment (Cavelti-Weder et al., 2017; Jawahar et al., 2019).

However, alteration of acinar-ductal cells ratio can induce inflammation and acinar-to-ductal metaplasia leading to pancreas dysfunction (Clayton et al., 2016). α-cells represent the most suitable candidates, as they are functionally more similar to β-cells and a decrease in their number apparently does not affect glucose metabolism (Thorel et al., 2010). The conversion of α-cells into β-cells has been achieved by forcing the expression of β-cell specific transcription factors as Pax4, Pdx1 and MafA (Collombat et al., 2009; Matsuoka et al., 2017; Xiao et al., 2018; Yang et al., 2017), or disrupting Dnmt1 and Arx, transcription factors crucial for maintaining the α-cell identity (Chakravarthy et al., 2017). Another approach consists in the regulation of GLP1 (glucagon-like peptide 1) expression, which modulates the PI3K/AKT/FOXO1 pathway, resulting in increased Pdx1 and MafA mRNA expression, without affecting the proliferation of other pancreatic cell population (Zhang et al., 2019b). Long-term administration of gamma-amino butyric acid (*GABA*) also results in robust conversion of α cells to β cells *in vitro* and *in vivo* (Ben-Othman et al., 2017).
Even tough successful β-cell generation has been achieved, additional evaluations that go beyond studies in mice will be required in order to test the safety of viral transfection and the effectiveness of the method *in vivo* (Osipovich and Magnuson, 2018).

1.1.4 β-cell replacement with stem-cell derived β-cell

Stem cells are able to proliferate and maintain their stemness indefinitely (process known as self-renewal) and to differentiate into different cell types under appropriate stimuli (Brafman, 2013; Nava et al., 2012). For these reasons, stem cells may represent an unlimited source of β-cell for transplantation and a unique model for pharmacological and developmental studies. Over the past ten years, increasing efforts have been focused on generating β-like cells from human embryonic stem cells (hESCs) and human-induced pluripotent stem cells (hiPSCs) (Tremmel and Odorico, 2018). Differentiation of stem cells toward β-cells is a long stepwise process that mimics *in vitro* the expression of selected transcription factors which normally regulate pancreas development *in vivo*. The first step is the conversion of pancreatic progenitor cells expressing Pdx1, into bipotent pancreatic cells characterized by the expression of Hnf6 (Murtaugh, 2006). The bipotent pancreatic progenitor generates either ductal cells if Hnf6 expression persists, or endocrine precursors if Ngn3 expression raises (Johansson et al., 2007). The final differentiation into insulin-producing β-cell is achieved through the time-dependent expression of several transcription factors, as Pax6, Pax4, Nkx2.2 and Nkx6.1 (Murtaugh, 2006). The first differentiation protocol aimed at large-scale β-cells production intended for clinical use was published in 2014 by Melton's group (Pagliuca et al., 2014). In the same year, Rezania et al., proposed another procedure for the differentiation of hiPSC toward an enriched β-cell population (Rezania et al., 2014). Despite the β-like cells obtained by these protocols had similar genetic profile and glucose stimulated insulin secretion (GSIS), they were still immature compared to primary human islets. Indeed, the proinsulin/insulin ratio was elevated and the dynamic GSIS was lower compared to primary islets. Furthermore, only approximately 50% of cells were insulin-positive (Pagliuca et al., 2014; Rezania et al., 2014). The differentiation rate was dramatically improved in 2019 by Hebrok's group, which proposed a strategy based on the *in vivo* endocrine clustering process. Insulin GFP tagged cells were sorted by Fluorescence-activated Cell Sorting (FACS) to obtain an enrichment of β-like cells, clustered and cultured for 6-8 days. The obtained population resulted highly enriched in insulin and chromogranin positive cells (about 99%), and performed a successfully dynamic GSIS. However, the second phase insulin release was very low and the insulin mRNA level was 10-fold lower than primary islets (Nair et al., 2019). Today,

only one device, the ViaCyte, carrying hESC-derived pancreatic progenitors has reached the phase II clinical trials. It consists of a semipermeable membrane (Encaptra) that allows the in-out flux of oxygen and nutrients, while blocking the immune cell attack (Figure 1.1) (Desai and Shea, 2017).

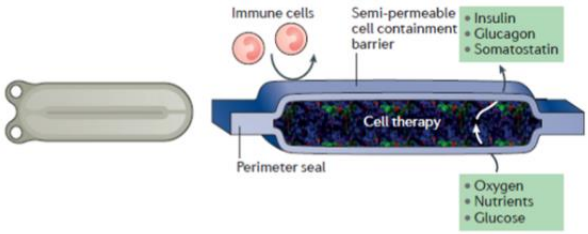

Figure 1.1. *Schematic representation of the ViaCyte device. Adapted from Desai and Shea, 2017.*

Although we can reproduce *in vitro* the time-dependent expression of transcription factors regulating β-cell differentiation, a completely mature β-cell phenotype has not been obtained yet. In addition to the genetic control of β-cell differentiation, there are several other factors that must be taken into consideration for the successfully generation of mature β-cells. Firstly, *in vivo* β-cells communicate with other cell types within the islets such as endocrine cells, neurons and endothelial cells. Their cross-talk is crucial for ensuring the β-cell proliferation, differentiation, and function. In addition, β-cells are supported by the extracellular matrix (ECM) which regulates the islet architecture and provides a plethora of signals that can promote β-cell maturation. Therefore, in order to replicate *in vitro* the full functional islet, a complete characterization and comprehension of the environmental cues of the islet niche is imperative (Galli et al., 2020).

1.2 The islet niche

The term niche, proposed for the first time by Schofield in 1978, indicates the natural microenvironment where cells develop and reside (Schofield, 1978). The islet niche is a complex and dynamic environment, consisting of different cell types and the ECM, which provides a myriad of signals crucial for regulating β-cell development, differentiation and function (Figure 1.2).

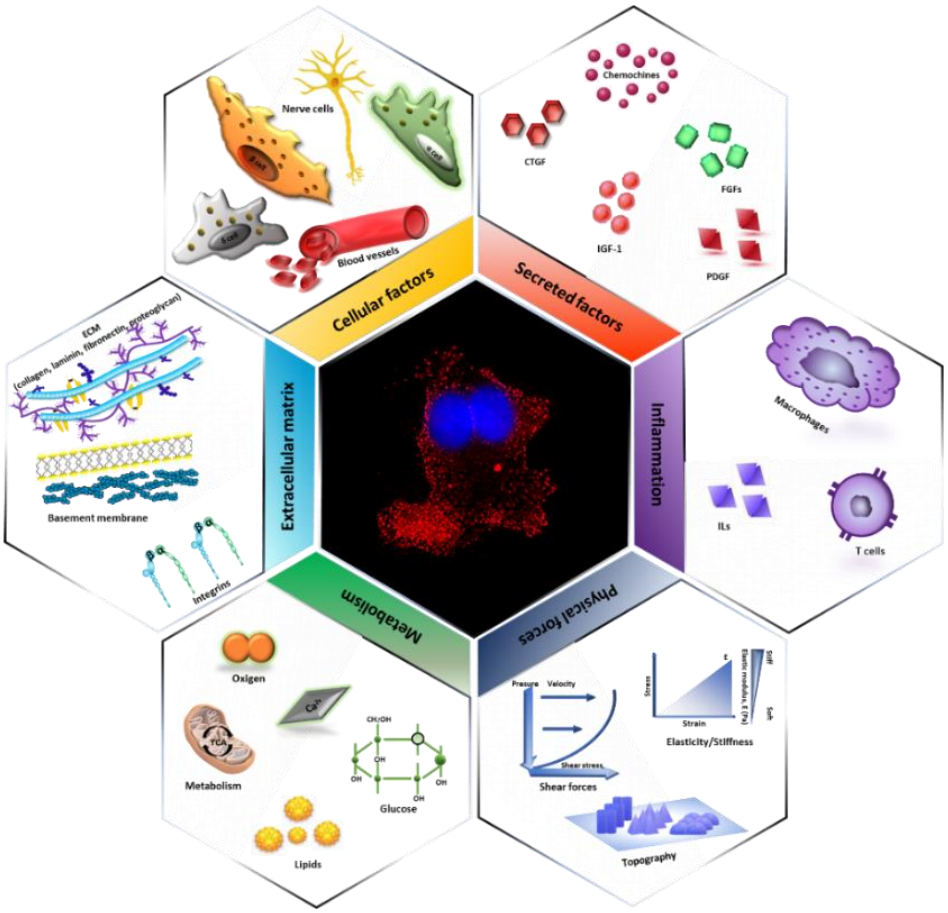

Figure 1.2. *The islet niche and the extracellular cues influencing β-cell development, differentiation and function. (Galli et al., 2020)*

1.2.1 Endocrine cells

In human islets, β-cells are dispersed within the other endocrine cells: the glucagon producing α-cells and the somatostatin-positive δ-cells. Minority populations of PP-cells, that produce the pancreatic polypeptide, and ghrelin cells, that secrete the ghrelin hormone, can also be detected (Stendahl et al., 2009). These cells not only secrete hormones crucial for regulating glucose homeostasis, but also produce paracrine signals that shape the β-cell fate. Among these signal molecules are neurotransmitters and neuropeptides. α-cells release glutamate and acetylcholine, which are known to regulate the β-cell survival. β-cells secrete γ-aminobutyric acid (GABA), serotonin, adenosine tri-phosphate (ATP), and dopamine that promote β-cell proliferation during pregnancy and adulthood (Di Cairano et al., 2016). The inter-endocrine cell interactions and the autocrine and paracrine effects produced by the secreted molecules, provide a myriad of signals regulating the islet physiology.

1.2.2 Other resident cells

Pancreatic β-cells are also strictly interconnected with the blood vessels which ensure the bidirectional exchange of signaling molecules and hormones (Bonner-Weir, 1988; Brunicardi et al., 1996). The islet vasculature regulates the hormone secretion, in addition provides several paracrine factors modulating the β-cell proliferation and survival. Endothelial cells produce VEGF-A (Vascular Endothelial Growth Factor A) which promotes the embryonic development of the pancreas and regulates the β-cell mass in adulthood (Brissova et al., 2006; Lammert and Thorn, 2019). In addition

to the VEGF-A signaling, other growth factors are secreted by the islet vasculature and strongly affect cellular behavior:

- the insulin-like growth factor (IGF-1) that regulates the glucose homeostasis by binding to the IGF-1 and insulin receptors (Assmann et al., 2009);
- the platelet-derived growth factor (PDGF) that modulates the β-cell proliferation by activating the ERK pathway (Chen et al., 2011);
- the connective tissue growth factor (CTGF) that is crucial for the endocrine cell commitment during pancreas development (Guney et al., 2011).

Autonomic neurons and macrophages are also detected within the islet niche. Neuronal cells fine-tune the hormone secretion and exert trophic function (Rodriguez-Diaz et al., 2012). Macrophages, whose phenotype is dictated by the signals provided by the environment, regulate the β-cell regeneration (Xiao et al., 2014).

1.2.3 The extracellular matrix

The extracellular matrix is a non-cellular macromolecular network that provides a plethora of signals crucial for cell adhesion, differentiation, survival and function (Shekaran and Garcia, 2011). Each tissue presents a unique and specific ECM composition which is generated during embryonic development and is constantly remodeled in adulthood (Frantz et al., 2010). Cells perceive and respond to the ECM shaping their activity and releasing macromolecules, which, in turn, affect the ECM composition (Galli et al., 2020). The pancreatic ECM is constituted by 3 different interconnected layers. The first one, known as stromal ECM, creates an incomplete capsule around the islets and it is closely associated with the underneath basement membrane (BM) (Stendahl et al., 2009; Townsend and Gannon, 2019). In human islets, the endocrine cells are surrounded by two different types of basement membrane: the vascular BM that is produced by the endothelial cells acts as a reservoir of growth factors and the peri-islet BM which invaginates into islets following the pervading microvasculature. The peri-islet BM is a thick, porous layer that provides a 3D scaffolds for cell attachment and regulates the exchange of signaling molecules within the islet (Aamodt and Powers, 2017; Stagner et al., 2004). In mammals, the ECM is composed of 300 proteins and glycoproteins that constitute the so-called core matrisome (Hynes and Naba, 2012). The islet ECM consists of a mixture of proteins, glycoproteins, proteoglycans and glycosaminoglycans (Table 1.2) (Hughes et al., 2006); although the pancreatic ECM composition is largely known, the function of some ECM molecules in regulating islets physiology needs to be fully characterized.

ECM component	*Structure*	*Function*	*References*
Collagens	Triple helical domain glycoproteins organized in fibrillar and non-fibrillar structures	Scaffolds for cell attachment; regulate pancreatic β-cell survival and proliferation	(Aamodt and Powers, 2017; Kaido et al., 2004; Stendahl et al., 2009; Townsend and Gannon, 2019)
Laminins	Trimeric glycoproteins constituted by α, β and γ chains	Maintain islet shape; regulate pancreas development; promote β-cell identity and metabolism	(Leite et al., 2007; Lin et al., 2010; Llacua et al., 2018)
Proteoglycans	Heterogeneous family of molecules composed of a core protein covalently linked to one or more glycosaminoglycans	Regulate the compressive resistance; control the post-natal islet growth and maturation; promote β-cell differentiation	(Beattie et al., 1996; Iozzo and Schaefer, 2015; Lammert and Thorn, 2019; Schaefer, 2014; Townsend and Gannon, 2019)
Fibronectin	Dimeric glycoprotein organized in fibrils that possess the RGD recognition motif	Regulate cell attachment; improve β-cell survival, differentiation and function	(Atchison et al., 2010; Hogrebe et al., 2017; Leite et al., 2007; Lin et al., 2010; Pankov and Yamada, 2002; Weber et al., 2007)

Table 1.2. *Components of islet extracellular matrix and their impact on cell development, survival and function.*

1.2.3.1 Collagens

Collagens are the most abundant glycoproteins accounting for the 90% of the ECM components (Frantz et al., 2010; Phillip et al., 2015). They regulate the stiffness and the tensile strength of the ECM and act as scaffolds for cell attachment (Rozario and DeSimone, 2010). To date, 28 types of collagens have been detected in vertebrates, which are classified into fibrillar (type I, II, III and V) and non-fibrillar (type IV and VI) molecules according to their chemical structure and organization (Ricard-Blum, 2011). Collagens are constituted by three α-chains that associate to form a right-handed triple helix thanks to the repeating Gly-X-Y motif (where X and Y can be any aminoacids) (Mouw et al., 2014). Collagen molecules are subjected to constant turnover and remodeling according to signals provided by the other cells within the niche. By the mRNA translation, the collagen producing cells, as fibroblasts, synthetize the pre-pro-collagen, which is imported into the rough endoplasmic reticulum (RER). Here, the proline and lysine residues of the α-chains are hydroxylated, favoring the triple-helix assembly that is further stabilized by disulfide bonds. The newly synthetized pro-collagen moves from the RER to the Golgi apparatus where it is further modified and packed into secretory vesicles. Once released in the extracellular space, proteolytic modifications lead to the formation of mature collagens which start to assembly into fibrils (20-100 nm in diameter) and fibres (0.5-20 µm in diameter) (Figure 1.3).

In human islets collagen I, II and III form long fibres, IV is organized in network and VI creates beaded. While all these molecules are distributed in the peripheral ECM, collagen IV and VI are most abundant in the BM where they regulate cell fate. Indeed, it has been demonstrated that collagen IV promotes cell survival and proliferation, and can reduce insulin production and secretion in β-cells (Kaido et al., 2004).

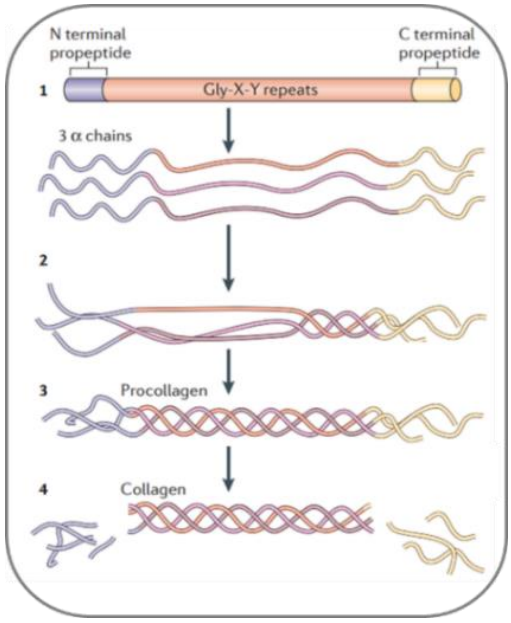

Figure 1.3. *Schematic representation of collagen synthesis. 1,2) Pre-pro-collagen is imported in the RER where it is chemically modified forming the typical triple-helical conformation. 3) Pro-collagen is transferred into the Golgi apparatus where it is stored in the secretory granules. 4) Proteolytic cleavages in the extracellular space generate the mature collagen. Adapted from Mouw et al., 2014.*

1.2.3.2 Laminins

Laminins, a family of 15 to 20 heterotrimeric glycoproteins, consist of three polypeptide chains (α, β and γ) linked by disulfide bonds (Llacua et al., 2018; Salvatori et al., 2014). Laminins can assume cross-shaped, Y-shaped or rod-shaped structures depending on the polypeptide chain isoforms/stoichiometry involved (Mouw et al., 2014) (Figure 1.4). The most abundant types of laminin (LM) detected in human islets are: LM-511 and 521 that are mainly expressed in the peri-islet BM, LM-411 and 421 that are present in the vascular BM and LM-322 that is closely associated to the α-cells. LM-111, which is completely replaced by the 511 isoform, is only expressed during pancreas development when promotes the β-cell differentiation and survival (Jiang et al., 1999, 2002; Virtanen et al., 2008). Aside from their structural activity, laminins modulate the expression of transcription factors (PDX1) and hormones (glucagon, somatostatin and insulin) which are crucial for the endocrine-cell commitment (Leite et al., 2007). In addition, these glycoproteins activate the AKT and ERK signaling pathways which are important players in the control of β-cell metabolism and insulin secretion (Lin et al., 2010).

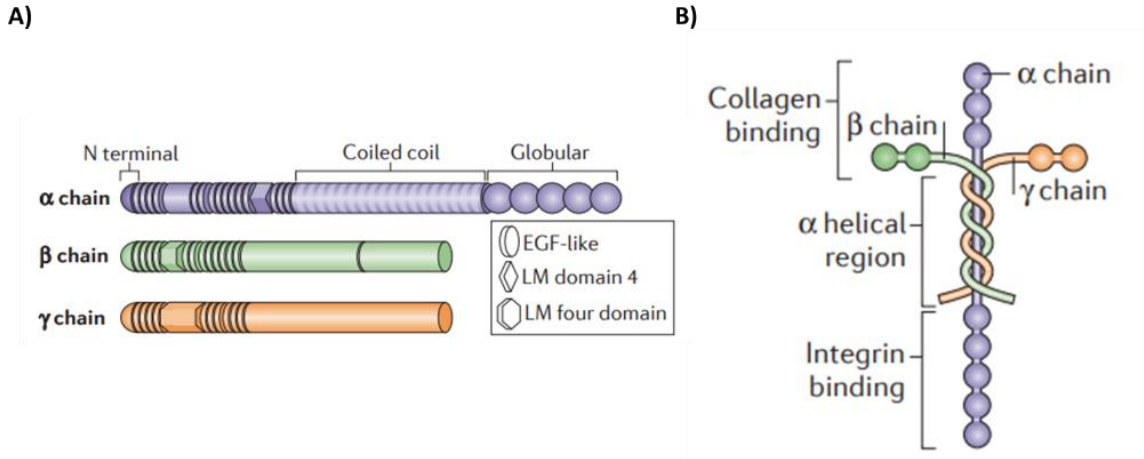

Figure 1.4. *Laminins structure.* ***A)*** *Schematic representation of α, β and γ chains.* ***B)*** *Three-dimensional spatial organization of the polypeptide chains. Adapted from Mouw et al., 2014.*

1.2.3.3 Proteoglycans

Proteoglycans represent a heterogeneous family of molecules with a protein core covalently linked to glycosaminoglycan (GAG) chains, linear, negatively charged, sugar complexes composed of hexosamine disaccharides units. An exception is the hyaluronan, the only proteoglycan that lacks the protein core (Iozzo and Schaefer, 2015; Schaefer, 2014). Heparan sulfate, hyaluronan, aggrecan and perlecan are the most abundant proteoglycans in human islets; they are preferentially distributed in the peri-islet capsule, except for the heparan sulfate (HS) that is concentrated in the inter-cellular spaces within the islet (Llacua et al., 2018; Mouw et al., 2014). According to their structure, these molecules sequester water and cations, regulating the ECM hydration which, in turn, affects the compressive resistance of tissues. In addition to their structural activity, by binding growth factors and signaling molecules, proteoglycans regulate their availability at the site of action (Frantz et al., 2010; Humphrey et al., 2014). For example, HS sequesters VEGF-A, indirectly affecting β-cell development, mass and function (Aamodt and Powers, 2017).

1.2.3.4 Fibronectin and vitronectin

These molecules belong to the large family of matrix glycoproteins (Hogrebe et al., 2017); while fibronectin is always expressed, vitronectin is only detectable during the pancreas development (Aamodt and Powers, 2017). Fibronectins are produced within the cells as dimers which assemble into fibrillar structures around the cells. Under stimuli, fibronectins expose the RGD (tripeptide arginine-glycine, aspartic acid) motif, a flexible loop that is recognized by integrin and non-integrin receptors (Pankov and Yamada, 2002). This binding not only facilitates the cell attachment, but also regulates islets survival by upregulating the activity of Bcl2 (B-Cell Lymphoma 2) (Atchison et al., 2010; Weber et al., 2007). In addition, it has been demonstrated that fibronectin stimulates the GSIS and promotes β-cell differentiation by modulating the expression of pro-differentiation genes (as Pdx1 and Pax6) (Leite et al., 2007; Lin et al., 2010).

1.2.4 Mechanical cues within the islets

As discussed above, biochemical cues arising from the islet niche regulate several aspects of islet physiology. Actually, β-cells are also subjected to biophysical signals such as those provided by the ECM stiffness and topography generated by the 3D assembly and turnover of matrix macromolecules, and the shear stress created by the blood flowing in the vessels. Despite being well known since the antiquity that mechanical forces enable us to breathe or move, their role in shaping the cell behavior and fate was recognized only in the 1970s (Humphrey et al., 2014; Li et al., 2017). In this chapter I will describe the mechanical cues within the islet niche but, as their effects on β-cells are yet to be fully characterized, I will mainly report their impact on other organs.

1.2.4.1 Shear stress

The shear stress is the friction force, reaching a magnitude of 2-4 kPa, generated and exerted by the blood flow on the cell surfaces. Endothelial cells are obviously the most influenced by this mechanical strain which modulates the expression of genes regulating the vascular homeostasis; furthermore, an abnormal shear stress can induce endothelial cells to become atherogenic (Brafman, 2013; Dunn and Olmedo, 2016; Wittkowske et al., 2016). Although the magnitude of the friction force is reduced outside the vascular system, shear stress can also influence cell behavior in non-vascular tissues, such as the MDCK cell line derived from kidney epithelial cells, in which the

deflection of the primary cilium causes influx of calcium (Praetorius and Spring, 2003). Human islets are pervaded by the microvasculature, suggesting a potential role of shear stress in their development and function. Lodh and colleagues demonstrated that blood flow, perceived by cilia, modulates the β-cell polarization during pancreas development (Lodh et al., 2014). In addition, shear stress indirectly regulates the insulin secretion. The opening of TRPP2 (Transient Receptor Potential non selective cation) channel, caused by the flow-induced deflection of the primary cilium, contributes to the intracellular calcium fluctuation necessary for the insulin granules fusion (DiIorio et al., 2014).

1.2.4.2 Stiffness

The stiffness is the force necessary to deform or deflect a "body" and it is measured in Pascal (Pa). It is empirically calculated by applying a force across a specific area and measuring the obtained deformation (Wozniak and Chen, 2009). In the field of mechanobiology, the tissue stiffness depends on the ECM composition and architecture; for instance, the deposition of calcium phosphate within the ECM renders the bone the stiffest tissue within the body (d'Angelo et al., 2019). Considering non-calcified organs, the stiffness correlates with the ECM hydration state regulated by the expression of proteoglycans, the collagen isoform, and the percentage of cross-linking; indeed, collagen networks are multi-fold softer than a single collagen fiber (van Helvert et al., 2018; Swift et al., 2013). Within the body, the stiffness ranges from 0.1-10 kPa in soft tissues (brain or pancreas) to 1-2 GPa in hard tissues (bones) (Brafman, 2013) (Figure 1.5).

ECM stiffness regulates cellular behavior and function, affecting numerous developmental, physiological and pathological processes (Pelham and Wang, 1997). The stiffness changes during development, as the embryonic tissues are much softer than the adult counterparts (von Dassow and Davidson, 2007), and can be modified by pathological states; for example, an infarcted myocardium is 10-fold stiffer than a healthy one and the mammary stiffness increases from 1 to 4 kPa in breast cancers (Herum et al., 2017; Yang et al., 2017) (Figure 1.5).

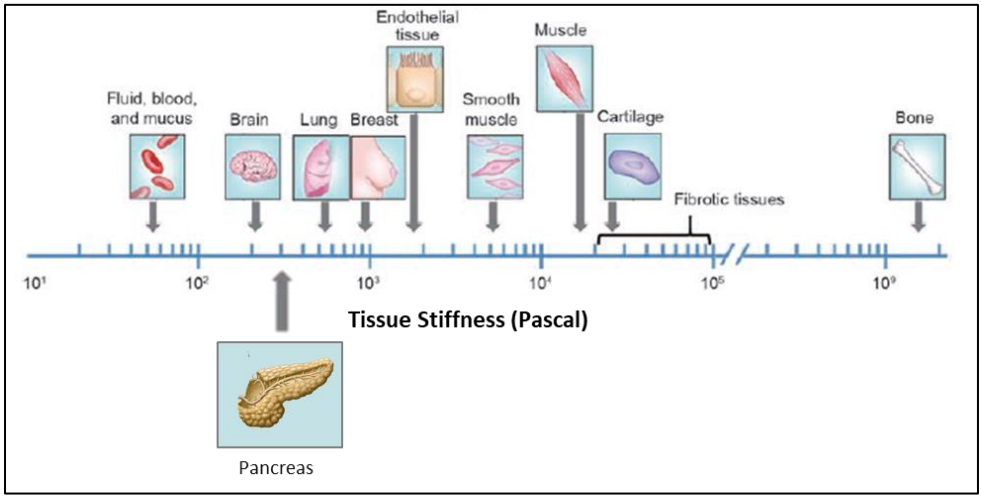

Figure 1.5. *Stiffness of tissues within the human body. The stiffness has been estimated to range from 0.1-10 kPa in soft tissues (brain or pancreas) to 1-2 GPa in hard tissues (bones). Fibrotic tissues become stiffer than those in healthy condition. Adapted from Yang et al., 2017*

Environmental stiffness has also been reported to dictate stem cell differentiation. For example, mesenchymal stem cell (MSCs) lineage specification can be guided by the tissue-specific rigidity as

the cells differentiate into neurons when cultured on soft matrices (0.1-1 kPa) mimicking the brain, while osteogenic cells are obtained when plated on stiffer substrates (25-40 kPa) (Engler et al., 2006). The matrix stiffness can also influence cell commitment within the same tissue as soft substrates (0.5 kPa) favor the neuronal differentiation, whereas stiffer environments (1-10 kPa) promote glial specification (Saha et al., 2008). In addition, the deformation of the matrix occurring in soft substrates allows the force transmission to neighboring cells, strongly influencing the collective cell behavior (Ladoux and Mège, 2017).

Pancreatic β-cells are surrounded by two types of BMs, whose stiffness, ranging from 0.1 to 17 kPa, classifies the pancreas as a soft tissue (Nyitray et al., 2014). Since standard culturing conditions have much higher stiffness, in the GPa range, than that observed in the islet niche, *in vitro* cultured, human isolated islets of Langerhans lose their inter-cellular organization, leading to an impairment of β-cell survival and function (Herum et al., 2017).

1.2.4.3 Topography

The topography defines the distribution of surface features and it is described by parameters as roughness, lateral spacing, height and periodicity (Nguyen et al., 2016). *In vivo*, cells are exposed to a variety of micro- and nano-topographical cues generated by the ECM organization and architecture (Donnelly et al., 2018; Kim et al., 2012) (Figure 1.6).

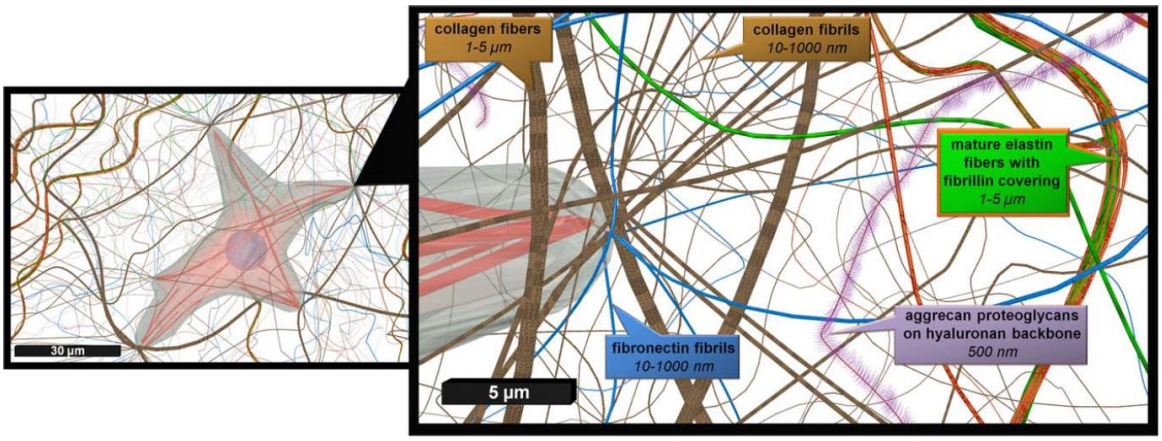

Figure 1.6. *Micro- and nano-environmental cues within the ECM. Micro-sized topography is dictated by the assembly of macromolecules, while the distribution of individual ECM proteins regulates the nano-topography. Average diameters of each ECM component are reported. (Hogrebe et al., 2017)*

ECM proteins self-assemble to form large-scale structures, as collagen fibers, ranging from ten to hundreds micrometers, that interact with cells influencing collective cellular behavior (Dalby et al., 2014; Kim et al., 2012). The most characterized example is the contact guidance, the process by which cells perceive the micro-sized topographical stimulus and respond by aligning themselves toward its direction (Bettinger et al., 2009; Curtis and Varde, 1964). While the micro-scale features affect the collective cell behavior, the nanoscale network, created by the distribution of individual ECM molecules, generates multiple cues that regulates single-cell differentiation and function (Donnelly et al., 2018). Nano-topography can solely dictate stem cell specification as clearly shown by Oh and colleagues in 2009. By plating MSCs on nanotubular-shaped titanium surfaces of different size they were able to demonstrate that cell fate was nanotube-size dependent. On small nanotubes (30 nm in diameter), MSCs retain a round-shape which promotes their proliferation,

whereas larger nanotubes (100 nm in diameter) induce a 10-fold increase of elongated cells resulting in osteogenic differentiation (Oh et al., 2009). The results were also confirmed in neuronal progenitor cells of rat by other groups (Christopherson et al., 2009; Migliorini et al., 2011). Furthermore, anisotropic patterning (nanoscale structures without any directional properties) enhances neuronal differentiation, while isotropic ones favor glial specification; a possible explanation is that cells establish and maintain their polarity in anisotropic environments (Yang et al., 2017). Giving the similarities between neurons and pancreatic β-cells, it is reasonable to believe that nano-sized cues can also affect the islet homeostasis but, to best of my knowledge, nothing is known about their role in regulating β-cell functions.

1.2.4.4 Geometry

Geometry describes the three-dimensional organization of the extracellular environment, generated by the distribution of cells and ECM molecules within the niche. Each component, which has a specific topography and stiffness, interacts with the others, creating stiffness and topography gradients crucial for regulating cell migration, polarity, and behavior. The best characterized impact of these gradients on cell fate is known as durotaxis, the phenomenon by which cells preferentially migrate from soft to stiffer substrates (Hartman et al., 2016). Furthermore, a 3D environment can indirectly promote a collective response to extracellular stimuli by favoring cell-cell interactions and preventing cell scattering (Doyle and Yamada, 2016; Vining and Mooney, 2017). For these reasons, modulating the geometry of the environment can be a promising strategy for shaping the β-cell function, but its effects are yet to be fully characterized.

1.3 Cellular machinery for sensing mechanical forces

The major challenge in studying the impact of these mechanical forces *in vivo* is to isolate the mechanical stimulus from other autocrine and paracrine signals (Guilak et al., 2009). For these reasons, the majority of studies are carried out *ex vivo* or *in vitro* culture systems, using biomaterial scaffolds or decellularized ECM. Despite these issues, nowadays, it is well established that cells perceive, exert, decipher, and respond to mechanical stimuli. The mechanoresponsiveness of cell can be divided into 2 main events, referred as mechanosensing and mechanotransduction (Argentati et al., 2019).

1.3.1 Mechanosensing

Mechanosensing is the ability of the cells to sense and discern environmental mechanical cues through the activation of specific mechanosensors, a heterogeneous group of biomolecules that undergo conformational and organizational changes in response to an applied force (DuFort et al., 2011; Galli et al., 2020; Martino et al., 2018). Several cellular structures have been reported to act as mechanosensors: cell-ECM, cell-cell adhesion complexes (Jansen et al., 2017; Ladoux and Mège, 2017), primary cilia (diIorio et al., 2014), stretch-activated ion channels (Nourse and Pathak, 2017), G-protein coupled receptors (Dunn and Olmedo, 2016), glycocalyx and growth factors receptors (Ingber, 2006) (Figure 1.7). Although they are all expressed in β-cells, their role in mechanosensing is still largely unresolved.

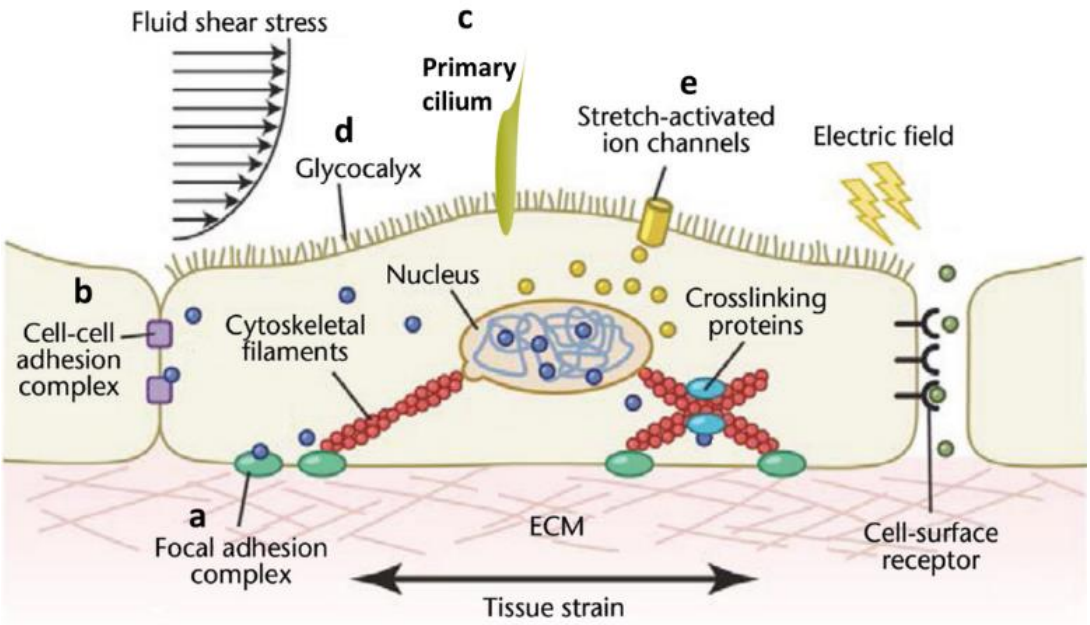

Figure 1.7. *Mechanosensing within the islet niche.* ***a)*** *Focal adhesion complexes sense the tissue strain and stiffness;* ***b)*** *cell-cell adhesions transmit the forces between adjacent cells;* ***c, d)*** *primary cilium and glycocalyx perceive the mechanical strain induced by the fluid shear stress;* ***e)*** *stretch-activated ion channels respond to plasma membrane deformation regulating the influx/efflux of ions. Adapted from Dunn and Olmedo, 2016.*

1.3.1.1 Cell-ECM adhesion complexes

Cell-ECM adhesion complexes are multilayers dynamic structures that sense the stiffness, topography and geometry of ECM and respond to mechanical strains. They are not just a passive physical link between cells and microenvironment, but they also serve as signaling hubs generating chemical and physical events, that lead to changes in the cellular program (Galli et al., 2020; Janoštiak et al., 2014a). Their composition differs according to the forces exerted by both the ECM molecules and the actin cytoskeleton and lead to the maturation of nascent adhesions (small transient dot-like complexes of 0.5-1 µm in diameters) into multilayered elongated structures (3-10 µm in diameter, 40-60 nm in length) known as focal adhesions (FAs) (Yang et al., 2017). Bioinformatic analyses revealed that mature FAs account for 180 different kinds of molecules that interacts to each other, creating a network of 742 interactions (Geiger et al., 2001).

FAs can be divided in at least 3 different compartments, based on their spatial and functional organization: an integrin signaling layer, a force transduction layer and an actin regulatory layer (Di Cio and Gautrot, 2016; Kanchanawong et al., 2010) (Figure 1.8).

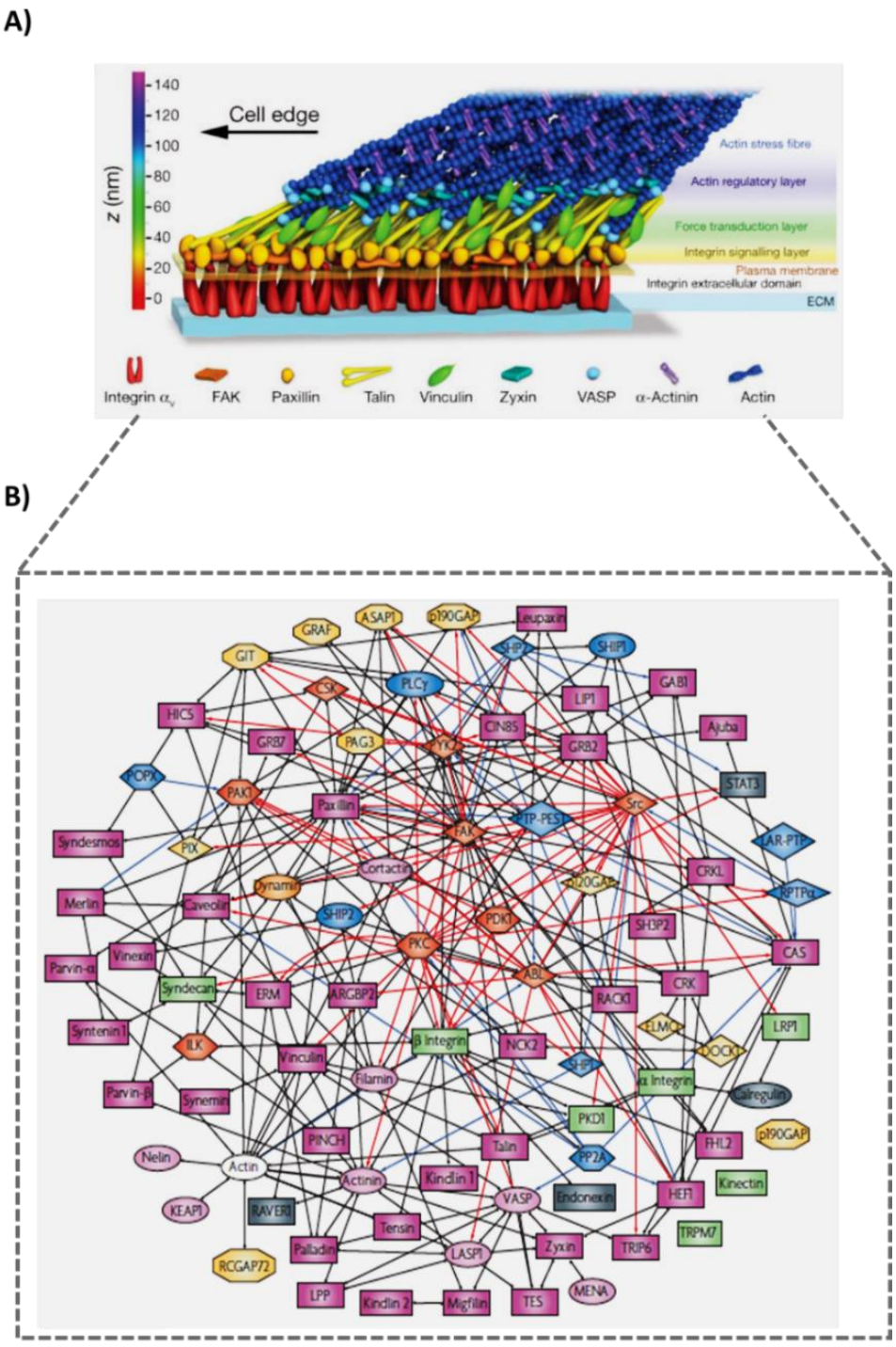

Figure 1.8. *Focal adhesions representation.* ***A)*** *Nanoscale organization of integrin-based cell adhesions. They consist of an integrin-signaling layer (yellow), a force transduction compartment (green) and an actin regulatory layer (light blue).* ***B)*** *Proteomic analysis of the proteome in mature focal adhesions. Red and blue arrows represent the activating and inhibitory interactions, respectively. The black edges show the intra-molecular interactions. Adapted from Kanchanawong et al., 2010 and Geiger et al., 2001.*

Integrin signaling layer

The integrin signaling layer, proximal to the plasma membrane, represents the core of the FAs, it is composed mainly of integrins and the adapter proteins FAK- Src complex and paxillin.

Integrins are heterodimeric transmembrane proteins consisting of α- and β-subunits. Each subunit contains a large extracellular head (700-1100 residues), a transmembrane domain and a short cytoplasmatic tail (30-50 residues). Mammals genome codifies for 24 α- and 9 β-subunits, whose

combination results in 24 integrin isoforms, ensuring the binding compatibility with a large variety of ECM components (Martino et al., 2018; Shekaran and Garcia, 2011). Indeed, most of integrins recognize the RGD motif on fibronectin, but specific subtypes can also bind collagens, laminins, and other ECM molecules (Humphries et al., 2006). The composition of the extracellular environment not only dictate the integrin subtypes, but also their localization at the plasma membrane, as integrins tend to diffuse along the lipid bilayer and cluster at specific areas of high ligand density (Wheeldon et al., 2011). Integrins are able also to respond directly to the physical stimuli of the extracellular environment by changing their conformation, which, in turn, leads to the clustering of integrins into aggregates, resulting in the reinforcement of the focal adhesions (Di Cio and Gautrot, 2016; Janoštiak et al., 2014a). It has also been suggested that ECM stiffness can affect the integrin isoforms located at the plasma membrane; indeed, while β1 subunit reside stationary within the FAs, increased stiffness recruits the β3 subunits, inducing a reinforcement of tractional forces (Milloud et al., 2017).
Human islets of Langerhans present different integrin isoforms, but the exact distribution and composition are still controversial. Mature endocrine cells present α3, α5, αv, β1, β3 and β5 integrin subunits, whereas α6 is expressed only by intraislet vasculature endothelial cells. β1 integrin is the most highly expressed in fetal pancreatic tissues, according to its pivotal role in regulating β-cell mass and proliferation (Diaferia et al., 2013; Llacua et al., 2018; Stendahl et al., 2009). Developing pancreas expresses mainly αvβ5, αvβ3, β1 integrins, interestingly αvβ5 and αvβ3 are downregulated upon maturation, raising the possibility that β1 integrin is not the main actor in pancreas development (Cirulli et al., 2000). Regardless the specific time-dependent expression and composition, it is well established that human pancreas presents several types of integrin receptors, crucial for regulating islet homeostasis.

FAK (focal adhesion kinase) is one of the first molecules engaged into the FAs by integrin activation. Its C-terminal contains the FAT (focal adhesion targeting) domain that acts as a scaffold for the recruitment of other proteins, its N-terminal domain interacts with the integrin β-subunits. Conformational changes of integrin receptors induce the autophosphorylation of FAK on tyrosine 397 in the N-terminal domain, which exposes a docking site for Src. Thus, Src binds to FAK inducing its full activation through the phosphorylation at Tyr 576 and 577 (Janoštiak et al., 2014a; Martino et al., 2018). The formed *Src-FAK complex* recruits p130Cas and paxillin. The Src-FAK-mediated phosphorylation of p130Cas (Crk associated substrate), a 130 kDa scaffolding protein, results in the exposure of 2 binding sites for FAK and 1 for vinculin, generating a cross-link between the integrin signaling and the force transduction layer (Janoštiak et al., 2014b; Polte and Hanks, 1995).

Paxillin, a 70 kDa protein, is phosphorylated by the FAK-Src complex at Tyr 31 and 118, which leads to the exposure of the binding sites for vinculin and p130Cas. Paxillin acts as a scaffolding protein by binding vinculin, but also activates indirectly the MAPK signaling cascade through the activation of p130Cas (Martino et al., 2018).

Force transduction layer

The force transduction layer is composed by talin and vinculin and plays a pivotal role in the force-mediating stabilization of focal adhesions (Janoštiak et al., 2014a).

Talin is a high molecular weight protein (270 kDa), formed by 3 different structural and functional domains. The C-terminal helices bind F-actin and regulate the protein dimerization (Golji and Mofrad, 2014). The N-terminal globular head contains the FERM (Four.one/Ezrin/Radixin/Moesin) domain, a docking site for β-integrins and F-actin, which also recruits the accessory 4.1, ezrin, radixin, and moesin proteins (Ciobanasu et al., 2018). Talin plays a crucial role in the integrin activation, triggering integrin conformational changes from a low to high binding affinity for ECM ligands. However, it was recently reported that talin alone is insufficient for the complete integrin activation; indeed, other proteins containing the FERM domain, as *kindlin 2* and *3*, are required for the maximal activation of integrins (Geiger et al., 2009). The mechanosensory ability of talin resides in the flexible rod domain, which contains two binding sites for actin and five for vinculin (VBS). In resting conditions, talin maintains its autoinhibited conformation, masking the vinculin binding sites. As mechanical forces increase, talin is stretched by the integrin conformational changes, revealing the VBS: the stronger the force, the higher the number of available VBS. This process is known as talin-vinculin mechanosensitivity (Gingras et al., 2005, 2009; del Rio et al., 2009).

Vinculin is the most abundant protein in FAs and represents an important link between cell-ECM and cell-cell adhesion complexes, allowing the flux of information to neighboring cells. As forehead mentioned, talin mechanical-activation is required for vinculin recruitment to FAs (Janoštiak et al., 2014a). In absence of force, vinculin exists in an autoinhibited state, characterized by the interaction between its tail and head domains. As forces raise, vinculin undergoes a conformational switch exposing its head domain to the talin VBS and its tail to α-actinin. Vinculin also interacts with p130Cas which promotes the vinculin active conformation, resulting in a reinforcement and enlargement of FAs (Janoštiak et al., 2014b; Martino et al., 2018) .

Actin regulatory layer

The actin regulatory layer consists of α-actinin, zyxin, filamins, and other proteins that interact directly with the actin cytoskeleton.

α-actinin, a protein of the spectrin superfamily, is an anti-parallel rod-shaped dimer with multiple docking sites (Argentati et al., 2019). Its N-terminal domain binds actin, while central and tail domains interact with zyxin and vinculin through multiple weak bonds, linking the FAs to actin. The force transmission within the FAs induces the elongation of α-actinin up to 5.5 nm, resulting in the relocation of zyxin from FAs to actin fibers (Yoshigi et al., 2005).

Zyxin is a multidomain protein that exerts its mechanosensing activity by binding different partners according to the mechanical load (Geiger et al., 2009). Under resting condition, zyxin is not engaged in the cell-cell adhesion sites, whereas, as force increased, it interacts with α-actinin and p130Cas. When FAs are mature, zyxin moves toward the actin cytoskeleton, where interacts with the Ena/VASP complex, promoting actin polymerization (Janoštiak et al., 2014b, 2014a; Martino et al., 2018).

Filamin family consists of 3 different isoforms, filamin A, B and C, which form large homodimers through the interaction of their C-terminal domains. Filamin acts as a scaffold for 90 partners of the so-called adhesome (Argentati et al., 2019). Under tension, filamins unfold exposing their binding sites for F-actin and integrin, acting as a cross-linker between FAs and actin cytoskeleton (Di Cio and Gautrot, 2016).

Although the ECM-cell interaction via FAs is the most widely characterized, other non-integrin receptors/complexes have been recognized in islets of Langerhans that can mediate mechanotransduction; for example, the laminin receptor-1, the dystroglycan complex, and the Lutheran blood group glycoprotein which bind ECM laminins (Otonkoski et al., 2008; Virtanen et al., 2008) and the tyrosine kinase discoidin domain that binds collagen IV regulating the ECM deposition (Chin et al., 2001).

1.3.1.2 Cell-cell adhesion complexes

Cell-cell adhesions are multi-protein assemblies that respond to tension and compressive forces exerted by neighboring cells and reinforce the integrin-mediated signaling. This inter-cellular mechanical coupling, that allows the force transmission between adjacent cells, is essential for maintaining tissue cohesiveness, ensuring a rapid flow of information among cells, which, in turn, modulates collective cell behavior (Gumbiner, 1990; Ladoux and Mège, 2017; Leckband and de Rooij, 2014). Cell-cell interactions are regulated by different adhesion complexes, as gap junctions and hemidesmosomes, but only adherens junctions have been recognized as mechanosensors in β-cells. Adherens junctions are extremely dynamic structures that undergo conformational changes in response to mechanical stress. They are populated mainly by cadherins and nectins, transmembrane proteins that interact via their ectodomains and bind actomyosin with the intracellular tails. Adaptor proteins are also necessary for functional adherens junctions: α- and β-catenin mediate the association between cadherins and F-actin, while afadin is the actin-linking protein for nectins (Figure 1.9). Increased mechanical stress induces a cis/trans shifting of cadherins ectodomains, favoring their oligomerization and clustering, thereby strengthening cell-cell interaction (Hong et al., 2013; Wu et al., 2015). α-catenin unfolds under forces, exposing the vinculin binding site (VBS), thus, inducing the vinculin recruitment within the adherens junction. The formed complex activates vinculin, favoring its association with F-Actin and the force transmission (Ladoux and Mège, 2017). Although nectins are essential components of adherens junction and dimerize in cis and trans, their role as mechanosensors is still unknown.

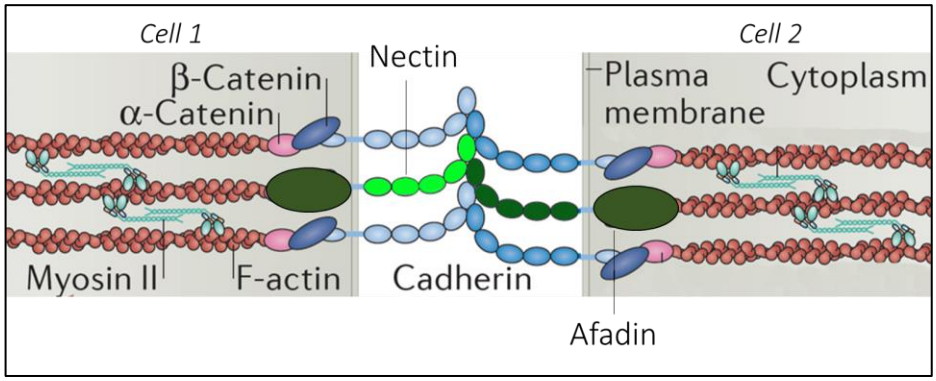

Figure 1.9. *Adherens junctions organization. Cadherins and nectins bind α-/β-catenin and afadin, respectively, allowing the force transmission between neighboring cells. Adapted from Ladoux and Mège, 2017.*

1.3.1.3 Primary cilium

Primary cilia are microtubule-containing extensions (10 nm long and 1 nm in diameter) usually localized at the cellular surface facing the blood flow and implicated in sensing mechanical forces, especially the shear stress (Wittkowske et al., 2016). The mechanosensing ability of cilia is directly correlated to the blood flow, which induces their deflection resulting in the activation of

intracellular signals. The primary cilium was first discovered in mouse pancreatic beta cells in 1898, since then several studies confirmed the presence of this structure not only in human β-cells, but also α-, δ-, and ductal cells, accounting for approximately 15% of total pancreatic cells (diIorio et al., 2014; Lodh et al., 2014; Munger, 1958). The first evidence suggesting a critical role of the cilium in pancreas development, was obtained in the pancreas-specific Kif3a (Kinesin Family Member 3A) knock-out mice. This mutation causes the loss of cilia in pancreatic cells, resulting in increased β-cell apoptosis, fibrosis, acinar-to-ductal metaplasia and cyst formation (Cano et al., 2006). It can be speculated that pancreatic cells lacking the cilia, are not able to sense the blood flow, resulting in increased pressure, which, in turn, activates other signaling pathways that induce fibroblast proliferation, ultimately leading to cystogenesis (Lodh et al., 2014). Furthermore, disruption of ciliary integrity by the suppression of Ofd1 (Oral-facial-digital syndrome 1) and BbS4 (Bardet–Biedl syndrome 4) genes expression, results in a reduction of the first phase glucose-stimulated insulin secretion both in murine islets and β-cell lines (Gerdes et al., 2014). Interestingly, a three-fold reduction of ciliated β-cells was found in diabetic rats, suggesting a potential role of cilium defects in the development and progression of T2D (Gerdes et al., 2014). Insulin secretion seems to be also affected by the position of the primary cilium, indeed Lkb1 (Liver Kinase B1) deficiency causes a relocation of cilia from the lateral membrane, closely associated with capillaries, to the opposite site, leading to a 65% increase in β-cell volume and a reduction of the insulin secretion (Granot et al., 2009).

1.3.1.4 Mechanosensitive ion channels

Stretch-activated ion channels are non-selective cation channels permeable to Ca^{2+}, Na^{+} and K^{+}. They were first characterized in sensory cells where they regulate taste, vision, hearing and nociception (Dunn and Olmedo, 2016; Gu and Gu, 2014). Since they are usually expressed at low levels in cells and are often associated to other transmembrane complexes able to perceive mechanical forces (as GPCRs or integrins), their mechanosensing activity is still debated (Chalfie, 2009; Ranade et al., 2015). Three models have been proposed for the mechanical-induced gating of these channels:

1. *membrane force model* based on studies conducted on the MscL and MscS mechanosensitive ion channels in bacteria. According to this model, the tensional forces exerted by the membrane lipid bilayer are sufficient to induce conformational changes of the transmembrane domain, thereby opening the channel.
2. *Dual-tethered model* based on the observation that stretch-activated ion channels are associated to other specialized structures in sensory cells; it predicts that the channel gating is mediated by the tethering of the accessory structures to the channels.
3. *Single-tethered model*, proposed by Kung, suggests that both tensional forces exerted by the plasma membrane and the tethering of accessory structures modulate the channel opening; to date, it is the most accepted model (Chalfie, 2009; Kung, 2005; Ranade et al., 2015).

Mechanosensing stretch-activated ion channels are divided into 4 classes according to their structure: DEG/ENaC, Piezo, K^{+}, and TRP channels.

DEG/ENaC channels

These channels consist of two transmembrane domains coupled to a large extracellular loop. Although they are involved in tactile mechanotransduction in *C. Elegans*, their role as mechanosensors in mammals remains uncertain (Orr et al., 2006).

Piezo channels

Piezos are large protein complexes, constituted by 2100-4700 amino acids, that contain numerous transmembrane domains (from 24 to 39) (Gu and Gu, 2014). The Piezo family includes two types of mechanosensors, the Piezo 1 and 2 channels. Piezo 1 was firstly identified in N2A cells, but it is also highly expressed in cells exposed to the fluid pressure, as endothelial and red blood cells. Piezo 2 is predominantly found in sensory cells, as DRG (dorsal root ganglia) neurons and Merkel cells, suggesting its role in regulating the touch sensation. These channels perceive changes in membrane curvature and respond by allowing the influx/efflux of cations (Nourse and Pathak, 2017; Volkers et al., 2015; Wu et al., 2017). Piezo 1 is crucial for the vasculature development and its deficiency leads to developmental lethality in mice, because endothelial cells are no longer able to perceive the hemodynamic shear stress (Li et al., 2014a; Ranade et al., 2014). Furthermore, gain-of-function mutations that slow the activation rate of Piezo 1 are associated with an increased fragility and dehydration of red blood cells: the massive influx of cations, reduces the activation of K^+ channels leading to an osmotic-mediated dehydration of red blood cells (Cahalan et al., 2015; Wu et al., 2017).

K^+ channels

Four types of K^+ channels have been identified according to their structure, but only the K^+ two pore domains channels, known as K2P, act as mechanosensors in mammals. Among these, TREK-1 (TWIK-1 related K^+ channel), TREK-2 (TWIK-2 related K^+ channel) and TRAAK (TWIK-related arachidonic acid stimulated K^+ channel) channels are reported to be activated by shear stress, cell swelling, and pressure. TREK-1 and TRAAK are preferentially expressed in sensory tissues, whereas TREK-2 is highly expressed in pancreas and kidney (Chalfie, 2009; Ranade et al., 2015).

TRP channels

Based on the sequence homology, TRP channels are divided into 8 subfamilies, TRPA, TRPC, TRPM, TRPML, TRPN, TRPP, TRPV, and TRPY, accounting for 28 members (MacDonald, 2011). They perceive several stimuli including temperature, chemical factors, intracellular messengers and mechanical stress. TRPs can be directly activated by changes in cytoskeletal tension, as revealed for TRPC1 and TRPC3, which are reported to be crucial in neuronal and adipose tissue development, respectively (Clark et al., 2008; Poteser et al., 2008; Tai et al., 2009). TRP channels have been also implicated in coordinating the shear stress-induced mechanotransduction in kidney endothelial cells (Ranade et al., 2015).

Human pancreatic β-cells present different types of membrane TRPs channels which are crucial to regulate the Ca^{2+} responsiveness and the glucose-stimulated insulin secretion. Furthermore, it has been reported that TRPC3 and TRPC6 support the Pdx1-induce β-cell proliferation (Hayes et al., 2013). Besides the membrane TRPs, pancreatic β-cells express the TRPP2 (Transient Receptor Potential Polycystin 2) channel that is localized to the plasma membrane of primary cilia. The shear

stress-induced deflection of cilia causes the gating of TRPP2 which modulates the basal concentration of intracellular calcium, crucial for the regulation of glucose-stimulated insulin secretion (Colsoul et al., 2011; MacDonald, 2011).

1.3.1.5 Other mechanosensors

G-protein coupled receptors (GPCRs) are seven-transmembrane domain proteins that have been widely characterized in the regulation of β-cell survival and function mediated by chemical signals, as growth factors, hormones and neuropeptides (Regard et al., 2007; Winzell and Ahrén, 2007). However, emerging evidence suggests that GPCRs may be also activated by the plasma membrane deformation induced by mechanical load, activating a signaling cascade within the cell (Dunn and Olmedo, 2016; Shen et al., 2012).

Glycocalyx consists of a mixture of glycoproteins and proteoglycans, especially hyaluronan, that covers the apical surface of cells (Wittkowske et al., 2016). It acts as mechanosensor in endothelial and bone cells, but nothing is known about its role in mechanosensation within the islets of Langerhans.

1.3.2 Mechanotransduction

Mechanotransduction is the process through which mechanical stimuli, perceived by mechanosensors, are transferred within the cells and converted into biochemical signals to elicit specific cell functions (Dunn and Olmedo, 2016; Martino et al., 2018). Although great attention has been focused on the impact of mechanical cues on cell behavior, it is well established that mechanotransduction is not a one-way path. Indeed, cells respond to the extracellular mechanical forces shaping their behavior and, in the meantime, they modify the organization and architecture of the environment where they reside. This cyclic process is known as mechanoreciprocipity and results in the cell-induced modification of tissue composition and mechanic (Discher et al., 2005; van Helvert et al., 2018; Herum et al., 2017).

Mechanotransduction can be mediated by two different pathways that operate in parallel at different timescale: the slow and the fast pathways (Figure 1.10).

The “slow” or canonical pathway operates through a cascade of phosphorylation events activated by the formation of FAs. An important mediator is the focal adhesion kinase (FAK) that phosphorylates some RhoA GEF/GAF regulators, leading to the activation of RhoA, which, in turn, induces a downstream signaling pathway mediated by the rho associated protein kinase (ROCK) and the myosin-light chain kinase (MLCK) (d’Angelo et al., 2019; Di Cio and Gautrot, 2016; Nyitray et al., 2014).

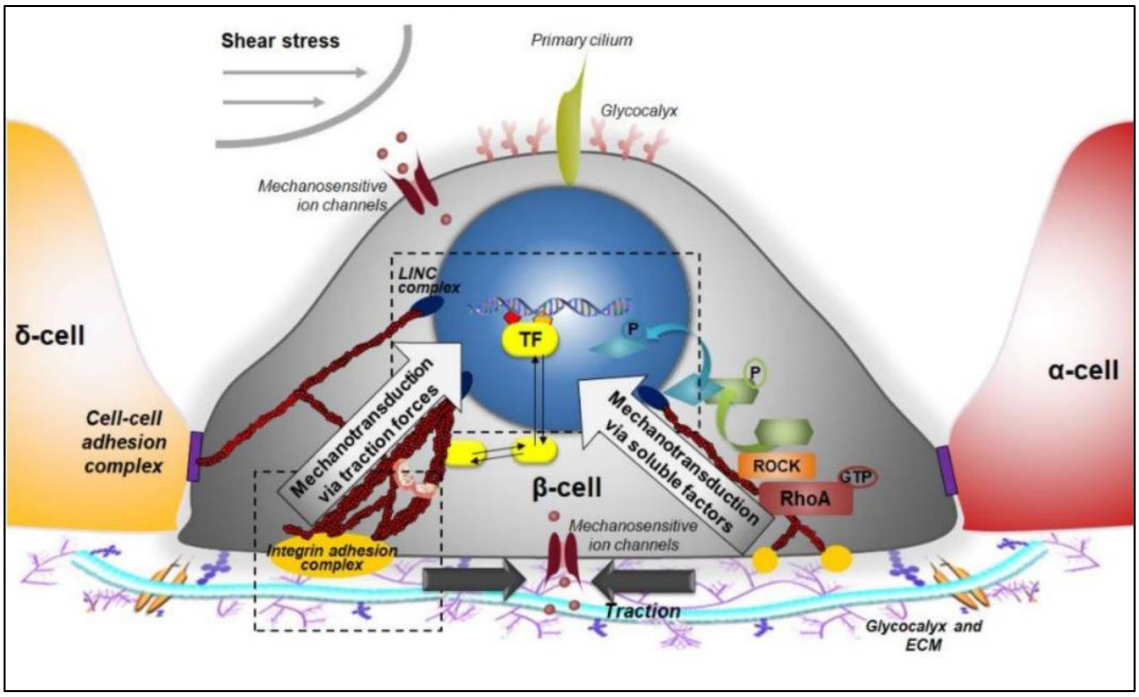

Figure 1.10. *Mechanisms of mechanotransduction. The 'fast' pathway is reported on the left. It is directly mediated by the spatial reorganization of the actin cytoskeleton, which generates compressive forces that cause the modification of nuclear architecture. The "slow" mechanoresponse (right side) is mediated by complex cascades of protein-protein interactions and phosphorylations.*

The "fast" pathway transmits the forces along the cytoskeletal filaments in just 5 μs and elicits a cellular response in few seconds (DuFort et al., 2011). In this model, mechanical forces are transferred to the nucleus as waves, through the cytoskeleton which acts as a hard-wired structure. This transduction pathway is based on the so called "tensegrity model", proposed by Ingber in 1993, which suggests that mechanical forces are preferentially transferred from soft to pre-stressed hard materials (Ingber, 1993). Accordingly, cells respond to applied mechanical stimuli by inducing traction and compressive forces, mainly mediated by the actin cytoskeleton, which are channeled to the nucleus by a stiffness gradient (the nucleus is 10-fold stiffer compared to the actin cytoskeleton) (Wang et al., 2009).

Once mechanical forces are perceived by mechanosensors, they must be transferred within the cell and converted into a biochemical signaling program that leads to a modification of cell behavior. This process can be basically divided into 3 steps: the maturation and stabilization of mechanotransducers localized at the plasma membrane, the force transmission along the actin cytoskeleton, and the nuclear mechanotransduction.

1.3.2.1 Mechanotransduction at the plasma membrane

Integrin-based cell-matrix interactions are the first to develop in response to environmental mechanical forces. Upon binding to ECM ligands, activated integrins recruit two talin molecules, that interact with F-actin, generating a weak initial connection with the actin cytoskeleton (Galli et al., 2020; Geiger et al., 2009). This complex, known as molecular clutch, is subjected to the mechanical stress provided by both the ECM ligands and the retrograde flow of actin, which dictate the fate of the nascent FA. If the force loading is too (s)low or excessive, the molecular clutch dissociates quickly. However, when the force loading exceeds a certain threshold, integrin catch

bond formation occurs, freezing these molecules in a long-live activated state, which induces the unfold of talin and the vinculin recruitment and activation (Humphrey et al., 2014). If the space between matrix ligands is 60 nm or less, the binding of vinculin to talin triggers the clustering of activated integrins and the association with the actin cytoskeleton, thereby strengthening the actin-integrin connection (Di Cio and Gautrot, 2016; Geiger et al., 2009). The maturation and reinforcement of integrin adhesion complexes into FAs occurs through the recruitment of other adaptor proteins (e.g. paxillin), actin crosslinkers (e.g. α-actinin and filamins), and signaling molecules (e.g. FAK, Src and p130Cas), converting the integrin adhesion complex into a signaling platform (Galli et al., 2020; Yang et al., 2017).

Despite less characterized, adherens junctions are also crucial players in plasma membrane mechanotransduction. Indeed, increased cell crowding induces cadherins clustering, α-catenin unfolding and vinculin recruitment/activation, resulting in the formation of a cortical actin cytoskeleton and force transmission along the actin structures.

Although the mechanotransduction by FAs and adherens junctions shows evident similarity, cells respond to the activation of these complexes in different, even opposite, ways. Indeed, while the maturation of FAs induces stress fibers formation (see below), cell-cell adhesion induced by cell crowding results in a reduction of the actin reinforcement at stress fibers. In part, it can be explained by the fact that adherens junction inhibits the formation of stress fibers, suggesting that cells sense different pools of contractile actin (cortical actin for cadherins, stress fibers for FAs) (Dupont, 2016; Puliafito et al., 2012).

1.3.2.2 Force transmission along the actin cytoskeleton

Force propagation within the cells is mediated by changes in cytoskeletal tension, which strictly depends on the dynamic, geometry, and polarity of its components. The cytoskeleton is constituted by filamentous proteins (F-actin, microtubules, and intermediate filaments) and cross-linking molecules (cofilin and myosin II); the first affect the mechanical properties, the latter modulate the force generation (Argentati et al., 2019; Harris et al., 2018). In resting condition, cofilin-mediated severing of F-actin filaments induces F-actin depolymerization and exposes the barbed ends. Upon mechanical stimulation, the severing capacity of cofilin is reduced by FAs phosphorylation, enabling actin polymerization and stress fibers formation (Hayakawa et al., 2011). Based on their organization and FAs connectivity, stress fibers (SFs) can be divided in the following subtypes:

- dorsal SFs that are bound directly to FAs and do not contain myosin II,
- transverse arc SFs that are indirectly connected to FAs trough dorsal SFs and contain both α-actinin and myosin II, and
- ventral SFs that are formed by the tethering of the previous ones and are enriched of myosin II.

The sliding of myosin II on ventral stress fibers generates compressive and extensile forces that push and pull actin filaments, ensuring the transmission of the mechanical cues within the cell (Argentati et al., 2019; Harris et al., 2018). In addition, mechanosensitive ion channels, localized at the plasma membrane and on the primary cilium, reinforce the integrin-based stress fibers formation by modulating the calcium influx (Hepler, 2016). Since integrins and cadherins are coupled to the actin cytoskeleton, which, in turn, is connected to the nuclear envelope, mechanical

stimuli applied at the plasma membrane can be transferred to the nucleus by a process known as “nuclear mechanotransduction”.

1.3.3 Nuclear mechanotransduction

Nuclear mechanotransduction provides a rapid and direct cellular response to the application of extracellular mechanical stimuli and acts in concert with other chemical signals provided by the ECM (Kirby and Lammerding, 2018; Wang et al., 2009). The transduction of physical events occurring at the plasma membrane to the nucleus can happen via physical transmission and/or biochemical signaling. The first one is regulated by the direct link between the actin cytoskeleton and the nuclear envelope and operates in a range from seconds to minutes. The biochemical signaling mechanism that elicits a cellular response in hours, is mediated by the detachment of transcription factors from mechanical-activated focal adhesion and adherens junctions and their shuttling to the nucleus (Uhler and Shivashankar, 2017).

1.3.3.1 Nuclear architecture

To better understand the transmission pathways, a brief description of nuclear architecture and associated structures is necessary (Figure 1.11).

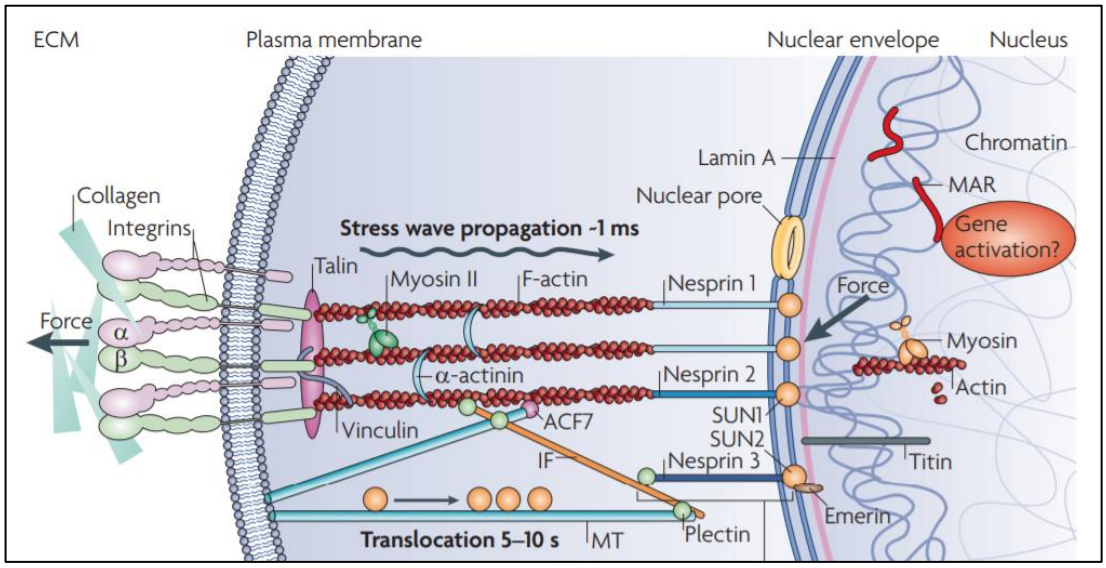

Figure 1.11. *Nuclear mechanotransduction. Environmental mechanical stimuli are perceived by plasma membrane adhesion complexes and channeled by the actomyosin contraction to the nucleus in around 1 ms. On the other side, transcription factors localized at mechanosensors and mechanotransducers can detach upon mechanical stimulation and enter the nucleus; this takes 5-10 seconds. Adapted from Wang et al., 2009.*

Nuclear architecture

The nucleus separates the genetic material from the cytoplasm, protecting it from biochemical and mechanical insults. The nucleus can be broadly divided into the nucleoplasm that contains chromatin, histones and other proteins, and the surrounding nuclear envelope (Kirby and Lammerding, 2018). The nuclear envelope consists of two concentric structures, the outer and the inner membranes, separated by a 30-50 nm perinuclear space (Stewart et al., 2007; Wilson and Foisner, 2010). The outer nuclear membrane (ONM) is functionally and physically linked with the rough endoplasmic reticulum (RER) and contains many attached ribosomes. The ribosomes-free nuclear inner membrane (INM) is indirectly connected to chromatin with the underneath nuclear

lamina which, in turn, is physically linked to the actin cytoskeleton by the so-called LINC (Linker of Nucleoskeleton and Cytoskeleton) complex (Bouzid et al., 2019; Chambliss et al., 2013; Cortelli et al., 2012). The ONM and the INM are also interrupted by the nuclear pore complexes (NPCs) that regulate the shuttling of molecules between the nucleus and the cytoplasm (Donnaloja et al., 2019; Kirby and Lammerding, 2018).
The nuclear-associated structures that are mainly involved in the nuclear mechanotransduction, both in a physical and biochemical manner, are the LINC complex, the nuclear pores and the lamina network.

The LINC complex

The LINC (Linker of Nucleoskeleton and Cytoskeleton) complex is a multilayered bridge, constituted by KASH- and SUN-domaining proteins, that connects the actin cytoskeleton to the nuclear lamina (Crisp et al., 2006). KASH (Klarsicht, ANC-1 and Syne Homology) proteins consist of N-terminal cytoplasmic domains that interact with the actin cytoskeleton and N-terminal KASH domains that bind the SUN proteins. Mammalian KASH proteins, also called nesprins, mediate the adhesion to the cytoskeleton in different ways: nesprin 1 and 2 bind, respectively, to actin and microtubules, nesprin 3 is connected to intermediate filaments through plectin, and nesprin 4 is linked to the microtubules through the kinesin1 motor protein (Bouzid et al., 2019; Méjat and Misteli, 2010; Sosa et al., 2012). Nesprin 1 and 2 interact with the spanning C-terminal domain of SUN proteins in the perinuclear space. SUN (Sad1-UNC-84 homology) proteins, in particular SUN 1 and 2, bind emerin and the nuclear lamina through the interaction with lamin A filaments. SUN proteins can also interact with the nuclear pore complexes regulating their distribution on the nuclear envelope (Crisp et al., 2006; Lombardi and Lammerding, 2011) (Figure 1.12). Through this complex network of protein-protein interactions, the LINC complex physically links the cell and the nuclear skeleton.

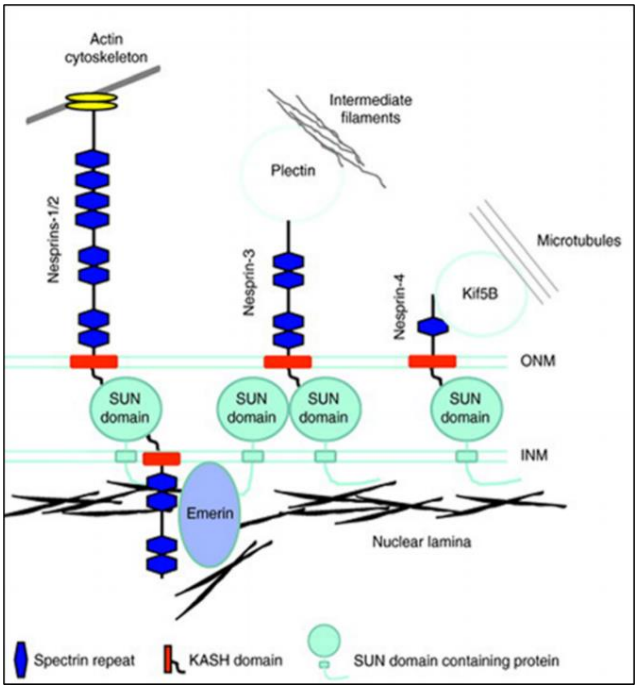

Figure 1.12. *Schematic representation of the LINC complex. The interactions of the nuclear envelop to the cytoskeleton are shown: nesprin-1/2 with the cytoskeleton (actin and microtubules, respectively), nesprin-3 with intermediate filaments, and nesprin-4 with microtubule. Adapted from Bouzid et al., 2019.*

The nuclear pore complexes

Nuclear pores are large protein complexes that mediate the transport of molecules between the cytoplasm and the nucleus (Boeri et al., 2019; Garcia et al., 2016). Small molecules and ions diffuse passively across the NPCs, whereas facilitate diffusion regulates the flux of high molecular weight molecules (>70 kDa) targeted with the NL/NE (nuclear localization and nuclear export) signals (Wente and Rout, 2010). NPCs present an octagonal structure ensured by the assembly of at least 30 nucleoporins (Nup) proteins into rings. Starting from the cytoplasmic side, the following rings can be found (Figure 1.13):

- the cytoplasmic ring, weakly connected with the ONM, with its filaments entraps cytoplasmic molecules in order to facilitate their transport within the NPCs
- the spoke ring constitutes the pore within the nuclear envelope and it is filled of proteins filaments and FG (phenylalanine-glycine) nucleoporins that regulate molecular flux within the pore; around this ring, a group of additionally channels modulate the exchange of ions and small molecules
- the transmembrane ring, located in the perinuclear space, confers structural stability
- the nuclear and distal rings, localized in the nucleoplasm, form the nuclear basket by the interaction between Nup153 and Trp proteins. Poorly is known about the nuclear basket functions, but recent evidence suggests its role in regulating molecules transport, DNA repair, and chromatin activity (Boeri et al., 2019; Garcia et al., 2016; Gu, 2018; Wente and Rout, 2010).

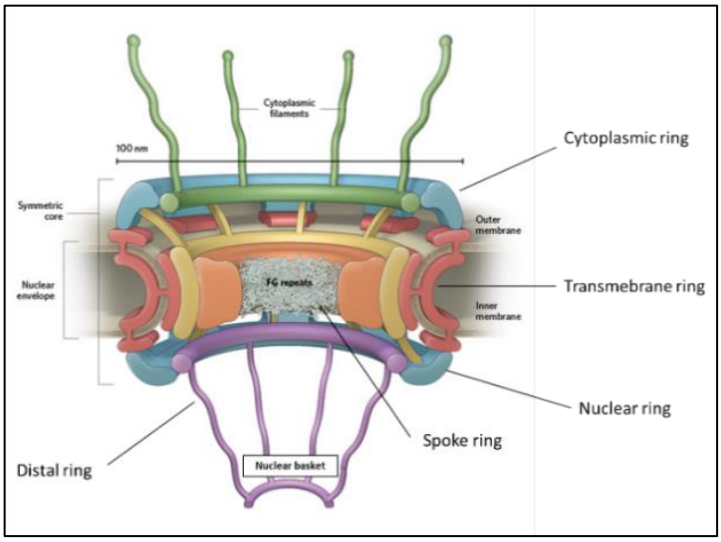

Figure 1.13. *Structural organization of the nuclear pore complex. The association of nucleoporins determines the formation of 5 functionally and structurally different rings (cytoplasmic, transmembrane, nuclear, spoke and distal rings). Adapted from Lin and Hoelz, 2016.*

The nuclear lamina

The nuclear lamina, a three-dimensional thin protein meshwork underneath the INM, regulates the nuclear shape, stiffness, and deformability. It interacts with the actin cytoskeleton through the LINC complex (Cortelli et al., 2012). The nuclear lamina is constituted by different isoforms of karyoskeletal V-type intermediate filaments, known as lamins. Based on their codifying gene, mammalian lamins can be classified in A- and B-types. The first group derives from the alternative splicing of the LMNA gene and includes the lamin A, C, AΔ10, and C2 isoforms. The B-type group comprises lamin B1, encoded by the LMNB1 gene, and lamins B2 and B3 deriving from the

alternative splicing of the LMB2 gene (Dittmer and Misteli, 2011; Donnaloja et al., 2020). Type-B lamins are crucial during development and their expression decreases during organ maturation, whereas lamin A/C are highly expressed in differentiated cells (Cortelli et al., 2012). Lamins can interact with other intranuclear proteins, called LAPS (lamina associated polypeptides), as emerin, LAP1 and LAP2, that share the LEM binding domain. By exposing the LEM domain, LAPS interact with the BAF (Barrier to Autointegration Factor) protein that binds histones and DNA, modulating the chromatin organization and the accessibility of transcription factors (Robin and Magdinier, 2016; Wilson and Foisner, 2010).

1.3.3.2 Nuclear mechanotransduction through cytoskeletal tension

How the nuclear lamina, the NPCs and the LINC complex cooperate for transmitting and converting the environmental mechanical stimuli into cellular response?

The nucleus presents a stiffness ranging from 0.1-10 kPa according to the cell type and/or culture conditions, which is 2-10 times higher compared to the actin cytoskeleton (Dahl et al., 2008; Guilak et al., 2000). Based on the tensegrity model, this stiffness gradient ensures the force transmission from the cytoskeleton to the nucleus (Ingber, 1993). For a small mechanical perturbation that do not induce the formation of mature FAs, forces are transmitted like waves from the plasma membrane to the nucleus, without a cytoskeletal rearrangement. Once external mechanical stimuli reach a certain threshold, FAs formation occurs and tunes the actomyosin contractility, which leads to the deformation of the nucleus, thereby modifying the transcriptional activity (Kim and Wirtz, 2015; Li et al., 2014b; Uhler and Shivashankar, 2017). The force transmission from the actin cytoskeleton to the nucleus is mediated by the LINC complex (rate 2 µs/µm), which channels the forces to the NPCs, the nuclear lamina and other associated structures (Donnaloja et al., 2019; Wang et al., 2009).

NPCs change their conformation under mechanical stimulation modifying the molecular transport. Two theories have been raised concerning the NPCs mechanical regulation. The first one suggests that the stretching of the nuclear envelope constricts or dilates the central channel, namely the spoke ring, changing its impedance to the molecular transport (Elosegui-Artola et al., 2017; Solmaz et al., 2013). According to the second theory, mechanical activation of SUN1 favors its binding to Nup153, which stretches the Trp proteins, modulating the nuclear basket conformation. In this view, it is the nuclear basket state (open/close) that modulates the flux of molecules within the NPCs (Boeri et al., 2019; Donnaloja et al., 2019).

Mechanical-induced modifications of the nuclear lamina not only modulates the nuclear stiffness and architecture, but also induces changes in chromatin conformation and epigenetic control, thereby resulting in altered transcriptional activity. Indeed, lamin A regulates the localization of the so-called Lamina-Associated Domains (LADs), high dynamic structures that bind histones (H3K9me2, H3K9me3 and H3K27me3) and control the gene expression (Donnaloja et al., 2019). Under mechanical tension, lamin A sequesters LADs regulating their spatial organization and their bond to chromatin, resulting in a remodeling of the DNA packing and transcription (Peric-Hupkes et al., 2010). In addition, the nuclear lamina binds BAF1 through LAP2 modulating the chromatin spatial organization and the interaction with the histones (Robin and Magdinier, 2016; Wilson and Foisner, 2010).

Another critical component in the mechanical-induced reorganization of chromatin is the nuclear actin. Upon mechanical strains, non-muscle myosin IIA and emerin favor F-actin polymerization

leading to the formation of a perinuclear actin ring that directly transmits the forces to chromatin (Miroshnikova et al., 2017).

In conclusion, the cooperation and interaction of all these nuclear structures allow a rapid transmission of the environmental mechanical cues to the nucleus, leading to a cellular response and reprogramming in order of seconds to minutes (Uhler and Shivashankar, 2017).

1.3.3.3 Nuclear mechanotransduction via soluble regulatory factors

ECM mechanosensing can be transmitted to the nucleus by regulating the shuttling of mechanotransducers and/or the activation of mechanoresponsive transcription factors (Galli et al., 2020).

Indeed, some molecules localized at the ECM-cell and cell-cell adhesion complexes can act as both structural constituents and transcription factors. Mechanical perturbation can induce the dissociation of these molecules from the adhesion complexes, probably changing their conformation and phosphorylation state, allowing their shuttling to the nucleus. The entrance of these regulatory molecules into the nucleus is facilitated by the mechanical regulation of the NPCs conformation, corroborating the hypothesis that the physical and biochemical mechanotransductive mechanisms act in concert to elicit the same cellular response (Shivashankar, 2011).

Among these regulatory molecules, the first to be identified as mechanical-activated shuttling protein was β-catenin. β-catenin is localized at the adherens junctions but under mechanical stress moves inside the nucleus, where it activates the T-cell factor/lymphoid enhancer-binding factor (TCF/LEF), a key regulator of β-cell differentiation and function (da Silva Xavier et al., 2009; Takamoto et al., 2014). Another intercellular adhesion protein, localized at tight junctions, that can shuttle to the nucleus is ZO-1 (Zonula Occludens 1), which accumulates into the nucleus in a cell-dependent fashion (Gottardi et al., 1996). It has also been reported that, upon mechanical activation, paxillin and zyxin can dissociate from FAs and shuttle to the nucleus, but poorly is known about their targets and effects (Kadrmas and Beckerle, 2004; Zhou et al., 2017).

Actin-binding proteins can also act as mechanoregulatory transcription factors. An example is MTRF (myocardin-related transcription factors) a protein that is normally bound to G-actin. Increased mechanical load induces G-actin polymerization into F-actin filaments, leading to MTRF release and its shuttling to the nucleus. MTRF binds to the serum response factor (SRF) inducing the expression of miRNAs and over 200 transcripts involved in actin dynamics and cell migration (McGee et al., 2011; Miralles et al., 2003; Olson and Nordheim, 2010).

In the last years, another class of transcriptional factors that shuttles to the nucleus upon mechanical stimulation without being directly connected to the adhesion complexes or the actin cytoskeleton has been identified and the most representative example is YAP/TAZ (Martino et al., 2018; Uhler and Shivashankar, 2017).

YAP/TAZ

The yes-associated protein (YAP) and its transcriptional coactivator with PDZ-binding motif (TAZ) are transcriptional factors that can be activated by several signaling pathways, as the Hippo kinase cascade and by metabolic signals, as the mevalonate biosynthesis, energy stress, autophagy and glycolysis (Dupont, 2016; Enzo et al., 2015; Mo et al., 2015; Piccolo et al., 2014) (Figure 1.14).

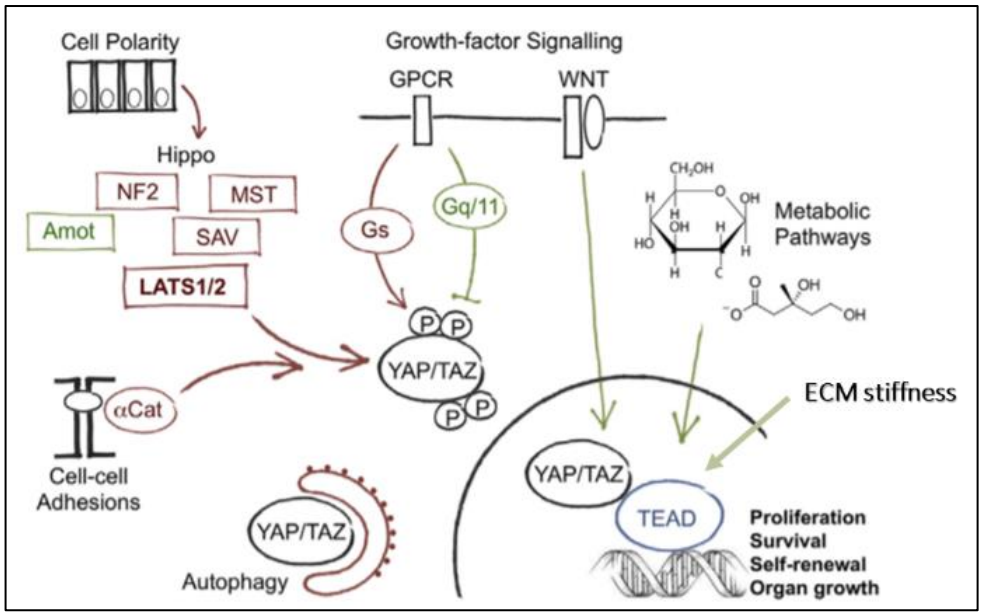

Figure 1.14. *YAP/TAZ multiple regulation. Metabolic inputs, as mevalonate or autophagy, signaling pathways, as GPCR, WNT and Hippo Kinase cascade, extracellular mechanical stimuli, as ECM stiffness, and cell crowding modulate YAP/TAZ activity. Inhibitory inputs are reported in red; activatory stimuli in green. Adapted from Dupont, 2016.*

The Hippo pathway is triggered by multiple undefined signals coming from the plasma membrane that activate the mammalian Ste-20-like kinase 1 and 2 (Mst1/2). Mst1/2 phosphorylates the large tumor suppressor 1 and 2 (Lats 1/2), which, in turn, phosphorylate YAP/TAZ. Phosphorylated YAP binds to 14-3-3 proteins that sequester it into the cytoplasm, favoring its proteasome degradation. In addition, increased phosphorylation of YAP at Ser127 promotes the YAP/TAZ extrusion from the nucleus and their subsequent degradation. It is now well established that intranuclear localization of YAP/TAZ induces cell proliferation by binding the transcription factors of TEAD family, whereas their cytoplasmic retention and degradation promote cell differentiation (Halder et al., 2012; Piccolo et al., 2014).

In addition to their role as Hippo pathway effectors, YAP/TAZ are also regulated by almost all types of mechanical stimuli. For example, matrix stiffness favors YAP/TAZ intranuclear localization, while a three-dimensional environment promotes YAP/TAZ cytoplasmic retention (Aragona et al., 2013; Dupont et al., 2011; Wada et al., 2011). In addition, cell spreading induces YAP/TAZ shuttling to the nucleus, whereas cell crowding promotes YAP degradation, suggesting a crucial role of YAP/TAZ in regulating the contact inhibition of proliferation (CIP) (Aragona et al., 2013; Zhao et al., 2007). The mechanical regulation of YAP/TAZ requires the actomyosin contractility, as revealed by the fact that actin depolymerizing agents or MLCK and ROCK inhibitors block mechanotransduction via YAP/TAZ (Aragona et al., 2013; Ohgushi et al., 2015). Even though the cytoskeletal-mediated regulation of YAP/TAZ is clear, the molecular mechanisms underlying this phenomenon are still under debated. One possibility is that some actin-binding proteins, as α-catenin or α-actinin, can associate/dissociate from YAP/TAZ upon mechanical stimulation, regulating its localization (Dupont, 2016; Miralles et al., 2003). Another proposed mechanism is that the actin polymerization rate modulates YAP/TAZ activity through the AMOT (angiomotin) protein, which is able to bind both the actin cytoskeleton and YAP/TAZ. At low cytoskeletal tension, AMOT preferentially binds YAP/TAZ favoring its cytoplasmic retention; once the actin polymerization raises, AMOT is recruited

by F-actin and releases YAP/TAZ which travel to the nucleus (Ernkvist et al., 2006; Gagné et al., 2009).

Some studies have also suggested a direct link between YAP/TAZ and adhesion complexes. For instance, YAP can be directly phosphorylated by Src-kinase and FAK, but whether this modification is directly involved in its activation is not yet clear (Hu et al., 2017; Taniguchi et al., 2015). In addition, various cell-cell junctional proteins as β-catenin and ZO-2 (Zonula Occludens 2) can directly bind YAP/TAZ, facilitating its accumulation into the nucleus (Oka and Sudol, 2009). Another possibility is that mechanical forces, by modulating the NPCs pore conformation, increase YAP/TAZ shuttling to the nucleus (Kirby and Lammerding, 2018). An intriguingly idea that has been raised recently, suggests that the calcium signaling mediated by the Piezo channels can affect YAP/TAZ activity (Dupont, 2016). Multiple YAP/TAZ regulatory pathways have been proposed, suggesting the possibility that mechanical cues regulate YAP/TAZ activity and localization through multiple and parallel mechanisms.

YAP/TAZ play a pivotal role in regulating the development, proliferation and differentiation of β-cell (Ardestani et al., 2018; George et al., 2012). In fact, at early stages, YAP is highly expressed and mainly localized in the nucleus of bipotent pancreatic progenitors, where it induces the expression of PDX1 that is crucial for sustaining their proliferation. Conversely, when differentiation of the endocrine lineages occurs, YAP loses its nuclear localization and its expression gradually decreases due to increased degradation. YAP decrease favors NGN3 and NKX6.1 expression and fate commitment (Cebola et al., 2015; George et al., 2012).

1.3.4 Crosstalk between mechanotransduction and mitochondria

Mitochondria are multifunctional organelles that can alter their localization, morphology, dimensions, and bioenergetics to meet the metabolic needs of the cell. They provide energy for the cell survival and proliferation and modulate signaling pathways involved in cell death and redox balance. Mitochondria respond to the nutrient availability modulating their morphology and bioenergetics through a process known as mitochondrial dynamics (Gökerküçük et al., 2020; Tilokani et al., 2018).

Mitochondrial dynamics consists of the balance between fusion and fission events, regulating mitochondrial shape, size, and number (Figure 1.15). Mitochondrial fusion is a two-step process, starting with the tethering of two adjacent mitochondria mediated by two large GTPase proteins, mitofusin 1 and 2 (MFNs). The conformational changes of MFNs induced by the GTP hydrolysis results in the docking and fusion of the adjacent OMMs (Brandt et al., 2016; Cao et al., 2015). The second step refers to the fusion of the inner mitochondrial membranes (IMM) that is mediated by the large GTPase optic atrophy 1 (OPA1) protein and specific IMM lipids, as cardiolipin (Ban et al., 2017). Mitochondrial fission is mainly mediated by DRP1 (dynamin-related protein 1), a large GTPase protein that binds the OMM through adaptor proteins, as the mitochondrial fission factor (MFF) and mitochondrial dynamics proteins 49 and 51 (MiD49 and MiD51) (Losón et al., 2013; Palmer et al., 2011). DRP1 forms a ring-like structure around the mitochondria leading to the GTP-mediated membrane constriction, which induces the recruitment of Dynamin 2 and the calcium influx which terminate membrane scission (Tilokani et al., 2018). Mitochondrial fission generates two mitochondria with different membrane potential. The mitochondrion with high membrane potential regains the mitochondrial network, the daughter mitochondrion characterized by low membrane potential is degraded by the lysosomal pathway (mitophagy). This process is part of the

quality control of the mitochondrial network which removes superfluous and faulty mitochondria from the cell (Liesa and Shirihai, 2013).

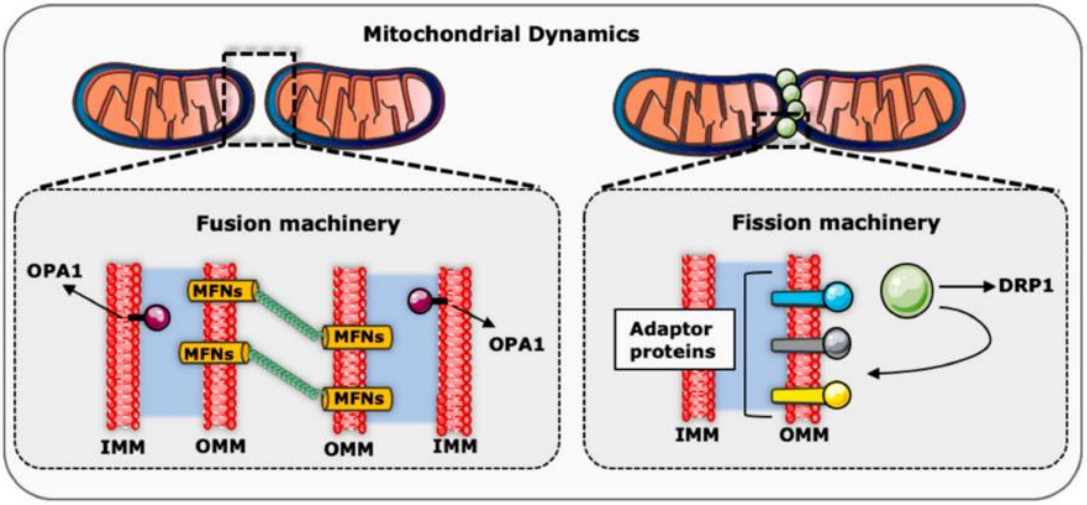

Figure 1.15. *Mitochondrial dynamics schematic representation. Mitochondrial fusion is mediated by mitofusin proteins and OPA1, generating a bigger and elongated mitochondrion (left panel). Mitochondrial fission is regulated by DRP1 recruitment at the OMM and generates two smaller daughter mitochondria (right panel). Gökerküçük et al., 2020*

Mitochondrial dynamics is crucial not only for tuning the cell response to nutrient availability, but also for the mitochondrial transport along the cytoskeleton, which ensures the enrichment of these organelles where their metabolic functions are required (Anesti and Scorrano, 2006). Mitochondria are tightly coupled to cytoskeletal proteins that track their movements and stop them in specific intracellular site. The long-distance mitochondrial trafficking is mediated by microtubules through the activation of kinesis and dynein proteins, whereas actin filaments modulate the short-distance mitochondrial movements, particularly in cellular region poor of microtubules (Hollenbeck and Saxton, 2005; Nogales, 2000). Intermediate filaments support the transport machinery and represent the stop signals that anchor mitochondria where their activity is required (Anesti and Scorrano, 2006). The coupling between mitochondrial transport and dynamics was suggested by Rutter's group which showed that the translocation of DRP1 from the cytosol to the mitochondria is regulated by dynein expression, suggesting that mitochondria must divide into small units for the cytoskeletal transport (Varadi, 2004).

A groundbreaking discovery in mitochondrial dynamics was that endoplasmic reticulum (ER) is a crucial regulator of mitochondrial fusion and fission events. Indeed, the 20% of mitochondria surface is in direct contact with the ER through a macromolecular complex known as mitochondria-associated endoplasmic reticulum membranes (MAM) (Figure 1.16). This multi-protein tethering complex contains several phospholipid enzymes, calcium channels, and also proteins involved in mitochondrial dynamics (MFN2) (Tubbs and Rieusset, 2017). Two recent studies report that the initial mitochondrial constriction that recruits DRP1 to mitochondria occurs at the ER-contact sites, probably due to an increase in calcium release from the ER. Indeed, it has been suggested that calcium entry into the IMM induces S-OPA1 accumulation which, in turn, destabilizes the tethering between the IMM and OMM (Chakrabarti et al., 2018; Cho et al., 2017).

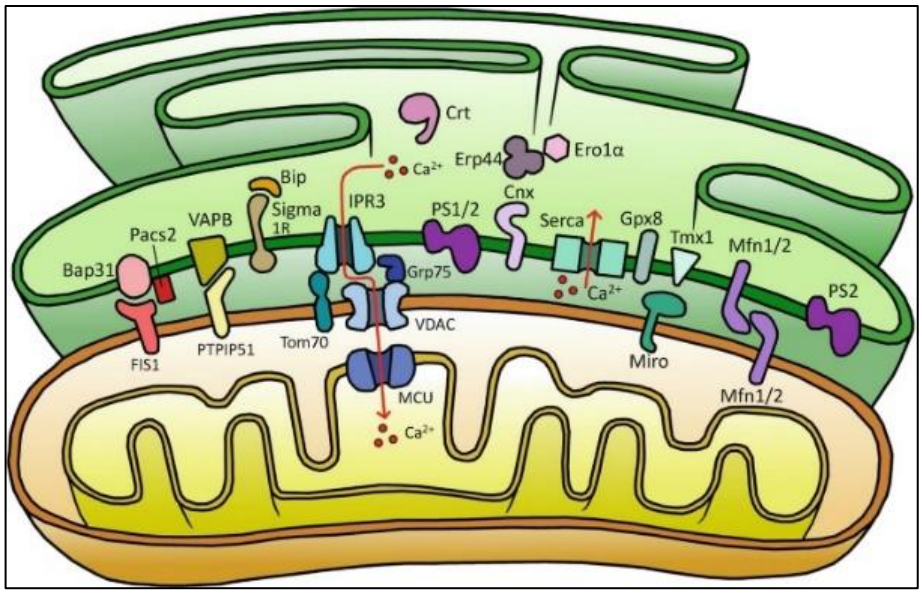

Figure 1.16. *Structural organization of mitochondria-associated endoplasmic reticulum membranes (MAM). MAM are multi-protein complexes that functionally couple mitochondria and endoplasmic reticulum. MAM contains phospholipid enzymes, calcium channel complexes (IPR3-Grp75-VDAC) and proteins involve in mitochondrial fusion (MFN1/2) and import/export (Tom70). Vallese et al., 2020*

Since mitochondria are tightly linked to the actin cytoskeleton, which regulates their dynamics, intracellular localization, and crosstalk with the ER, it is reasonable to believe that modifications of the cytoskeletal organization can affect mitochondrial activity. However, the crosstalk between mechanotransduction and mitochondrial metabolism is emerging only in the last months and a detailed characterization of the phenomenon is still missing.

1.4 Aim of the project

Diabetes mellitus is characterized by a gradual reduction of the pancreatic β-cell functional mass and the regeneration or replacement of their mass represent the most promising strategies to treat this pathology. To restore the β-cell mass, several approaches have been proposed such as the allogenic islet transplantation (Pepper et al., 2018; Shapiro et al., 2017) or the expansion/generation of β-cells from alternative sources (Guney et al., 2020; Rezania et al., 2014). Recent scientific breakthroughs enabled derivation of large quantities of human pancreatic β-like cells *in vitro*. However, although enormous advances have been made in this field in the last years, we are not yet able to produce cells that completely mirror mature functional β-cells (Hrvatin et al., 2014).

For their proper growth and functioning, β-cells require a very specific environment, the islet niche, which provides a myriad of chemical and physical signals. While the involvement of biochemical signals has been largely explored, poorly is known about the impact of the mechanical cues on regulating β-cell differentiation and function. Furthermore, the mechanosensing ability of β-cells has been recognized, however its underlying mechanism remains largely unexplored. Therefore, the aim of the proposed research was to investigate the contribution of biophysical cues to β-cell differentiation, survival and function. We focused in particular on the role of the ECM topography, which is not flat but organized at nanoscopic levels. To mimic the nanotopography of the extracellular matrix, nanostructured zirconia substrates were employed. Previous experiments performed on the neuron-like PC12 cell line and primary cultures of rat hippocampal neurons

demonstrated that these substrates promote neuronal differentiation (Schulte et al., 2016, 2017). Given the similarities between β-cells and neurons, we reasoned that these substrate might also play a similar role in β-cell differentiation and function (Di Cairano et al., 2016). Nanostructured substrates were produced by assembling zirconia clusters using the Supersonic Cluster Beam Deposition (SCBD) technique (Borghi et al., 2016), while flat zirconia substrates (flat-ZrO_2 - roughness <0.1 nm), obtained by atom assembling with an electron beam evaporator, were used as controls.

Firstly, we investigated the impact of the nanotopography on β-cell differentiation and function. To this end, human islets of Langerhans were cultured on the indicated substrates for up to 25 days and their differentiation was evaluated using immunofluorescence and immunoblotting techniques. Since the ability to respond to fluctuation of glucose concentration is the hallmark of a completely mature β-cell, we evaluated the glucose-stimulated insulin secretion and calcium currents by means of ELISA assays and calcium imaging. Once we demonstrated that the nanotopography promotes long-term β-cell differentiation and function, we investigated the possible molecular mechanisms involved using a label-free shotgun proteomic approach. The bioinformatic analysis revealed that the nanotopography induces the upregulation of proteins involved in the organization of the cell-substrate adhesion sites, the actin cytoskeleton and the nuclear architecture, suggesting the activation of a mechanotransductive pathway. Therefore, we investigated the distribution and dimension of the focal adhesions, the reorganization of the actin cytoskeleton and the nuclear envelope by quantitative indirect immunofluorescence. The proteomic analysis also revealed the upregulation of pro-survival, anti-apoptotic and anti-inflammatory pathways, which were further confirmed by TUNEL, ELISA assays and immunoblotting techniques. By exploiting the proteomic dataset, we also found that the nanostructure induces the upregulation of protein involved in metabolic processes, in particular the catabolic metabolism of carbohydrates, suggesting a potential role of nanotopography in the regulation of cell metabolism. Since β-cell metabolism is strictly controlled by mitochondria which, in turn, are tightly connected to the actin cytoskeleton, we evaluated whether the extracellular nanotopography might modulate mitochondrial morphology and function. To gain insight into the molecular mechanism, as human islets represent an extremely complex and heterogeneous model, βTC3 and INS1E cell lines were employed. After confirming the ability of these cells to sense and respond to the extracellular nanotopography, we investigated whether the reorganization of the actin cytoskeleton induced by the nanostructure might affect the mitochondrial function by measuring the mitochondrial membrane potential. To understand at molecular level the impact of the nanostructure on mitochondria, changes in the mitochondrial proteome were identified by a shotgun label-free proteomic approach performed on a mitochondrial sub-fractionation. The bioinformatic analysis revealed that the nanotopography modulates the expression of proteins involved in mitochondrial dynamics and cristae shaping, as well as enzymes and other proteins regulating glycolysis, TCA cycle and aerobic respiration. Super-resolution fluorescence microscopy and immunoblotting analysis confirmed the mitomorphosis program suggested by the proteomic analysis. By scanning the proteome, we also found proteins mainly localized in compartments tightly associated to mitochondria such as the ER and lysosomes, therefore, we evaluated the interplay between mitochondria and these organelles by means of quantitative indirect immunofluorescence.

2. Materials and Methods

2.1 Cluster assembled Zirconia substrates

Nanostructured zirconia substrates with tailored nanoscale roughness were produced by the laboratory of Prof. Milani and Lenardi (Department of Physics, Università degli Studi di Milano). Zirconia clusters were deposited on glass coverslips (Ø 13 and 22 mm) using the supersonic cluster beam deposition (SCBD) technique, which ensures the reproducibility and the quantitative control of the roughness at the nanoscopic level (Borghi et al., 2018). The supersonic cluster beam apparatus is formed by: a sputtering chamber equipped with a Pulsed Micro-plasma Cluster Source (PMSC), where the clusters are generated; an expansion chamber, where the seeded supersonic beam is formed; a deposition chamber, where the clusters are deposited onto their supports (Figure 2.1A) (Wegner et al., 2006). The main steps of the deposition process are the following:

- sputtering of a zirconium rod by the PMCS, ignited by an electric discharge;
- zirconium ablated atoms thermalized in a quenching inert gas (argon) and condensed into clusters;
- the synthetized clusters and the argon gas are extracted into the expansion chamber trough a nozzle to obtain a seeded supersonic beam;
- clusters, carried into the deposition chamber by the seeded beam, are deposited onto the glass coverslips placed on a manipulator, which intersects perpendicularly the beam flux.

The obtained zirconia films are oxidized in a substoichiometric manner (herein ns-ZrO_x, x<2) due to the residual oxygen in the deposition chamber and the exposure to air. As controls, flat substrates were produced by electron beam evaporation of a solid Zr target, resulting in a fully oxidized zirconia film (ZrO_2) with a roughness minor of 0.5 nm (Galli et al., 2018; Maffioli et al., 2020).
The surface morphology of the zirconia films was evaluated by atomic force microscopy (ATM) using the tapping mode (single-crystal silicon tips with a nominal radii curvature of 5–10 nm and cantilever resonance frequency of 300 kHz); 2 µm x 1 µm images were acquired (scan rates of 1.5–2 Hz and sampling resolution of 2048 × 512 points). In order to remove artifacts, images were processed through line-by-line subtraction of first and second polynomials and the substrates root-mean-square (RMS) surface roughness Rq was evaluated (Borghi et al., 2018; Piseri et al., 2001). Figure 2.1B,C shows the typical 3D and top-views of the flat (flat-ZrO_2) and nanostructured substrates (ns-ZrO_x).

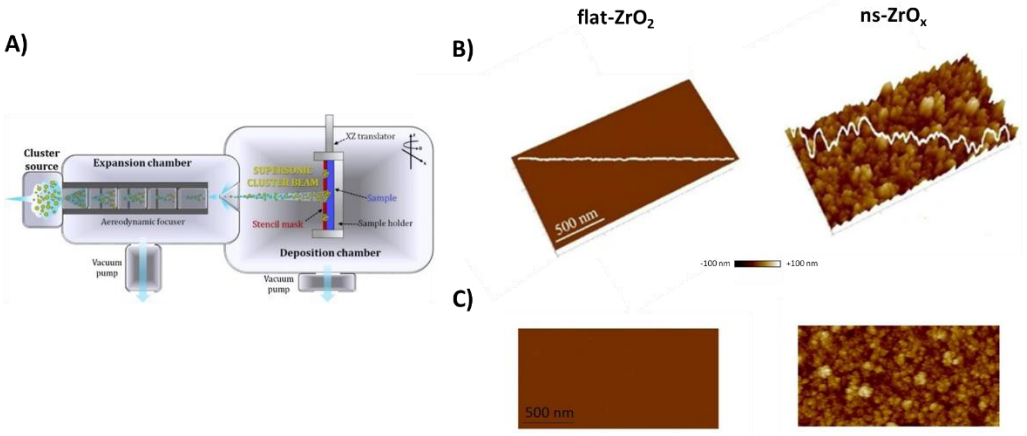

Figure 2.1. *Cluster assembled zirconia substrates preparation and characterization.* ***A)*** *Organization of the supersonic cluster beam deposition apparatus.* ***B,C)*** *Three-dimensional (B) and top (C) views of nanostructured (rms 15 nm roughness) and flat substrates obtained by AFM characterization; white lines represent the topographic profiles. Adapted from Bongiorno et al., 2005; Galli et al., 2018.*

Our experiments were performed on nanostructured substrates of 10, 15, 20, 25 nm roughness and flat films (rms roughness <0.5 nm), which were sterilized under UV for 20 minutes directly before seeding the cells. Gelatin covered substrates and glass coverslips were also used as controls; gelatin (1 mg/mL) was deposited on glass coverslips (Ø 13 and 22 mm) and dried for 20 minutes at room temperature before seeding the cells.

2.2 Cell culture conditions and processing

Isolated human islets of Langerhans and two different cell lines, namely mouse βTC3 and rat INS1E cells, were used.

2.2.1 Isolated human islets of Langerhans

Human islets of Langerhans were isolated in Niguarda Ca' Granda Hospital (Milano, Italy) following the procedure described by Ricordi et al., (Ricordi et al., 1988). The isolated islets were provided by cadaveric multiorgan donors with no medical history of diabetes or other metabolic disorders. In this study, at least 12 different islets preparations were tested; the donor characteristics were: 5 women and 7 men, donor age 52 ± 5 years, BMI 25.8 ± 3.7 kg/m^2, islets purity 83 ± 6.5% (Galli et al., 2018).

Human isolated islets were cultured in RPMI 1640 medium (ECB900, EuroClone) containing 5.5 mmol/L glucose, 10% (v/v) heat-inactivated fetal bovine serum (ECS0180L, EuroClone), 0.7 mM Glutamine (ECB300, EuroClone) and 50 units/mL penicillin-streptomycin (ECB3001D, EuroClone).

Within 3 days after isolation, pancreatic islets were dispersed into small clusters and single cells through the following protocol:

- centrifuge the islets for 5 minutes at 350 x g and discard the cell medium
- wash in PBS LS (Phosphate Buffer Low Salts), centrifuge for 5 minutes at 350 x g and discard the supernatant
- resuspend the pellet in 1 mg/mL trypsin-EDTA (ECM0920D, EuroClone) + 0.25 mg/mL DNAse I (18068015, Thermo Fisher) solution: the digestion was carried out by pipetting up and down the cell suspension at 22 °C for 3 minutes
- halt the digestion by adding 2 volumes of PBS LS
- collect the islets by centrifugation at 350 x g for 5 minutes
- discard the supernatant and resuspend the islets in complete medium.

Islets were seeded on the indicated substrates at a density of 30 islets/mm^2 (the total number of the islet preparation was provided by the Ca' Granda Hospital) and were maintained in culture in humidified atmosphere containing 5% of CO_2 at 37 °C for up to 20 days. Once a week, half of the total medium was replaced with fresh ones.

2.2.2 Cell lines

βTC3 cells (kindly provided by Prof. Douglas Hanahan, Department of Biochemistry and Biophysics, University of California, San Francisco, CA) were obtained by expression of the SV40 T antigen (Tag) under control of the insulin promoter in transgenic mice, herein the name βtc (beta tumor cells) (Efrat et al., 1988); the Tag expression results in immortalization of these cells that maintain a

differentiated phenotype for 50 passages in culture. Differentiated βTC3 cells produce both proinsulin I and II, efficiently process them into mature insulin but they secrete the hormone with a lower threshold for maximal stimulation when compared to primary β-cells (Skelin et al., 2010). βTC3 cells were cultured in RPMI 1640 medium (ECB900, EuroClone) supplemented with 10% (v/v) heat-inactivated fetal bovine serum (ECS0180L, EuroClone), 50 units/mL penicillin-streptomycin (ECB3001D, EuroClone) and 1 mM L-glutamine (ECB300, EuroClone).

INS1E cells (kindly provided by Prof. Claes B. Wollheim, Department of Internal Medicine, University Medical Centre of Geneva, Geneva, Switzerland) were produced for the first time by Asfari and coworkers in 1922 through the X-ray irradiation of rat insulinoma cells (Asfari et al., 1992). INS1E cells show some important characteristics of mature β-cells such as the expression of GLUT2 and glucokinase, ensuring the glucose stimulated insulin secretion within the physiological range (Skelin et al., 2010). As βTC3, INS1E cells synthetize both proinsulin I and II that are efficiently stored into secretory granules to be processed to mature insulin. INS1E cells were cultured in RPMI 1640 medium (ECB900, EuroClone) integrated with 10% (v/v) heat inactivated fetal bovine serum (ECS0180L, EuroClone), 50 units/mL penicillin-streptomycin (ECB3001D, EuroClone), 1 mM L-glutamine (ECB300, EuroClone), 2 mM HEPES-NaOH pH 7.4, 1 mM sodium pyruvate (59203C, Sigma Aldrich) and 50 µM β-mercaptoethanol (M3148, Sigma Aldrich).
Cells were cultured in humidified atmosphere containing 5% of CO_2 at 37 °C using tissue-culture treated supports. Reached the 80% confluence, cells were trypsinizated for 5 minutes with trypsin-EDTA (trypsin 0.5 g/L + EDTA 0.221 g/L - ECM0920D, EuroClone), counted, seeded on the indicated substrates at a density of 80 cells/mm^2 and cultured for 3 days.
To demonstrate the involvement of the fast mechanotransductive pathway in the β-cell adaptation to the nanostructure, βtc3 cells were treated with 50 µM Blebbistatin (B0560, Sigma Aldrich) for 1 hour and fluorescence experiments were performed for morphological and functional evaluations.

2.3 Immunofluorescence: principles and techniques

Immunofluorescence (IF) exploits antibodies conjugated with organic compounds, known as fluorochrome or fluorophore, to detect specific target antigens. Thanks to its high specificity, immunofluorescence has become an important tool in cell biology.

2.3.1 Fluorescence microscopy: basic concepts

Fluorophores absorb energy at a specific wavelength and emit it at a longer one. The mechanism consists of three different steps:

- an incoming photon hits the fluorochrome leading to an excited electronic single state
- the fluorochrome interacts with the environment and undergoes conformational changes
- the fluorochrome returns to its ground state by the emission of a photon at a longer wavelength.

Fluorochrome can repeat this cycle from hundreds to thousands of times before fluorescence decay. The molecular structure of the fluorochrome, the exposure to illumination and the local environment (pH, temperature, solutions) play a crucial role in regulating the timing and the nature of the fluorescent signal. Phenylenediamine or other mounting media that chemically protect the fluorophore, can be used to preserve the signal.

An Axio Observer Z1 (Zeiss Inc.) motorized inverted fluorescence microscope was used to visualize and analyze the cellular structures labelled with fluorochromes. The light beam emitted by a xenon arc lamp is filtered by the excitation filters and directed toward the sample by a dichroic mirror. The light emitted by the sample is captured by the emission filters and leaded towards the microscope Retiga Camera for recording. Since the excitation and emission light pass through the same objective lens, this technique is known as epifluorescence (the term επι in Greek means "same") (Webb and Brown, 2013).

The following filters were used:

- n.52 (excitation wavelength 488/10 nm; emission wavelength 525/50 nm)
- n.43 (excitation wavelength 445/25 nm; emission wavelength 605/70 nm)
- DAPI (excitation wavelength 417/60 nm; emission wavelength 352/60 nm)

Epifluorescence is particularly useful when imaging cellular structures over 10 µm deep, as nuclei and organelles; however, it is not completely suitable for the visualization of thinner structure, as the plasma membrane, since the illumination of molecules outside the focal plane can produce images with a high background signal. To improve the signal-to-noise ratio and acquire information at the nanometer-scale level, Total Internal Reflection Fluorescence (TIRF) microscopy was used.

2.3.2 Total Internal Reflection Fluorescence (TIRF) microscopy

TIRF microscopy limits the fluorophore excitation to a thin field of about 100 nm by exploiting the total internal reflection phenomenon. In general, when a light beam reaches an interface between two media at different refractive indexes, it is both reflected and refracted according to the Snell's law (Figure 2.2).

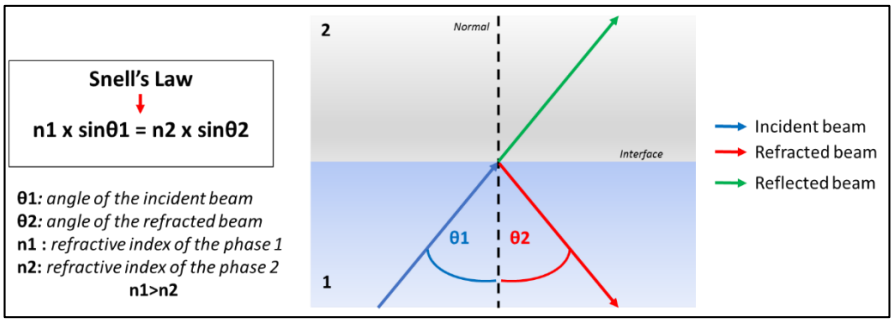

Figure 2.2. *Snell's law description.*

In microscopy, the glass coverslip is the higher refractive index phase, while the cell cytosol is the lower one. When the incident beam strikes the interface with an angle larger than the critic one, it is completely reflected into the first medium (Fish, 2009). The reflection generates a restricted electromagnetic field that extends for a few hundred nanometers into the lower-index phase medium and declines sharply with the increasing distance from the interface, leading to the visualization of a limited region in the proximity of the interface, as the plasma membrane (Figure 2.3). A crucial parameter to successfully perform TIRF experiments is the numerical aperture of the objective, since it must be sufficient to reach and overcome the critical angle (Fish, 2009). The numerical aperture (NA) of an objective is dependent on the refractive index of the lowest-index phase (n) and the angular aperture, in accordance with this mathematical relation: NA= n x sin µ, where µ is one-half the angular aperture. Since the cell cytosol has a refractive index of 1.38, an objective numerical aperture exceeding that value is necessary.

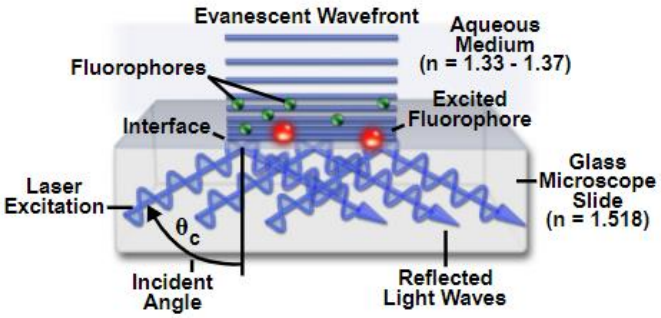

Figure 2.3. *Schematic representation of TIRF microscopy process. When the light beam exceeds the critical angle, total internal reflection occurs and an evanescent field (100 nm) is generated. The refractive indexes of the aqueous medium (cytosol) and the glass coverslip are reported. Image source: https://www.microscopyu.com/techniques/fluorescence/total-internal-reflection-fluorescence-tirf-microscopy*

2.3.3 Immunofluorescence protocol

Human islets of Langerhans, βTC3 and INS1E cells were stained with the following protocol:

1. *Fixation*: wash once the islets in PBS LS, fix them in 4% paraformaldehyde (158127, Sigma Aldrich) solution for 20 minutes and wash three times in PBS LS.
2. *Labelling*: the labelling was performed in a humidified atmosphere keeping the samples in the dark:

- incubate the islets with primary antibodies diluted in GDB 1x
- wash one time in PBS HS (Phosphate buffer high salts) for 5 minutes
- wash twice in PBS LS for 5 minutes
- incubate the islets with the secondary antibody diluted in GDB 1x for 1 hour
- wash three times in PBS LS (5 minutes/each)
- mount on microscope slides using 1 mg/mL phenylenediamine solution.

<u>Antibodies/fluorescent markers</u>

Primary antibodies

- Monoclonal mouse anti-smooth muscle actin (A2547, Sigma Aldrich); dilution 1:200 - 2 hours incubation at room temperature (RT).
- Polyclonal guinea pig anti-insulin (A0564, Dako); dilution 1:500 - 2 hours incubation at RT.
- DAPI or 4',6-diamidino-2-phenylindole (A1001, Applichem); dilution 1: 10 000.
- Monoclonal mouse anti-Ki67 (M7240, Dako); dilution 1:150 - 2 hours incubation at RT.
- Monoclonal rabbit anti-chromogranin (ab254322, Abcam); dilution 1:150 - 2 hours incubation at RT.
- Monoclonal mouse anti-glucagon (MAB1249, Biotechne); dilution 1:75 - 2 hours incubation at RT.
- Monoclonal rat anti-somatostatin (ab30788, Abcam); dilution 1:50 - overnight incubation at 4 °C.
- Monoclonal mouse anti-acetylated tubulin (T7451, Sigma Aldrich); dilution 1:75 - 2 hours incubation at RT.
- Monoclonal mouse anti-vinculin (V9131, Sigma Aldrich); dilution 1:75 - overnight incubation at 4 °C.

- Texas red phalloidin (315-075-049, Jackson ImmunoResearch); dilution 1:500 - 20 minutes incubation at RT.
- DAPI or 4',6-diamidino-2-phenylindole (A1001, Applichem); dilution 1: 10 000 - 20 minutes incubation at RT.

Secondary antibodies

- Polyclonal anti-mouse fitc IgG (715-096-151, Jackson ImmunoResearch); dilution 1:150.
- Polyclonal anti-guinea pig tritc IgG (106-025-006, Jackson ImmunoResearch); dilution 1:500.
- Polyclonal anti-mouse cy5 IgG (115-175-166, Jackson ImmunoResearch); dilution 1:150.
- Polyclonal anti-rabbit fitc IgG (ab6717, Abcam); dilution 1:150.
- Polyclonal anti-rat fitch IgG (ab6840, Abcam); dilution 1:150.

2.3.4 Image acquisition and analysis

Images acquisition was performed using the motorized inverted microscope Axio Observer Z1 (Zeiss Inc.) TIRF microscopy was preformed to visualize the vinculin clusters localized close to the plasma membrane. Images were acquired by using a multi-line 100 mV Argon laser and the 100x oil immersion objective with 1.45 numerical aperture (NA) (Zeiss). Green fluorescence was excited using the 488/10 nm laser line and imaged through a band-pass emission filter (525/50 nm) mounted on a Fast Retiga SVR CDD camera (Galli et al., 2018). Images were captured using the Image ProPlus software (Media Cybernetics, Bethesda, MD).

Image analysis of vinculin clusters, nuclear architecture and cilium length was carried out using the Image ProPlus software. Firstly, to reduce the background and enhance the signal of fluorescent structures, a high Gauss filter (7 x 7) was applied. After selecting an AOI containing the cell of interest, the area and the background fluorescence were measured and all the structures with a fluorescent signal higher than four times the fluorescence background were counted. The following parameters were measured in a software-assisted manner: the area (μm^2), major axis (µm), minor axis (µm) and the number of vinculin-positive clusters per cell; the nuclear area (μm^2) and Feret's diameter (µm); the cilium length (µm). Actin fibers length (µm) and width (µm) were measured using the ridge detection plug-in of the ImageJ FiJi software.

2.4. Western blotting

Western blot was used to evaluate the different expression of proteins involved in cell inflammation, differentiation and mitochondrial dynamics.

2.4.1 Protein lysate preparation

Cells were collected and lysed in RIPA buffer added with 0.01% SDS (only for human islets), 1 µg/mL aprotinin, 1 mg/mL PMSF and 1x Roche inhibitors for 40 minutes at 4 °C. Protein concentration was determined by Bradford assay using Bradford Reagent (B6916, Sigma Aldrich), an organic compound able to shift its maximum absorption from 465 to 595 nm when tied to proteins. According to the protein concentration, the lysate volume was calculated as follow:

$$\mu L\ Lysate = 15\ \mu g\ /\ [sample]\mu g/\mu L$$

Samples were prepared by adding to the calculated volume of lysate the β-mix 2x solution, containing the reducing agent β-mercaptoethanol and the tracking marker bromophenol blue.

Samples were boiled on a dry plate at 100 °C for 2 minutes to unfold the 3D protein structure and keep on ice until use.

2.4.2 Gel electrophoresis and electrotransfer

Polyacrylamide Gel Electrophoresis (PAGE) was used for protein separation, in particular, a 10% polyacrylamide gel was prepared to separate proteins in the lysates. The polyacrylamide gel was mounted vertically between two buffer chambers, filled with the running buffer. Samples and a prestained protein marker (EPS025500, EuroClone) were loaded, an electric field of 100 V was applied to allow samples entering into the running gel, then the separation was performed at 60 V for 3 hours. The application of the electrical field across the buffer chambers forces the migration of proteins through the gel.

Proteins, separated according to their electrophoretic mobility, were electro-transferred from the gel to a 0.45 µm pore size PDVF membrane (Immobilon®-P, IPVH00010, Millipore). Briefly, PVDF membranes were activated by incubating them in methanol (15 seconds) and deionized water (2 minutes) and then equilibrated for 5 minutes in the blotting buffer. The sandwich, castled as reported in figure 2.4, was mounted into the transfer chamber filled with the blotting buffer. The electrotransfer was performed overnight at 90 mA in the cold room. During the transfer, proteins negatively charged moving from the anode to the cathode were immobilized on the PVDF membrane. The evaluation of protein transfer was performed by labelling the membranes with a solution of 0.1% (w/v) Ponceau S in 5% acetic acid (P-7170, Sigma Aldrich). Ponceau S, a sodium salt of a diazo dye, rapidly reacts with proteins on the membrane resulting in a replica of the gel band patterns.

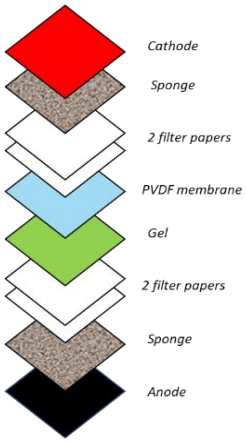

Figure 2.4. *Sandwich assembly*

2.4.3 Immunodetection

To detect the proteins, a chemiluminescent (ECL) assay was performed by using antibodies conjugated to horseradish peroxidase (HRP), a chemiluminescent substrate (luminol) and an oxidizing agent (hydrogen peroxide).

The immunodetection was performed with the following protocol:

- *Blocking*: incubate the membrane with the blocking buffer for 1 hour at room temperature to prevent non-specific binding of the antibodies; the buffer type is strictly dependent on the antibody used.
- *Primary antibody staining*: incubate the membrane with the primary antibody diluted in the incubation buffer on a shaker; the timing and the buffer used for the labelling are strictly dependent on the antibody.
- *Washes*: wash three times in 1x TBS-T 0.1% (5 minutes/each) on a shaker.
- *Secondary antibody staining*: incubate the membrane with the HRP-conjugated antibody diluted in the blocking buffer for 1 hour at room temperature on a shaker.
- *Washes*: wash three times in 1x TBS-T 0.1% (5 minutes/each) on a shaker.

The ETA C 2.0 WESTAR kit (XLS075, Cyanagen) was used as HRP-substrate. Mix 1:1 the luminol and the peroxide solutions, then incubate the membrane in the ECL solution for 5 minutes, in the dark at room temperature. The signal of the ECL-based reaction was detected with the Odyssey Fc

Imaging system (Li-Cor, Biosciences). The optical density of the bands was quantified by using the Image Studio™ Lite software (version 3.1, Li-Cor, Biosciences).

2.4.4 PVDF membrane stripping

Two different types of stripping were used. For antibodies against the phosphorylated form of a protein, the membranes were firstly labelled with the antibodies for the phosphorylated forms, mild stripped and re-stained with the antibodies against the non-phosphorylated proteins. The following protocol was used:

- incubate the membrane for 10 minutes in stripping solution
- wash four times in 1x TBS
- incubate the membrane for 10 minutes in stripping solution
- wash four times in 1x TBS
- incubate the membrane for 10 minutes in stripping solution
- wash twice in PBS LS (10 minutes/each)
- wash twice in 1x TBS-T 0.1% (5 minutes/each).

A hard stripping was performed for proteins presenting a similar molecular weight. The stripping was performed by incubating the membrane in the hard stripping solution for 30 minutes at 45 °C, then it was washed 3 times in 1x TBS-T 0.1% (10 minutes/each).

Antibodies

Primary antibodies

- Monoclonal mouse anti-smooth muscle actin (A2547, Sigma Aldrich); dilution 1:2000 - 2 hours incubation at RT.
- Polyclonal rabbit anti-β catenin (C2206, Sigma Aldrich); dilution 1:2000 - 2 hours incubation RT.
- Monoclonal mouse anti-YAP/TAZ (sc-101199, Santa Cruz); dilution 1:500 - overnight incubation at 4 °C.
- Monoclonal mouse anti-β actin (NB600-501, Novus Biologicals); dilution 1:10 000 - 2 hours incubation RT.
- Polyclonal rabbit anti-HIF1α (SAB2101039, Sigma Aldrich); dilution 1:500 - 2 hours incubation RT.
- Monoclonal rabbit anti-Phospho-IκBα (Ser32) (2859, Cell Signaling); dilution 1:1000 - overnight incubation at 4 °C.
- Monoclonal mouse anti-IκBα (4814, Cell Signaling); dilution 1:1000 - overnight incubation at 4 °C.
- Monoclonal rabbit anti-Phospho-NFκB p65 (Ser536) (3033, Cell Signaling); dilution 1:1000 - overnight incubation at 4 °C.
- Monoclonal rabbit anti-NFκB p65 (8242, Cell Signaling); dilution 1:1000 - overnight incubation at 4 °C.
- Monoclonal mouse anti-β tubulin (T8328, Sigma Aldrich); dilution 1:500 - 2 hours incubation RT.

- Monoclonal rabbit anti-mitofusin2 (9482, Cell Signaling); dilution 1:1000; overnight incubation at 4 °C.
- Monoclonal rabbit anti-DRP1 (8570, Cell Signaling); dilution 1:1000 - overnight incubation at 4 °C.
- Monoclonal rabbit anti-OPA1 (80471, Cell Signaling); dilution 1:1000 - overnight incubation at 4 °C.
- Monoclonal rabbit anti-TOM20 (42406, Cell Signaling); dilution 1:1000 - overnight incubation at 4 °C.
- Monoclonal rabbit anti-phospho-eIF2α (Ser51) (3597, Cell Signaling); dilution 1:1000 - overnight incubation at 4 °C.
- Monoclonal rabbit anti-eIF2α (5324, Cell Signaling); dilution 1:1000 - overnight incubation at 4 °C.
- Monoclonal rabbit anti-PERK (3192, Cell Signaling); dilution 1:1000 - overnight incubation at 4 °C.

Secondary antibodies

- Polyclonal anti-mouse IgG, HRP linked (7076, Cell Signaling); dilution 1:1000.
- Polyclonal anti-rabbit IgG, HRP linked (7074, Cell Signaling); dilution 1:1000.

2.5 FACS analysis

In order to evaluate cell proliferation, the NovoCyte™3000 flow cytometer (ACEA biosciences, Agilent) was used. This system is able to detect and record fluorescent light of 13 different colors thanks to three different lasers (the argon ion, the red helium neon and the violet diode lasers) and 13 emission filters.

2.5.1 Cell staining

Human islets clusters were disaggregated using 1 mg/mL collagenase II solution (C6885, Sigma Aldrich) for one hour at 37 °C. Once obtained a single cell suspension, cells were fixed and labelled with the following protocol:

- resuspend the pellet in 100 µL of fixing solution
- incubate for 30 minutes in ice to fix and permeabilize the cells
- centrifuge at 4000 x g for 7 minutes and discard the supernatant
- incubate the cells with the unconjugated primary antibody diluted in the permeabilizing solution for 30 minutes, keeping the sample on ice and in the dark
- wash one time in 1x MACS buffer
- incubate the cells with the secondary/conjugated primary antibodies diluted in the permeabilizing solution for 30 minutes, keeping the sample on ice and in the dark
- wash one time in 1x MACS solution
- resuspend the pellet in 300 µL of 1x MACS buffer.

Antibodies

Polyclonal guinea pig anti-insulin (A0564, Dako); dilution 1:50.
Polyclonal anti-guinea pig tritc IgG (106-025-006, Jackson ImmunoResearch); dilution 1:50.
Monoclonal mouse anti-Ki-67 (20Raj1), eFluor 450 (48-5699-41, eBioscience™); dilution 1:25.

2.5.2 Quantification and analysis

Samples were analyzed with the NovoCyte™3000 flow cytometer (ACEA biosciences, Agilent). Insulin positive cells were detected by using the argon ion laser (488) and the PE emission filter (572/28 nm), while Ki67 fluorescence was excited with the violet diode laser (405) and collected with the Pacific Blue™ Brilliant Violet emission filter (445/45 nm). The obtained dataset was then analyzed with the Novoexpress software. In order to select only β-cells within the cell suspension, PE fluorescence emission was correlated to the forward scatter light (FSC); only the cells presenting an FSC greater than 2 x 10^5 and a PE fluorescence emission exceeding 10^4, were considered for further analysis. The selected β-cell population was then correlated to the Ki67 positive cells and the median intensity of fluorescence was calculated.

2.6 Insulin secretion experiments

The glucose stimulated insulin secretion (GSIS) was evaluated in mouse βTC3 cells and human islets of Langerhans with the following procedure.

- *Equilibration phase 1*: incubate the cells for 1 hour in Krebs ringer buffer (KRH) supplemented with 1 mM (βTC3) or 3.3 mM (human islets) glucose and 0.2% w/v BSA (A8022, Sigma Aldrich); discard the supernatants.
- *Basal release:* cells were incubated for 45 minutes in Krebs ringer buffer (KRH) supplemented with 1 mM (βTC3) or 3.3 mM (human islets) glucose and 0.2% BSA; collect the supernatants into fresh tubes.
- *Stimulated release:* incubate the cells for 45 minutes in Krebs ringer buffer (KRH) supplemented with 20 mM (βTC3) or 16.7 mM (human islets) glucose and 0.2% BSA; collect the supernatants into fresh tubes.
- *Cell collection:* lysis buffer integrated with 1 µg/mL aprotinin, 1 mg/ mL PMSF and 1x Roche inhibitors was added into wells and the cells were detached from the substrate by pipetting.
- *Cell lysis:* cell suspensions were incubated on a rotary shaker (slow rotation) for 30 minutes at 4 °C and centrifuged at 13600 x g for 5 minutes at 4 °C; supernatants were collected and transferred into fresh tubes.

The total insulin content and the glucose-stimulated insulin secretion were measured by means of ELISA immunoassays (10-1247-01 for βTC3 and 10-1113-01 for human islets, Mercodia), following the manufacturer's protocol.

2.7 Calcium imaging

Changes in intracellular free Ca^{2+} were determined by single cell Fluo3 fluorescence imaging. The islets were incubated at 37 °C for 40 minutes with 2 mM Fluo3/acetoxymethyl ester (Fluo3-AM) (46393, Sigma Aldrich) supplemented with 0.0125% Pluronic F-127 (P2443, Sigma Aldrich) in KRH solution containing 20 mM HEPES pH 7.4, 2 mM $CaCl_2$, 3.3 mM glucose. Prior to imaging, islet were incubated for 10 minutes at room temperature in KRH solution. The images were acquired every 10 s with the high resolution Retiga SRV CCD camera attached to the Axio Observer Z1 (Zeiss) inverted fluorescence microscope. The fluorescence signal of single cells was measured over time using the Image-ProPlus (Media Cybernetics) software and the data were expressed as relative total

fluorescence [F/F0: ratio of fluorescence signal in each frame to basal value (F0)] as a function of time.

2.8 Proteomic analysis of human islets of Langerhans

Proteomic analysis was carried out using the Liquid Chromatography Electrospray Ionization Tandem Mass Spectrometer (LC-ESI-MS/MS) by the laboratory of prof. Tedeschi (Department of Veterinary Medicine, Università degli Studi di Milano). The main steps of LC-ESI-MS, represented in figure 2.5, are:

1. Separation of the protein mixture through Liquid Chromatography (LC). This method is based on the physical separation of the analytes between two immiscible phases, namely the mobile and the stationary phases. In the reverse-phase method, the most widely used, the first one is a polar solvent (methanol, ethanol, acetonitrile…) mixed with water, while the stationary phase is hydrophobic (Dass, 2007). The analytes are separated depending on the affinity for the mobile and stationary phases and they flow out of the column at different times according to their partitioning between the two phases (Niessen, 2006). Critical parameters are the column diameter and the flow rate of the mobile phase (ranging from sub µL/min to 1 mL/min); the lower they are, the higher the sensitivity and the resolution of the method (Pitt, 2009).
2. Nebulization through the Electrospray Ionization Source (ESI). The eluate of the LC column is pumped through a capillary maintained at 3-5 kV and nebulized to form a spray of charge droplets. The droplets are rapidly evaporated by heat and dry nitrogen and the residual electrical charge is transferred to the analytes, which are carried into the chamber of the MS (Fenn et al., 1989; Kebarle, 2000).
3. Analysis by Mass Spectrometry (MS). The charged particles derived from the ESI enter in the high vacuum chamber of the MS, where their mass to charge ratio (m/z) is measured. The main components of the MS are the mass analyzer, which sorts the ions by their mass through the manipulation of their motion by the application of magnetic/electric fields, and the detector, which detects the abundancy of each mass-resolved ions by measuring and amplifying the ion current (Dass, 2007).

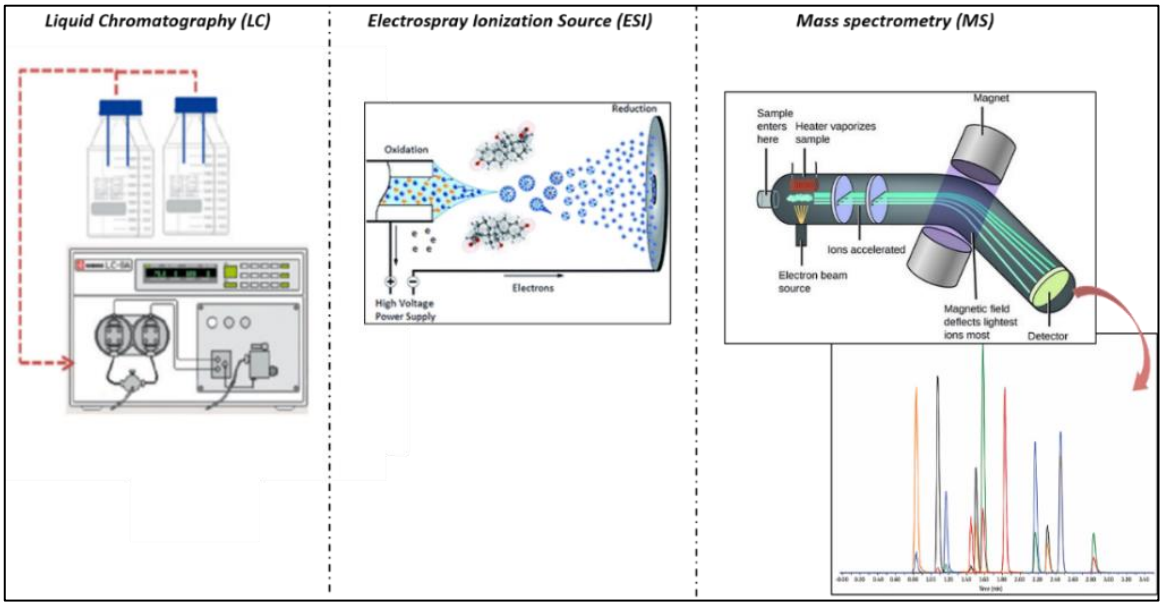

Figure 2.5. *Schematic representation of the Liquid Chromatography Electrospray Ionization Mass Spectrometric (LC-ESI-MS) technique. Adapted from Alymatiri et al., 2015 and Torre et al., 2015.*

In order to enhance the specificity of the method, tandem mass spectrometry (MS/MS) consisting of a double analysis of the samples by two different MS, was used. The ions with a specific m/z ratio, produced in the MS1, are selected and fragmented into smaller ions which, in turn, are analyzed by the second MS (MS2) (Pitt, 2009).

2.8.1 Liquid Chromatography Electrospray Ionization Tandem Mass Spectrometric (LC-ESI-MS/MS)

Human islets were collected by scratching the substrates with cold PBS LS supplemented with one tablet of cOmplete™ Mini Protease Inhibitor Cocktail (11836153001, Merck), 10 nM Microcystin-LR (33893, Merck), 10 nM Calyculin A (208851, Merck) and one tablet of 1x Phosphatase Inhibitor Cocktail (P2850, Merck). Cells were centrifuged at 720 x g for 5 minutes and after derivatization and reduction, proteins were digested using the trypsin sequencing grade reagent (TRYPSEQ-RO, Roche) using a protein:trypsin ratio of 50:1 for 16 hours at 37 °C.

The analysis was performed on a Dionex UltiMate 3000 HPLC System with a PicoFrit ProteoPrep C18 column (200 mm, internal diameter of 75 µm). Firstly, the proteins were separated by gradients (flow rate 0.3 µL/min):

- 1% acetonitrile (ACN) in 0.1% formic acid for 10 minutes
- 1-4 % acetonitrile (ACN) in 0.1% formic acid for 6 minutes
- 4-30 % acetonitrile (ACN) in 0.1% formic acid for 147 minutes
- 30-50 % acetonitrile (ACN) in 0.1% formic acid for 3 minutes.

The eluate was electrosprayed into an LTQ Orbitrap Velos through a Proxeon nanoelectrospray ion source (Thermo Fisher Scientific). For data acquisition, the instrument was set in positive mode in order to automatically alternate between a full scan in the Orbitrap and subsequent CID MS/MS (tandem mass spectroscopy with collision induced dissociation) in the linear ion trap of the 20 most intense peaks from full scan (Galli et al., 2018). The following parameters were used:

- Orbitrap full scan: resolution 6000, AGC (automatic gain control) target 1000000 and mass/ion charge number ratio (m/z) of 350-2000
- CID MS/MS: 35% normalized collision energy with 10 ms of activation
- Isolation window set at 3 Da; the exclusion list reported 200 proteins, which were scanned as reported in table 2.1:

Charge state	
Unassigned	Rejected
1+	Rejected
2+	Dynamic exclusion enabled (60 s)
3+	Dynamic exclusion enabled (60 s)
4+	Dynamic exclusion enabled (60 s)

Table 2.1. *Parameters used for the dynamic exclusion.*

Data acquisition was checked by Xcalibur 2.0 and Tune 2.4 software (Thermo Fisher Scientific). Four technical replicate analyses of each sample were performed.

2.8.2 Mass spectra analysis and quantification

Mass spectra were analyzed with the MaxQuant software (version 1.3.0.5) and the following parameters were settled:

- enzyme specificity: set to trypsin with a maximum of two missed cleavages allowed
- fixed protein modifications: only for carbamidomethylcysteine
- variable protein modifications: N-terminal acetylation, methionine oxidation and serine/ threonine/tyrosine phosphorylations.

The Andromeda search engine against the human (release 04.07.2014) and mouse (release 29.06.2015) Uniprot sequence databases was used to scan the spectra (Galli et al., 2018).
The quantification was carried out by using the built-in XIC-based fast label free quantification (LFQ) algorithm, setting the false positive rate at 1% for both peptide and protein levels against a concatenated target decoy database and a minimum peptide length of 6 amminoacids. Only proteins present in at least three counts of the four technical replicates were considered for the statistical analysis (Perseus software version 1.4.0.6). To determine the proteins differentially expressed in islets grown on the different substates, the ANOVA test was carried out with a false discovery rate of 0.05 (FDR).

2.8.3 Data interpretation and representation

In order to exclude proteins that are pancreas contaminants, the dataset was first compared with high quality islets proteome reported in literature (Martens 2015; Waanders et al., 2009) and proteins were classified for their function, molecular pathways and interactions.
Proteins differentially expressed in the experimental conditions were classified according to their function using the PANTHER and DAVID software. PANTHER (Protein Analysis Through Evolutionary Relationships) is a comprehensive library of phylogenic trees of protein-coding gene families, derived from 104 organisms, classified by their evolutionary history and functions (Mi et al., 2017). DAVID (Database for Annotation, Visualization and Integrated Discovery) software classifies the related and heterogenous many-genes-to-many-terms relationships in a simple and well organized view, enabling the users to efficiently identify differences and similarities between the experimental conditions (Huang et al., 2009). Proteins were classified based on their molecular function, biological process, localization in cellular components through the Gene Ontology (GO) annotations, and for the signaling pathways using the Kyoto Encyclopedia of Genes and Genomes (KEGG).
To have insights on protein-protein interactions, the dataset was scanned with Reactome and STRING softwares. The Reactome Knowledgebase is not only an archive of biological processes but also a tool for discovering unexpected functional relationships in the proteome, focusing on signal transduction pathways, DNA replication and metabolism (Fabregat et al., 2016). Molecular pathways are organized hierarchically as reported in the Gene Ontology (GO) classification, making the Reactome a graphic implementation for the GO data set (Ashburner et al., 2000; Gene Ontology Consortium, 2015). STRING (Search Toll for the Retrieval of Interacting Genes and proteins) database provides a global view of protein-protein physical and functional interactions using the calibrated and reliable information derived by the KEGG pathway platform (Kanehisa et al., 2014). Protein-protein interactions are reported into graphs where the network nodes represent the proteins and their dimensions are related to the availability of information about the 3D protein structure. The lines, which indicate protein associations, may be colored differently according to the evidence used for predicting the interaction and their thickness indicates the prediction confidence (Szklarczyk et al., 2015) (Figure 2.6). The following rules are considered:

- neighborhood evidence (green line): interactions that are observed in one organism are transferred to the others with similar genomic context by pre-computed orthology relations
- fusion evidence (red line): proteins fused in the genome of one species are functionally linked, even if they are not fused in the genome of the studied organism
- co-occurrence evidence (dark blue line): proteins with similar functions or occurrence in the same metabolic pathway, must be expressed together and have similar phylogenetic profile
- co-expression evidence (black line): interactions are predicted by using co-expression algorithms based on observed patterns of simultaneous expression of genes
- experimental evidence (purple line): interactions are experimentally validated and imported from primary databases
- database evidence (light blue line): interactions are analyzed by exploiting manually curated databases, i.e. KEGG.
- textmining evidence (yellow line): interactions are predicted by using an automated search within Medline abstracts and full-text articles (Huynen et al., 2003; Valencia and Pazos, 2002).

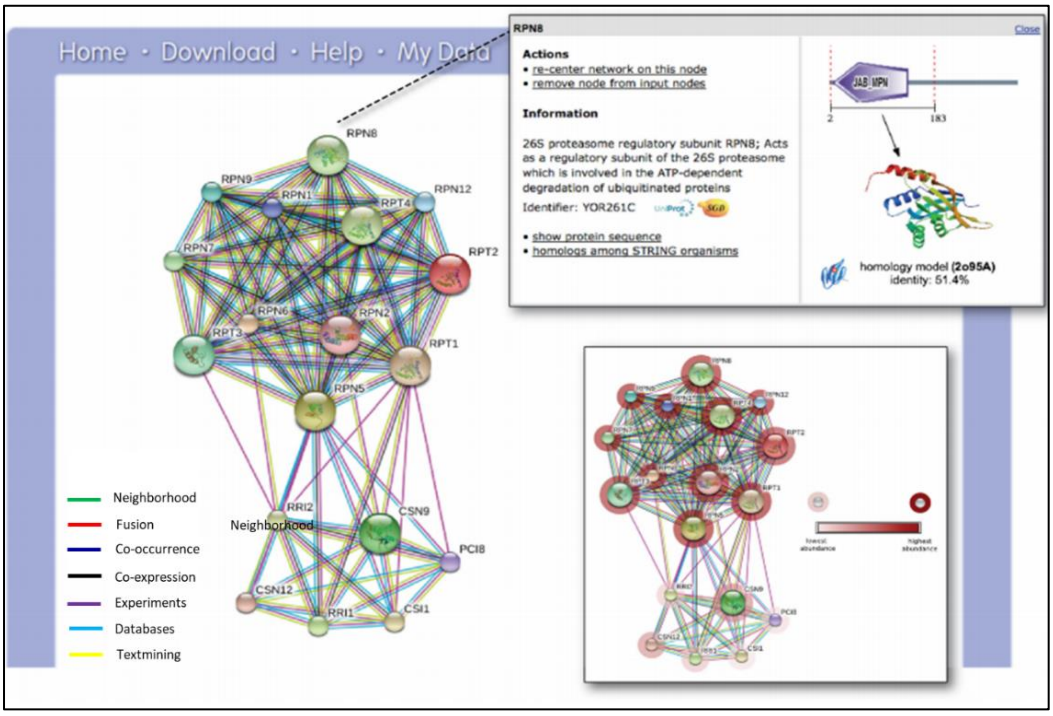

Figure 2.6. *Example of the STRING network view. Edges represent protein-protein interactions: their color and thickness indicate the evidence used for predicting the interaction and the confidence of the prediction, respectively. Upper box: accessory information about the selected proteins including annotations, cross-link, domains and 3D structure. Lower box: color-coded protein indicates abundance information and reveals differences in the expression. Adapted from Szklarczyk et al., 2015*

The mass spectrometry proteomics data have been deposited to the ProteomeXchange Consortium (http://proteomecentral.proteomexchange.org) via the PRoteomics IDEntifications (PRIDE) partner repository with the dataset identifier PXD007569.

2.9 Cell viability and apoptosis assays

2.9.1 ReadyProbes® Cell Viability Imaging

βTC3 viability was evaluated using the ReadyProbes® Cell Viability Imaging Kit (R37609, Invitrogen) following the manufacturer's protocol. It consists of 2 dyes: the NucBlue Live® reagent that stains all the cells nuclei and the NucGreen® Dead dye that labels only the nuclei of cells with compromised plasma membrane. Images were acquired with the motorized inverted microscope Axio Observer Z1 at 40 x magnification. Dead and live cells were detected using the n.52 and the DAPI filters, respectively. To quantify the percentage of dead cells over total cells, the number of NucBlue Live® and NucGreen® Dead positive cells was counted in at least 30 images for sample.

2.9.2 LDH release assay

Islet necrosis was quantified using the CyQUANT™ LDH Cytotoxicity Assay (C20300, Thermo Fisher Scientific) following the manufacturer's protocols. Absorbance emission was quantified at 490 nm and data were expressed as percentage of positive controls.

2.9.3 Terminal Deoxynucleotidyltransferase-mediated dUTP-biotin Nick End Labeling (TUNEL) Assay

Cell apoptosis was detected using the DeadEnd™ Fluorometric TUNEL System (G3250, Promega) following the manufacturer's protocol. In order to evaluate the β-cell apoptosis, islets were stained with anti-insulin antibody and DAPI as reported in chapter 3.3. Random fields were imaged at 40x magnification and the number of TUNEL-positive cells was counted in at least 100 insulin-immunoreactive cells (β cells) and 100 insulin-negative cells (non-β cells). To evaluate the percentage of β-cell apoptosis, the number of cells double positive for TUNEL and insulin was compared to the total number of insulin-immunoreactive β-cells.

2.10 Intracellular ROS quantification

Intracellular ROS were monitored by loading the cells with 2′,7′-dichlorofluorescin diacetate (DCFDA - D6883, Sigma Aldrich). It is a membrane permeable dye that is converted into non-fluorescent DCFH (dichlorofluorescein) by cytoplasmic esterases. When DCFH reacts with ROS, it is oxidized into the fluorescent DCF (dehydrogenated dichlorofluorescein) (Cumaoğlu et al., 2011). According to these mechanisms, the higher the fluorescence detected, the higher are the intracellular ROS. βTC3 cells were pre-loaded with 15 µM DCFDA in KRH buffer supplemented with 11 mM glucose at 37 °C for 60 minutes. Fluorescence emission (485/528 nm Ex/Em) was recorded with the microplate reader TECAN infinite® F500 (Tecan, GmbH) using the following parameters: excitation filter 485/20 nm, emission filter 535/25 nm and bottom - cyrcle filled (4x4) read option.

2.11 Functional and morphological characterization of mitochondria

Mitochondrial activity, localization and function were evaluated by labelling the organelles with MitoTracker probes, a family of organic compounds that passively diffuses across the plasma membrane and accumulates into the mitochondria (Gökerküçük et al., 2020). The following dyes were used (Figure 2.7):

- MitoSpy™ Orange CMTMRos (424803, Biolegend). A derivative of the orange-fluorescent tetramethylrosamine, which accumulates into the mitochondrial matrix according to their

membrane potential. Since its accumulation is strictly related to the membrane potential, it can be a valuable tool for monitoring mitochondrial function (Poot et al., 1996).

- MitoSpy™ Green FM (424805, Biolegend). It accumulates in mitochondria by binding the free thiols groups of cysteine residues. Since it accumulates in the organelles regardless of their membrane potential, it is particularly useful to evaluate mitochondrial mass and morphology (Pendergrass et al., 2004).

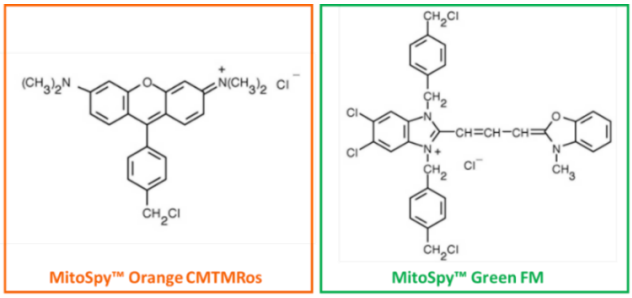

Figure 2.7. *Chemical structures of Mitospy™ Orange CMTMRos and Green FM.*

2.11.1 Mitochondrial membrane potential

Mitochondrial membrane potential was quantified by loading βTC3 cells with 100 nM MitoSpy™ Orange CMTMRos in KRH buffer supplemented with 11 mM glucose at 37 °C for 30 minutes. Fluorescence emission (551/576 nm Ex/Em) was recorded with the microplate reader TECAN infinite® F500 (Tecan, GmbH) using the following parameters: excitation filter 535/25 nm, emission filter 590/20 nm and bottom - cyrcle filled (4x4) read option.

2.11.2 Mitochondrial morphology and network

βTC3 and INS1E cells were labelled with 300 µM MitoSpy™ Green FM in KRH buffer supplemented with 11 mM glucose at 37 °C for 30 minutes. Samples were transferred into an imaging chamber and covered with 11 mM glucose KRH. Images were acquired with the motorized inverted microscope Axio Observer Z1 at 100 x magnification, using the n. 52 filter (Mitospy™ Green FM: 490/516 nm Ex/Em). Image analysis was performed using the ImageJ FiJi software. To enhance the mitochondrial structures, the fluorescence background was reduced and the Unsharp Mask filter was applied. Structures considered for the analysis were filtered imposing a threshold value of 4 times the background fluorescence. The following parameters were analyzed using the analyze particles plug-in: area (µm^2), aspect (major axis/minor axis), maximum Feret's diameter (µm) and the number of mitochondria per cell. According to Stiles and Shirihai (2012), labelled structure with a maximum Feret's diameter major of 17 µm were excluded from the analysis. The analyses of the mitochondrial network were carried out adapting the image processing reported by Valente et al., 2017. The number of mitochondrial networks per cell, the mean length of branches and the number of isolated mitochondria were measured using the analyze skeleton (2D/3D) plug-in.

2.12 Proteomic analysis of mitochondrial fraction

Mitochondrial fraction was extracted using the MITOISO2 kit (Sigma-Aldrich), which enables a fast and easy isolation and ensures the integrity of the mitochondria inner and outer membranes, following the manufacturer's protocol. Proteins were derivatized, reduced and digested for 16 hours at 37 °C using the trypsin sequencing grade reagent (TRYPSEQ-RO, Roche) with a

protein:trypsin ratio of 20:1 (Maffioli et al., 2017; Tedeschi et al., 2011). The proteomic analysis was performed using the Liquid Chromatography Electrospray Ionization Tandem Mass Spectrometric (LC-ESI-MS/MS) technique by the laboratory of prof. Tedeschi (department of Veterinary medicine, Università degli Studi di Milano). The analysis was carried out using a Dionex UltiMate 3000 HPLC System with an EASY-Spray PepMap RSLC C18 column (150 mm, internal diameter of 75 µm - Thermo Fisher Scientific). Firstly, the proteins were separated by liquid chromatography (LC) using the following gradients (flow rate 0.3 µL/min):

- 4% acetonitrile (ACN) in 0.1% formic acid for 3 minutes
- 4-40 % acetonitrile (ACN) in 0.1% formic acid for 90 minutes
- 40-45 % acetonitrile (ACN) in 0.1% formic acid for 10 minutes
- 45-90 % acetonitrile (ACN) in 0.1% formic acid for 16 minutes
- 90-94 % acetonitrile (ACN) in 0.1% formic acid for 14 minutes.

The eluate was electrosprayed into an Orbitrap Fusion Tribrid through a nanoelectrospray ion source (Thermo Fisher Scientific). For data acquisition, the instrument was set in positive mode in order to automatically alternate between a full scan in the Orbitrap and subsequent HCD MS/MS (tandem mass spectroscopy with higher-energy collisional dissociation) of the 20 most intense peaks from full scan (Maffioli et al., 2020). The following parameters were used:

- Orbitrap full scan: resolution 120000, AGC (automatic gain control) target 4000000 and mass/ion charge number ratio (m/z) of 300-15000
- HCD MS/MS: resolution 15000 with a 30% normalized collision energy
- Isolation window set at 1.6 Da; the charged particles were scanned as reported in table 2.2:

Charge state	
Unassigned	Rejected
1+	Rejected
2+	Dynamic exclusion enabled (30 s)
3+	Dynamic exclusion enabled (30 s)
4+	Dynamic exclusion enabled (30 s)
5+	Dynamic exclusion enabled (30 s)
6+	Dynamic exclusion enabled (30 s)
7+	Dynamic exclusion enabled (30 s)

Table 2.2. *Parameters used for the dynamic exclusion.*

Data acquisition was checked by Xcalibur 4.1 and Tune 3.0 software (Thermo Fisher Scientific). Three technical replicate analyses of each sample were performed (Maffioli et al., 2020).

2.12.1 Mass spectra analysis and quantification

Mass spectra were analyzed using the MaxQuant software (version 1.6.0.1) and the following parameters were set:

- mass deviation: 6 ppm for monoisotipic precursor ions and 0.5 Da for MS/MS peaks
- enzyme specificity: set to trypsin with a maximum of two missed cleavages allowed
- fixed protein modifications: only for carbamidomethylcysteine
- variable protein modifications: N-terminal acetylation, methionine oxidation and asparagine/glutamine deaminations.

The Andromeda search engine against the human Uniprot sequence database (release 03.06.2019) was used to scan the spectra and the targets reversed sequences were used as a decoy database

(Maffioli et al., 2020). The quantification was carried out using the built-in XIC-based fast label free quantification (LFQ) algorithm of MaxQuant software, setting the false positive rate at 1% for both peptide and protein levels against a concatenated target decoy database and a minimum peptide length of 7 amminoacids (Vernocchi et al., 2014). Only the proteins present in at least two of the three technical replicates were taken into account for the statistical analysis performed using the Perseus software (version 1.5.5.3).

2.12.2 Data interpretation and representation

The obtained proteome was scanned with MitoMiner (3.1 version), a freely accessible mitochondrial localization database. This software integrates the information from other public resources such as UniProt, Gene Ontology (GO) for cellular function, the Kyoto Encyclopedia of Genes and Genomes (KEGG) for metabolic pathways and the Online Mendelian Inheritance in Man (OMIM) database for diseases (Smith and Robinson, 2016). In our study, an Integrated Mitochondrial Proteomic Index (IMPI) ≥ 0.5 was set to filter out the mitochondrial proteins used for the analysis (Maffioli et al., 2020). Filtered proteins were classified according to their molecular function, biological process, localization in cellular components through the Gene Ontology (GO) annotations and for the signaling pathways by the Kyoto Encyclopedia of Genes and Genomes (KEGG), using the PANTHER and DAVID software. Functional clustering was based on a DAVID enrichment score of 3, with at least three counts, with a p-value ≤ 0.05 and protein-protein interactions were evaluated using the STRING software. The mass spectroscopy proteomics data were deposited on the ProteomeXchange Consortium with the dataset identifier PXD007569.

2.13 Vectors: amplification, purification and transfection

In our experiments, ER-GFP (kindly provided by Dr. Giovanni Piccoli, University of Trento, Italy) and LAMP1-GFP constructs were used to visualize the endoplasmic reticulum (ER) and the lysosomes, respectively. The amplification of DNA vectors was performed in JM109 bacteria (genotype: endA1 glnV44 thi-1 relA1 gyrA96 recA1 mcrB+ Δ(lac-proAB) e14- [F' traD36 proAB+ lacIq lacZΔM15] hsdR17(rK -mK +), an *Escherichia coli* strain.

2.13.1 Preparation of competent JM109 bacteria

Original JM109 bacteria were cultured in 3 mL of lysogeny broth (LB) overnight under agitation (220 rpm) at 37 °C. The day after, the bacterial culture was transferred into a sterile plastic flask containing 100 mL of LB and were grown under agitation (220 rpm) at 37 °C. Since bacteria can be made competent only during the exponential growth, an aliquot of the bacterial culture was taken every 30 minutes and their growth was analyzed by spectrophotometry (600 nm wavelength. When the measured optical density (OD) was around 0.6, bacteria reached the exponential growth phase and were processed as follow:

- centrifuge at 3000 rpm for 10 minutes at 4 °C
- resuspend the pellet in cold TB JAP solution and incubate in ice for 10 minutes
- centrifuge at 2500 rpm for 10 minutes at RT
- resuspend the pellet in TB JAP supplemented with 7% (v/v) DMSO and incubate in ice for 10 minutes.

2.13.2 JM109 transformation, DNA extraction and purification

DNA vectors were inserted into competent JM109 bacteria through thermal shock (30 minutes in ice, 1 minute at 42°C and 1 minute in ice). JM109 were then incubated at 37 °C for 90 minutes under agitation (220 rpm). Ampicillin (50 µg/mL), the antibiotic used for bacteria selection, was added to the bacterial culture, which was incubated overnight at 37 °C. Transformed bacteria were then incubated at 37 °C overnight under agitation (220 rpm) for amplification. DNA vectors were extracted and purified using the EuroGold Plasmid Miniprep kit (EMR500050, EuroClone), following the manufacturer's protocol. The concentration of the extracted cDNAs was quantified by gel electrophoresis.

2.13.3 Cell transfection

βTC3 and INS1E cells were transfected with the following protocol (volumes reported are referred to a 6-well plate):

- dilute 3.75 µL of Lipofectamine™ 3000 Reagent (L3000015, Thermo Fisher) in 125 µL Opti-MEM™ Medium (31985054, Thermo Fisher) and mix by vortexing
- prepare the DNA master mix by diluting 2.5 µg DNA in 125 µL OptiMEM™ Medium, add 5 µL P3000™ Reagent (L3000015, Thermo Fisher) and mix by vortexing
- add the DNA master mix to the diluted Lipofectamine reagent and incubate for 15 minutes at room temperature
- add the DNA-lipid complex to the cells and incubate in humidified atmosphere containing 5% of CO_2 at 37 °C.

2.14 Colocalization analyses

Transfected βTC3 and INS1E cells were labelled with 100 nM MitoSpy™ Orange CMTMRos, fixed in 4% paraformaldehyde solution for 20 minutes and mount on microscope slides using 1 mg/mL phenylenediamine (487473, Sigma Aldrich) solution. Images were taken with the motorized inverted microscope Axio Observer Z1 at 100x magnification, using the n.52 and n.43 filters. To enhance the image quality prior to colocalization analysis, the background was subtracted and images were pre-processed using the unsharp mask filters. ER-mitochondria contact sites were quantified through the Pearson's colocalization coefficient, while the lysosomes-mitochondria connections were evaluated by means of the ImageJ colocalization plug-in. The analyses of the ER network were carried out adapting the image processing reported by Valente et al., 2017. The number of ER networks per cell was measured using the analyze skeleton (2D/3D) plug-in.

2.15 miRNAs expression

βTC3 grown on the indicated substrate for 3 days were collected in QIAzol lysis reagent (79306, QIAGEN) and RNA extraction for miRNA analysis was performed with the miRNeasy Micro kit (217084, QIAGEN) following the manufacturer's protocol. Measurement of miRNAs expression were performed using the quantitative RT-qPCR miRCURY LNA SYBR Green detection kit (339347, QIAGEN).

2.16 Statistical analysis

Statistical analysis was performed using GraphPad Prism (version 5) software. Data were expressed as means ± S.E. (standard errors) or S.D. (standard deviations) of at least three independent experiments. Statistical comparisons were carried out using the unpaired student's t-test, the one-way and two-way ANOVA followed by multiple comparison. Differences were considered statistically significant when the p value was < 0.05.

2.17 Reagents and solutions

1 mg/mL Gelatin solution -20 mL

Weigh 20 mg of gelatin powder (48723, Sigma Aldrich) and dissolve it in 20 mL of deionized water by vortexing. Filter the solution using 0.22 µm filter and sonicate it for 30 seconds. Aliquot and store it in -20 °C.

50 mM Blebbistatin solution - 5 mL

Weigh 5 mg of Blebbistatin powder (B0560, Sigma Aldrich) and dissolve it in 5 mL of DMSO by vortexing. Aliquot and store it in -20 °C.

4% Paraformaldehyde (PFA) solution - 200 mL

Weigh 8 g of PFA powder, add 200 mL of 120 mM phosphate buffer pH 7.4 and dissolve the powder keeping the solution at 50 °C in a water bath. Filter and store the aliquots at -20 °C (avoid freeze-thaw cycles).

PBS LS (Phosphate buffer low salts) - 500 mL

	Initial concentration	***Final concentration***	***Volume***
Sodium chloride	4 M	150 mM	18.8 mL
Phosphate buffer pH 7.4	240 mM	10 mM	20.8 mL
Deionized water			up to 500 mL

PBS HS (Phosphate buffer high salts) - 500 mL

	Initial concentration	***Final concentration***	***Volume***
Sodium chloride	4 M	500 mM	62.4 mL
Phosphate buffer pH 7.4	240 mM	20 mM	41.6 mL
Deionized water			up to 500 mL

Gelatin buffer (GDB) 2x solution - 20 mL

	Initial concentration	***Final concentration***	***Volume***
Sodium chloride	4 M	450 mM	4.5 mL
Phosphate buffer pH 7.4	240 mM	10 mM	3.33 mL
Triton	100 %	0.6 %	120 µL
Gelatin	20 %	2 %	2 mL
Deionized water			up to 20 mL

The solution was diluted 1:1 in deionized water before using (GDB 1x).

1 mg/mL Phenylenediamine solution - 5 mL

Weigh 5 mg of Phenylenediamine (487473, Sigma Aldrich) into a tube and add 0.5 mL PBS LS, 3.5 mL of Glycerol and 1 mL of Deionized water. Keeping the solution in the dark, dissolve the phenylenediamine powder by vortexing. Stored it at - 20 °C.

1 mg/mL Aprotinin - 1 mL

Weigh 1 mg of aprotinin powder (A4529, Sigma Aldrich) and dissolve in 1 mL of deionized water. Store at -20 °C and dilute 1:1000 for the experiments.

200 mg/mL PMSF (**PhenylMethaneSulfonyl Fluoride)** - 10 mL

Weigh 200 mg of PMSF powder (10837091001, Sigma Aldrich), add 10 mL Absolute Ethanol and dissolve the powder by heating. Store at -20 °C and dilute 1:200 for the experiments.

25x Roche inhibitors - 2 mL

Dissolve one tablet of the cOmplete™ ULTRA Protease Inhibitor Cocktail (5892953001, Sigma Aldrich) into 2 mL of 100 mM phosphate buffer pH 7.4. Store at -20 °C and dilute 1:25 for the experiments.

RIPA (RadioImmunoPrecipitation Assay) buffer – 50 mL

	Initial concentration	***Final concentration***	***Volume***
Sodium chloride	4 M	150 mM	1.8 mL
Tris-HCl pH 7.6	1 M	50 mM	2.5 mL
EDTA	0.5 M	1 mM	0.1 mL
NP_{40}	100%	1%	0.5 mL
Deoxycholate	10%	0.5%	2.5 mL
Deionized water			up to 50 mL

2x β-mix - 5 mL

	Initial concentration	***Final concentration***	***Volume***
Sodium dodecyl sulfate (SDS)	10 %	5 %	2.5 mL
Glycerol	100 %	20 %	1 mL
Tris-HCl pH 8.9	1.5 M	300 mM	1 mL
β-mercaptoethanol	100 %	10 %	0.5 mL
Bromophenol blue	100 %	10 %	0.5 mL

10% polyacrylamide running gel

	Initial concentration	***Final concentration***	***Volume***
Bis-Acrylamide	30%	10%	3.33 mL
Tris HCl pH 8.9	1.5 M	375 mM	2.5 mL
Sodium dodecyl sulfate (SDS)	10 %	0.1 %	100 µL
Tetramethylethylenediamine (TEMED)	100 %	0.05 %	5 µL
Ammonium persulfate (APS)	10 %	0.025 %	25 µL
Deionized water			Up to 10 mL

Polyacrylamide stacking gel

	Initial concentration	*Final concentration*	*Volume*
Bis-Acrylamide	30 %	4 %	0.5 mL
Tris HCl pH 6.8	0.5 M	62.5 mM	0.5 mL
Sodium dodecyl sulfate (SDS)	10 %	0.1 %	37.5 µL
Tetramethylethylenediamine (TEMED)	100 %	0.1 %	37.5 µL
Ammonium persulfate (APS)	10 %	0.05 %	18.7 µL
Deionized water			Up to 3.75 mL

10x Tris Buffer Saline (TBS) pH 7.4 - 500 mL

Weigh 30.27 g Trizma® base (T1503, Sigma Aldrich) and 42.5 g sodium chloride (S9888, Sigma Aldrich) and dissolve them in 400 mL deionized water. Adjust the pH to 7.4 with 10 N HCl, then add deionized water up to 500 mL.

Running buffer - 500 mL

	Initial concentration	*Final concentration*	*Volume*
Tris-Glycine	10x	1x	50 mL
SDS	10 %	0.1 %	5 mL
Deionized water			up to 500 mL

Blotting buffer - 1 L

	Initial concentration	*Final concentration*	*Volume*
Tris-Glycine	10x	1x	100 mL
Methanol	100 %	10 %	100 mL
Deionized water			up to 1 L

Wash solution (TBS-T) - 100 mL

	Initial concentration	*Final concentration*	*Volume*
TBS	10x	1x	10 mL
Tween 20	100%	0.1 %	100 µL
Deionized water			up to 100 mL

1x blocking buffer- 50 mL

	Initial concentration	*Final concentration*	*Quantity*
non-fat dried milk	100%	5 or 3%	2.5 or 1.5 g
TBS	10x	1x	5 mL
Tween 20	100%	0.1 %	50 µL
Deionized water			up to 50 mL

1x incubation buffer- 50 mL

	Initial concentration	*Final concentration*	*Quantity*
non-fat dried milk or BSA	100%	5% or 1%*	2.5 g or 0.5 g
TBS	10 x	1 x	5 mL
Tween 20	100%	0.1 %	50 µL
Deionized water			up to 50 mL

Hard stripping solution - 50 mL

	Initial concentration	*Final concentration*	*Volume*
β-mercaptoethanol	12.8 M	100 mM	390 µL
SDS 10%	10 %	2%	10 mL
Tris HCl pH 6,7	1 M	62.5 mM	3,125 mL
Deionized water			up to 50 mL

Mild stripping solution- 1L

Weigh 15 g Glycine (1610718, Bio-Rad) and 1 g SDS (L3771, Sigma Aldrich) and dissolve them in 800 mL of deionized water. Add 10 mL of 100% Tween 20 (final concentration 1% - P1379, Sigma Aldrich), adjust the pH to 2.2 with 10 N HCl, then add deionized water up to 1 L.

1x MACS (magnetic-activated cell sorting) buffer- 50 mL

	Initial concentration	*Final concentration*	*Volume*
FBS HI	100%	2%	1 mL
EDTA	1 M	2 mM	100 µL
PBS LS			up to 50 mL

KRH (Krebs Ringer Buffer) - 50 mL

	Initial concentration	*Final concentration*	*Volume*
Sodium chloride	4 M	125 mM	1.56 mL
Potassium chloride	1 M	5 mM	250 µL
Magnesium sulfate	120 mM	1.2 mM	500 µL
Potassium di-hydrogen phosphate	120 mM	1.2 mM	500 µL
Hepes-NaOH pH 7.4	100 mM	25 mM	12.5 mL
Calcium chloride	100 mM	2 mM	1 mL
Deionized water			Up to 50 mL

Lysis buffer - 50 mL

	Initial concentration	*Final concentration*	*Volume*
Sodium chloride	4 M	150 mM	1.87 mL
Magnesium chloride	1 M	1 mM	50 µL
Tris HCl pH 7.4	1 M	20 mM	1 mL
Triton	100%	1%	50 µL
Deionized water			up to 50 mL

15 mM DCFDA solution - 10 mL

Dissolve 73 mg of DCFDA powder (D6883, Sigma Aldrich) in 10 mL of deionized water. Mix by vortexing, aliquot and store in - 20 °C. Dilute 1: 1000 for the experiments.

1 mM MitoSpy™ Orange CMTMRos solution

Add 117 µL of sterile dimethyl sulfoxide (DMSO – D2438, Sigma Aldrich) to 50 µg of MitoSpy™ Orange CMTMRos powder (424803, Biolegend). Mix by vortexing, aliquot and store in -20 °C (avoid freeze-thaw cycles). Dilute 1:10000 for the experiments.

1 mM MitoSpy™ Green FM solution

Add 74 µL of sterile dimethyl sulfoxide (DMSO – D2438, Sigma Aldrich) to 50 µg of MitoSpy™ Green FM powder (424805, Biolegend). Mix by vortexing, aliquot and store in -20 °C (avoid freeze-thaw cycles). Dilute 1:1000 for the experiments.

Lysogen broth (LB) - 500 mL

Weigh 5 g tryptone (A1553, BioChemica), 2.5 g yeast extract (A1552, BioChemica) and 2.5 g sodium chloride (S9888, Sigma Aldrich) powders and add 500 mL of deionized water; dissolve solid agglomerates and sterilize by autoclaving.

TB JAP - 100 mL

Weigh 0.303 g PIPES (P6757, Sigma Aldrich), 0.221 g calcium chloride (223506, Sigma Aldrich) and 1.864 g potassium chloride (P3911, Sigma Aldrich) powders and dissolve in 80 mL deionized water; adjust the pH to 6.7 with NaOH 1 N. Dissolve 1.09 g of manganese chloride (1375127, Sigma Aldrich) and add deionized water up to 100 mL. Filter the solution with 0.22 µm filters and store at 4 °C.

3. Results and Discussion

3.1 Nanostructured substrates promote long-term differentiation and functioning of human islets of Langerhans

In the last years, emerging evidence suggests the crucial role of mechanical features of the extracellular environment in regulating cell development, differentiation and functions both *in vivo* and *in vitro* culture (Kim et al., 2019; Martino et al., 2018). It is particularly evident in tumor cells, where the stiffening of the ECM favors the metastatic phenotype, or in other tissues normally subjected to the fluid flow, as the endothelial cells and the hair cells of the inner ear (Jaalouk and Lammerding, 2009).

Pancreatic β-cells *in vivo* reside in a complex environment that provides a plethora of signals that regulates their survival and functions (Aamodt and Powers, 2017; Di Cairano et al., 2016; Galli et al., 2020; Stendahl et al., 2009). Among the critical components of the islet niche is the ECM which not only serves as a scaffolding material for cell attachment but also provides important instructional cues for cell differentiation, survival and function. Human β-cells *in vitro* poorly survive, do not replicate and often de-differentiate to a non-mature phenotype, possibly for the enzymatic digestion during islet isolation that may disrupt the niche environment.

Although it has been reported that modulation of the expression of ECM biomolecules improves β-cell/human islet culture conditions, poorly is known about the impact of the mechanical cues in regulating β-cell differentiation and function. As the basement membrane is a 3D scaffold organized at the micro- and nanometer scale, in this work we focus on the nanotopography and we investigate its impact on β-cell fate in long term culture of human isolated islets.

To mimic the ECM nanotopography, in collaboration with the department of Physics (prof. Milani and Lenardi, Università degli Studi di Milano), nanostructured substrates were produced by assembling zirconia clusters using the Supersonic Cluster Beam Deposition (SCBD) technique (Borghi et al., 2016). This bottom-up approach to nanofabrication allows the random deposition of zirconia nanoclusters on glass coverslips and the resulting surfaces have extracellular matrix-like nanotopographies characterized by a reproducible roughness (rms). Previous experiments performed on a neuron-like PC12 cell line and primary cultures of rat hippocampal neurons demonstrated that these substrates promote neuronal differentiation due to their impact on mechanotransductive processes (Schulte et al., 2016, 2017). Given the similarities between β-cells and neurons, we speculated that these substrates might also influence β-cell behavior (Di Cairano et al., 2016). Flat zirconia substrates (flat-ZrO_2), obtained by atom assembling with an electron beam evaporator, were employed as controls. They are fully oxidized films of zirconia (same material of the nanostructured substrates) but their roughness is less than 0.5 nm, i.e. they are flat and therefore they allow to understand the nanotopography contribution on cell behavior. As a further control, islets were also plated on gelatin covered substrates which are normally employed in our laboratory for their culture (Di Cairano et al., 2011). Gelatin covered substrates show some irregularities due to protein clustering, but the roughness is less than 1 nm (Borghi et al., 2016; Schulte et al., 2017). Figure 3.1 shows the top and three-dimensional topographical maps of flat and cluster assembled zirconia films (rms 15 nm and 20 nm) obtained by atomic force microscopy (AFM).

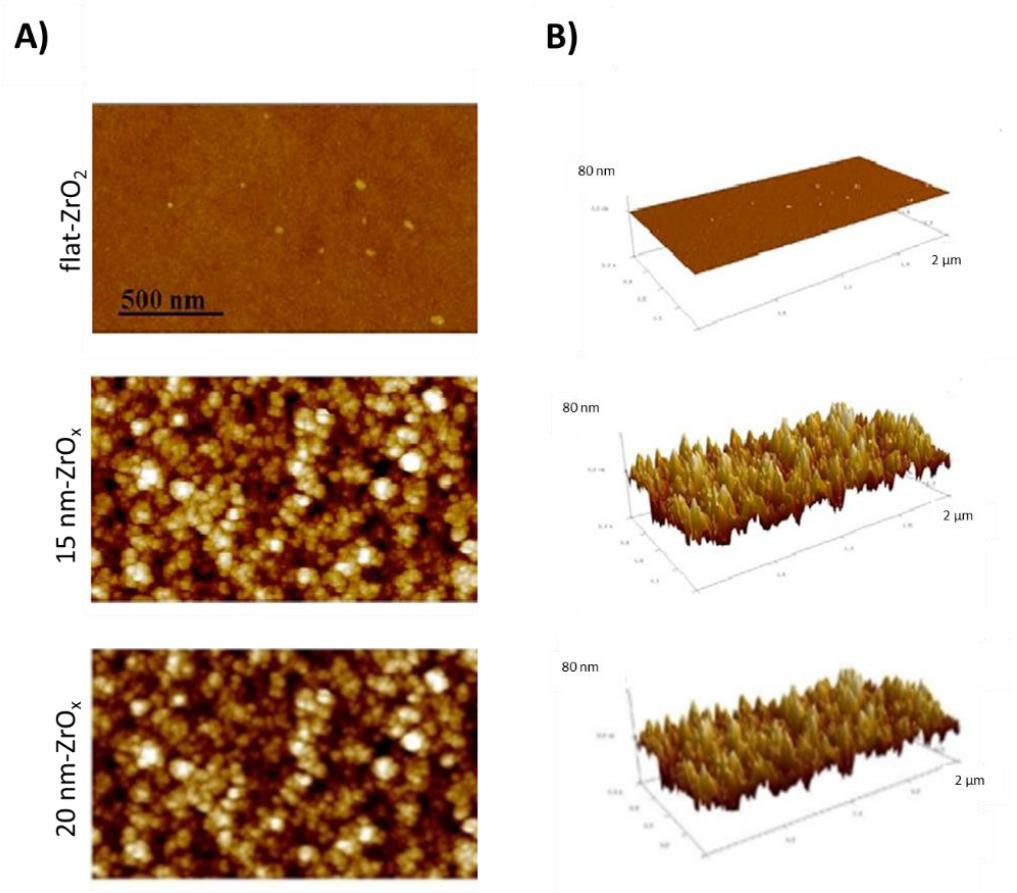

Figure 3.1. *AFM characterization of flat, 15 nm and 20 nm zirconia substrates. Flat zirconia films were produced by e-beam evaporation, while nanostructured substrates were obtained using the supersonic cluster beam deposition (SCBD) technique. Top (A) and three-dimensional (B) views are reported; for all images the scan area is 2 × 1 µm². Galli et al., 2018; Singh et al., 2012*

3.1.1 Nanostructured substrates promote long-term β-cell differentiation

Human islets of Langerhans were dispersed by a short trypsinization and cultured on the above-mentioned substrates for up to 30 days. Islet digestion and dispersion resulted in small cell clusters (10-30 cells/cluster) in which about 50% of the cells was in direct contact with the substrate.

During the first days of cultures, islet cells attached efficiently to the different substrates, except for 20 nm-ns-ZrO_x. Phase contrast optical images showed that human islets cultured on 15 nm-ns-ZrO_x retained an islet-like cell cluster organization after 20 days in culture, which was partially lost in islets grown on the gelatin and flat substrates (Figure 3.2A). On control substrates a population of elongated cells surrounding the islet was detectable, which was barely observed on 15 nm-ns-ZrO_x samples. The cell density was similar on the different substrates except for 20-ns-ZrO_x where it was lower, probably due to inefficient cell adhesion observed over the 24 hours (Figure 3.2B). For this reason, the 20-ns-ZrO_x substrate was excluded from further analyses.

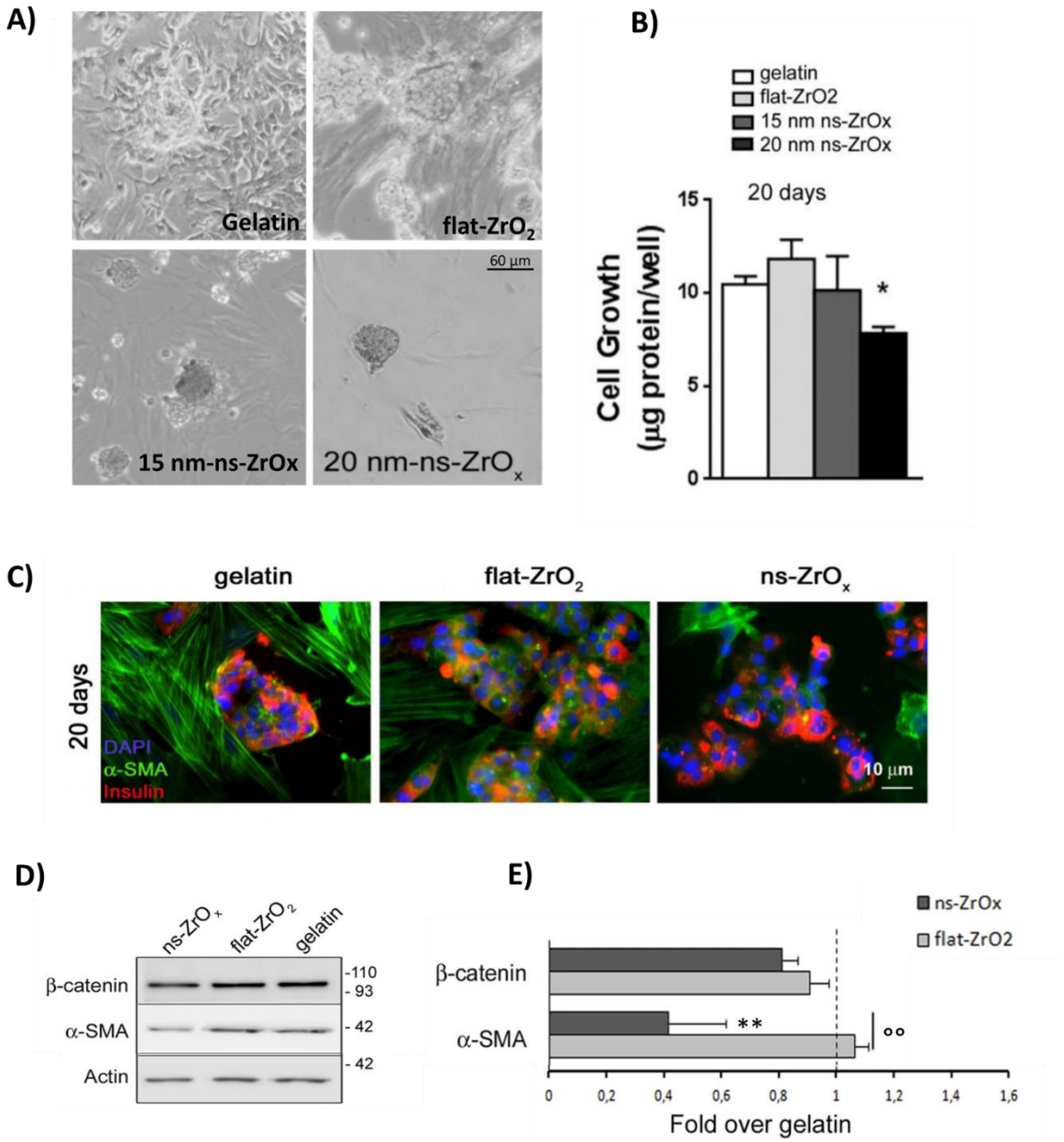

Figure 3.2. *Nanostructured zirconia substrates preserve the cluster organization of native islets and prevent the proliferation of fibroblasts/mesenchymal cells in long term cultures.* ***A)*** *Representative phase contrast optical images of human islets grown on gelatin, flat-ZrO_2, 15 nm-ns-ZrO_x and 20 nm-ns-ZrO_x. Bar: 60 µm.* ***B)*** *Total protein quantification of human islets grown on gelatin, flat and nanostructured (15 and 20 nm) substrates. Bars represent the mean ± SE of three independent experiments performed in triplicate. (* p<0.05 all vs 20 nm-ns-ZrO_x).* ***C)*** *Human islets of Langerhans were seeded on gelatin, flat and nanostructured substrates and cultured for 20 days. Representative images of islets triple stained with α-SMA (green), insulin (red) and DAPI (blue). Bar: 10 µm.* ***D)*** *Western-blotting analysis of α-SMA and β-catenin expression (15 µg protein/sample). On the right, the molecular weight of the protein standard is reported in kDa.* ***E)*** *Quantitative analysis of protein expression shows a significant reduction of α-SMA expression in cells grown on ns-ZrO_x compared to flat-ZrO_2 and gelatin. Data (mean values ± S.E.; n = 5 independent experiments) are expressed as fold change over gelatin (dashed line). (**p < 0.01, ns-ZrO_x vs gelatin; °°p < 0.01, ns-ZrO_x vs flat-ZrO_2).*

To understand the origin of these elongated cells, long term cultured islets were stained with α-SMA (smooth muscle actin) antibody, a marker of myofibroblasts and mesenchymal cells. As shown in figure 3.2C, α-SMA positive cells were barely detected in the islets grown on the nanostructure but were abundant on both control substrates (flat-ZrO_2 and gelatin). Results were confirmed by western blot analyses that revealed a significant reduction of α-SMA expression in cells grown on nanostructured substrate compared to flat-ZrO_2 and gelatin (Figure 3.2D,E). Even though the origin

of these α-SMA positive cells was not fully characterized, they might represent proliferating fibroblasts/mesenchymal cells originally associated within the islets or dedifferentiated β-cells.

In order to verify the endocrine-nature of cells in culture and to reveal whether the nanostructure preserves β-cell differentiation, the samples were stained with chromogranin and insulin at different time in culture (Figure 3.3A). The percentage of chromogranin-positive endocrine cells and insulin positive β-cells was similar on the different substrates during the first days of culture. However, in long term culture (>15 days), a significantly higher percentage of β cells was detected in the islet grown on the nanostructure compared to controls (41 ± 15% increase), while no changes were observed in the total number of endocrine cells (Figure 3.3B).

Triple staining with insulin, glucagon and somatostatin allowed us to monitor the presence of differentiated β-, α- and δ-cells, respectively (Figure 3.3C). While a similar proportion of the three cells populations was observed on the different substrates 5 days after plating, this organization was retained only on the nanostructure in long-term culture. Conversely, several glucagon- and somatostatin- but few insulin-positive cells were detected on control substrates, thus indicating that probably the nanostructure prevents the dedifferentiation of β-cells *in vitro*.

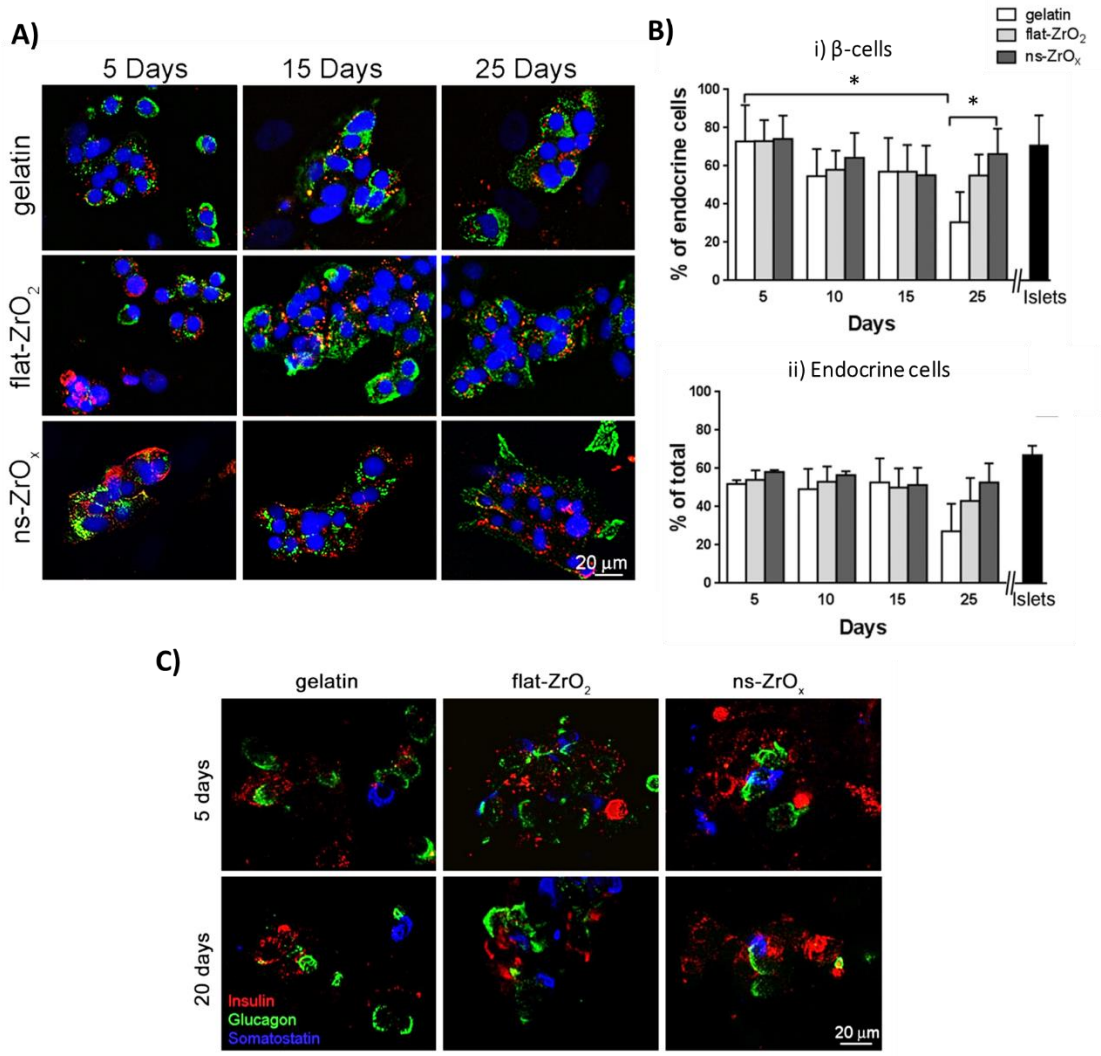

Figure 3.3. *Nanostructured substrates promote long term β-cell survival. Human islets of Langerhans were plated on gelatin, flat and nanostructured substrates and fixed in 4% PFA at different stages in culture.* ***A)*** *Representative immunofluorescence images of human islets grown on different substrates for 5, 10, 15 or 25 days and triple stained with anti-insulin (red), anti-chromogranin A (green) antibodies and DAPI (blue). Bar: 20 µm.* ***B)*** *Quantification of β- and endocrine cells density. Black bars indicate the percentage in freshly isolated islets. i) Insulin-positive β-cells are expressed*

*as percentage of total endocrine cells (chromogranin A-positive cells). ii) Chromogranin A-positive endocrine cells are expressed as percentage of total DAPI-positive cells. Data are expressed as mean ± SE of five independent experiments, performed in duplicate. (*p < 0.05, ns-ZrO_x vs gelatin).* ***C)*** *Representative confocal images of human islets grown on different substrates for 5 and 20 days and triple stained with anti-insulin (red), anti-glucagon (green) and anti-somatostatin (blue) antibodies. Bar: 20 µm.*

We finally excluded that the nanostructure might increase the β-cell mass by activating a proliferation program. To this purpose, islets cultured on different substrates were stained with insulin and Ki67, a marker of proliferation, at 5 and 15 days in culture (Figure 3.4A,B). As expected, the rate of β-cell proliferation was two-fold lower than that of non-endocrine cells under all experimental conditions ($p < 0.05$). At each time point we found a higher percentage of proliferating β-cells on ns-ZrO_x than on control substrates, even though the difference was not statistically significant. A similar trend was observed when β-cell proliferation was assessed by FACS analysis evaluating the percentage of Ki67-PDX1 double-positive cells grown for 5 and 10 days on different substrates (Figure 3.4C,D).

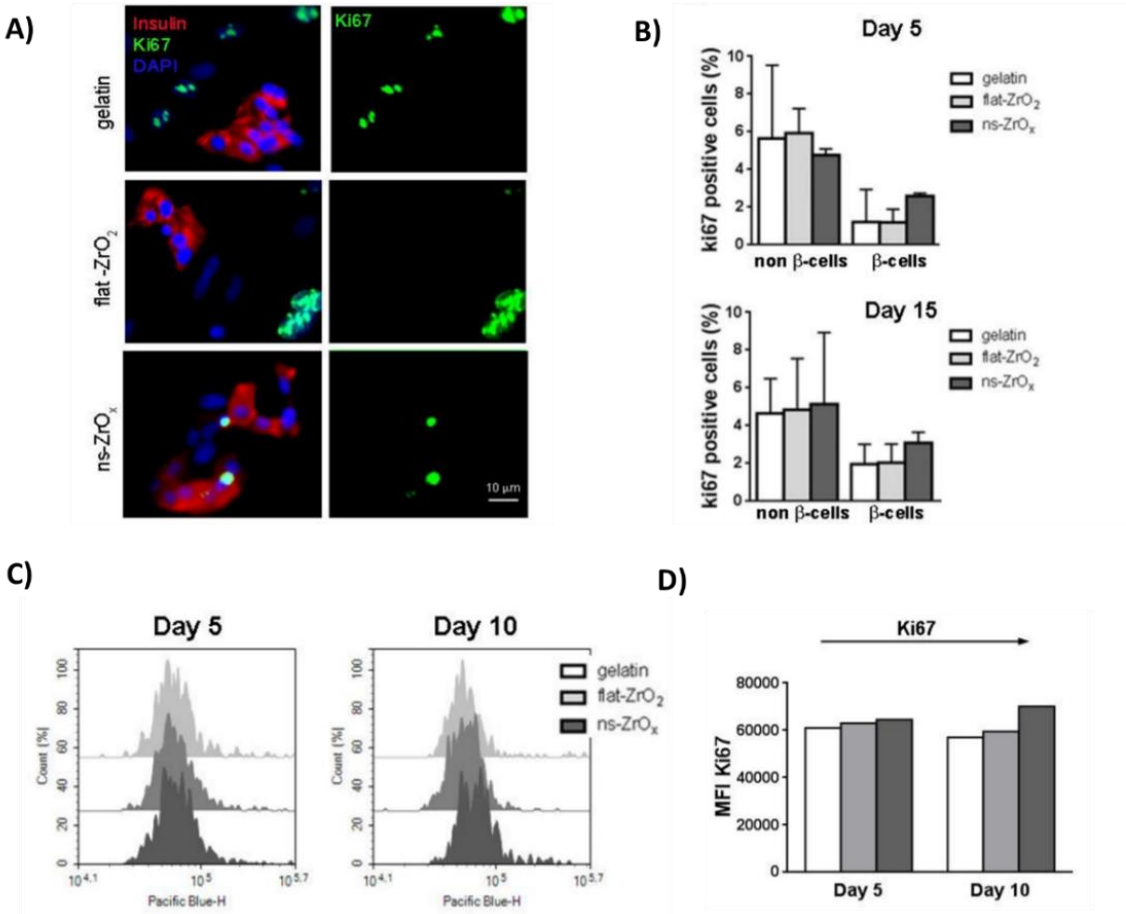

Figure 3.4. *β-cell proliferation in islets grown on different substrates. Human islets of Langerhans were plated on the indicated substrates and β-cell proliferation was evaluated after 5, 10 and 15 days in culture.* ***A)*** *Representative immunofluorescence images of islets triple stained with anti-Ki67 (green), anti-insulin (red) antibodies and DAPI (blue). Bar: 10 µm.* ***B)*** *Quantification of β-cell proliferation in human islets grown on different substrates for 5 and 15 days. β-cell proliferation is expressed as the percentage of Ki67-insulin-double positive cells over total insulin-positive cells, while non β-cell proliferation is reported as the percentage of Ki67-positive cells over total DAPI-positive and insulin-negative cells. Data represent the mean ± SD of three different islet experiments, performed in triplicate (N>100 cells for each substrate).* ***C,D)*** *FACS analysis of β-cell proliferation. Islets were dissociated with collagenase and stained with ef450 conjugated anti-human Ki67 and primary anti-human insulin followed by secondary PE conjugated anti-guinea pig.* ***C)*** *Median intensity of fluorescence for ef450 conjugated anti-human Ki67 of insulin-positive cells detected after 5 and 10 days in culture.* ***D)*** *Representative histograms from one experiment are shown.*

Taken together, these data reveal that the nanotopography preserves the clustered cellular organization, typical of intact islets. Interestingly, recent evidence suggests that different cell types (neurons, osteoblasts and fibroblasts) retain a cluster organization when seeded on nanoscale systems suggesting that on this substrate cell-cell adhesions dominate over the interactions with the substrate (Brammer et al., 2011; Chen et al., 2012; Dalby et al., 2007).
Standard culturing supports (petri dishes and glass covers) have stiffness in the GPa range that favors the cell-substrate interactions and probably for this reason, human isolated islets of Langerhans lose their inter-cellular organization, leading to impairment β-cell survival and function (Herum et al., 2017).
Therefore, the nanostructured supports provide a scaffold that better mimics the nanoscale architecture formed by the islet ECM, preventing the β-cell dedifferentiation.

3.1.2 Quantitative proteomic analyses

A proteomic approach was followed to characterize the molecular mechanisms responsible for the increased β-cell differentiation occurring in islets grown on the nanostructure. To this purpose, islets grown on the different substrates for 20 days were collected, lysed and processed by a shotgun proteomic approach using label-free quantification following the workflow described in Figure 3.5 A and B (the proteomic analysis was performed by the laboratory of prof. Tedeschi, Department of veterinary medicine, Università degli Studi di Milano). High purity islet preparations (80-90% of islets) were selected for the analysis to avoid possible contamination by proteins derived from non-endocrine cell populations. Furthermore, to filter out the proteins deemed to be possible contaminants, the proteomic data were compared with those obtained by high quality islet proteome reported in literature (Martens, 2015; Waanders et al., 2009).
The analyses identified 49, 64 and 65 proteins exclusively expressed in gelatin, ns-ZrO_x and flat-ZrO_2, respectively, and 1379 common proteins of which 97 were differentially expressed (Anova test FDR 0.05) (Figure 3.5C). Data sets were compared to identify the proteins that were differentially expressed under specific conditions, namely ns-ZrO_x versus gelatin, ns-ZrO_x versus flat-ZrO_2 and flat-ZrO_2 vs gelatin, as shown in the Vulcano plots (Figure 3.5D). To dissect the impact of the nanostructure, bioinformatic analyses were performed by comparing ns-ZrO_x vs gelatin and ns-ZrO_x vs flat-ZrO_2.

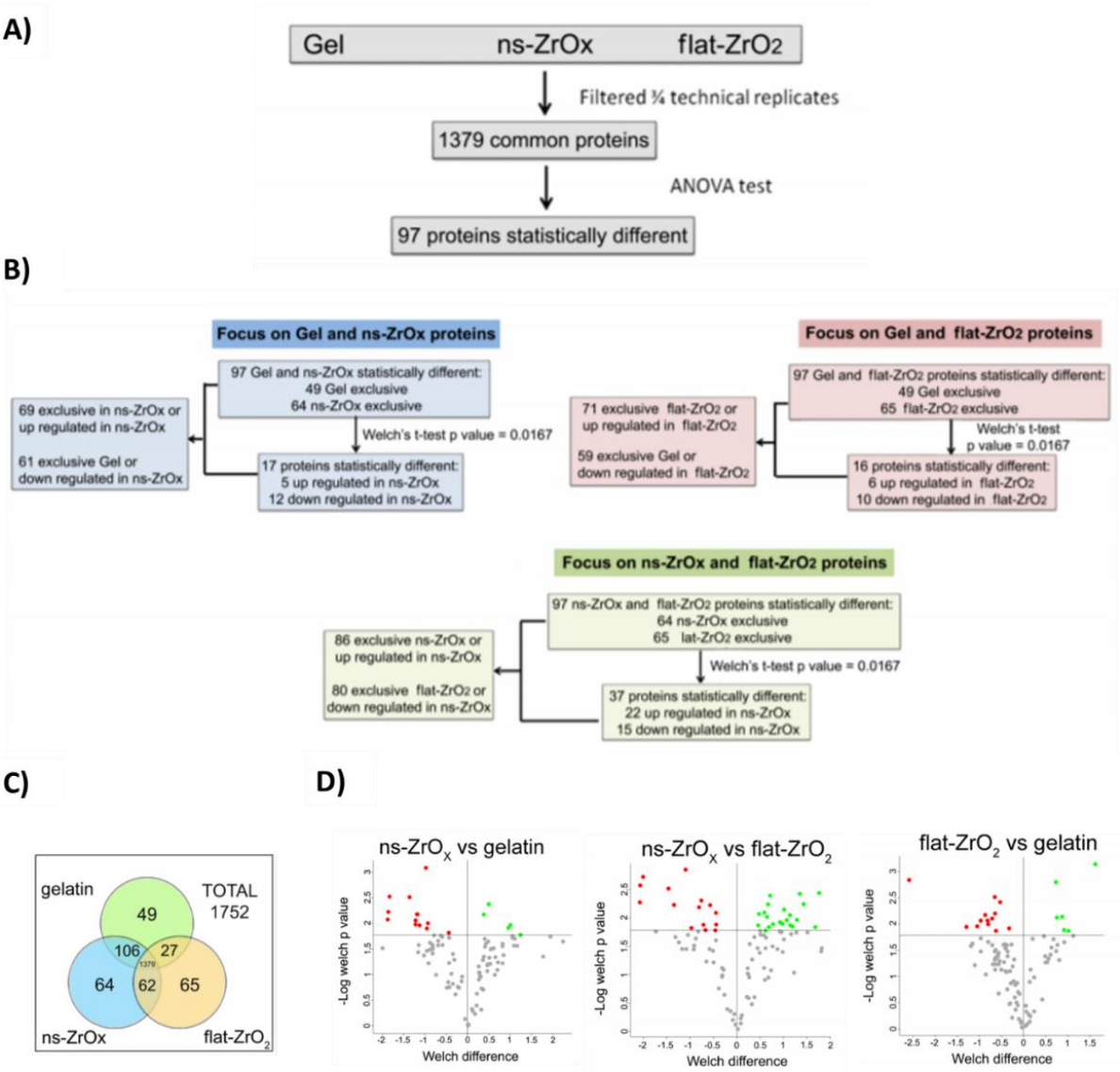

Figure 3.5. *Workflow of the quantitative proteomic analyses. Human islets grown on the indicated substrates for 20 days were collected, lysed and processed by a shot-gun proteomic approach using label-free quantification.* ***A)*** *Proteins differentially expressed among the three conditions were identified by an ANOVA test (FDR 0.05).* ***B)*** *Comparison between specific data sets carried out by Welch's t-test (p value 0.0167): common proteins were considered differentially expressed if they were present only in one of the growing condition or showed significant t-test difference.* ***C)*** *Venn diagram showing the number of genes only expressed and common among ns-ZrO_x, gelatin and flat-ZrO_2.* ***D)*** *Vulcano plots of proteins differentially expressed in ns-ZrO_x versus gelatin, ns-ZrO_x versus flat-ZrO_2 and flat-ZrO_2 vs gelatin (Welch's t-test p value 0.0167). Proteins differentially expressed are reported in GREEN (increased expression) or RED (decreased expression); in GREY the proteins whose difference is not statistically significant. (Laboratory of Prof. Tedeschi)*

Regarding the comparison between ns-ZrO_x and gelatin, the gene ontology (GO) analysis revealed that the proteome of the islets grown on ns-ZrO_x was enriched in GO terms GO:0009653 anatomical structure morphogenesis and GO:0005200, GO:0015629, GO:0005856 structural constituents of cytoskeleton, thus suggesting a morphogenic process involving the remodeling of the actin cytoskeleton (Figure 3.6A). The ns-ZrO_x substrate also induced the upregulation of a number of chromatin-associated proteins (GO:0031497), spliceosoma (GO:0005681) and heterogeneous nuclear ribonucleoprotein (GO:0030529) complexes, thus suggesting the activation of a robust program of transcriptional and translational regulation. Figure 3.6B and C show the protein-protein interactions and the cellular pathways obtained by bioinformatic analyses of the same data set.

Interestingly, the GO analysis of the proteins only expressed or upregulated in ns-ZrO_x compared to flat-ZrO_2 substrates (Figure 3.7) identified a pattern of proteins similar to the one observed when comparing ns-ZrO_x and gelatin. Indeed, islets grown on ns-ZrO_x were enriched in GO cellular component terms related to morphogenesis (GO:0032989), anatomical structure morphogenesis (GO:0009653) and structural constituent of the actin cytoskeleton (GO:0005856) (Figure 3.7).

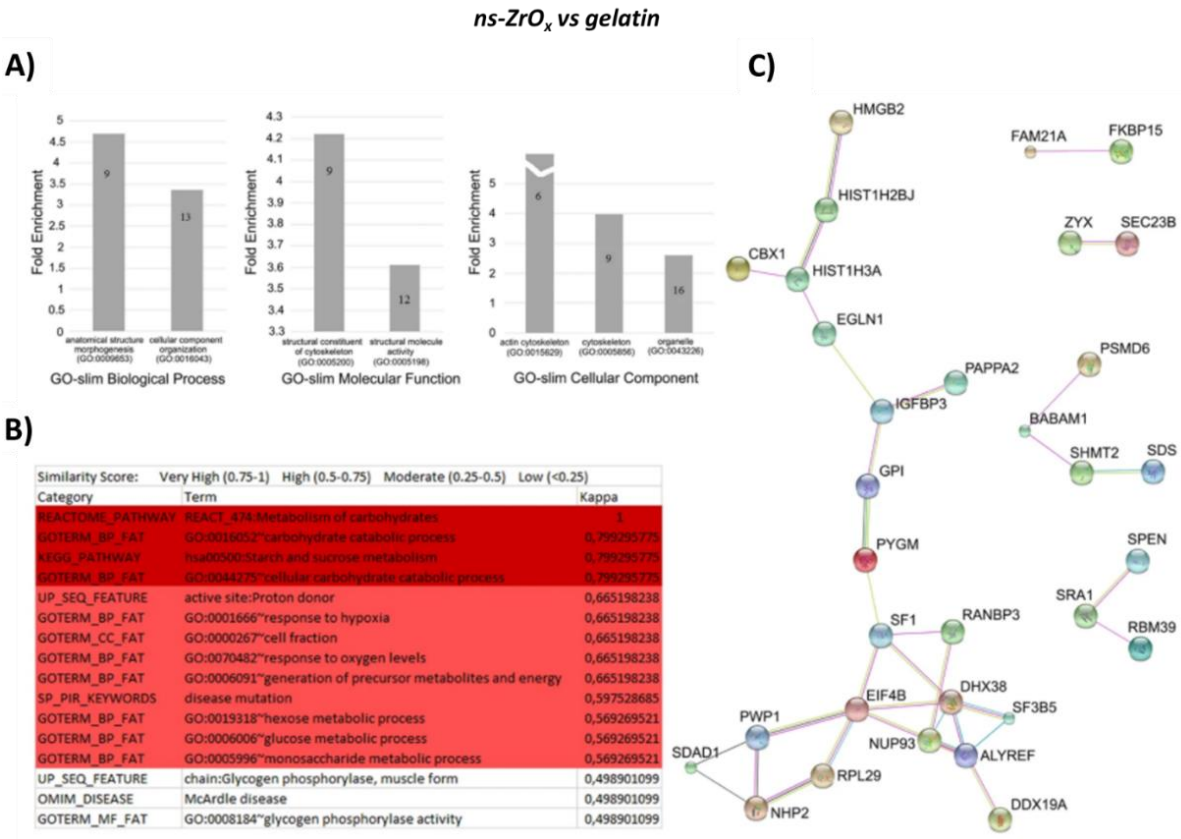

Figure 3.6. *Bioinformatic analysis of proteins increased or exclusively expressed in cells grown on ns-ZrO_x compared to gelatin.* ***A)*** *Gene Ontology analyses was carried out using Panther software and the protein were classified in GO-biological process (GOBP), GO-cellular component (GOCC) and GO-molecular function (GOMF) (GO). Functional grouping was based on p value ≤ 0.05. The numbers in the bars indicate the genes number for each category.* ***B)*** *Reactome analysis. Only categories with confidence level Very High (K value 0.75–1) (Dark Purple) and High (K value 0.5–0.75) (Purple) are reported.* ***C)*** *String analysis of network interactions. Active interactions: text mining, experiments, databases; edges thickness indicates "confidence". The proteins are indicated by the official gene symbol. (Laboratory of Prof. Tedeschi)*

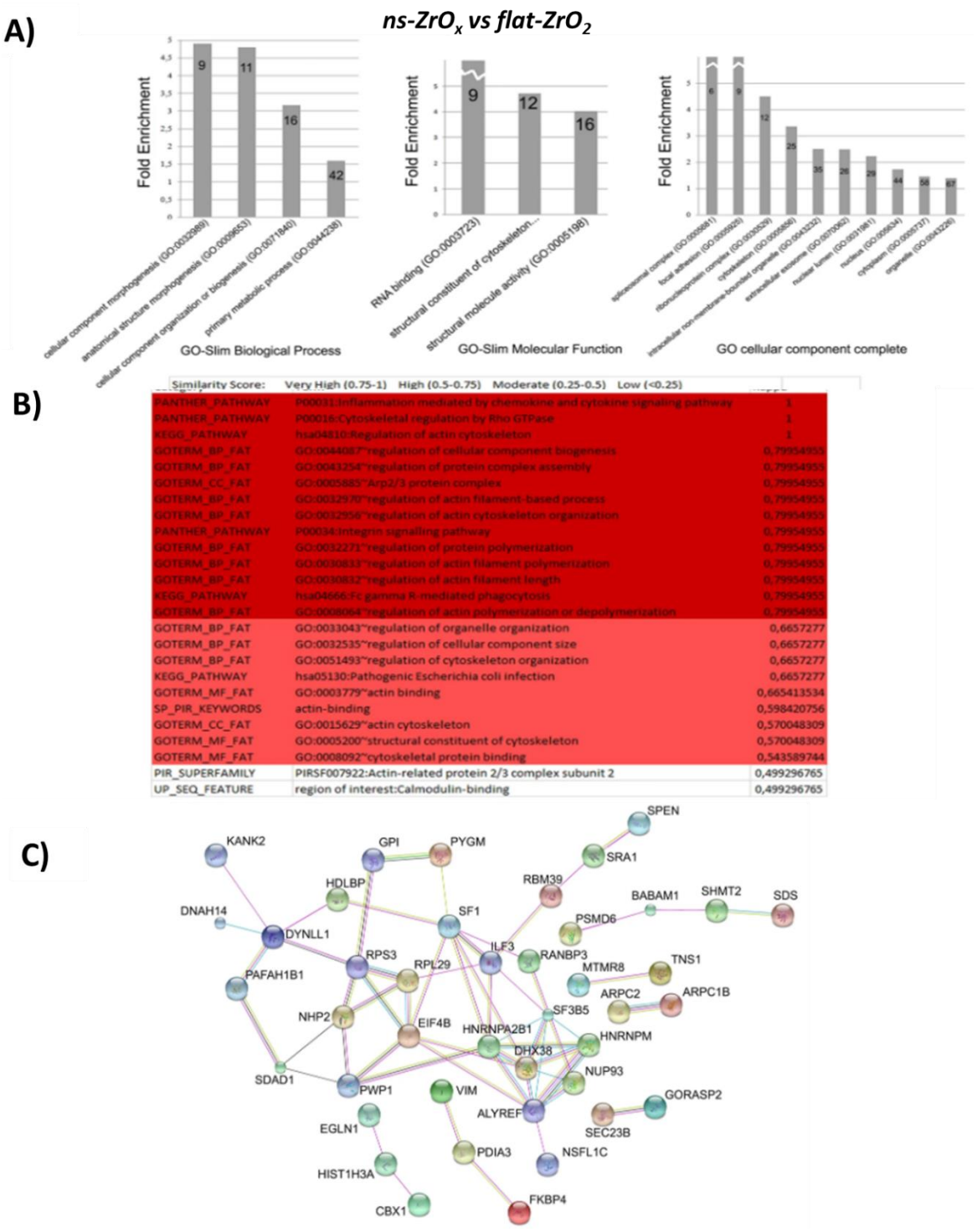

Figure 3.7. *Bioinformatic analysis of proteins increased or exclusively expressed in cells grown on ns-ZrO$_x$ compared to flat-ZrO$_x$.* ***A)*** *Gene Ontology analyses was carried out using Panther software and the protein were classified in GO-biological process (GOBP), GO-cellular component (GOCC) and GO-molecular function (GOMF) (GO). Functional grouping was based on p value ≤ 0.05. The numbers in the bars indicate the genes number for each category.* ***B)*** *Reactome analysis. Only categories with confidence level Very High (K value 0.75–1) (Dark Purple) and High (K value 0.5–0.75) (Purple) are reported.* ***C)*** *String analysis of network interactions. Active interactions: text mining, experiments, databases; edges thickness indicates "confidence". The proteins are indicated by the official gene symbol. (Laboratory of Prof. Tedeschi)*

The bioinformatic comparison of ns-ZrO$_x$ vs gelatin and ns-ZrO$_x$ vs flat-ZrO$_2$ showed similar upregulated networks, highlighting the fundamental role of the nanotopography in the induction

of the morphogenic program. Therefore, we confirmed proteomic data by functional and morphological assays focusing on four major pathways identified by the analysis:

- proteins involved in mechanotransduction
- proteins involved in the organization of the secretory apparatus
- anti-apoptotic and pro-survival proteins
- proteins involved in the control of redox homeostasis.

3.1.3 The nanotopography induces the reorganization of the cell-substrate adhesion sites, the actin cytoskeleton and modifies the nuclear architecture

Among the upregulated or uniquely expressed proteins on ns-ZrO_x, we found proteins involved in the mechanotransduction signaling pathways such as focal adhesion molecular components (GO:0005925) and proteins important for actin polymerization such as TNS1, ARPC2, ARPC1B, DYNLL1, DNAH14, KANK2 protein complexes, as well as proteins involved in controlling nuclear architecture (GO:0031891) and nuclear import/export (GO:0005634) (Figure 3.7B,C and Tables S1, S3 and S5[1]) (Sun et al., 2016). In addition, a statistically significant enrichment of the integrin signaling pathway (P00034) was detected in the islets grown on ns-ZrO_x (Figure 3.7B).

In order to confirm the proteomic results, the organization of cell-substrate adhesive contacts and actin cytoskeleton were analyzed. TIRF microscopy showed discrete vinculin-positive clusters distributed at the cell periphery in cells grown on gelatin and flat-ZrO_2. On ns-ZrO_x substrates the organization and the distribution of adhesive contacts differed significantly. Diffuse punctate staining, indicating nanoclusters or small focal contacts, was visible in the cell, but organized focal adhesions like those observed on flat substrates did not form (Figure 3.8A). The quantitative analyses confirmed these observations revealing fewer vinculin clusters per cell on gelatin and flat-ZrO_2 cells, which had significantly larger areas and dimensions than those observed on ns-ZrO_x (Figure 3.8B-a,b,c). A similar trend was observed for the correlated formation of high order actin filament structures. Stress fibers were mainly detected on gelatin and flat-ZrO_2, but seldom formed on ns-ZrO_x, where actin filaments were shorter and organized in bundles at cell-cell contact (Figure 3.8A,B-d). The distribution of focal contacts and actin filaments in the proximity of cell-cell contacts suggests that the nanotopography promotes cell-cell interactions, instead of the cell-substrate binding, partially explaining the cell cluster formation detected on the ns-ZrO_x.

The proteomic analyses also showed the upregulation of proteins involved in controlling nuclear architecture and nuclear import/export, as RANBP3 and NUP93 (Tables S1 and S3[1]). Therefore, since it has been reported that mechanical forces exerted by the actin cytoskeleton can modify the nuclear envelope and architecture, we investigated its dimension and shape by DAPI staining. Quantitative analyses revealed the presence of smaller nuclear structures with increased roundness (major/minor axis) on ns-ZrO_x compared to gelatin and flat-ZrO_2 (Figure 3.8A,B-e,f), suggesting changes in chromatin conformation and hence in the transcriptional program. Accordingly, among the uniquely expressed or upregulated proteins in ns-ZrO_x cultured islets there were proteins controlling transcription and translation (DHX38, PWP1, ALYREF, HNRPA2B1), thus suggesting a significant increase in protein synthesis rates (Tables S1, S3 and S5[1]).

The transduction of physical events occurring at the plasma membrane to the nucleus can also be mediated by mechanical-activated transcription factors that shuttle to the nucleus and modulate

[1] https://doi.org/10.1038/s41598-018-28019-3

gene transcription (Uhler and Shivashankar, 2017). One of the best characterized examples are YAP/TAZ transcriptional factors whose cellular localization is regulated by almost all types of mechanical stimuli (Aragona et al., 2013; Dupont et al., 2011; Wada et al., 2011). It is well established that intranuclear localization of YAP/TAZ induces cell proliferation by binding the TEAD family of transcription factors, whereas their cytoplasmic retention promotes their degradation, resulting in increased cell differentiation (Halder et al., 2012; Piccolo et al., 2014). Preliminary data showed a significant reduction of YAP/TAZ expression in the cells grown on the nanostructured substrates compared to gelatin and a trend toward decrease compared to flat-ZrO_2 (Figure 3.8C,D). Further experiments are necessary to confirm this observation and to address the impact of YAP/TAZ on β-cell differentiation and function.

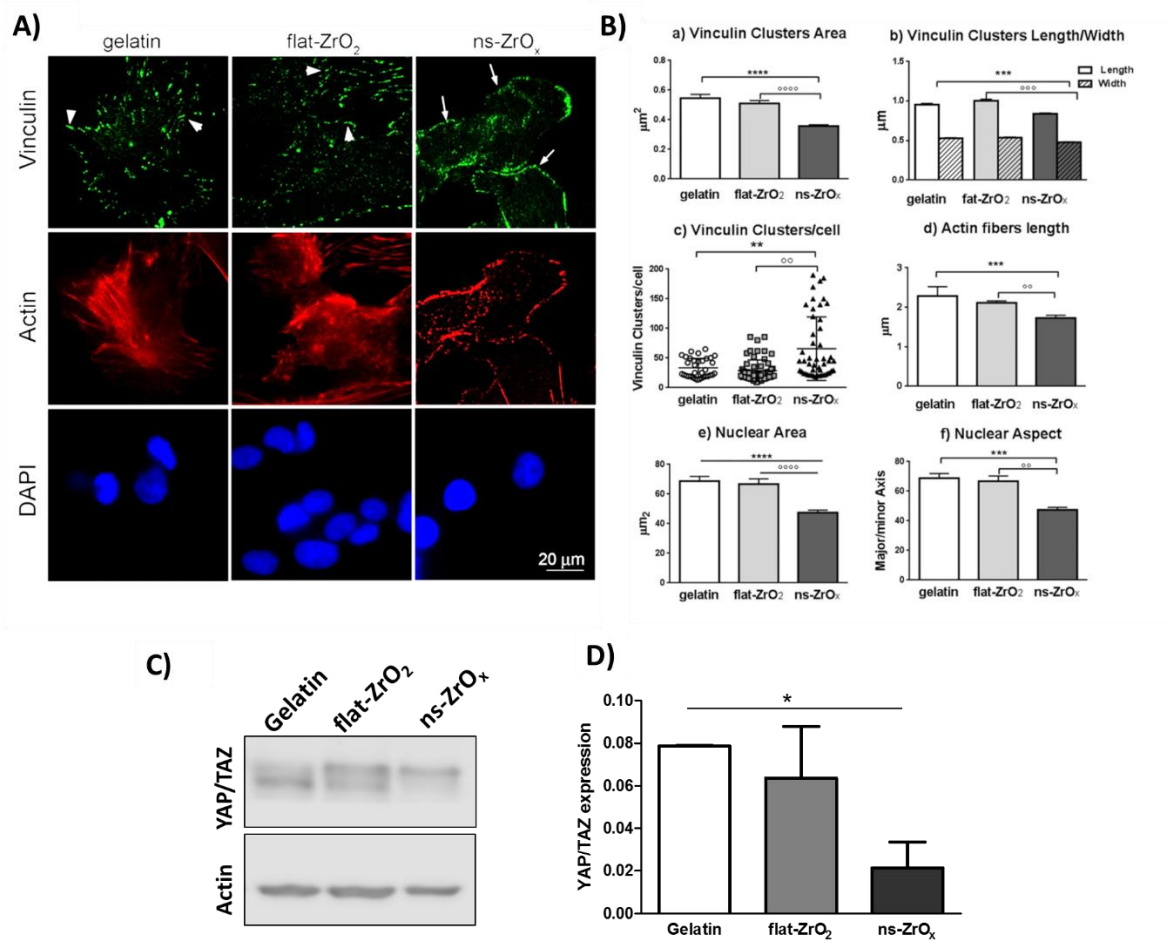

Figure 3.8. *Nanostructured substrates promote the activation of a mechanotransduction pathway.* ***A)*** *Cells, grown on different substrates for 15 days, were triple stained with anti-vinculin antibody (green), phalloidin (actin, red) and DAPI (blue). Representative epifluorescence (actin and DAPI) and TIRFM (vinculin) images are shown. Bar: 20 µm. Arrows indicate focal complexes, arrowheads indicate focal adhesion.* ***B)*** *Quantitative analyses of adhesive complexes, actin fibers organization and nuclear architecture of cells grown on different substrates. (a,b) Vinculin-positive clusters area, length and width; (c) number of vinculin clusters per cell; (d) cytoskeletal actin fibers length; (e,f) nuclear area and aspect (major/minor axis). Bars illustrate the average responses ± SE (N = 40–100 cells for each substrate) in two different islet preparations. (***p < 0.005, ns-ZrO_x vs gelatin; °°p < 0.01, °°°p < 0.005, ns-ZrO_x vs flat-ZrO_2).* ***C)*** *Western-blotting analysis of YAP/TAZ expression (15 µg protein/sample) in human islets grown on the indicated substrates for 20 days. On the right, the molecular weight of the protein standard is reported in kDa.* ***D)*** *Quantitative analysis of protein expression shows a significant reduction of YAP/TAZ expression in cells grown on ns-ZrO_x compared to gelatin. Data are expressed as mean values ± S.D. of 4 independent experiments. (*p < 0.05, ns-ZrO_x vs gelatin).*

Taken together, these data indicate that modification of the cell behaviors on the nanostructure is paralleled by a progressive reorganization of adhesive contacts and of the actin cytoskeleton, as

well as the modification of the nuclear architecture, thus suggesting the activation of a mechanotransductive pathway.

3.1.4 Nanostructured substrates preserve the β-cell function in long term culture

Bioinformatic analyses revealed that the ns-ZrO_x substrate upregulates the expression of proteins involved in membrane trafficking, among which TGN38B and GORASP2 that are required for the ER to Golgi trafficking of insulin (Tables S1 and S3[2]). TGN38B/SEC23B is a GTPase-activating protein abundantly expressed in professional secretory tissues; in embryos, its deficiency causes the accumulation of proteins in the endoplasmic reticulum and activation of the pro-apoptotic pathway of the unfolded protein response, leading to defects in pancreas development (Tao et al., 2012). The golgi reassembly stacking protein 2 GORASP2/GRASP55 is a matrix protein involved in Golgi stack and ribbon formation, interference with its expression strongly inhibits intra-Golgi transport of large cargoes like insulin (Lavieu et al., 2014).

Since the distinctive hallmark of completely mature and functional β-cells is the presence of a well-organized insulin secretory apparatus, we evaluated the distribution of insulin secretory granules in human islets cultured for 20 days. β-cells grown on the nanostructured substrate contained several insulin-positive granules, distributed in the cytoplasm and in the proximity of the plasma membrane, a similar organization was also observed in islets grown on flat-ZrO_2 and in freshly intact islets (three day after isolation). Conversely, β-cells grown on gelatin presented few insulin-positive granules of increased dimensions distributed in the perinuclear region (Figure 3.9A). This observation was further confirmed by the quantification of the total insulin by ELISA assay that showed a significantly lower insulin content in the islets grown on gelatin, compared to flat-ZrO_2, ns-ZrO_x and freshy isolated islets (Figure 3.9B). The upregulation of TGN38B/SEC23B and GORASP2/GRASP55 could explain, at least in part, the well-structured insulin secretory apparatus and the preserved glucose stimulated insulin secretion observed in the islet grown on ns-ZrO_x.

In order to have a better insight, the insulin secretion under basal (3.3 mM glucose) and stimulated (16.7 mM glucose) conditions was evaluated in islets grown on the indicated substrates for 20 days (Figure 3.9C). Interestingly, although a similar insulin content was observed in flat-ZrO_2 and ns-ZrO_x, only the islets grown on the nanostructured substrate maintained an efficient glucose-stimulated insulin secretion, even comparable to the freshly intact isolated islets. Furthermore, while islets grown on ns-ZrO_x presented a low basal insulin release, islets grown on flat-ZrO_2 or gelatin showed a similar, or paradoxically higher, insulin secretion under basal condition compared to the high glucose stimulation. This alteration of the basal/stimulated insulin secretion, which is a typical feature of dedifferentiated and stressed β-cells, further suggested that the nanotopography preserves a mature β-cell phenotype (Di Cairano et al., 2011).

The increased glycolytic flux in β-cells induces an increase of the ATP/ADP ratio and the subsequent closure of the ATP sensitive K^+ channels, leading to cell depolarization and the opening of the voltage-dependent Ca^{2+} channels (L-type). The rise in intracellular calcium is the primary mediator of insulin release as it regulates the docking, priming and fusion of insulin granules to the plasma membrane (Boland et al., 2017; Rutter et al., 2017). Therefore, we monitored the glucose-induced changes in intracellular calcium by Ca^{2+}-imaging with Fluo3 and we found that islets grown on ns-

[2] https://doi.org/10.1038/s41598-018-28019-3

ZrO_x showed increased integrated Ca^{2+} currents after glucose stimulation than the cells grown on gelatin and flat-ZrO_2 (45% and 70% increase, respectively) (Figure 3.9D,E). Interestingly the nanostructure increased the expression of the voltage-dependent calcium channel gamma-like subunit (TMEM37) (Tables S1 and S3[3]), an auxiliary subunit of calcium channel complex which modifies the time course of current activation and inactivation of the P/Q type alpha (1A) subunit, thus directly controlling insulin release (Klugbauer et al., 2000).

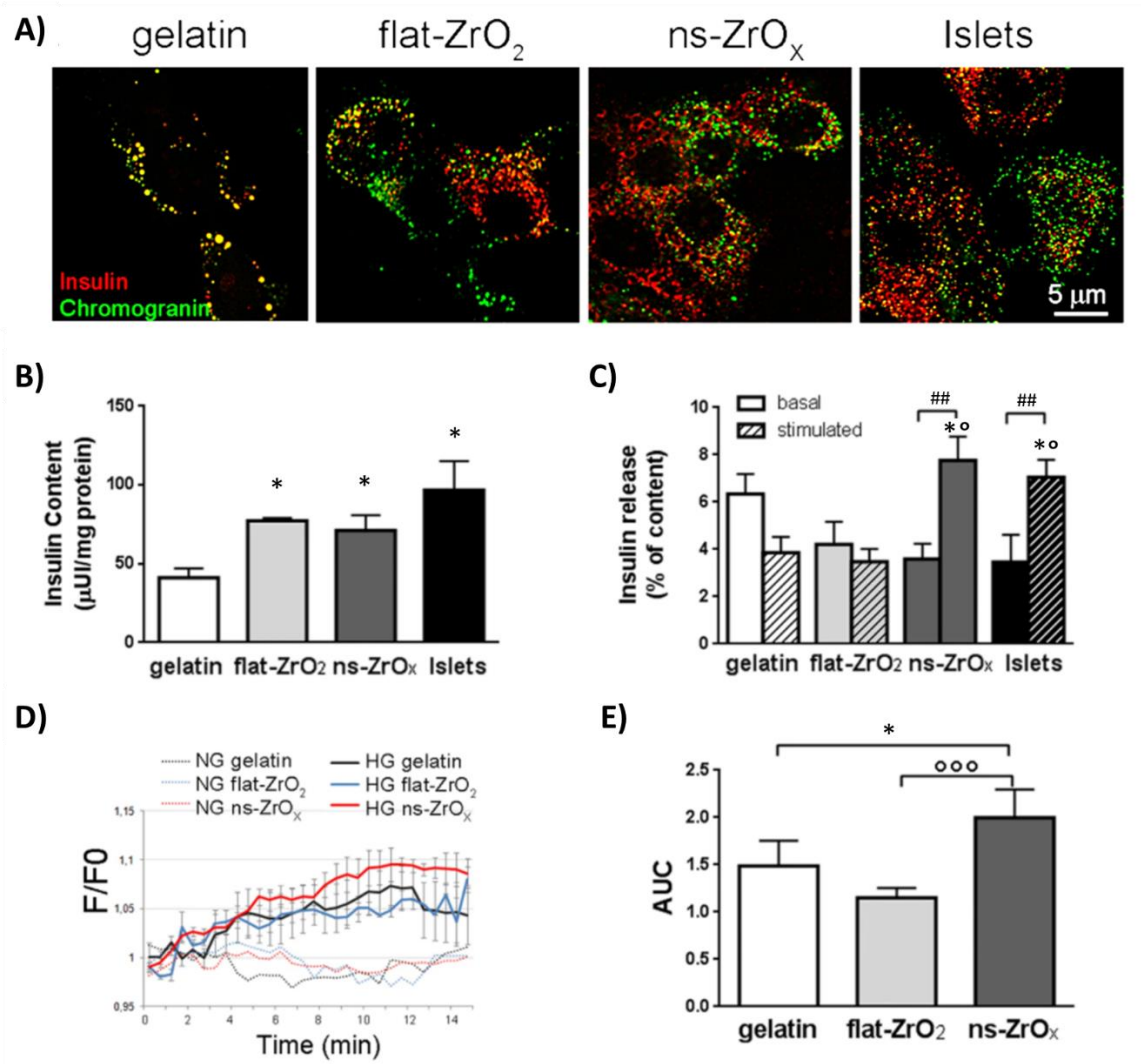

Figure 3.9. *Nanostructured substrates and the insulin secretory apparatus. Human islets of Langerhans were cultured on the indicated substrates for 20 days.* ***A)*** *Evaluation of the granules density and distribution: representative confocal images of islets double stained with anti-insulin (red) and anti-chromogranin (green) antibodies. Bar: 5 µm.* ***B)*** *Quantification of the total insulin content by ELISA assay. Black bar represents the insulin content in intact freshly isolated islets (three-days in culture). Data (mean ± SD) are expressed as µUi of insulin per mg of protein (n = 3, in duplicate) (*p < 0.05, vs gelatin).* ***C)*** *Insulin secretion under basal (3.3 mM glucose) and stimulated (16.7 mM glucose) in islets grown on the indicated substrates for 20 days. Data (mean ± SD) are expressed as % of insulin content (n = 3, in duplicate). (*p < 0.05, vs gelatin; °p < 0.05, vs flat-ZrO2; ##p < 0.001 stimulated vs basal).* ***D)*** *The cells were loaded with Fluo3 and Ca^{2+} imaging was performed under basal (3.3 mM glucose) (dotted lines) and stimulated (20 mM glucose) (continue lines) conditions. The time course of changes in fluorescence signals (F/F0) induced by glucose application (bars over traces) were recorded from islets grown on gelatin (black), flat-ZrO_2 (blue) and ns-ZrO_x (red). The curves illustrate average responses ± S.E. from four different islet preparations (N = 20 cells for each experiment) (p < 0.005, ns-ZrO_x vs gelatin; P < 0.0001 ns-ZrO_x vs flat-ZrO_2).* ***E)*** *Area Under the Curves (AUC) of experiments reported in D (*p < 0.05, ns-ZrO_x vs gelatin; °°°p < 0.001, ns-ZrO_x vs flat-ZrO_2).*

[3] https://doi.org/10.1038/s41598-018-28019-3

In summary, these data indicate that the ns-ZrO_x not only supports β-cell differentiation, but also promotes β-cell function preserving the glucose stimulated insulin secretion.

3.1.5 Nanostructured substrates prevent β-cell death by apoptosis and necrosis

Bioinformatic analysis revealed the expression of anti-aging and anti-apoptotic proteins such as BABAM1, PSMD6 and SHMT2 and the upregulation of known proteins involved in pro-survival and pro-differentiation signaling pathways, such as the insulin Growth Factor (IGF) and the steroidogenic signal pathways (Figure 3.7C and Tables S1,S3[4]). In order to confirm the activation of pro-survival and anti-apoptotic pathways, we evaluated the β-cell apoptosis by TUNEL assay in islets grown on different substrates for 2, 10 and 20 days (Fig. 3.10A). After two days in culture, β-cell apoptosis was identical and relatively high for all three substrates (7.3 ± 0.5%), probably due to the isolation procedure and the trypsinization process. However, over time in culture, β-cell apoptosis was three-fold lower in islets grown on ns-ZrO_x than on the other supports (1.5 ± 0.2%; $p < 0.05$) (Fig. 3.10B). Besides apoptosis, necrosis was also significantly reduced on ns-ZrO_x relative to flat-ZrO_2 or gelatin (two-fold decrease; $p < 0.005$), thus indicating that ns-ZrO_x substrates prevent β-cell death (Figure 3.10C).

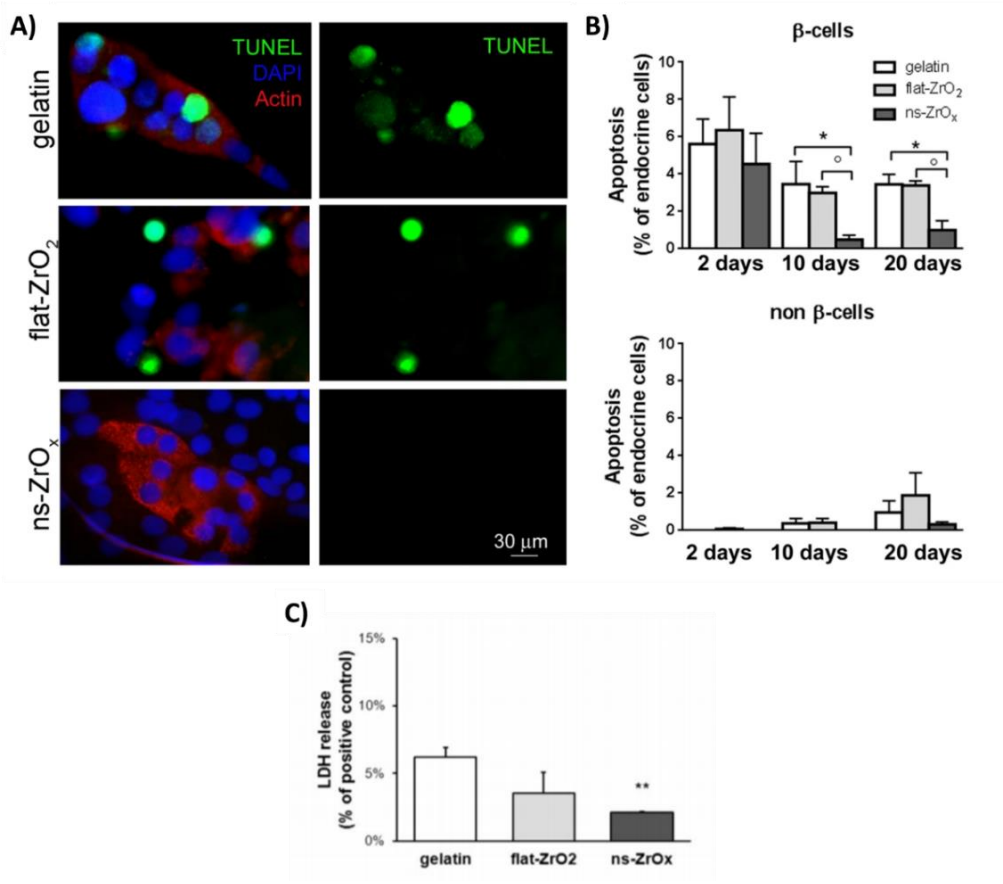

Figure 3.10. *Nanostructured substrates prevent β-cell death.* ***A)*** *Representative immunofluorescence images of islets triple stained with TUNEL (green), anti-insulin antibody (red) and DAPI (blue). Bar = 30 µm.* ***B)*** *Quantification of β-cell apoptosis by TUNEL assay in human islets grown on different substrates for 2, 10 and 20 days. β-cell apoptosis represents the percentage of TUNEL- and insulin-double positive cells over total insulin-positive cells; non β-cell apoptosis represents the percentage of TUNEL-positive cells over total DAPI-positive and insulin-negative cells. The experiment was performed in triplicate, with three different islet preparations. A minimum of 100 cells for islet preparation was counted (*p < 0.05* vs

[4] https://doi.org/10.1038/s41598-018-28019-3

*gelatin; °p < 0.05 vs flat-ZrO_2). **C)** Quantification of cell necrosis in human islets grown on the different substrates for 20 days. Data (mean values ± SD) are expressed as percentage of positive control (100% death cells). (n=3, in triplicate) (*p<0.05 ns-ZrO_x vs gelatin).*

In summary, these data revealed that the increased β-cell number observed in the islets grown on the nanostructured substrate is due, at least in part, to decreased β-cells death by apoptosis and necrosis.

3.1.6 Nanostructured substrates promote β-cell survival and differentiation by modulating NF-κB and HIF1α signaling pathways

Bioinformatic analysis revealed that ns-ZrO_x increases the expression of the oxygen sensor EGLN1/PHD2, a prolyl hydroxylase domain protein which catalyzes the hydroxylation of proline residues in an oxygen-dependent manner and targets proteins for degradation through the proteasomal complex (Fong and Takeda, 2008) (Figure 3.7C).

Among the PHD2 target proteins are hypoxia inducible factor 1α (HIF-1α) and IκB kinase 2 (IKK2), the major regulator of NF-κB activation and β-cell inflammation (Liuwantara et al., 2006). Since hypoxia and inflammation are the key determinants of β-cell death in culture systems, we evaluated the expression of HIF-1α and NF-κB pathway selected proteins by western blot. Quantitative analyses revealed decreased expression of HIF1α, IκBα, NF-κB and decreased phosphorylation of IκBα in cells grown on zirconia substrates compared to gelatin (Figure 3.11). These modifications were significantly more prominent in islets grown on ns-ZrO_x substrate than on flat-ZrO_2.

In line with these findings, the proteomic analysis showed a decreased expression of the proteins involved in the activation and regulation of NF-κB (TICAM1 (Tables S2 and S6[5]), USP51 (Tables S4 and S5[5]) and COPS8 (Table S4[5])) and upregulation of proteins promoting NF-κB degradation such as the ribosomal protein S3 (rpS3) and the N-ethylmaleimide-sensitive factor L1 cofactor (NSFL1C) (Stanborough et al., 2014). Proteins with anti-inflammatory properties, such as the Interleukin enhancer-binding factor 3 (ILF3) which controls interleukin 2 transcription are also upregulated by ns-ZrOx (Figure 3.7C).

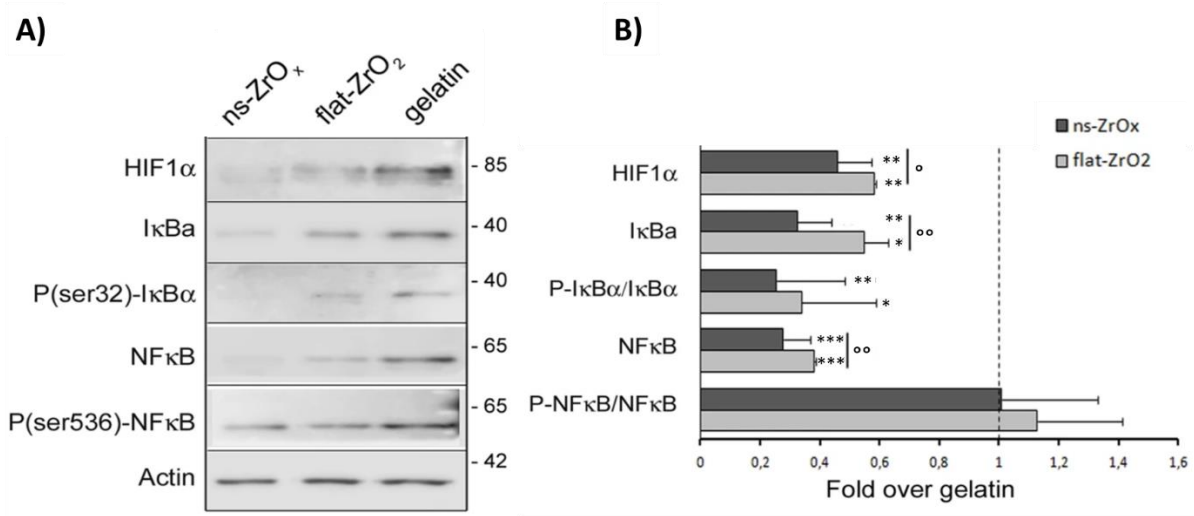

Figure 3.11. *Nanostructured substrate promotes β-cell survival and differentiation by modulating NF-κB and HIF1α signaling pathways.* ***A)*** *Western-blotting analysis of hypoxia and NF-κB pathways selected proteins in islets grown on the indicated substrates for 20 days (15 µg protein/sample). On the right, the proteins molecular weight in kDa is reported.* ***B)***

[5] https://doi.org/10.1038/s41598-018-28019-3

*Quantitative analysis of protein expression shows that flat-ZrO_2 and ns-ZrO_x substrates downregulate the hypoxia and NF-κB pathways. Data (mean values ± S.E.; n = 5 independent experiments) are expressed as fold change over gelatin (dashed line). (*p < 0.05, **p < 0.01, ***p < 0.005, ns-ZrO_x vs gelatin. °p < 0.05, °°p < 0.01, ns-ZrO_x vs flat-ZrO_2).*

Giving that EGLN1/PHD2 is an oxygen sensor, ns-ZrO_x may modulate β-cell differentiation and function by regulating hypoxia and the redox-state of the cells.

In normoxia, HIF-1α subunit is marked for proteasomal degradation through hydroxylation by EGLN1/PHD2 and its interacting partner HIF-1β can drive the expression of genes involved in β-cell differentiation and function. Under hypoxic conditions, the stabilization of HIF-1α leads to the formation of a heterodimer complex with HIF-1β and diverges the latter from the control of β-cell differentiation program (Fraker et al., 2009; Gunton et al., 2005).

Accordingly and together with the downregulation of HIF-1α, we also detected a decreased expression of alcohol dehydrogenase (CFB) (Table S2[5]) which is normally abundantly expressed under hypoxic conditions and the upregulation of L-serine dehydratase (SDS) which is the enzyme that catalyzes the conversion of L-serine into ammonia and pyruvate, whose gene expression is oxygen dependent (Table S1 and S3[5]) (Samoylenko et al., 2007).

Interestingly, while PHDs regulate HIF-1α protein stability, EGLN1/PHD2 is subject to feedback up-regulation by HIF-1α, given that the EGLN1/PHD2 gene contains a hypoxia-response element (HRE) that can be recognized by HIF-1α (Metzen et al., 2005). This feedback mechanism may be important to ensure a basal level of HIF-1α expression required for activating a metabolic response to oxidative stress during culture conditions. In line with this possibility, there is also upregulation of proteins, usually induced by HIF-1α, that reduce ROS production, modulate oxygen consumption and prevent possible hypoxic injuries. Moreover, one of the proteins upregulated by the nanostructure is the mitochondrial serine hydroxymethyltransferase (SHMT2) (Tables S1 and S3[6]). SHMT2 limits pyruvate kinase activity and reduces oxygen consumption, thus creating a metabolic state that confers a significant survival advantage to cells in poorly oxygenized regions (Ye et al., 2014). By transferring a methyl group from serine to tetrahydrofolate (THF), the protein can initiate the degradation of serine to CO_2 and NH_4^+, producing glycine and methylene-THF which is essential for NADPH production, thus increasing the NADPH/NADP ratio required to replenish GSH, repress ROS generation in mitochondria and promoting insulin secretion.

EGLN1 may also promote β-cell survival by acting through NF-κB, given that the IκBα kinase can be directly hydroxylated by the enzyme (Cummins et al., 2006). In the brain, with a NF-κB-mediated mechanism, PHD1, an EGLN1 isoform, fine-tunes biochemical pathways and energy metabolism, according to oxygen availability (Quaegebeur et al., 2016). In β-cells NF-κB controls inflammation and cytokine-mediated β-cell apoptosis, which are the key components of β-cell dysfunction in diabetes (Liuwantara et al., 2006).

In conclusion, our data reveal that the nanotopography promotes β-cell survival by regulating the expression of pro-survival and anti-apoptotic pathways and by modulating the redox-state of the cells. In addition, β-cells grown on the nanostructure are perfectly functional, suggesting that the nanostructure preserves the mature β-cells phenotype *in vitro*. Changes in β-cell behavior are paralleled by the reorganization of the actin cytoskeleton and the nuclear architecture and correlates with the expression of a set of proteins involved in the mechanotransductive pathway, suggesting that this pathway may be activated by the nanostructure. This pathway through

[6] https://doi.org/10.1038/s41598-018-28019-3

generation of cytoskeletal tension, modulates the nuclear architecture, the chromatin conformation and the epigenetic machinery, leading to changes in cellular program. Increased cell clustering was also observed on the nanostructure, thus supporting the possibility that the nanotopography allows the perfect polarization of cells (see also section 2.1) which is crucial for preserving a fully mature β-cell phenotype.

3.2 The nanotopography evokes a mitomorphosis program

Bioinformatic analysis showed that ns-ZrO_x induces a significant enrichment of GO terms related to metabolic processes (GO:0044238) and, particularly, proteins related to the catabolic metabolism of carbohydrates (GPI, PYGM) (Figure 3.7B,C), suggesting a potential role of nanotopography in the regulation of cell metabolism. β-cell metabolism is strictly controlled by mitochondria, which provide the energy necessary for β-cell survival, participate to redox homeostasis, integrate different apoptotic stimuli and control insulin secretion (Maechler and Wollheim, 2001).

Mitochondria are extremely dynamic organelles organized in complex and dynamic networks that continuously change to meet the metabolic needs of the cells. This functional plasticity is ensured by the balance between fusion and fission events and requires mitochondria mobility which is controlled by the actin cytoskeleton (Anesti and Scorrano, 2006; Tilokani et al., 2018). As the nanostructure induces the cytoskeleton reorganization in β-cells, we speculated that this modification may directly impact on mitochondria morphology and activity. However, islets represent an extremely complex and heterogeneous model, as they are composed of several cell populations that respond to different stimuli. Therefore, to gain insight into the molecular mechanisms by which nanotopography may affect mitochondria and eventually cell metabolism, we employed mouse βTC3 cell lines and confirmed the main results in insulinoma INS1E cells.

3.2.1 β-cell lines sense and respond to the substrate nanotopography

We first verified whether βTC3 cells can sense changes in the ECM topography and activate a mechanotransduction pathway. Cells were cultured for 3 days on nanostructured (ns-ZrO_x) substrates of different roughness (10, 15, 20, and 25 nm) and the organization of cell-substrate adhesions and actin cytoskeleton were analyzed by indirect immunofluorescence (Figure 3.12A,B and Figure S1). Flat zirconia (flat-ZrO_2) substrates and glass coverslips were used as controls (Glass). As the major differences were detected on the 15 nm ns-ZrO_x, Figure 3.12 shows only the comparison between Glass, flat-ZrO_2 and 15 nm ns-ZrO_x. The analysis of vinculin clusters, actin fibers and nuclear area in the cells grown on all the different substrates tested in the work are shown in Figure S1.

TIRF microscopy revealed the presence of vinculin-positive clusters distributed at the cell periphery in cells grown on glass covers and flat-ZrO_2. On ns-ZrO_x substrate, vinculin structures were smaller in size and diffuse in cells (Figure 3.12B-a and Figure S1-a). A similar trend was observed for actin filaments (Figures 3.12A,B-b,c and Figure S1-b,c). Long actin fibers were mainly detected on glass covers and flat-ZrO_2, but they seldom formed on ns-ZrO_x where shorter and thinner actin-labeled structures were observed. Western blot analysis showed increased actin and tubulin expression in cells grown on nanostructured substrates compared to control covers, indicating a general reorganization of the cytoskeleton in the cells grown on ns-ZrO_x (Figures 3.12C,D).

As above reported, the reorganization of the actin cytoskeleton can induce nuclear envelope modifications resulting in changes in nuclear shape and architecture. Consisting with this, DAPI

staining revealed the presence of smaller and less elongated (Feret's diameter) nuclei in the cells grown on ns-ZrO_x compared to flat-ZrO_2 and glass covers (Figure 3.12A,B-d,e and Figure S1-d,e).

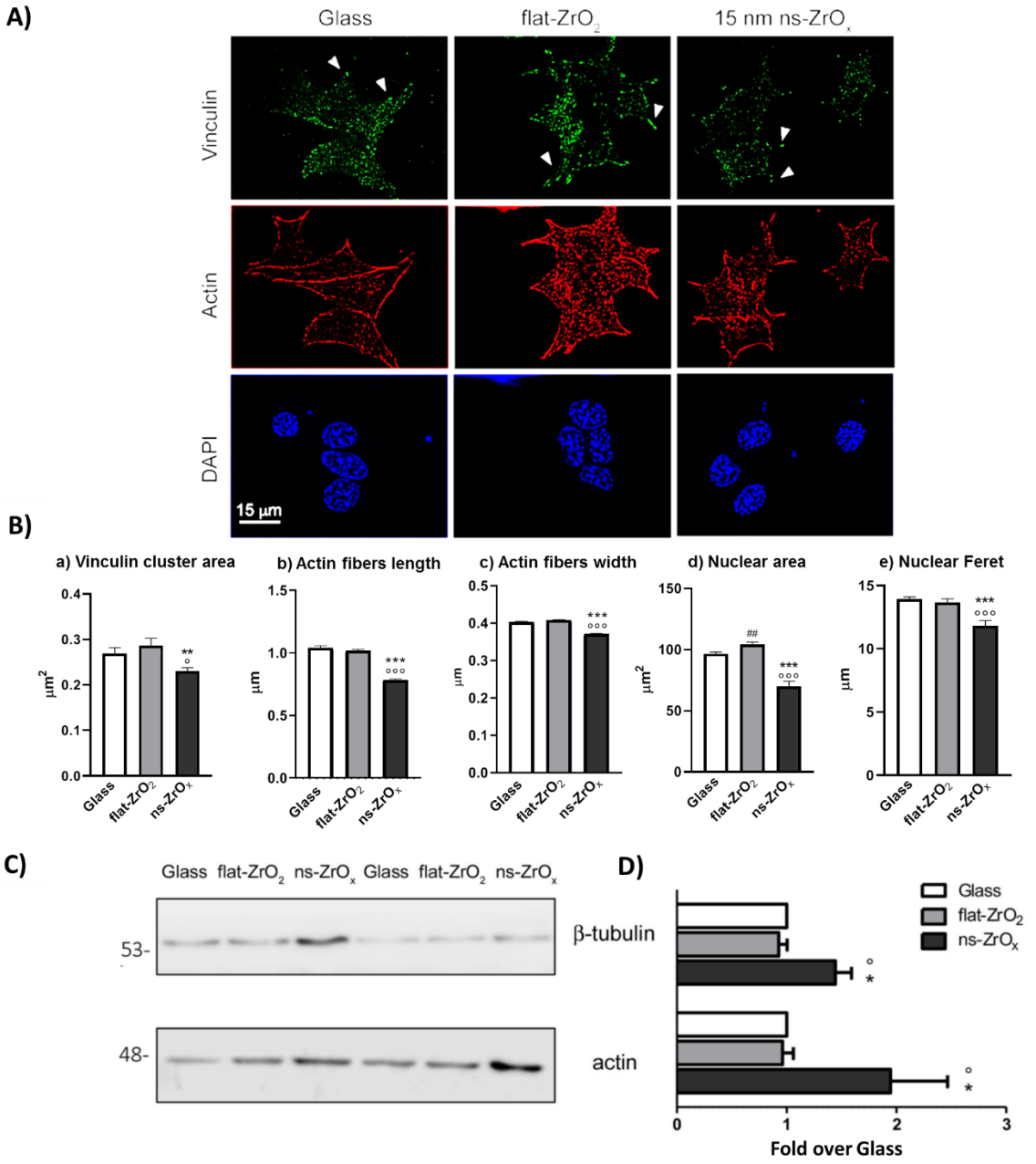

Figure 3.12. *Nanostructured zirconia substrates promote the activation of a mechanotransduction pathway in ßTC3 cells.* ***A)*** *Cells grown on glass covers (Glass), flat- (flat-ZrO_2) or 15 nm nanostructured-zirconia (ns-ZrO_x) substrates for 3 days were triple stained with anti-vinculin antibody (green), phalloidin (actin, red), and DAPI (blue). Representative epifluorescence (actin and DAPI) and TIRFM (vinculin) images are shown. Bar: 15 µm. Arrowheads indicate focal complexes.* ***B)*** *Quantitative analyses of vinculin-positive area (a), cytoskeletal actin fibers length (b) and width (c), and (c) nuclear area (d), Feret's diameter (e) in cells grown on Glass, flat-ZrO_2 and 15 nm ns-ZrO_x. Bars illustrate the average responses ± SE (N = 30–40 cells for each substrate, three independent experiments (**p < 0.01, ***p < 0.005, ns-ZrO_x vs flat-ZrO_2; °p < 0.05, °°°p < 0.005, ns-ZrO_x vs Glass; ## p<0.01, Glass vs flat-ZrO_2).* ***C)*** *Western-blotting images of ß-tubulin and actin in ßTC3 cells grown on the Glass, flat-ZrO_2 and 15 nm-ns-ZrO_x for three days (15 µg protein/sample). On the left, the protein molecular weight in kDa is reported.* ***F)*** *The quantitative analysis shows the upregulation of cytoskeletal proteins expression in cells grown on 15 nm ns-ZrO_x. Data (mean values ± S.D.; n = 5 independent experiments) are expressed as fold-change over Glass (*p < 0.05 ns-ZrO_x vs flat-ZrO_2; °p < 0.05 ns-ZrO_x vs Glass).*

Similar results were obtained in INS1E cells grown on Glass, flat-ZrO_2 and 15 nm nanostructured-zirconia (ns-ZrO_x) substrates for 3 days. Cells grown on ns-ZrO_x showed shorter actin filaments with decreased dimension compared to Glass and flat-ZrO_2 (Figure 3.13A,B-a,b), suggesting a reduction

of the intracellular tension channeled by the cytoskeleton on the nuclear envelope. Accordingly, smaller and less elongated nuclei were detected in INS1E cells grown on ns-ZrO_x compared to controls (Figure 3.13A,B-c,d).

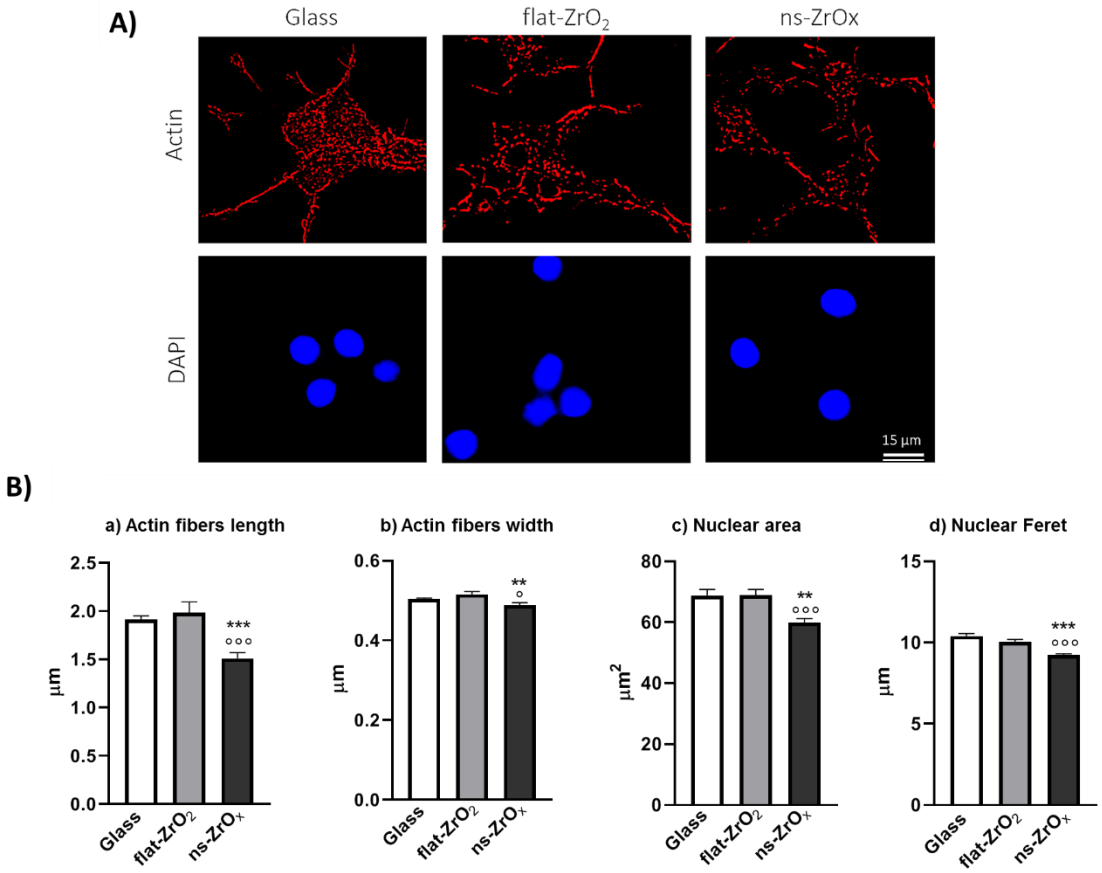

Figure 3.13. A) *Representative epifluorescence images of INS1E cells grown on glass covers (Glass), flat- (flat-ZrO_2) or 15 nm nanostructured-zirconia (ns-ZrO_x) substrates for 3 days, doubled stained with phalloidin (actin, red) and DAPI (blue). Bar: 15 µm.* ***B)*** *Quantitative analyses of cytoskeletal actin fibers length (a), width (b) and nuclear area (c), Feret's diameter (d) in cells grown on Glass, flat-ZrO_2 and ns-ZrO_x are shown. Bars illustrate the average responses ± SE (**p < 0.01, ***p<0.005 ns-ZrO_x vs flat-ZrO_2; °p < 0.05, °°°p < 0.005 ns-ZrO_x vs Glass).*

As reported in the introduction, in the fast mechanotrasduction hypothesis, generation of tension at the nascent cell-substrate interaction contact points, may drive the reorganization of the cell shape. To investigate the involvement of the mechanotransductive signaling pathway, βtc3 cells, grown on the indicated substrates for 3 days, were treated for 1 hour with 50 µM blebbistatin, which reduces the cytoskeletal tension, by inhibiting myosin II contractility. Interestingly, blebbistatin treatment induces an evident reduction of actin fibers length and width in the cells grown on flat-ZrO_2 and a similar trend was observed in the glass sample, while no significant changes were detected in the cells grown on ns-ZrO_x (Figure 3.14A,B-a,b). In line with these modifications, DAPI staining revealed the presence of smaller and more roundness nuclei in the cells grown on glass and flat-ZrO_2 after blebbistatin treatment (Figure 3.14C,D-c,d).

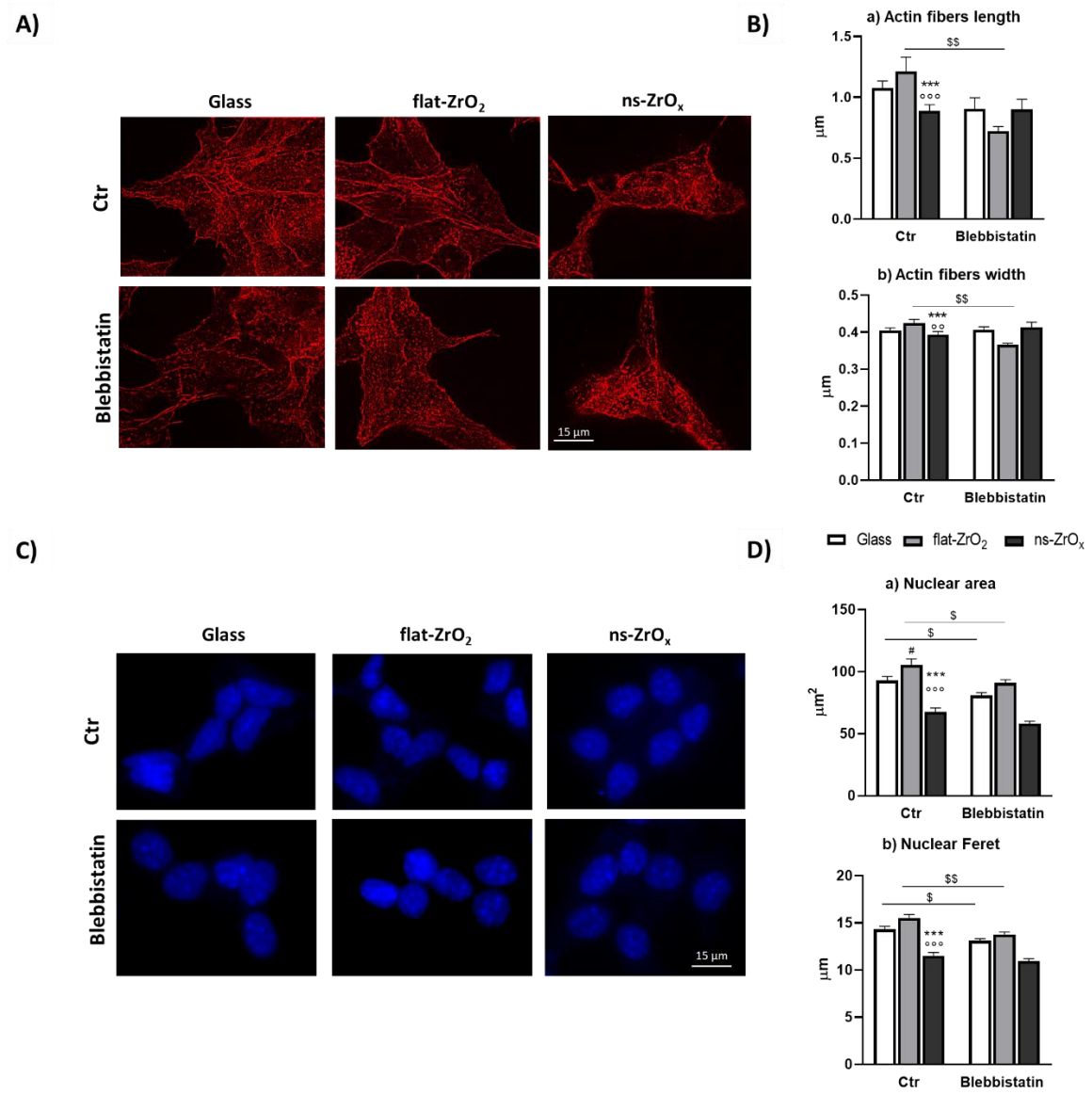

Figure 3.14. *βtc3 cells grown on glass, flat and nanostructured substrates for 3 days were treated with 50 µm blebbistatin for 1 hour.* ***A,C)*** *Representative epifluorescence images of βtc3 cells labelled with phalloidin (actin, red) and DAPI (blue). Bar: 15 µm.* ***B,D)*** *Quantitative analyses of cytoskeletal actin fibers length (a), width (b) and nuclear area (c), Feret's diameter (d) in cells grown on Glass, flat-ZrO_2 and ns-ZrO_x are shown. Bars illustrate the average responses ± SE (***p<0.005 ns-ZrO_x vs flat-ZrO_2; °°p < 0.01, °°°p < 0.005 ns-ZrO_x vs Glass; $ p<0.05, $$ p<0.01 Ctr vs Blebbistatin).*

These data suggest that the nanostructure generates low intracellular tension, as a consequence the cell assume a more relaxed, round shape which, probably, supports the formation and maintenance of cell–cell contacts. On the other hand, when β-cells are plated on flat substrates the increased cytoskeletal tension induces a flat, irregular shape of the cells that favours cell scattering and prevents cell-cell interactions (Figure 3.15A). Accordingly, as previously observed in human islet of Langerhans, we found that βTC3 and INS1E cells aggregate into islet-like clusters when plated on the nanostructure (Figure 3.15B,C); further experiments will aim at characterizing the observed phenomenon and to dissect the molecular mechanisms involved.

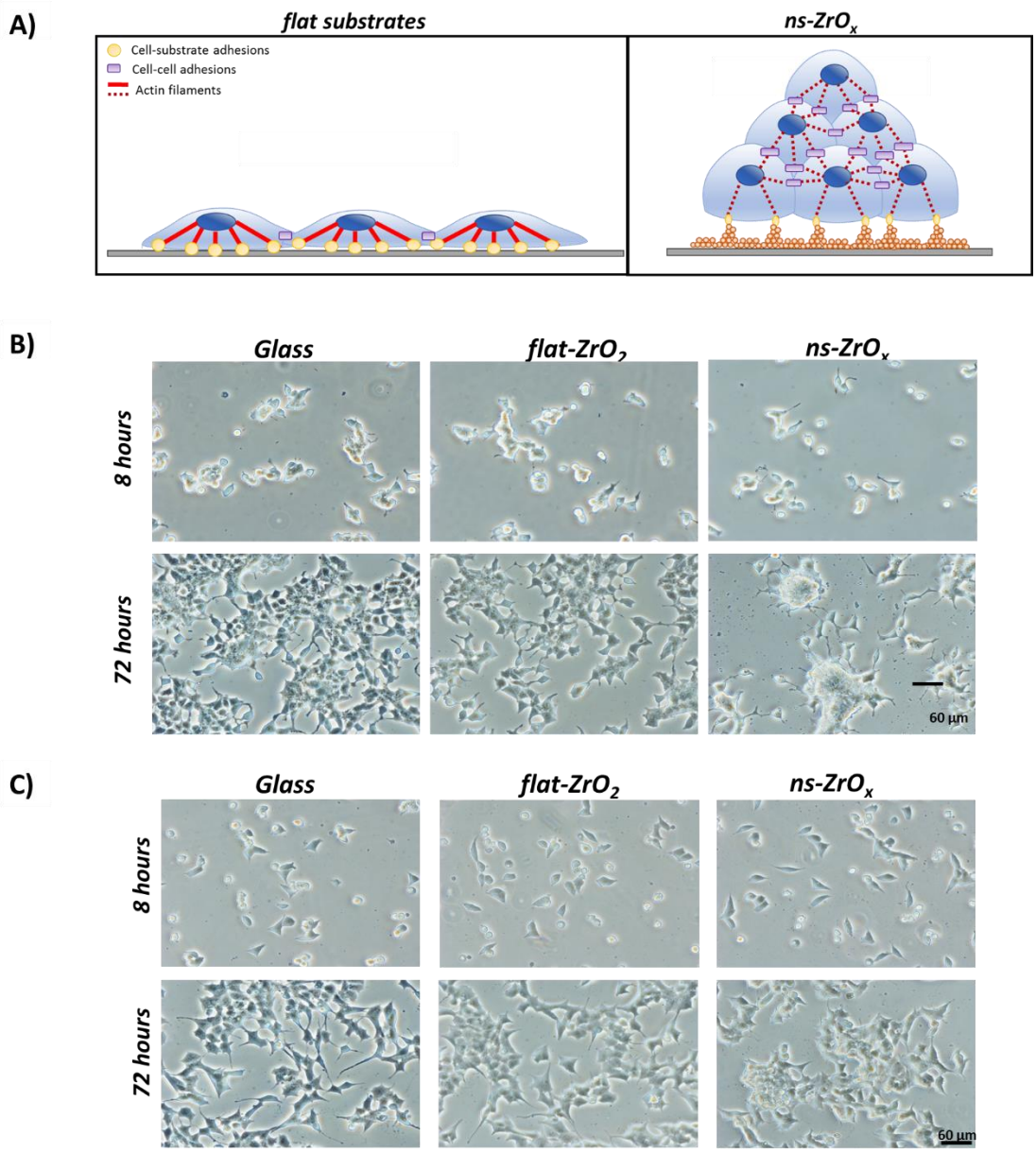

Figure 3.15. A) *Schematic representation of shape and organization of β-cells grown on flat and nanostructured substrates. Cell-matrix interactions predominate on flat substrate inducing the formation of stress fibers, thereby resulting in cell flattening. Cell grown on nanostructured substrates retain a round shape that favors the cell-cell interaction and reduces the stress fibers formation. Adapted from Galli et al., 2020.* ***B,C)*** *Nanostructured substrates promote β-cell aggregation. Representative phase contrast optical images of INS1E (A) and βTC3 (B) cells grown on Glass, flat-ZrO_2, ns-ZrO_x substrates. Bar: 60 µm.*

Taken together, these data strongly suggest that β-cell lines sense the substrate topography and respond by activating a mechanotransductive pathway that involves the reorganization of the actin cytoskeleton and the nuclear architecture. Probably, the nanotopography, preventing the generation of intracellular cytoskeleton tension, preserves the original shape of the cells and promotes their clustering, fundamental to ensure survival and differentiation.

3.2.2 The nanotopography modulates the mitochondrial activity

In order to test whether the nanotopography might also affect mitochondria, the organelle membrane potential was evaluated by quantification of MitoSpy™ Orange, a dye whose concentration is proportional to the inner mitochondrial membrane potential. As reported in Figure

S2, the mitochondrial membrane potential was particularly sensitive to the nanoscale modification of substrate features, as it progressively increased with the nanostructure roughness and then dropped dramatically on the 25 nm substrate. Interestingly, the most relevant effect was observed in cells grown on 15 nm-ns-ZrO_x where major changes in cell morphology were also detected. Since the most relevant effects were detected on 15 nm-ns-ZrO_x, further experiments were performed on this substrate.

As shown in Figure 3.16A,B, the mitochondrial membrane potential was significantly higher in the cells grown on the nanostructured substrate when compared to glass; a similar trend was observed in the comparison ns-ZrO_x versus flat-ZrO_2, even though the difference was not statistically significant. These data suggest that Zirconia itself may influence mitochondrial membrane potential and this effect is probably potentiated by the nanostructure. Of note, zirconia substrates are layer of oxidized materials, but while the stoichiometry is well defined in flat substrates (ZrO_2), it is not yet defined in the nanostructure (ZrO_x). To verify whether the different membrane potential was due to a mechanotransductive phenomenon, βtc3 cells were treated with 50 µm blebbistatin for 1 hour and the mitochondrial membrane potential was measured. Intriguingly, a significant increase of the mitochondrial membrane potential was observed in the cells grown on flat-ZrO_2 and glass substrates after blebbistatin treatment, while no changes were detected for the ns-ZrO_x sample (Figure 3.16C), again suggesting an important role of cytoskeleton tension in the modification of mitochondrial functional activity.

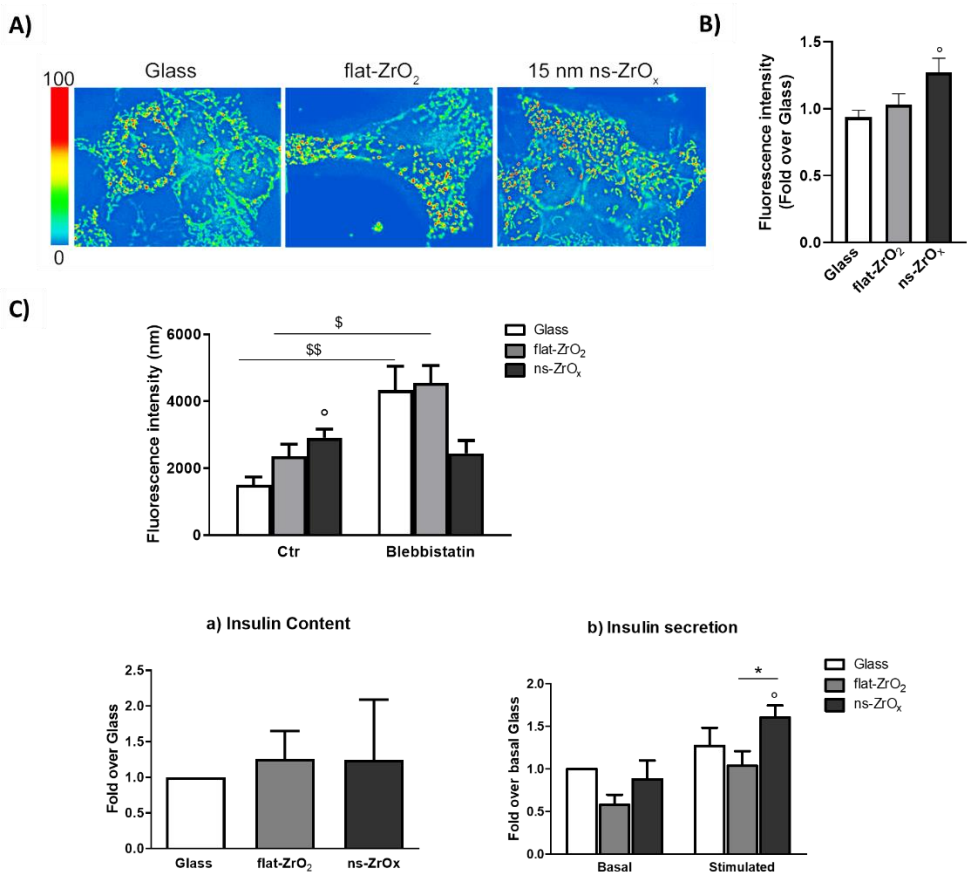

Figure 3.16. *Nanostructured substrate of 15 nm roughness improves mitochondrial activity and GSIS.* ***A)*** *βtc3 cells grown on the indicated substrates for 3 days were loaded with MitoSpy™ Orange CMTMRos and the mitochondrial membrane potential was measured by fluorimetry (551/576 nm Ex/Em).* ***A)*** *Representative images in pseudocolor are shown (blue low intensity, red high intensity).* ***B)*** *Bars illustrate the average responses (fluorescence intensity) ± SE (n = 4 independent experiments in triplicate) (°p < 0.05 ns-ZrO_x vs Glass).* ***C)*** *Quantitative analysis of the mitochondrial membrane potential of βtc3 cells cultured on the indicated substrates and treated with 50 µM blebbistatin for 1 hour. Bars illustrate the average responses (fluorescence intensity) ± SD (°p < 0.05 ns-ZrO_x vs Glass; $ p<0.05, $$ p<0.01 Ctr vs Blebbistatin).*

In summary, these data suggest a direct involvement of the actin cytoskeleton in the regulation of the mitochondrial activity. Mitochondria are, indeed, tightly coupled to cytoskeletal proteins that track their movements and stop them in specific intracellular site, where their metabolic functions are required (Anesti and Scorrano, 2006).

3.2.3 Proteomic analyses of the mitochondrial proteome

To understand the impact of the nanostructure on mitochondria, at molecular level, a β-cell lysate fraction enriched in the mitochondrial component was analyzed by a label-free shotgun proteomic approach (analysis performed by the laboratory of prof. Tedeschi, Department of veterinary medicine, Università degli Studi di Milano).

Similar to studies performed in islets of Langerhans, specific analyses were carried out by comparing (i) cells grown on glass coverslips (Glass) versus cells grown on ns-ZrO_x, (ii) cells grown on flat-ZrO_2 versus cells grown on ns-ZrO_x, and (iii) cells grown on Glass vs cells grown on flat-ZrO_2. In each comparison, proteins were considered differentially expressed if they were present only in one condition or showed significant t-test difference ($p \leq 0.05$). Volcano plots (Figure 3.17) show the proteins differentially or exclusively expressed in the following comparison:

- Glass vs ns-ZrO_x: 194 proteins are exclusively expressed or upregulated in ns-ZrO_x, while 467 are exclusively expressed in Glass or downregulated in ns-ZrO_x (Figure 3.17A);
- flat-ZrO_2 vs ns-ZrO_x, 145 proteins are exclusively expressed or upregulated in ns-ZrO_x, while 622 are exclusively expressed in flat-ZrO_2 or downregulated in ns-ZrO_x (Figure 3.17B);
- Glass vs flat-ZrO_2, 439 proteins are exclusively expressed or upregulated in flat-ZrO_2, while 231 are exclusively expressed in Glass or downregulated in flat-ZrO_2 (Figure 3.17C).

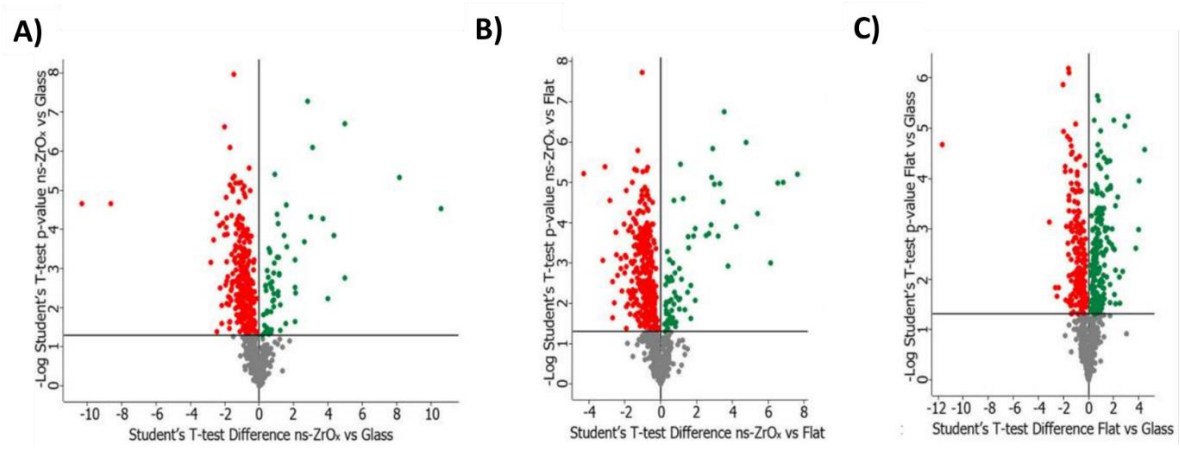

Figure 3.17. *Volcano plots of proteins differentially expressed in the comparison ns-ZrO_x vs Glass (**A**), ns-ZrO_x vs flat-ZrO_2 (**B**) and flat-ZrO_2 vs Glass (**C**). Proteins were considered differentially expressed if they were present only in one condition or showed significant t-test difference (t-test $p \leq 0.05$). The proteins up- or downregulated are indicated in green and red, respectively.*

Proteins were then scanned with Mitominer, a mitochondrial localization database, confirming that almost 28% of all the proteins identified in each comparison are indeed mitochondrial components. Non-mitochondrial proteins were also identified, mainly localized in compartments tightly associated to mitochondria such as the ER, Golgi apparatus, and vacuoles, in line to data reported in the literature using this enrichment method (Alberio et al., 2017). Only the proteins exclusively or differentially ($p<0.05$) expressed with an Integrated Mitochondrial Protein Index ≥ 0.5 were further analyzed in terms of GO classification and pathways.

To dissect the impact of the nanostructure, bioinformatic analyses were performed by comparing ns-ZrO_x vs glass and ns-ZrO_x vs flat-ZrO_2.

Regarding the comparison between ns-ZrO_x and glass, the gene ontology (GO) analysis revealed that the nanostructure induced a downregulation of proteins involved in mitochondrial cristae formation and shaping (GO:0007005, GO:0006626), mitochondrial import/export (GO:0030150, GO:0098660, GO:0098662) and proteins involved in pyruvate metabolism, TCA cycle and aerobic respiration (GO:0019752, GO:0006099, GO:004533) (Figure 3.18). In addition, a significant reduction of proteins involved in protein localization, folding and processing in the ER (GO:0006457, GO:0034620, GO:0006986) was also detected in the cells grown on the nanostructured substrate (Figure 18). Conversely, the nanostructure induces the upregulation of proteins involved in the lysosomal transport (GO:0007041) (Figure 3.18) and glycolytic enzymes (Figure 3.23).

A similar pattern of proteins was detected in the comparison ns-ZrO_x vs flat ZrO_2, indicating that the majority of these effects was related to the nanostructure (Figure 3.18B). In particular, cells grown on ns-ZrO_x showed a decreased expression in GO cellular component terms related to mitochondrial cristae formation and shaping (GO:0007005, GO:0006626), mitochondrial import/export (GO:0030150, GO:0098660, GO:0098662), proteins involved in pyruvate metabolism, TCA cycle and aerobic respiration (GO:0019752, GO:0006099, GO:004533) and proteins involved in protein localization, folding and processing in the ER (GO:0006457, GO:0034620, GO:0006986). The upregulation of the glycolytic pathway was also detected in the comparison between ns-ZrO_x and flat-ZrO_2 (Figure 3.24).

The proteomic analyses revealed the upregulation of cytoskeletal proteins as ACTN1, MAPK1 and MYH9 in cells grown on the nanostructure compared to both flat and glass substrates, further supporting the close interplay between mitochondria and cytoskeleton (Figure 3.18B). An important difference was observed in the expression of proteins involved in the lysosomal transport (GO:0007041) that were upregulated in the ns-ZrO_x vs Glass substrates but were downregulated in the ns-ZrO_x vs Flat ZrO_2.

A)

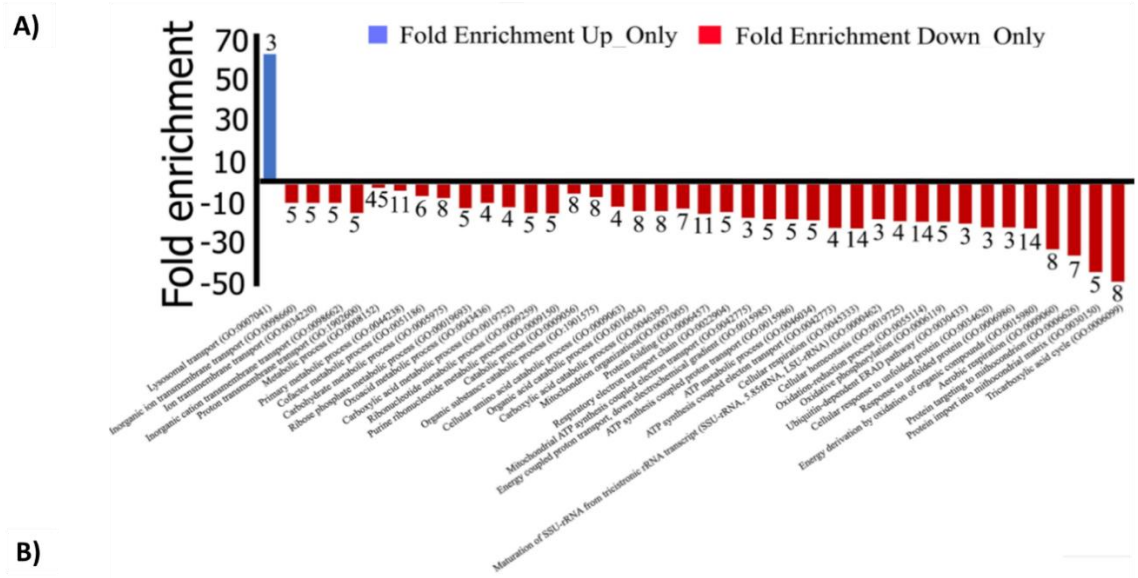

B)

Category	GO classification	ns-ZrO_x *vs* Glass		ns-ZrO_x *vs* flat-ZrO_2	
		Genes	***Exp.***	***Genes***	***Exp.***
Mitochondrial proteins involved in cristae formation and shaping	Mitochondrion organization (**GO:0007005**), protein targeting to mitochondrion (**GO: 0006626**).	ATP5A1, ATP5B, ATP5C1, ATP5D, ATP5H, CHCHD3, IMMT, LETM1, ROMO1 OPA1, DNML1 and GDAP1	↓	ATP5A1, ATP5B, ATP5C1, ATP5D, ATP5H, CHCHD3, IMMT, LETM1, OPA1 and GDAP	↓
Mitochondrial proteins involved in import/export	Protein import into mitochondrial matrix (**GO:0030150**), inorganic ion transmembrane transport (**GO:0098660**), ion transmembrane transport (**GO:0098662**).	TOMM20, TIMM17A, TIMM23B and SAMM50	↓	TOMM20, TIMM17A, TIMM23B and SAMM50	↓
Mitochodrial proteins involved in pyruvate metabolism, TCA cycle, aerobic respiration and ATP synthesis	Carboxylic acid metabolic process (**GO:0019752**), carboxylic acid catabolic process (**GO:0046395**), tricarboxylic acid cycle (**GO:0006099**), aerobic respiration (**GO:0009060**), oxidative phosphorylation (**GO:0006119**), proton transmembrane transport (**GO:1902600**), ATP synthesis coupled proton transport (**GO:0042775**, **GO:0015985**, **GO:0042773**), ATP metabolic process (**GO:0046034**), respiratory electron transport chain (**GO:0022904**), cellular respiration (**GO:0045333**).	DLD, PHDHB, PCK2, PDHA1, MDH2, PC, FH, SUGCLG2, SUCLG1, OGDH, PDHB, PCK2, IDH3B, CS, PDHA1, SDHA, MDH2 ,ACLY, IDH2, FH, IDH3A, DLD, PC, SUCLA2_NDUFA4, SDHA, ATP5D, NDUFV1, ATP5B, NDUFV2, COX6B1, ATP5C1, NDUFA13, ATP5A1, UQCRQ, NDUFS2, ATP5H, NDUFA12, NDUFA12, NDUFV1, NDUFS4, SDHA, UQCRQ, COA3, COX6B1, NDUFA4, MT-CO2, ATP5B, ATP5C1, ATP5A1 and ATP5D	↓	PHDHB, PCK2, PDHA1, MDH2, FH, OGDH, PDHB, PCK2, IDH3B, CS, PDHA1, SDHA, MDH2 ,ACLY, IDH2, FH, NDUFA4, SDHA, ATP5D, NDUFV1, ATP5B, COX6A1, ATP5C1, NDUFA13, ATP5A1, UQCRQ, UQCRQC1, NDUFS2, ATP5H, NDUFA12, NDUFV2, NDUFS2, NDUFS3 , NDUFV1, NDUFS4, SDHA, UQCRQ, COA3, COX6A1, NDUFA4, MT-CO2, ATP5B, ATP5C1, ATP5A1 and ATP5D	↓
Proteins involved in oxidative stress and cell apoptosis	Cellular homeostasis (**GO:0019725**).	TXN2, PRDX3, PARP1, AIFM1, ETFDH, NDUFA12, NDUFS2, PRDX5, ROMO1, HYOU1, AIFM1 and VDAC1	↓	TXN2, PRDX3, AIFM1, ETFDH, NDUFA12, HYOU1, AIFM1 and VDAC1	↓
Cytoskeletal proteins	Cytoskeleton (**GO:0005858**).	ACTN1, MAPK1 and MYH9	↑	ACTN1 and MYH9	↑
Proteins involved in lysosomal transport	Lysosomal transport (**GO:0007041**).	XSPA8, STXBP1 and RAB7A	↑	XSPA8 and RAB7A	↓
Proteins involved in protein loalization,folding and processing in the ER	Protein folding (**GO:0006457**), cellular response to unfolded protein (**GO:0034620**, **GO:0006986**).	CALR, CLPX, CRPX, DNAJA1, FKBP2, GNB1, GRPEL1, HSP90B1, HSPA5, HSPA9, HSPD1, MLEC, P4HB, PDIA3, PPIB, PRDX4 and TRAP1	↓	CALR, CLPX, DNAJA1, FKBP2, GNB1, GRPEL1, HSP90B1, HSPA5, HSPA9, HSPD1, MLEC, P4HB, PDIA3, PPIB and TRAP1	↓

Figure 3.18. A) *Schematic representation of the proteins differentially expressed in comparison Glass vs ns-ZrOx. The differentially expressed proteins were classified into different biological processes (GOBP-slim). Functional grouping was based on p-value ≤0.05 and minimum three counts. Negative values (Red) refer to fold enrichment of proteins less expressed at ns-ZrOx or only expressed in Glass whereas positive value (Blue) refer to proteins more or only expressed on ns-ZrOx in the comparison Glass vs ns-ZrOx. The numbers on the bars represent the counts.* ***B)*** *Gene ontology classification of the proteins differentially expressed in the comparison between glass vs ns-ZrO_x (on the left) and flat-ZrO_2 vs ns-ZrO_x (on the right). (Laboratory of Prof. Tedeschi)*

In summary, the bioinformatic analyses of ns-ZrO_x vs glass and ns-ZrO_x vs flat-ZrO_2 showed similar modifications of the mitochondrial proteome, highlighting the fundamental role of the nanotopography in the mitomorphosis program.

3.2.4 The nanotopography modulates the mitochondrial dynamics and morphology

The proteomic analysis revealed a reduction of proteins involved in cristae formation (ATP5A1, ATP5B, ATP5C1, ATP5D, ATP5H, CHCHD3, IMMT, LETM1 and SAMM50) and shaping (MICOS 19, 60, 10) suggesting that the nanostructure has a profound impact on the organization of the mitochondrial inner membrane (Figure 3.18B). These modifications are probably due to the

decrease expression of the ROS modulator 1 (ROMO1) (only in glass vs ns-ZrO_x) and optic atrophy 1 protein (OPA1). The former is a redox-regulated protein required for mitochondrial fusion and normal cristae morphology (Cogliati et al., 2016). OPA1 promotes the inner membrane fusion, governing the delicate balance between fusion and fission in the dynamic mitochondrial network, but also controls cristae structure remodeling (Liesa and Shirihai, 2013).

Data were confirmed by western blot analysis of proteins involved in mitochondrial fusion and fission namely OPA1, mitofusin 2 (MNF2) and dynamin-related protein 1 (DRP1) (Figures 3.19). In agreement with proteomic data, a significant decrease in the expression of MFN2 and OPA1 proteins was observed in cells grown on ns-ZrO_x compared to glass cover, while no significant change in DRP1 expression was detected. A similar trend was observed in the comparison ns-ZrO_x vs flat-ZrO_2, even though the OPA1 downregulation was not statistically significant (p value=0.07).

These data apparently suggest increased mitochondrial fission, which results in mitochondrial fragmentation, a phenomenon often observed under stress and pathologic conditions. However, by exploiting the proteomic dataset, we also found a decreased expression of dynamin-1 like protein (DNM1L) (only in glass vs ns-ZrO_x) and ganglioside-induced differentiation-associated protein 1 (GDAP1), which regulate the mitochondrial network by promoting mitochondrial fission (Bartolák-Suki et al., 2017; Tilokani et al., 2018) (Figure 3.18B). Taken together these observations suggest that the nanotopography induces a remodeling of the machinery involved in mitochondrial dynamics, maintaining the delicate balance between fusion and fission events.

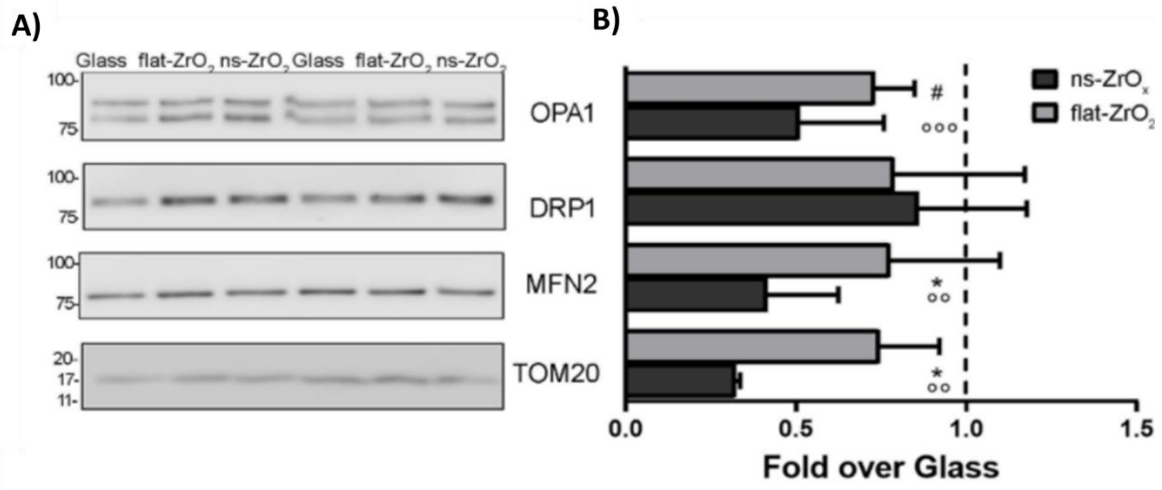

Figure 3.19. *Nanostructured substrate modulates mitochondrial dynamics. Mouse βTC3 were cultured on the indicated substrates for 3 days.* ***A)*** *Western-blotting analysis of mitochondrial pro-fission (DRP1), pro-fusion (MFN2 and OPA1) and import (TOM20) proteins (15 µg protein/sample). On the left, the protein molecular weight in kDa is reported.* ***B)*** *The quantitative analysis shows the downregulation OPA1, MFN2 and TOM20 expressions in cells grown on 15 nm ns-ZrO_x. Data (mean values ± SD; n = 5 independent experiments) are expressed as fold-change over Glass (*p < 0.05 ns-ZrO_x vs flat-ZrO_2; °°p < 0.01, °°°p < 0.005 ns-ZrO_x vs Glass; #p < 0.05 flat-ZrO_2 vs Glass).*

Since mitochondrial dynamics regulates mitochondrial number, morphology, location and networking (Stiles and Shirihai, 2012), we decided to evaluate the mitochondrial morphology by labeling the organelles with MitoSpy™ Green FM, an organic dye which selectively binds mitochondrial proteins. The mitochondrial network was different among cells grown on different substrates and elongated mitochondria were often observed in cells grown on ns-ZrO_x (Figure 3.20A). The quantitative analyses confirmed these observations: cells grown on the nanostructure showed an increased average mitochondrial area (Figure 3.20B-b), maximum diameter (Feret max) (Figure 3.20B-c) and aspect (major/minor axis) (Figure 3.20B-d) compared to those observed on

both glass and flat-ZrO_2 covers. In addition, the number of mitochondria per area (Figure 3.20B-a) was significantly lower in cells grown on the nanostructured substrate when compared to controls, probably because they tend to organize in networks. In line with this possibility, quantitative analyses revealed increased mitochondrial network in the cells grown on ns-ZrO_x, which had also significantly longer branches when compared to control substrates (Figure 3.20C-a,b). These observations suggest that mitochondrial fusion and fission events are counterbalanced in our system, but, in the meantime, the nanostructure evokes profound changes in mitochondrial organization and connections.

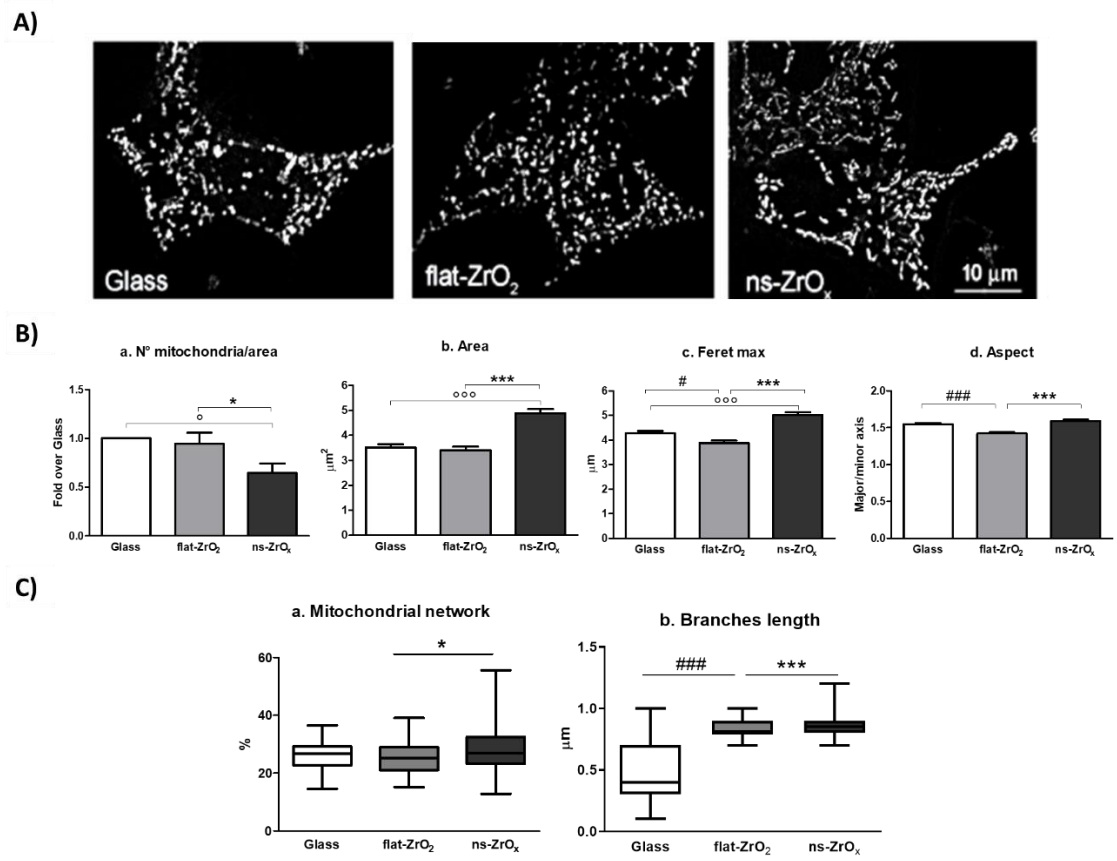

Figure 3.20. *Nanostructured substrate regulates mitochondrial morphology and networking.* ***A)*** *Cells grown on the indicated substrates for 3 days were loaded with MitoSpy™ Green FM and imaged by epifluorescence microscopy. Representative images are shown. Bar: 10 µm.* ***B)*** *The quantitative analyses of mitochondrial morphology show (a) mitochondria number per area, (b) single mitochondria area (µm²), (c) feret maximum (µm), and (d) mitochondria aspect (major/minor axis) in cells grown on different substrates. Bars illustrate the average responses ± SE (N = 15-20 cells for each substrate in three independent experiments). (*p < 0.05, ***p < 0.005 ns-ZrO_x vs flat-ZrO_2; °p < 0.05, °°°p < 0.005 ns-ZrO_x vs Glass; #p < 0.05, ###p < 0.005 flat-ZrO_2 vs Glass).* ***C)*** *Quantitative analysis of mitochondrial network: a) percentage of mitochondrial network per cell; b) network branches length. Bars illustrate the average responses ± SE (N = 15-20 cells for each substrate in two independent experiments). (*p < 0.05, ns-ZrO_x vs flat-ZrO_2; °°°p < 0.005 ns-ZrO_x vs Glass; # p<0.05, ###p < 0.005 flat-ZrO_2 vs Glass).*

Mitochondrial dynamics, by controlling organelle morphology, can directly influence the organelle function, which is crucial for ensuring appropriate insulin secretion (Park et al., 2008; Stiles and Shirihai, 2012). After its transport into β-cells, glucose is metabolized via glycolysis and processed in the tricarboxylic (TCA) cycle into mitochondria. This increases the ATP/ADP ratio and causes the closure of ATP-dependent K^+ channels at the plasma membrane. The resulting change in membrane potential modifies intracellular Ca^{2+}, via voltage-gated Ca^{2+}-channels, and triggers insulin exocytosis (Rorsman and Ashcroft, 2018; Rutter et al., 2017). Compelling evidence suggests that a high nutrient

environment (free fatty acids and/or glucose) promotes mitochondrial fragmentation which is often associated with changes in the proton leak and mitochondrial membrane potential, leading to an impairment of the insulin secretion (Molina et al., 2009; Stiles and Shirihai, 2012). Therefore, we decided to monitor the glucose-stimulated insulin secretion by ELISA assays. Consisting with the increased mitochondrial networking and membrane potential observed previously, βTC3 cells grown on the nanostructured substrate showed increased glucose-stimulated insulin secretion when compared to controls, while no change in the total insulin content was detected (Figure 3.21).

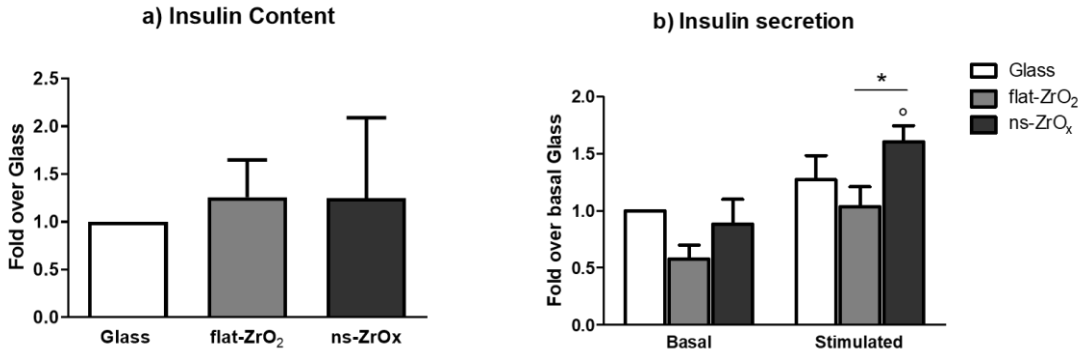

Figure 3.21. *(a) Quantification of the total insulin content (µg) by ELISA assay. Data (mean ± SD) are expressed as fold change over Glass (n = 3). (b) Insulin secretion under basal (2 mM glucose) and stimulated (20 mM glucose) in βTC3 cells grown on the indicated substrates for 3 days. Data (mean ± SD) are expressed as fold change over Glass basal release (n = 3, in duplicate). (° p<0.05, stimulated vs basal; *p < 0.05, vs flat-ZrO_2).*

Interestingly, the proteomic analysis revealed an upregulation of IDE (insulin degrading enzyme) and ANXA1 (annexin A1) expression in the cells grown on ns-ZrO_x, further supporting our observation of increased insulin secretion (Tables S1 and S3[7]). IDE is a metalloprotease involved in the degradation of insulin and for this reason it has always been considered as a negative regulator of insulin secretion (Fernández-Díaz et al., 2019). However, in the last years, emerging evidence demonstrates that IDE deletion/inhibition leads to impaired glucose-stimulated insulin secretion (GSIS), identifying IDE as a positive regulator of the β-cell function. ANXA1, also known as lipocortin 1, is a Ca^{2+} and phospholipid binding protein, mainly localized at the insulin granules, which positively modulates the GSIS (Rackham et al., 2015).

Since βtc3 is a clonal cell line, to confirm the relevance of the nanostructure on mitochondrial morphology and function we confirmed our data in INS1E cells, a rat β-cell line. Western blotting experiments revealed the downregulation of MFN2 in cells grown on ns-ZrO_x compared to glass coverslip, while no changes in DRP1 and OPA1 expression were detected (Figure 3.22A,B). Regarding the morphology, as shown in Figure 3.22C, INS1E mitochondria are generally more elongated and elaborated than those observed in the mouse model but, exactly as reported for βTC3 cells, their average area (Figure 3.22D-b) and maximum diameter (Feret max) (Figure 3.22D-c) increased when cells were grown on the nanostructure compared to glass coverslips. Furthermore, as observed for βTC3 cells, mitochondria tend to organize in more complex network in the cells grown on ns-ZrO_x (Figure 3.22E-a,b).

[7] https://doi.org/10.3389/fcell.2020.00508

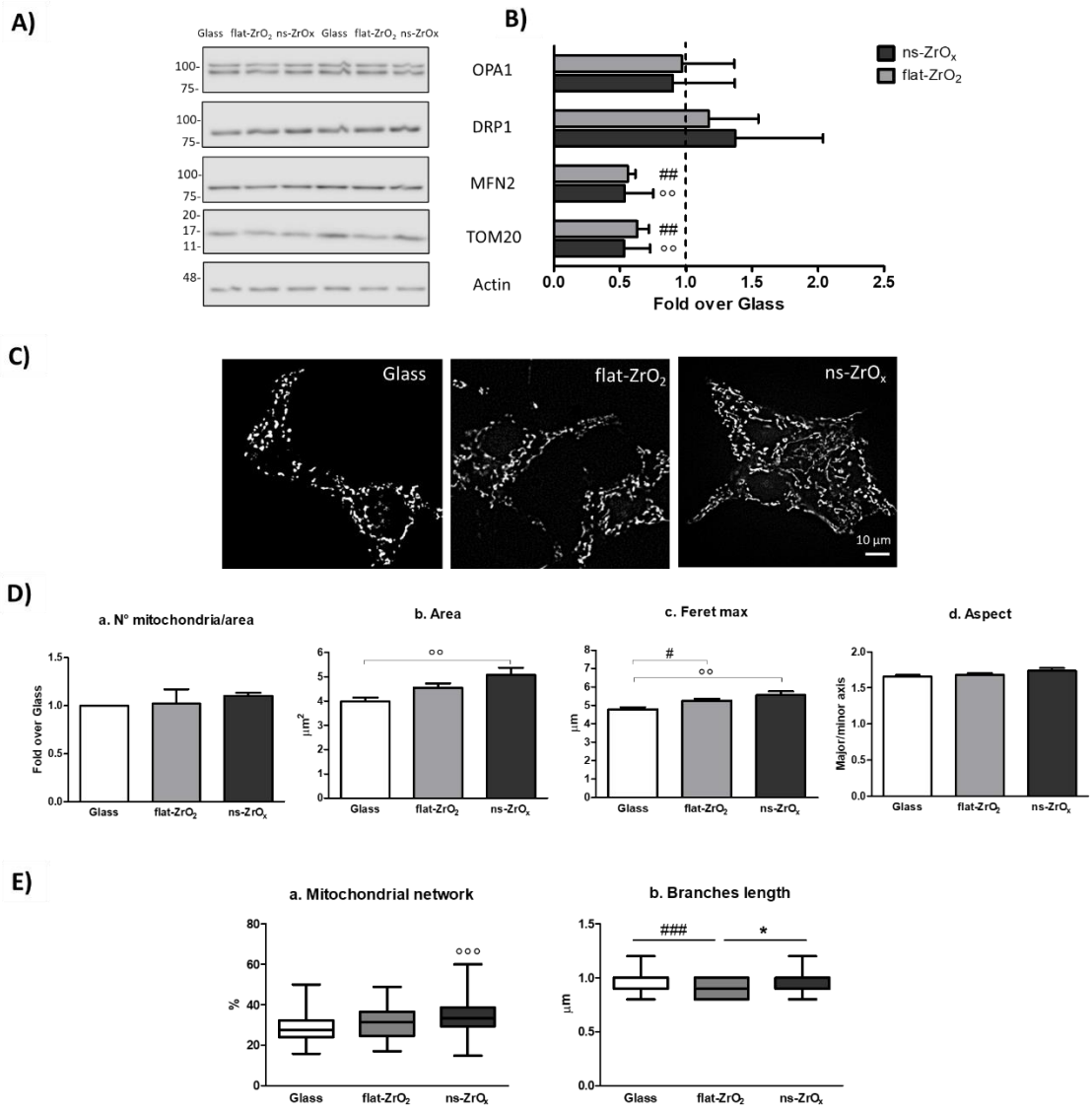

Figure 3.22. *Nanotopography influences mitochondrial proteome, morphology and network in INS1E cells.* ***A)*** *Western-blotting analysis of mitochondrial pro-fission (DRP1), pro-fusion (MFN2 and OPA1) and import (TOM20) proteins in INS1E cells grown on the indicated substrates for 3 days (15 µg protein/sample). On the left, the proteins molecular weight in kDa is reported.* ***B)*** *The quantitative analysis shows the downregulation MFN2 and TOM20 expressions in cells grown on 15 nm ns-ZrO_x. Data (mean values ± SD; n = 3 independent experiments) are expressed as fold-change over Glass ($p < 0.01$ ns-ZrO_x vs Glass; ##$p < 0.01$ flat-ZrO_2 vs Glass).* ***C)*** *Cells grown on the indicated substrates for 3 days, were loaded with MitoSpy™ Green FM and imaged by epifluorescence microscopy. Representative images are shown. Bar: 10 µm.* ***D)*** *Quantitative analyses of mitochondrial morphology in cells grown on different substrates show: (a) mitochondria number per area, (b) single mitochondria area (µm^2), (c) Feret maximum (µm), and (d) mitochondria aspect (major/minor axis). Bars illustrate the average responses ± SE (°°$p < 0.01$ ns-ZrO_x vs Glass; #$p < 0.05$ flat-ZrO_2 vs Glass).* ***E)*** *Quantitative analysis of mitochondrial network: a) percentage of mitochondrial network per cell; b) network branches length. Bars illustrate the average responses ± SE (N = 15-20 cells for each substrate in two independent experiments). (*$p < 0.05$, ns-ZrO_x vs flat-ZrO_2; °°°$p < 0.005$ ns-ZrO_x vs Glass; #$p<0.05$, ###$p < 0.005$ flat-ZrO_2 vs Glass).*

Generally, the obtained data confirmed the changes in mitochondrial morphology and dynamics observed in βtc3, however differences were statistically significant only in the ns-ZrO_x vs glass comparison, suggesting that a combination of chemistry (zirconia) and nanostructure can affect the mitochondrial organization and function. Interestingly, the INS1E mitochondrial are more elongated than those observed in βtc3, therefore it is also possible that the 15 nm roughness may not be the best nanotopographical environment for this cell line and further experiments need to be performed to address this hypothesis.

Taken together, the morphological and proteomic data suggest that the nanostructure modulates the delicate balance between fusion and fission, preserving β-cell homeostasis but concomitantly allowing a cellular response to the mechanical stimulus. The observed changes (increased mitochondria elongation and networking) are typical of efficient mitochondria resulting in an efficient glucose-stimulated insulin secretion.

3.2.5 Nanostructured substrate induces a metabolic shift at mitochondrial level

Bioinformatic analyses highlighted that the nanostructure hampers the oxidative metabolism and the expression of proteins involved in TCA cycle, pyruvate metabolism, aerobic respiratory and ATP synthesis coupled to proton transport (Figure 3.23 and 3.24), probably due to the cristae remodeling mediated by OPA1 and ROMO1. Indeed, cristae mediate the localization of oxidative phosphorylation complexes, creating a specialized and highly dynamic compartment that undergoes massive remodeling, with a direct impact on the energetic state of the cell (Cogliati et al., 2016). Accordingly, the expression of the most abundant import machineries of proteins into the mitochondrial inner membrane is altered by the nanostructure that decreases the mitochondrial import receptor subunit TOM20 homolog (TOMM20) and the mitochondrial import inner membrane translocases subunit (TIMM17A, TIMM23B), as well as the sorting and assembly machinery component 50 homolog (SAMM50), thus hampering the inner mitochondrial membrane organization (Figure 3.18B). Western blot analysis confirmed a statistically significant downregulation of TOM20 expression in the cells grown on the nanostructured substrate compared to flat-ZrO_2 but only in the βtc3 cells, thus suggesting that the 15 nm roughness may be not ideal for INS1E cells (Figure 3.20 and Figure 3.22A,B). Concomitantly, the nanostructure triggers the higher expression of the glycolytic enzyme enolase (ENO1) as well as arginase1 (ARG1) (Figure 3.23 and 3.24). The latter is involved in the homeostasis of L-arginine in competition with nitric oxide synthase (NOS) that utilizes the intracellular substrate arginine for NO synthesis, a possible source of ROS production. In accordance, we observed the decrease of oxidative stress response proteins (TXN2, PRDX3, PARP1, AIFM1, ETFDH, NDUFA12, NDUFS2, PARP1, PRDX3, PRDX5, ROMO1) associated to an increase in glutathione S-transferase P (GSTP1) (Figures 3.23 and 3.24 Tables S2,S3[8]). Even though increased glycolysis could suggest a hypoxic condition, characteristic of a stressed β-cell, the mitochondrial fraction of cells grown on ns-ZrO_x showed a lower expression of hypoxia upregulated protein 1 (HYOU1) as well as a decrease in the apoptosis-inducing factor 1 (AIFM1) and the mitochondrial outer-membrane voltage-dependent anion channel 1 (VDAC1). Particularly interesting is VDAC1 that acts as a mitochondrial gatekeeper modulating the energy homeostasis, as well as the mitochondria-mediated apoptosis (Pittala et al., 2020). Several studies reported an upregulation of VDAC1 expression in islets from T2D patients, further confirming the crucial role of this channel in maintaining the appropriate β-cell function (Zhang et al., 2019a). The proteomic data suggest that the metabolic effect exerted by the nanostructure is not caused by increased oxidative stress, in accordance, a similar ROS content was observed in cells grown on different substrates (Figure 3.25A). To further confirm that the metabolic shift induced by the nanostructure did not result in a stressed or apoptotic β-cell, cell viability was measured and as expected, no changes in the cell viability were detected between Glass, flat-ZrO_2 and ns-ZrO_x (Figure 3.25B,C).

[8] https://doi.org/10.3389/fcell.2020.00508

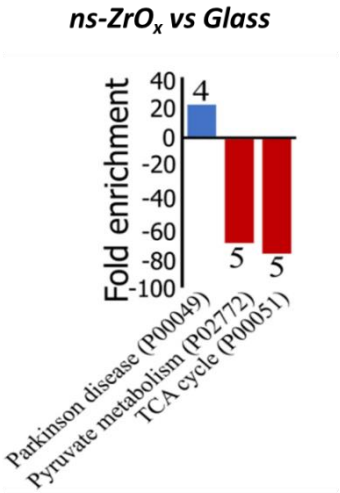

Increased or only expressed in ns-ZrO_x

DAVID KEGG Pathway

Term	Count	*p*-Value	Genes	Fold Enrich.
Biosynthesis of antibiotics	7	1.7E-04	GOT2, PKM, ARG1, NME1, OGDHL, ALDH9A1, ENO1	7.8
Arginine and proline metabolism	4	1.0E-03	GOT2, LAP3, ARG1, ALDH9A1	19.0
Viral carcinogenesis	6	1.3E-03	PKM, MAPK1, YWHAZ, YWHAH, ACTN1, DNAJA3	6.9
Biosynthesis of amino acids	4	3.0E-03	GOT2, PKM, ARG1, ENO1	13.2
Alzheimer's disease	5	4.4E-03	MAPK1, NDUFB4, NDUFS4, NDUFB8, IDE	7.1
Carbon metabolism	4	1.0E-02	GOT2, PKM, OGDHL, ENO1	8.4
Metabolic pathways	11	1.8E-02	GOT2, PKM, LAP3, ARG1, NDUFB4, NDUFS4, NDUFB8, NME1, OGDHL, ALDH9A1, ENO1	2.1
Glycolysis/Gluconeogenesis	3	3.0E-02	PKM, ALDH9A1, ENO1	10.6

Decreased in ns-ZrO_x or only expressed in Glass

DAVID KEGG Pathway

Term	Count	*p*-value	Genes	
Citrate cycle (TCA cycle)	16	8.7E-22	SUCLG2, SUCLG1, CS, IDH3B, ACLY, OGDH, PCK2, PDHB, IDH3A, SDHA, DLD, IDH2, PDHA1, MDH2, PC, FH	42.7
Parkinson's disease	18	8.3E-13	NDUFA4, ATP5D, SLC25A5, SLC25A6, ATP5B, NDUFA13, UQCRQ, VDAC3, NDUFA12, VDAC1, SDHA, NDUFV1, NDUFV2, ATP5C1, COX6B1, ATP5A1, ATP5H, NDUFS2	10.1
Metabolic pathways	41	3.7E-10	ATP5D, ALDH18A1, GANAB, GLUD1, ATP5B, NFS1, OGDH, UQCRQ, PDHB, IVD, IDH2, COX6B1, PDHA1, RPN2, HADH, NDUFS2, ATP5H, FH, NDUFA4, SUCLG2, SUCLG1, CS, MAOB, NDUFA13, IDH3B, ACLY, PCK2, NDUFA12, IDH3A, SDHA, DHRS4, NNT, NDUFV1, NDUFV2, DLD, ATP5C1, ATP5A1, PCCB, OAT, MDH2, PC	2.7
Ribosome	15	8.2E-10	RPL13, RPLP2, RPS15A, RPS8, RPS18, MRPL12, RPS16, RPL23, RPL6, RPL34, RPS14, RPL8, RPL5, RPL4, RPL10A	8.8
Oxidative phosphorylation	14	6.6E-09	NDUFA4, SDHA, ATP5D, NDUFV1, ATP5B, NDUFV2, COX6B1, ATP5C1, NDUFA13, ATP5A1, UQCRQ, NDUFS2, ATP5H, NDUFA12	8.4
Alzheimer's disease	14	1.1E-07	NDUFA4, SDHA, ATP5D, NDUFV1, ATP5B, NDUFV2, COX6B1, ATP5C1, NDUFA13, ATP5A1, UQCRQ, NDUFS2, ATP5H, NDUFA12	6.7
Pyruvate metabolism	7	8.2E-06	DLD, PDHA1, PCK2, MDH2, PDHB, PC, FH	14.0
Protein processing in ER	10	2.2E-04	HYOU1, P4HB, HSP90B1, GANAB, PDIA3, RRBP1, DNAJA1, HSPA5, RPN2, CALR	4.7
Oxocarboxylic acid metabolism	4	1.1E-03	CS, IDH2, IDH3B, IDH3A	18.8
Biosynthesis of amino acids	6	1.9E-03	ALDH18A1, CS, IDH2, IDH3B, IDH3A, PC	6.7
Glyoxylate and dicarboxylate metabolism	4	4.3E-03	DLD, CS, PCCB, MDH2	11.9
Valine, leucine and isoleucine degradation	4	2.0E-02	IVD, DLD, HADH, PCCB	6.8
Propanoate metabolism	3	4.6E-02	SUCLG2, SUCLG1, PCCB	8.6
Glycolysis/Gluconeogenesis	4	5.0E-02	DLD, PDHA1, PCK2, PDHB	4.8

Figure 3.23. A) *Gene Ontology classification of proteins differentially expressed in the comparison Glass vs ns-ZrO_x classified into different pathways using the Panther software. Functional grouping was based on p-value ≤ 0.05 and minimum three counts. Negative values (Red) refer to fold enrichment of proteins less expressed at ns-ZrOx or only*

expressed in Glass whereas positive values (Blue) refer to proteins more or only expressed on ns-ZrO_x. The numbers on the bars represent the counts. ***B)*** *DAVID functional grouping in terms of KEGG Pathways of the mitochondrial proteins differentially expressed in cells grown in ns-ZrO_x in comparison with cells grown on Glass. (Laboratory of prof. Tedeschi)*

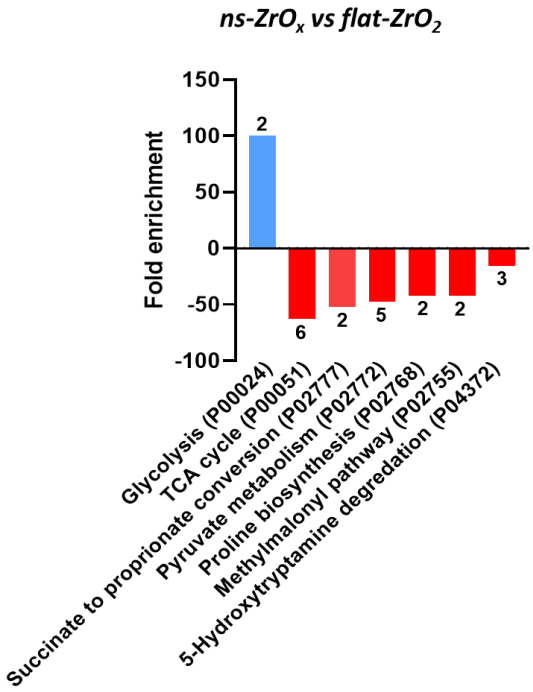

Increased or only expressed in ns-ZrO_x

KEGG Pathway

Term	Count	p-Value	Genes	Fold enrich.
Glycolysis	2	1.77E-04	PKM, ENO1,ALDH9A1, ARG1	>100

Decreased in ns-ZrO_x or only expressed in flat-ZrO_2

KEGG Pathway

Term	Count	p-Value	Genes	Fold enrich.
TCA cycle	6	4.85E-09	OGDH, PDHB, PCK2, IDH3B, CS, PDHA1, SDHA, MDH2 ,ACLY, IDH2, FH	62.99
Succinate to proprionate conversion	2	1.30E-03	PCCB, MCCC2	52.49
Pyruvate metabolism	5	2.86E-07	PHDHB, PCK2, PDHA1, MDH2, FH	47.72
Proline biosynthesis	2	1.80E-03	PYCR2, ALDH18A1	41.99
Methylmalonyl pathway	2	1.80E-03	PCCB, MCCC2	41.99
5-Hydroxytryptamine degredation	3	1.28E-03	ALDH2, ALDH1L2, MAOB	15.75

Figure 3.24. A) *Gene Ontology classification of proteins differentially expressed in the comparison flat-ZrO_2 vs ns-ZrO_x classified into different pathways using the Panther software. Functional grouping was based on p-value ≤ 0.05 and minimum three counts. Negative values (Red) refer to fold enrichment of proteins less expressed at ns-ZrOx or only expressed in flat-ZrO_2 whereas positive value (Blue) refer to proteins more or only expressed on ns-ZrO_x. The numbers on the bars represent the counts.* ***B)*** *DAVID functional grouping in terms of KEGG pathways of the mitochondrial proteins differentially expressed in cells grown in ns-ZrO_x in comparison with cells grown on flat-ZrO_2. (Laboratory of prof. Tedeschi)*

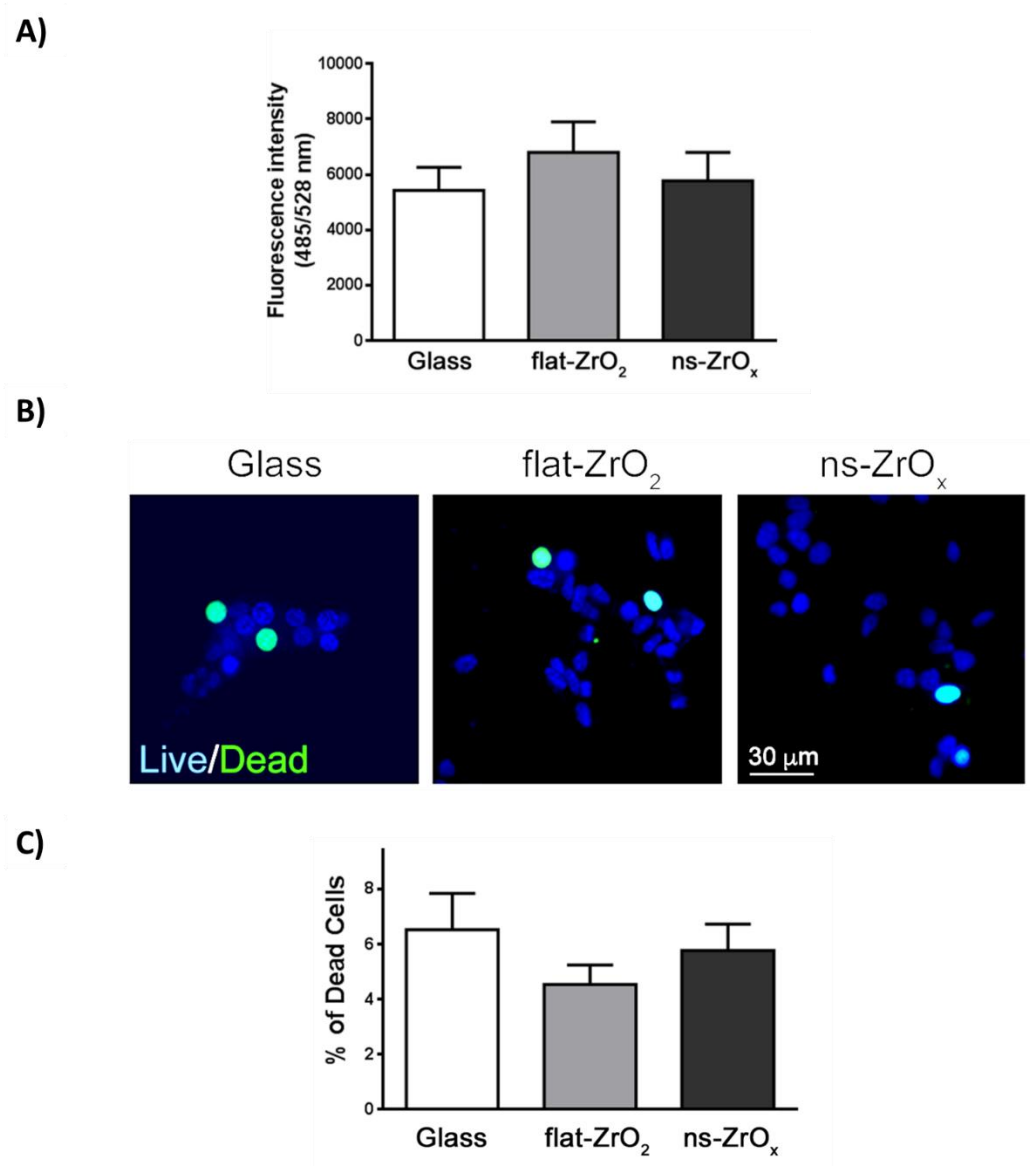

Figure 3.25. A) *Βtc3 cells were grown on the indicated substrates for 3 days and the intracellular ROS content was monitored by DCFDA quantification (485/528 nm Ex/Em). Data are expressed as mean ± SD of three independent experiments.* ***B)*** *Representative images of cells stained with NucBlue® (Live cells) and NucGreen® (Dead cells). Bar: 30 µm.* ***C)*** *Bars represent the percentage of dead cells over the total cells. Data are expressed as mean ± SD of three independent experiments (a minimum of 100 cells for experiment was counted).*

Taken together, our data indicate that the nanostructure induces a reshaping of the mitochondrial cristae organization and import/export, which results in a metabolic shift without affecting β-cell survival.

3.2.6 Nanostructured substrate modulates the interplay with organelles

Bioinformatic analyses revealed the downregulation of proteins involved in protein localization, folding and processing in the ER (CALR, CLPX, DNAJA1, FKBP2, GNB1, GRPEL1, HSP90B1, HSPA5, HSPA9, HSPD1, MLEC, P4HB, PDIA3, PPIB, PRDX4, and TRAP1) in the cells grown on ns-ZrO_x when compared to both flat and glass substrates (Figure 3.18B). Since almost 20% of the mitochondrial membranes are in direct contact with the ER cisternae, it is not surprising to find ER proteins in the mitochondrial fraction (Naon and Scorrano, 2014). Most of the identified proteins (CALR, PDIA3, P4HB, GNB1, HSPA5, HSP90B1, HSPD1 and TRAP1) are normally upregulated in response to stress

and involved in apoptotic processing; therefore, their downregulation further suggests a healthy state of the cells.

Mitochondria and ER are closely related through the so-called mitochondria-associated endoplasmic reticulum membranes (MAM), multiprotein complexes that play a pivotal role in calcium (Ca^{2+}) signaling, lipid transport, mitochondrial functions and cell survival (Tubbs and Rieusset, 2017). Giving the crucial role of mitochondrial-ER contact sites for cell function, modifications of the ER-mitochondria network were evaluated in βTC3 and INS1E cells grown on the different substrates. To this end, cells were transfected with an ER-GFP construct selectively targeted to the ER compartment and mitochondria were labeled with MitoSpy™ Orange. Intricated ER cisternae networks spanning the whole cellular volume were clearly detectable in high magnification images (Figure 3.26A-a), and no differences in their organization were observed in cells grown on different substrates (Figure 3.26B-a). Mitochondria of similar size were visible in all samples, but only in cells grown on the nanostructure they were clearly tethered to the ER. Observations were corroborated by the Pearsons' colocalization analysis which revealed increased ER–mitochondria juxtaposition in cells grown on the nanostructure compared to glass cover (Figure 3.26B-b).

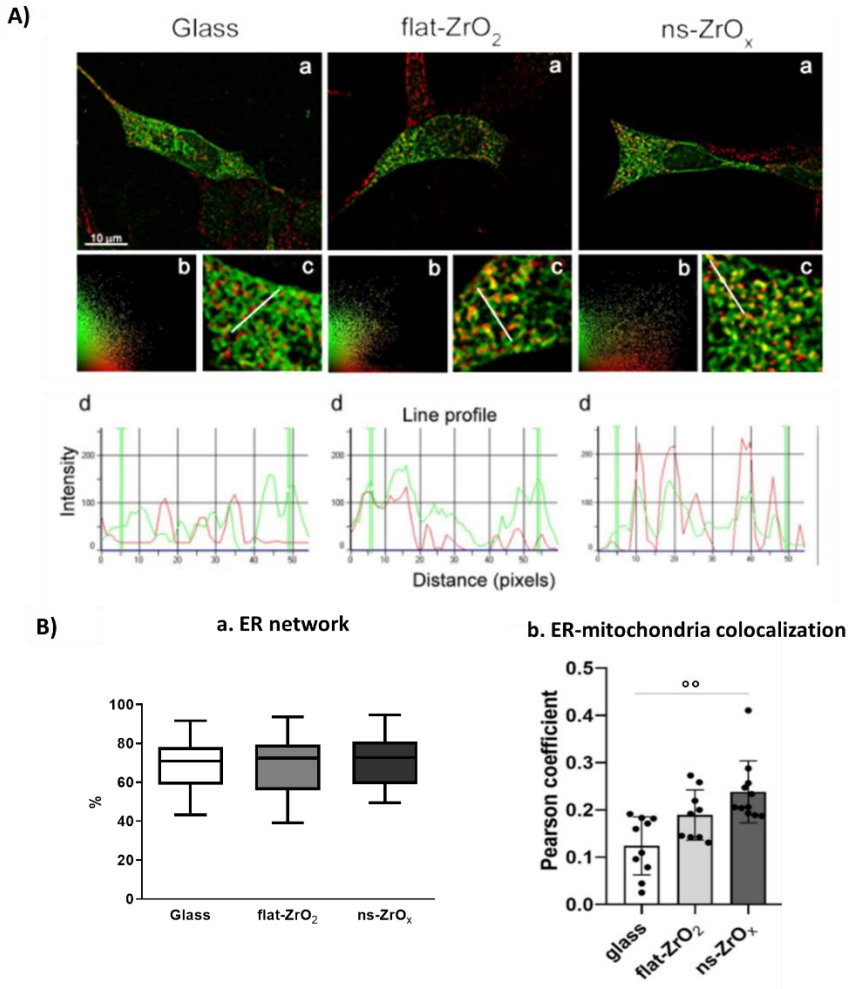

Figure 3.26. *Nanostructure modulates the ER-mitochondrial contact sites in βTC3 cells.* ***A)*** *βTC3 cells, plated on the different substrates, were transfected with ER-GFP (green) and, after 48 h, the mitochondria were labeled with MitoSpy™ Orange (red). a) Representative images of ER-mitochondrial networks in cells grown on the indicated substrates. The yellow/orange staining highlights ER-mitochondria juxtaposition. Bar: 10 µm. b) Relative scatter plot analysis of red and green stainings; c) particular of panel a at higher magnification (3X); and d) plot of red and green fluorescence intensities along the line profile reported in c.* ***B)*** *a) Quantitative analysis of the percentage of ER networks in βTC3 cell grown on the*

indicated substrates. Data are expressed as mean ± SE of three indipendent experiments. b) Quantitative colocalization analyses expressed as Pearson's coefficient. Data are expressed as mean ± SE and single values are reported. (°°p < 0.01 ns-ZrO_x vs Glass).

A similar trend was observed in INS1E cells (Figure 3.27A): no differences in the organization of ER network were detected in cells grown on different substrates (Figure 3.27B-a), however, a significantly higher juxtaposition between ER and mitochondria was detected in cells grown on the nanostructured substrate when compared to the Glass (Figure 3.27B-b).

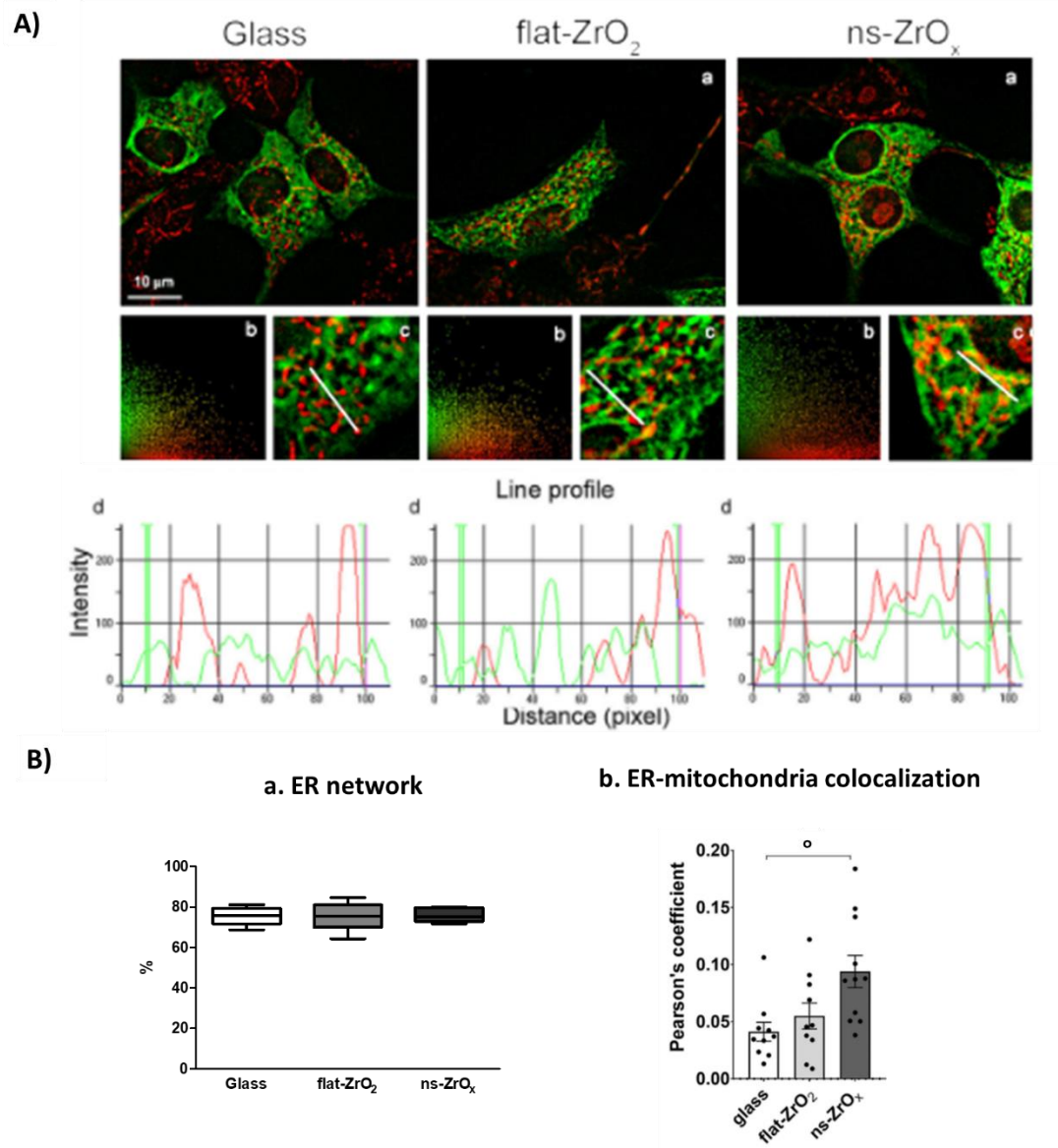

Figure 3.27. *Nanostructure modulates the ER-mitochondrial contact sites in INS1E cells.* ***A)*** *INS1E plated on Glass, flat-ZrO_2 and ns-ZrO_x substrates were transfected with ER-GFP (green) and after 48 h, mitochondria were labeled with MitoSpy™ Orange (red). (a) Representative images of ER-mitochondrial networks in cells grown on the indicated substrates. The yellow/orange staining highlights ER-mitochondria juxtaposition. Bar 10 µm. (b) Scatter plot analysis of image a. (c) Particular of panel a at higher magnification (3X); and (d) plot of red and green fluorescence intensities along the line profile reported in c.* ***B)*** *a) Quantitative analysis of the percentage of ER networks in INS1E cells grown on the indicated substrates. Data are expressed as mean ± SE of three indipendent experiments. b) Quantitative colocalization analyses expressed as Pearson's coefficient. Data are expressed as mean ± SE and single values are reported. (*p < 0.05 ns-ZrO_x vs Glass).*

One of the most well characterized function of ER is the regulation of protein folding. Alteration of ER-mitochondria network might result in the so-called unfolded protein response (UPR), caused by the accumulation of misfolded proteins within the ER (Tubbs and Rieusset, 2017). Since it has been

reported that UPR response induces β-cell stress, misfunction and death, key features in the development of type 2 diabetes (Rieusset, 2011), we evaluated the expression of UPR stress markers in βTC3 cells grown on the indicated substrates (Figures 3.28). A decreased expression of Eukaryotic Initiation Factor 2 alpha (eIF2α), its phosphorylated form (P-eIF2α), and protein kinase RNA-like ER kinase (PERK) was detected in cells grown on ns-ZrO_x compared to glass cover, indicating that the Unfolded Protein Response was not activated on the nanostructure, again supporting a healthy state of the cell. A significant reduction of eIF2α expression was also detected in the ns-ZrO_x substrates compared to flat-ZrO_2 sample, while no changes in PERK and P-eIF2α expressions were observed. As for mitochondria, changes in ER-stress proteins were more evident in the ns-ZrO_x vs the glass comparison, suggesting that a combination of chemistry and nanotopography might affect the cellular response.

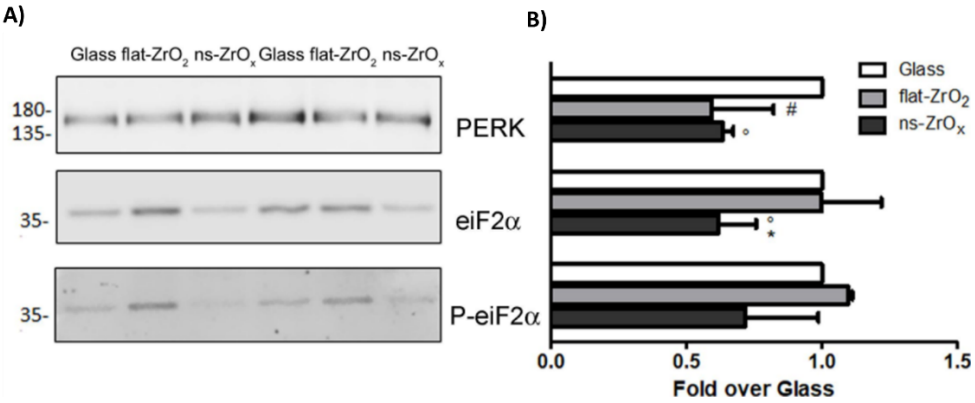

Figure 3.28. *UPR response is not induced by the nanostructure.* ***A)*** *Western-blotting analysis of eIF2α, P-eIF2α and PERK in cells grown on the indicated substrates for 3 days (15 µg protein/sample).* ***B)*** *The quantitative analysis of protein expression shows downregulation of PERK and eIF2α expression in cells grown on 15 nm ns-ZrO_x. Data (mean values ± SD; n = 3 independent experiments) are expressed as fold-change over Glass (*p < 0.05 ns-ZrO_x vs flat-ZrO_2; °p < 0.05 ns-ZrO_x vs Glass; #p < 0.05 flat-ZrO_2 vs Glass).*

Mitochondria actively interact also with the lysosomes both in physiological condition, mediating the regulation of mitochondrial division, the transfer of lipids, calcium and iron (Liesa and Shirihai, 2013; Wong et al., 2019) or upon cellular stress, promoting mitochondrial degradation via mitophagy (Hutagalung and Novick, 2011). Interestingly, the bioinformatic analysis revealed the upregulation of proteins involved in vesicle-mediated transport (HSP90AA1, HSPA8, MYH9, RAB7A, YWHAH, and YWHAZ) and lysosomal transport (XSPA8, STXBP1, and RAB7A) (Figure 18B) in the cells grown on ns-ZrO_x compared to glass cover. Conversely, the comparison between ns-ZrO_x and flat-ZrO_2 indicates the downregulation of this pathway, in the cells grown on the nanostructure. To have a better insight of the phenomenon, βTC3 cells were transfected with a LAMP1-GFP construct, selectively targeted to lysosomes and mitochondria were labelled with MitoSpy™ Orange. Intriguingly, the quantitative analysis revealed increased colocalization of mitochondria and lysosomes in cells grown on the ns-ZrO_x compared to flat-ZrO_2 (Figure 3.29), while no changes were detected compared to glass cover. Other studies are necessary to understand the significance of this finding.

Taken together, these data revealed that the nanotopography induces a general reorganization of the interplay between mitochondria and other organelles. Intriguingly, it has been reported that 15 nm is the optimal distance between mitochondria and ER for ensuring calcium transfer and MAM function, while the maximum tethering of mitochondria and lysosomes occurs at a distance of 10

nm (Csordás et al., 2010; Giacomello and Pellegrini, 2016). Since the nanostructured substrates with 15 nm roughness exerted the most prominent effects, we speculated that substrates roughness may create a pattern of peaks and valleys that may act as constrains, forcing cytoplasmic components and organelles to get closer and to interact with each other.

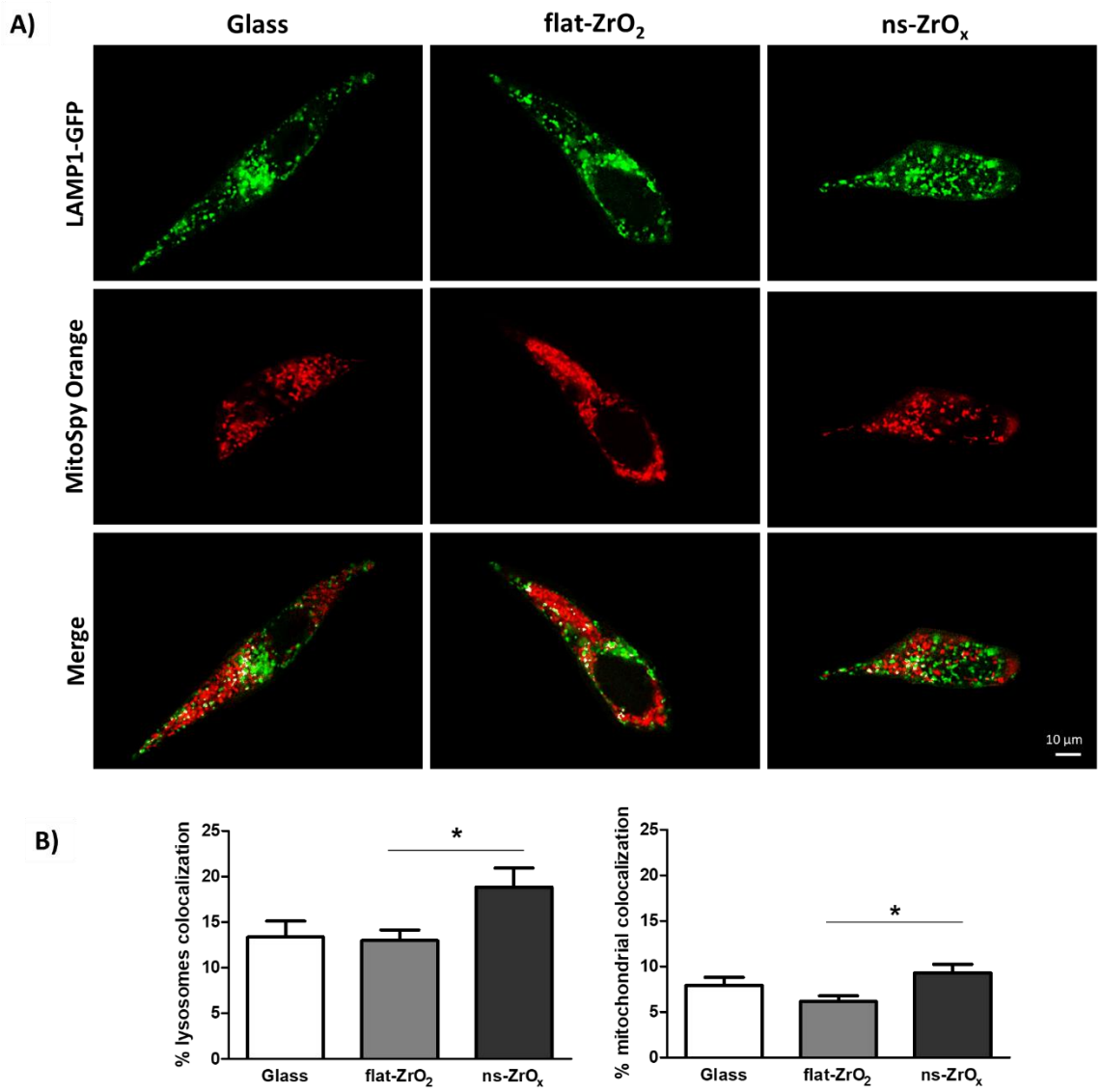

Figure 3.29. *Nanostructured substrate modulates the interplay between mitochondria and lysosomes.* ***A)*** *βTC3 cells plated on Glass, flat-ZrO_2 and ns-ZrO_x substrates were transfected with LAMP1-GFP (green) and after 48 h, mitochondria were labeled with MitoSpy™ Orange (red). Representative images of ER-lysosomes networks in cells grown on the indicated substrates are reported. The yellow/white staining highlights ER-lysosomes juxtaposition. Bar 10 µm.* ***B)*** *Quantitative analysis of the lysosomes and mitochondrial percentage colocalization. Data are expressed as mean ± SE. (*p < 0.05 ns-ZrO_x vs flat-ZrO_2).*

In conclusion, proteomic and morphological studies suggest that the nanotopography affects mitochondrial dynamics, shape and network. Since mitochondria are tightly connected to the cytoskeleton, we speculate that modifications of the cytoskeletal organization induced by the nanostructure, may modulate mitochondrial distribution, localization and even their shape which, in turn, fine-tune their metabolic response (Tilokani et al., 2018). Furthermore, mechanical forces transmitted directly from the cytoskeleton to the mitochondria may induce conformational changes of the mitochondrial inner membrane modulating mitochondrial cristae formation, which, in turn, affects the assembly and function of respiratory complex (Pasqualini et al., 2016).

Accordingly, proteomic analyses revealed major differences in proteins regulating cristae formation and shaping, which probably drags the modifications in the expression of the TCA cycle and aerobic respiration enzymes observed in cells grown on nanostructured substrates. In addition, the nanostructure may induce a cytoskeletal-mediated deformation of the mitochondrial OMM membrane, which may modify the permeability of transition pores and voltage dependent anion channels, resulting in increased mitochondrial membrane potential and glucose-stimulated insulin secretion (Kumazawa et al., 2014; Rostovtseva et al., 2008). To confirm this hypothesis, it will be necessary to evaluate the mitochondrial calcium currents. The nanotopography by regulating the cytoskeletal tension may also modulates cell shape resulting in a reorganization of the dense intermingled meshwork of organelles within the cytoplasm. In line with this possibility, increased mitochondria ER and lysosomes contact sites were detected in the cells grown on the nanostructured substrate.

In summary, we favor the idea that the morphological and proteomic changes induced in mitochondria by the nanostructure can prime the organelle for a metabolic switch necessary for cellular adaptation to the new extracellular cue. Since transformed β-cell lines were used in this study, further work aimed at monitoring the

mitochondrial proteome on human isolated islets of Langerhans will be necessary to confirm our observations and to have a better insight in the complex interplay between mitochondria and extracellular cues.

3.3 Ongoing experiments

3.3.1 Impact of nanoscale features on cell aggregation and polarity

Cell aggregation is an obligatory step for obtaining mature and functional β-cells. During pancreas organogenesis, endocrine cells first are scattered into the pancreatic epithelium and then aggregate into islet clusters where they undergo a progressive morphological and functional maturation (Nair et al., 2019). The cluster-like organization not only dictates β-cell maturation during development, but also favors the tight connections between endocrine cells ensuring an extremely rapid flow of important signals for regulating β-cell function (Ladoux and Mège, 2017). Loss of intercellular connectivity, indeed, impairs β-cell responses to inputs, both in terms of Ca^{2+} signaling and magnitude of the insulin release (Rutter and Hodson, 2015). Increasing evidence suggests that the mechanical properties of the extracellular environment regulate cell-cell adhesions and the aggregation process. In particular, recent works from the Gentile's group have showed that nanoroughness substrates favor the self-assembly of neurons into small-cortical-like mini columns (Onesto et al., 2017, 2019). They suggested that the aggregation of the cells into clusters is controlled by the competition between the binding energy of cell-cell adhesion, the interaction with the substrate and the kinetic energy of the system. Since β-cell plated on the nanostructured substrates present tiny focal adhesions compared to flat substrates, we hypothesized that the nanostructure may induce cell aggregation by reducing the strength of the interaction with the substrate and favoring cell-cell interactions. Preliminary observations, showed in Figure 3.15, suggested that nanoscale topography drives the aggregation of βTC3 and INS1E cells into islet-like cluster structures; further experiments will be required to characterize the observed phenomenon and to dissect the molecular mechanisms involved.

Nanotopography may also act as a positional cue which drives β-cell polarity. Giving the pivotal role of the primary cilium in regulating β-cell function and survival and more generally cell polarity, we investigated its distribution and dimension in βTC3 cells and human islets of Langerhans grown on the indicated substrates (Figure 3.30). Quantitative analysis revealed an increase percentage of cells bearing cilia in cells grown on the nanostructured substrates (Figure 3.30B,C). The increased number of ciliated cells can be partially explained by the upregulation of the axonemal dynein (DNAH14), a protein involved in the assembly of primary cilia, in the cells grown on the nanostructured substrates (Tables S1,S3 and S5[9]).

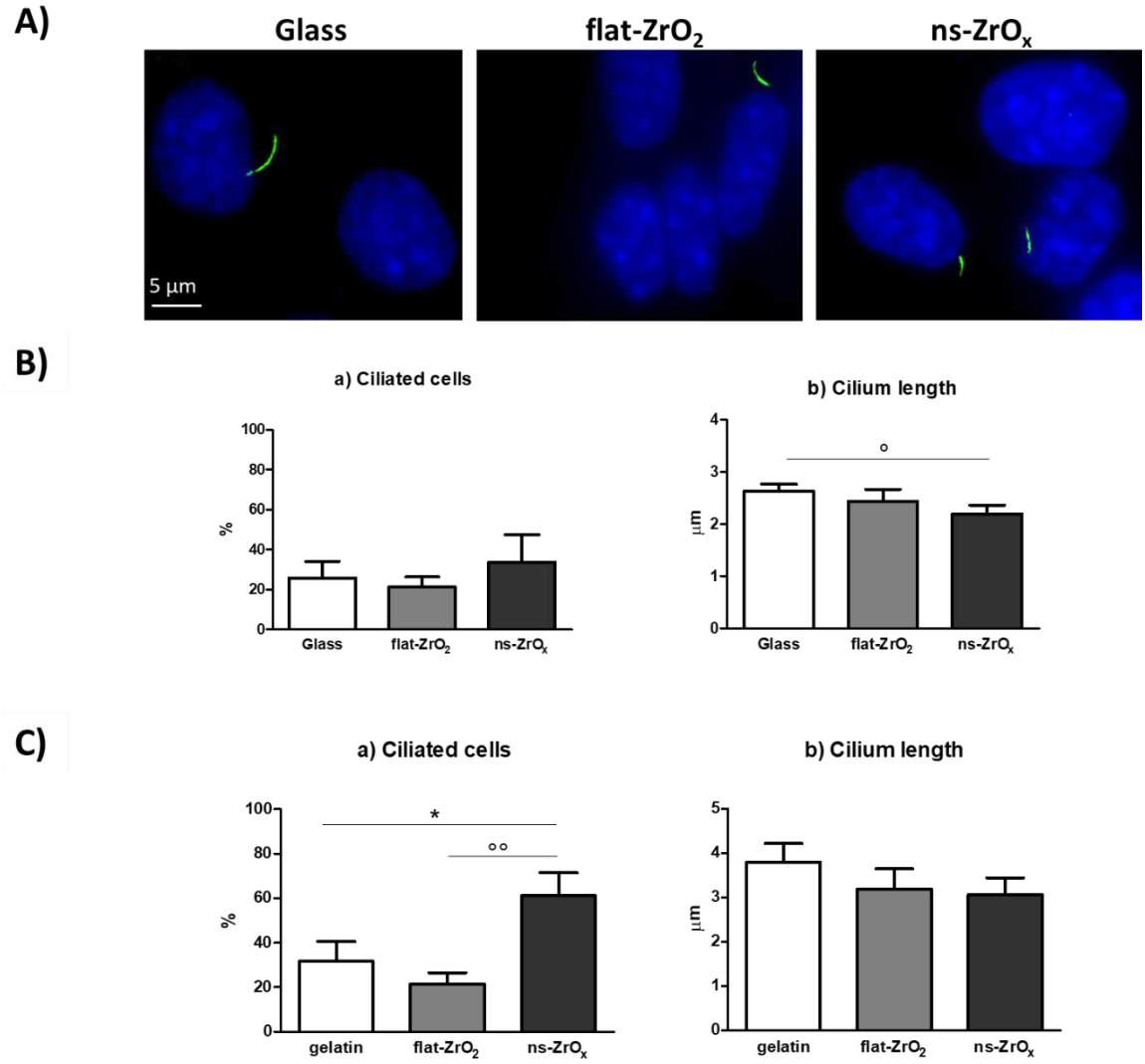

Figure 3.30. *Nanostructured substrates impact cilia distribution and length.* ***A)*** *Representative confocal images of βTC3 cells grown on Glass, flat-ZrO_2 and ns-ZrO_x substrates for 3 days and double stained with anti-acetylated tubulin antibody (green) and DAPI (blue). Bar: 5 µm.* ***B)*** *Quantitative analysis of primary cilia. Bars represent a) the percentage of ciliated cells over the total cells and b) the cilium length (µm). Data are expressed as mean ± SD of three independent experiments (N=15-20 cells for each substrate). (°p<0.05, Glass vs ns-ZrO_x).* ***C)*** *Quantitative analysis of primary cilia distribution and dimension in human islets of Langerhans grown on the indicated substrates for 20 days. Bars represent a) the percentage of ciliated cells over the total cells and b) the cilium length (µm). Data are expressed as mean ± SD of three independent experiments (N=15-20 cells for each substrate). (°°p<0.01, Glass vs ns-ZrO_x; p<0.05, flat-ZrO_2 vs ns-ZrO_x).*

Interestingly, on the nanostructure cilia were shorter than on control substrates. Even though other experiments will be necessary to verify this possibility, we believe that the decreased cilium length

[9] https://doi.org/10.3389/fcell.2020.00508

is just the effect of a different spatial orientation of the cells. Indeed, on flat substrates, cell-substrates interactions prevail, cells spread over the surface and the cilium is longitudinally oriented. Conversely, on the nanostructure increased cell-cell interactions promote the vertical organization of the cells and the cilium is perpendicular to the observation axis. Further experiments will be necessary to understand the impact of the nanotopography on the cilium organization and more generally on the β-cell polarity.

3.3.2 Mechanotransduction and microRNAs: an open question

The role of MicroRNAs (miRNAs) in regulating cell function has been emerging dramatically in the last years; indeed, miRNAs regulate tissues development, organization and function by modulating redox homeostasis, apoptosis, metabolism, inflammation and alteration of their expression leads to different pathological outcomes (Bushati and Cohen, 2007; Stefani and Slack, 2008). This holds true also for β-cells, where miRNAs regulate cell survival and function, and changes in their expression result in diabetes pathogenesis (Eliasson and Esguerra, 2020; Eliasson and Regazzi, 2020).

miRNAs are small (around 23 nucleotides) non-coding RNAs that contribute to gene regulatory networks by binding to the 3' untranslated region (UTR) of their target mRNAs (Bushati and Cohen, 2007; Shukla et al., 2011). Most miRNAs are transcribed by RNA polymerase II to generate capped and polyadenylated primary miRNAs (pri-miRNA), which are cleaved by the nuclear complex Drosha/DGCR8 into shorter precursor miRNAs (pre-miRNAs) hairpin structure. Pre-miRNAs are exported by exportin5 to the cytosol, where are converted into mature miRNAs by the RNase II, Dicer, generating a short miRNA duplex. miRNA duplex is loaded in the miRNA-induced silencing complex (miRISC), where the conformational changes of Argonaute protein promote the expulsion of one of the miRNAs strands (miRNA*) (Bushati and Cohen, 2007; Shukla et al., 2011; Stefani and Slack, 2008). Once the single-strand miRNA silencing complex is formed, miRNA interacts with specific region of the target mRNAs, known as seed sequences, to regulate their expression. miRNAs use multiple mechanism for regulating gene expression; if the base-pair complementarity is perfect, target mRNA is cleaved and degraded by the Argonaute proteins, otherwise miRNAs repress the mRNA translation. In addition, miRNAs can also target promoter regions activating gene expression (Bartel, 2009; Bushati and Cohen, 2007). According to the partial base-pairing of miRNAs to target mRNA, one miRNA can target multiple mRNAs and the translation of one mRNA can be regulated by many miRNAs, as such a complex network governates gene expression (Esguerra et al., 2018).

Giving that mechanical forces modulate the translation and transcriptional program (proteomic data on human isolated islets), we speculated that mechanotransduction might also impact the miRNAs expression profile. The first paper that directly correlates the regulation of miRNAs expression to mechanical forces was published in 2019 (Moro et al., 2019) and few works have been published regarding the mechanical regulation of miRNAs expression (D'Angelo et al., 2019; Wei et al., 2018), but nothing is known about pancreatic β-cells. In order to study and investigate the impact of the nanotopography on miRNAs, I spent a period of three months in the Regazzi's group at the University of Lausanne, a group leader in non-coding RNAs profiling in β-cells.

Although, given the complexity of the system, a systematic study would be necessary, as a first approach, we decided to evaluate the expression of selected miRNAs in cells grown on the different substrates. The proteomic analysis performed on human islets after 20 days in culture revealed a clear downregulation of the EGLN1/PDH2-HIF1α-NFκB axis by the nanoscale topography that was

also confirmed by western blotting experiments. Computational tools for miRNA target prediction revealed that several miRNAs can target this pathway; we focused on miR375, miR21-5p and miR146a-5p which are known to be expressed by β-cells.

miR375, the most abundant and characterized miRNA within the islets, regulates pancreatic development, β-cell proliferation and function by interacting with multiple targets (Eliasson, 2017; Esguerra et al., 2018; LaPierre and Stoffel, 2017). Among these, myothrophin (Mtpn) is a protein involved in the actin cytoskeleton remodeling, it is also a transcriptional activator of NF-κB (Poy et al., 2004).

miR21-5p inhibits the activation of NF-κB by targeting PDCD4 (proinflammatory tumor suppressor programmed cell death protein 4) mRNA for degradation (LaPierre and Stoffel, 2017; Roggli et al., 2010), exerting anti-apoptotic activity in β-cells. In addition, miR21-5p has been suggested to directly regulate EGLN1/PHD2 mRNA expression in other cell types (Jiao et al., 2017).

miR146a-5p indirectly regulates NF-κB activity through the inhibition of its target IRAK1 (interleukin-1 receptor-associated kinase 1) and TRAF6 (tumor necrosis factor receptor-associated factor 6) (Roggli et al., 2010; Wu et al., 2018).

The expression of these miRNAs was evaluated by RT-qPCR experiments in mouse βTC3 cells grown on Glass, flat-ZrO_2 and ns-ZrO_x substrates for 3 days. Giving the complexity of miRNAs regulation, our experiments were performed on a simplified model and the three-days incubation was selected according to the major changes in the mechanotransductive process observed previously. As shown in Figure 3.31, no differences were detected in miR375, miR21-5p and miR146a-5p expression in cells grown on the different substrates.

Emerging data report the crosstalk between YAP signaling and miRNA regulome, as YAP regulates miRNAs expression by controlling the miRISC and miRNAs modulate YAP expression by targeting its mRNA (D'Angelo et al., 2019; Moro et al., 2019). Giving the crucial role of YAP/TAZ signaling pathway in the mechanical regulation of β-cell behavior, we decided to evaluate the expression of miR29a, a regulator of YAP expression in cancer cells. Data are reported in Figure 3.31 and ,also in this case, no changes were detected.

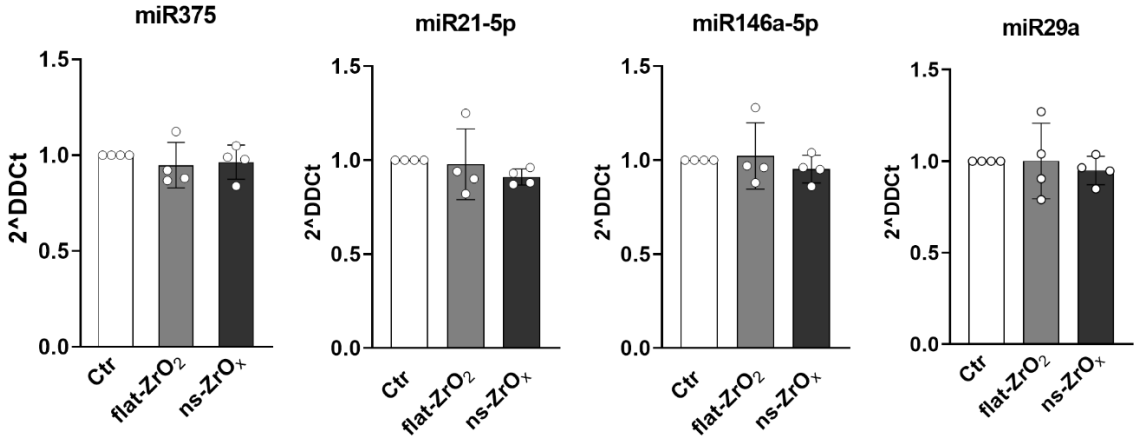

Figure 3.31. *Nanotopography and miRNAs. βTC3 cells were cultured on Glass (Ctr), flat-ZrO_2 and ns-ZrO_x for 3 days and miRNAs expression was evaluated by RT-qPCR experiments. Data are expressed as mean ± SD of four independent experiments, performed in duplicate. Single values are reported.*

These preliminary data do not support a major role of nanotopography in the control of miRNAs expression. However, several factors may explain these disappointing preliminary results.

First, the redundancy of the miRNAs regulatory complexes; human genome codifies for 2237 mature miRNAs, each of which has the potential to control hundreds of target mRNAs (Guay and Regazzi, 2013). Probably a top-down analysis might be more successful in identifying miRNAs involved in the phenomenon we are observing. To this purpose, a miRNA sequencing will be performed in our samples in order to evaluate all the potential miRNAs regulated by the nanostructure.

Another aspect that needs to be considered is the timing of miRNAs expression assessment. Indeed, in the experiments reported above, the miRNAs were evaluated only after 3 days of cells culture on the different substrates. Although, this time point correlates with the most relevant morphological and functional modifications observed in β-cells, it is possible that changes in miRNAs expression precede the observed behavioral changes. Time-course expression experiments of the selected miRNAs will be necessary before definitively excluding their involvement in mechanotransduction.

In conclusion, further experiments will be necessary to better understand the impact of nanotopography on miRNAs regulome.

4. Conclusion

In summary, our results show that nanostructured substrates favor long-term culture of human islets of Langerhans by supporting β-cell survival and preserving β-cell differentiation and function. Our data demonstrate that β-cell sense the nanotopography and respond by activating a mechanotransductive pathway that induces the modification of cell-substrate adhesion sites and the reorganization of the actin cytoskeleton, which affects cellular behavior through different mechanisms (Figure 4.1).

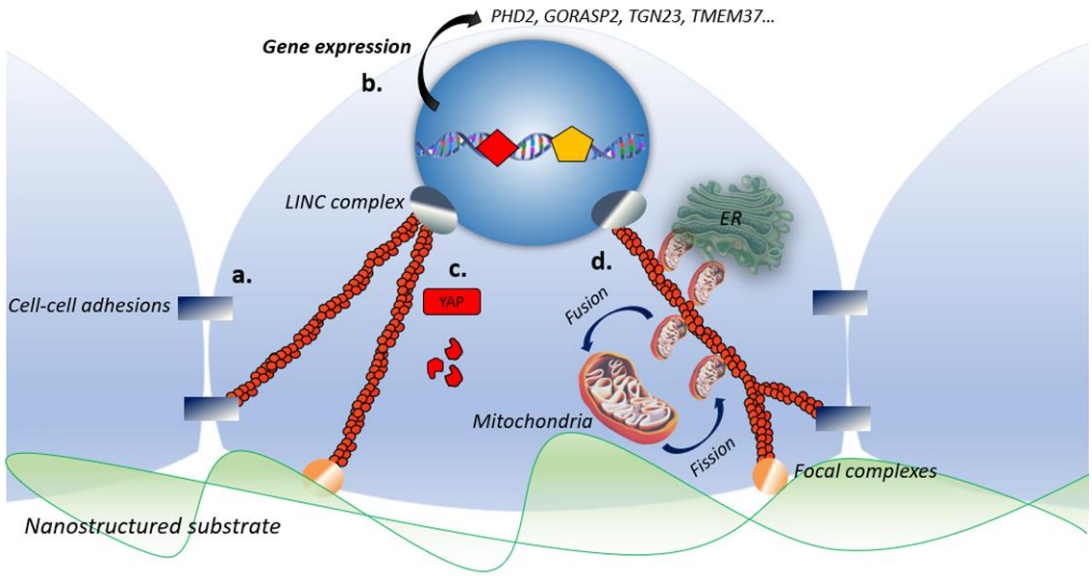

Figure 4.1. *The nanotopography promotes β-cell differentiation, survival and function through the activation of a mechanotransductive pathway.* ***a)*** *The actin cytoskeleton reorganization reduces the intracellular tension favoring a round cellular geometry that, in turn, promotes the inter-cellular connectivity.* ***b)*** *Modification of the actin cytoskeletal tension affects the nuclear shape and architecture increasing the expression of pro-survival and pro-differentiation genes.* ***c)*** *The deformation of the nuclear envelope regulates the access of transcription factors to the nucleus. Nanotopographical cues promote YAP cytoplasmic retention and degradation, resulting in increased β-cell differentiation.* ***d)*** *The actin cytoskeleton reorganization shapes mitochondrial morphology, dynamics and indirectly promotes the connection with other organelles by modulating the cell shape. These modifications prime the mitochondria for a metabolic switch necessary for cellular adaptation to the new extracellular cue.*

Firstly, the alteration of the intracellular tension generated by the actin cytoskeleton reorganization promotes a more relaxed, round cellular shape which, in turn, favors the formation of cell–cell contacts. Increased intercellular connectivity promotes the maintenance of the islet-like cluster organization, which is crucial for ensuring a coordinated β-cell response to the extracellular stimuli (Figure 4.1a). Probably, the integrated Ca^{2+} signaling and insulin release observed in the islet grown on the nanostructured substrates are due, at least in part, to the rapid flux of signals between adjacent cells that potentiate the glucose-stimulated insulin secretion.

The nanotopography, by modulating the reorganization of the actin cytoskeleton, may also modifies the nuclear shape; we can hypothesize that changes in the nuclear architecture might affect the chromatin conformation and the epigenetic machinery, leading to changes in gene expression. Among the proteins upregulated by the nanotopography are those involved in granules trafficking (GORASP2, SEC23B) and calcium signaling (TMEM37), suggesting another mechanism underlying the increased insulin secretion observed in the islets grown on the nanostructure. The proteomic analysis also revealed the upregulation of proteins involved in the oxygen response and redox homeostasis, as the oxygen sensor PHD2/EGLN1 which promotes β-cell survival and differentiation by controlling both the HIF1α and NF-κB pathways (Figure 4.1b). The increased β-

cell differentiation can be also related to the decrease of YAP/TAZ expression in the cells grown on the ns-ZrO_x. Although the molecular mechanisms underlying this phenomenon need to be fully characterized, we can speculate that the deformation of the nuclear envelope induced by the actin cytoskeleton modifies the size and impedance of nuclear pore complexes promoting YAP/TAZ cytoplasmic retention and degradation (Figure 4.1c).

Furthermore, our data suggest that the nanostructured substrate not only promotes β-cell differentiation but also affects their metabolism, probably through multiple mechanisms that act in concert (Figure 4.1d). Firstly, we hypothesized that nanoscale features modulate cell metabolism by inducing changes in the expression of genes involved in this process and accordingly, the proteomic analysis revealed the upregulation of proteins involved in metabolic processes (GO:0044238). Even though it is partially true, emerging evidence revealed that the metabolic shift often precedes the modulation of gene expression and cell fate commitment (Bartolák-Suki et al., 2017; Feng and Kornmann, 2018). Our data indicate that changes in cell metabolism correlate with modifications of the cytoskeletal and mitochondrial organization, suggesting that the nanotopographical cues of the extracellular environment, by modulating the cytoskeleton organization, may affect cell metabolism by shaping mitochondrial morphology, dynamics and cristae formation. Accordingly, recent findings show that the actin cytoskeleton organization and the extracellular mechanical cues are two important regulators of mitochondrial activity, morphology and ATP production (Bartolák-Suki et al., 2017). An additional mechanism may be the detachment of metabolic enzymes from the cytoskeleton or adhesion complexes under mechanical stimulation. An interesting example is the mechanical regulation of phosphofructokinase (PFK), a glycolytic enzyme whose concentration is regulated by TRIM21 (Tripartite motif containing-21). On stiff substrates, stress fibers entrap TMR21 that is unable to target PFK for degradation, increasing the glycolytic flux (Park et al., 2020). A similar behavior was observed for aldolase, another glycolytic enzyme. Aldolase, which normally binds to F-actin, is released in response to actin polymerization and stress fibers formation, resulting in enhanced glycolysis (Kusakabe et al., 1997). Even though the expression of these enzymes do not change in our experimental conditions, we can speculate that cytoskeletal reorganization may affect the availability of other enzymes thereby regulating cell metabolism, but further experiments are necessary to confirm this hypothesis. Lastly, modification of cell shape and architecture induced by the reduction of cytoskeletal tension can modulate the cross-talk between intracellular organelles which, in turn, fine-tune the metabolic response.

Although several aspects of the mechanotransductive pathway need to be further investigated, our data demonstrate the crucial role of nanoscale features in regulating pancreatic β-cell differentiation, survival and function, and suggest, for the first time, a correlation between mechanical forces, mitochondrial function and β-cell metabolism.

In conclusion, by exploiting the unique properties of cluster-assembled films, we can gain a better understanding of the interaction between cells and nanostructures, and investigate how mechanical forces contribute to β-cell fate and function. This approach will provide valuable insight for developing substrates with well-defined nanotopography that can improve the efficacy of islet cells transplantation therapies. Furthermore, as β-cell dedifferentiation is a hallmark of diabetes pathogenesis, a better understanding of the molecular mechanisms promoting β-cell differentiation and function will enable us to define novel molecular targets of intervention for preventing β-cell failure in diabetes mellitus.

5. Supplementary figures and tables

5.1 Supplementary figures

Figure S1

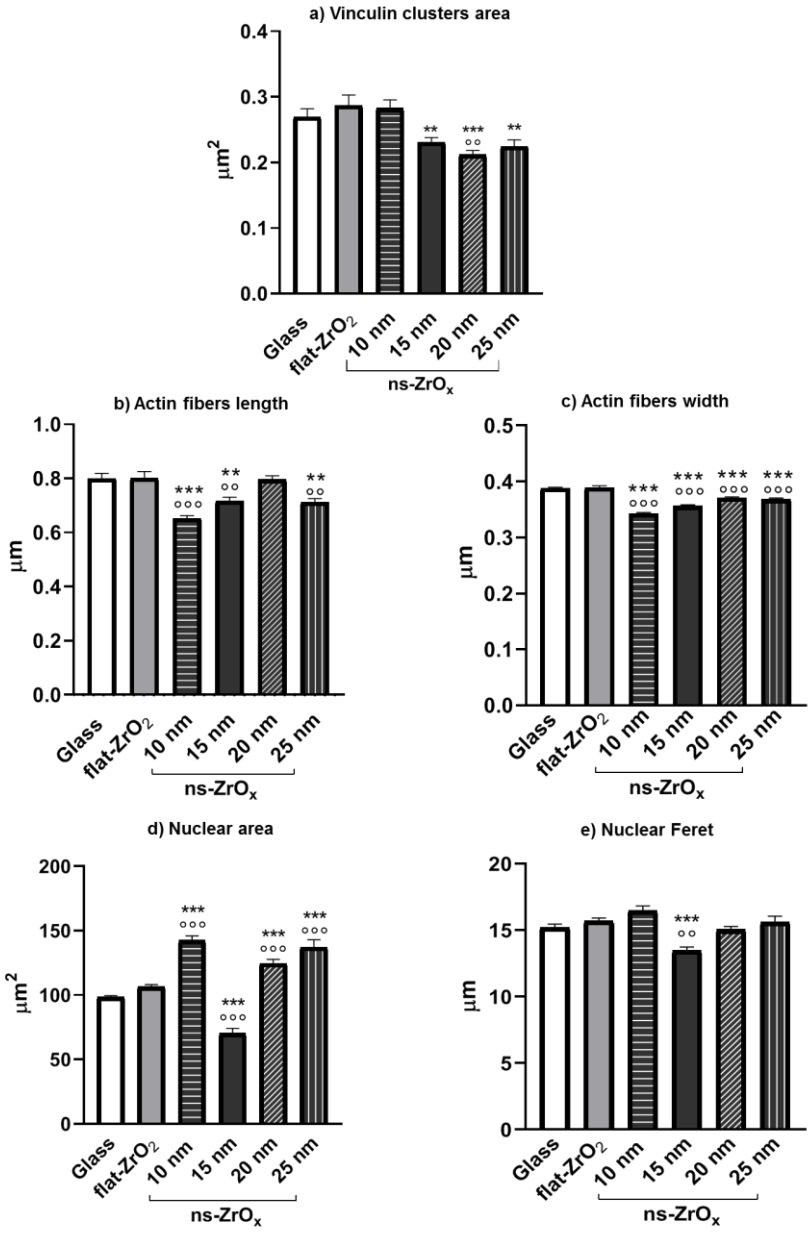

Figure S1. *Nanostructured zirconia substrates promote the activation of a mechanotransduction pathway in βTC3 cells. Cells grown on glass covers (Glass), flat- (flat-ZrO_2) or 10, 15, 20 and 25 nm nanostructured-zirconia (ns-ZrO_x) substrates for 3 days were triple stained with anti-vinculin antibody (green), phalloidin (actin, red), and DAPI (blue). The quantitative analysis of vinculin-positive area (a), cytoskeletal actin fibers length (b) and width (c), and (c) nuclear architecture area (d) and Feret's diameter (e) is reported. Bars illustrate the average responses ± SE (N = 30–40 cells for each substrate, three independent experiments (**p < 0.01, ***p < 0.005, ns-ZrO_x vs flat-ZrO_2; °°p < 0.01, °°°p < 0.005, ns-ZrO_x vs Glass).*

Figure S2

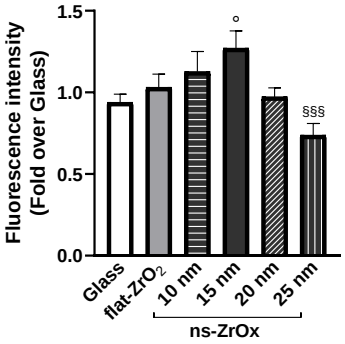

Figure S2. *βtc3 cells grown on the indicated substrates for 3 days were loaded with MitoSpy™ Orange CMTMRos and the mitochondrial membrane potential was measured by fluorimetry (551/576 nm Ex/Em). Bars illustrate the average responses (fluorescence intensity) ± SE (n = 4 independent experiments in triplicate) (°p < 0.05 ns-ZrO$_x$ vs Glass; §§§ p < 0.005 25nm vs 15 nm ns-ZrO$_x$).*

Figure S3

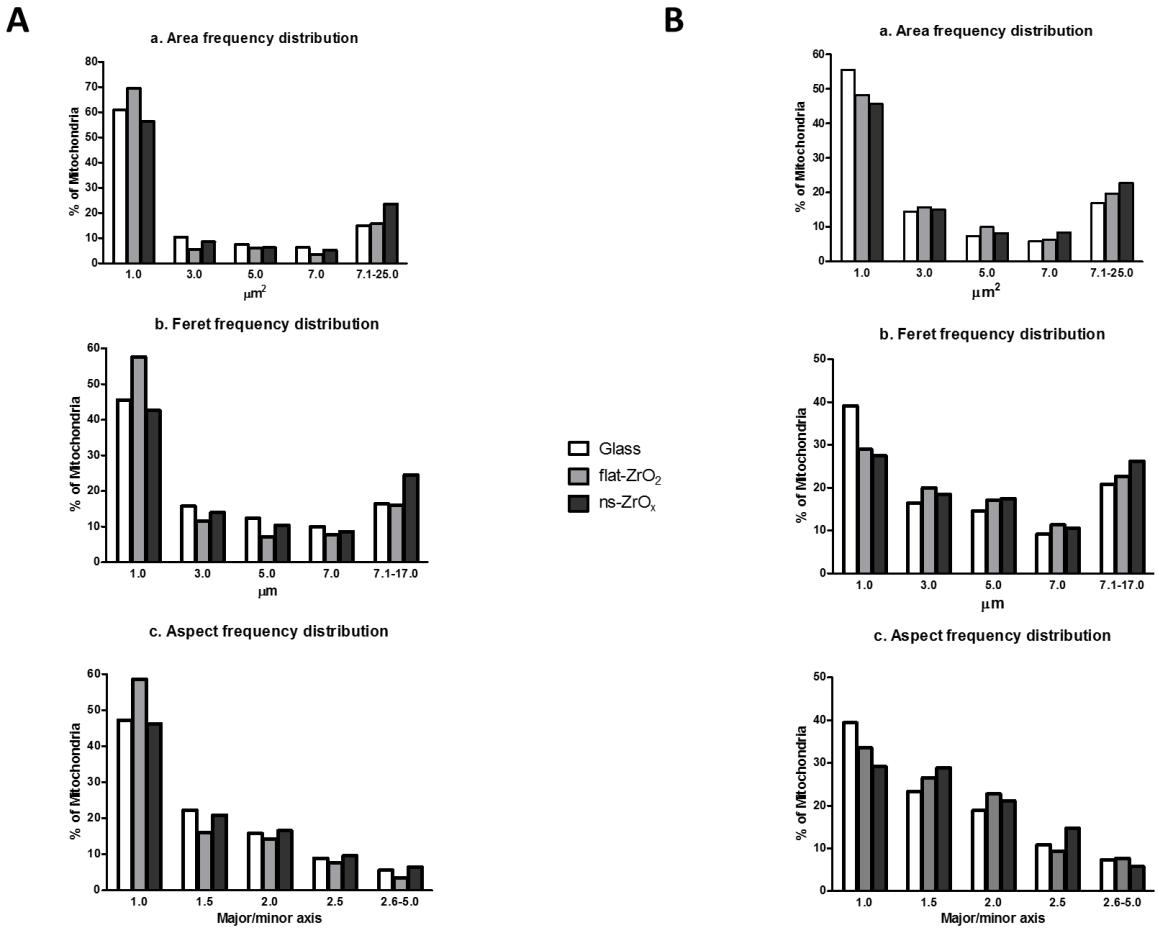

Figure S3. *Relative frequency distribution (percentage) of mitochondrial area (a), Feret's diameter (b) and aspect (c) in βtc3 (A) and INS1E (B) cells grown on the indicated substrate for 3 days.*

Figure S4

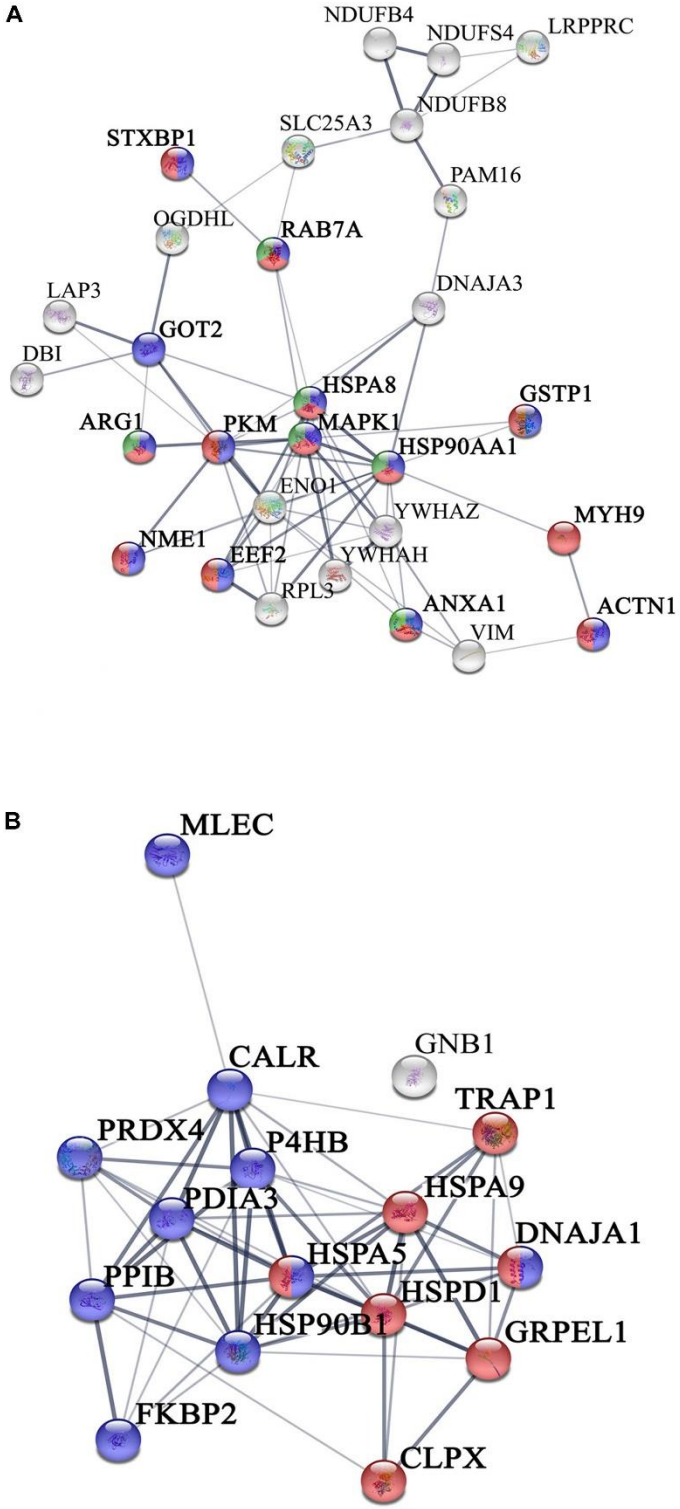

Figure S4. *Network interactions of the proteins differentially expressed in the comparison Glass vs ns-ZrO_x.* ***(A)*** *Proteins up regulated or only expressed in ns-ZrO_x and* ***(B)*** *proteins downregulated in ns-ZrO_x or exclusively expressed in Glass. Data sets were analyzed by String considering active interactions: text mining, experiments, and databases; edge thickness indicates "confidence." The proteins are indicated by the official gene symbol. Nodes are colored to highlight the more significant enrichment classification.* ***(A)*** *Proteins upregulated or only expressed in ns-ZrO_x involved in vesicle mediated transport (red), secretion (blue), and lysosome transport (green).* ***(B)*** *Network of proteins down regulated on ns-ZrO_x or only expressed on Glass involved in protein localization, folding, and processing in mitochondria (red) and ER (blue). (Laboratory of prof. Tedeschi)*

5.2 Supplementary tables

Table 1

Increased or only expressed in ns-ZrO_x

DAVID KEGG Pathway

Term	Count	*p*-Value	Genes	Fold Enrich.
Biosynthesis of antibiotics	7	1.7E-04	GOT2, PKM, ARG1, NME1, OGDHL, ALDH9A1, ENO1	7.8
Arginine and proline metabolism	4	1.0E-03	GOT2, LAP3, ARG1, ALDH9A1	19.0
Viral carcinogenesis	6	1.3E-03	PKM, MAPK1, YWHAZ, YWHAH, ACTN1, DNAJA3	6.9
Biosynthesis of amino acids	4	3.0E-03	GOT2, PKM, ARG1, ENO1	13.2
Alzheimer's disease	5	4.4E-03	MAPK1, NDUFB4, NDUFS4, NDUFB8, IDE	7.1
Carbon metabolism	4	1.0E-02	GOT2, PKM, OGDHL, ENO1	8.4
Metabolic pathways	11	1.8E-02	GOT2, PKM, LAP3, ARG1, NDUFB4, NDUFS4, NDUFB8, NME1, OGDHL, ALDH9A1, ENO1	2.1
Glycolysis/Gluconeogenesis	3	3.0E-02	PKM, ALDH9A1, ENO1	10.6

Decreased in ns-ZrO_x or only expressed in Glass

DAVID KEGG Pathway

Term	Count	*p*-value	Genes	
Citrate cycle (TCA cycle)	16	8.7E-22	SUCLG2, SUCLG1, CS, IDH3B, ACLY, OGDH, PCK2, PDHB, IDH3A, SDHA, DLD, IDH2, PDHA1, MDH2, PC, FH	42.7
Parkinson's disease	18	8.3E-13	NDUFA4, ATP5D, SLC25A5, SLC25A6, ATP5B, NDUFA13, UQCRQ, VDAC3, NDUFA12, VDAC1, SDHA, NDUFV1, NDUFV2, ATP5C1, COX6B1, ATP5A1, ATP5H, NDUFS2	10.1
Metabolic pathways	41	3.7E-10	ATP5D, ALDH18A1, GANAB, GLUD1, ATP5B, NFS1, OGDH, UQCRQ, PDHB, IVD, IDH2, COX6B1, PDHA1, RPN2, HADH, NDUFS2, ATP5H, FH, NDUFA4, SUCLG2, SUCLG1, CS, MAOB, NDUFA13, IDH3B, ACLY, PCK2, NDUFA12, IDH3A, SDHA, DHRS4, NNT, NDUFV1, NDUFV2, DLD, ATP5C1, ATP5A1, PCCB, OAT, MDH2, PC	2.7
Ribosome	15	8.2E-10	RPL13, RPLP2, RPS15A, RPS8, RPS18, MRPL12, RPS16, RPL23, RPL6, RPL34, RPS14, RPL8, RPL5, RPL4, RPL10A	8.8
Oxidative phosphorylation	14	6.6E-09	NDUFA4, SDHA, ATP5D, NDUFV1, ATP5B, NDUFV2, COX6B1, ATP5C1, NDUFA13, ATP5A1, UQCRQ, NDUFS2, ATP5H, NDUFA12	8.4
Alzheimer's disease	14	1.1E-07	NDUFA4, SDHA, ATP5D, NDUFV1, ATP5B, NDUFV2, COX6B1, ATP5C1, NDUFA13, ATP5A1, UQCRQ, NDUFS2, ATP5H, NDUFA12	6.7
Pyruvate metabolism	7	8.2E-06	DLD, PDHA1, PCK2, MDH2, PDHB, PC, FH	14.0
Protein processing in ER	10	2.2E-04	HYOU1, P4HB, HSP90B1, GANAB, PDIA3, RRBP1, DNAJA1, HSPA5, RPN2, CALR	4.7
Oxocarboxylic acid metabolism	4	1.1E-03	CS, IDH2, IDH3B, IDH3A	18.8
Biosynthesis of amino acids	6	1.9E-03	ALDH18A1, CS, IDH2, IDH3B, IDH3A, PC	6.7
Glyoxylate and dicarboxylate metabolism	4	4.3E-03	DLD, CS, PCCB, MDH2	11.9
Valine, leucine and isoleucine degradation	4	2.0E-02	IVD, DLD, HADH, PCCB	6.8
Propanoate metabolism	3	4.6E-02	SUCLG2, SUCLG1, PCCB	8.6
Glycolysis/Gluconeogenesis	4	5.0E-02	DLD, PDHA1, PCK2, PDHB	4.8

The Table reports the proteins statistically differentially expressed among the two different conditions (t-test $p \leq 0.05$). The column "Counts" indicate the number of genes present in each category. Functional grouping was based on $p \leq 0.05$ and at least three counts.

Table 1. *DAVID functional grouping in terms of KEGG Pathways of the mitochondrial proteins differentially expressed in cells grown in ns-ZrO_x in comparison with cells grown on Glass. (Laboratory of prof. Tedeschi)*

Table 2

DAVID Clustering				
Term	**Count**	***p*-Value**	**Genes**	**Fold Enrich.**
Annotation Cluster 1 Enrichment Score: 17.5				
Citrate cycle (TCA cycle)	16	8.7E-22	SUCLG2, SUCLG1, CS, IDH3B, ACLY, OGDH, PCK2, PDHB, IDH3A, SDHA, DLD, IDH2, PDHA1, MDH2, PC, FH	42.7
tricarboxylic acid cycle	14	6.2E-21	SUCLG2, SUCLG1, CS, IDH3B, OGDH, PDHB, IDH3A, SDHA, NNT, DLD, IDH2, PDHA1, MDH2, FH	64.9
Annotation Cluster 2 Enrichment Score: 10.9				
SRP-dependent cotranslational protein targeting to membrane	14	1.9E-13	RPL13, RPLP2, RPS15A, RPS8, RPS18, RPL23, RPS16, RPL6, RPL34, RPS14, RPL8, RPL5, RPL4, RPL10A	20.0
structural constituent of ribosome	18	6.5E-13	RPL13, SLC25A5, SLC25A6, RPS15A, RPLP2, RPS8, RPS18, MRPL12, SLC25A25, RPS16, RPL23, RPL6, RPL34, RPS14, RPL8, RPL5, RPL4, RPL10A	10.9
Ribosomal protein	16	7.8E-13	RPL13, RPLP2, RPS15A, RPS8, RPS18, MRPL12, RPS16, RPL23, RPL6, RPL34, RPS14, RPL8, RPL5, MRPL48, RPL4, RPL10A	13.6
translation	18	5.1E-12	RPL13, RRBP1, SLC25A5, SLC25A6, RPS15A, RPLP2, RPS8, RPS18, SLC25A25, RPS16, RPL23, RPL6, RPL34, RPS14, RPL8, RPL5, RPL4, RPL10A	9.6
Annotation Cluster 3 Enrichment Score: 9.3				
Parkinson's disease, Huntington's disease	18	8.3E-13	NDUFA4, ATP5D, SLC25A5, SLC25A6, ATP5B, NDUFA13, UQCRQ, VDAC3, NDUFA12, VDAC1, SDHA, NDUFV1, NDUFV2, ATP5C1, COX6B1, ATP5A1, ATP5H, NDUFS2	10.1
Oxidative phosphorylation	14	6.6E-09	NDUFA4, SDHA, ATP5D, NDUFV1, ATP5B, NDUFV2, COX6B1, ATP5C1, NDUFA13, ATP5A1, UQCRQ, NDUFS2, ATP5H, NDUFA12	8.4
Annotation Cluster 4 Enrichment Score: 5.7				
nucleotide phosphate-binding region: FAD	7	2.9E-06	SDHA, GPD2, IVD, AIFM1, DLD, ETFDH, ETFA	17.4
Annotation Cluster 5 Enrichment Score: 5.1				
mitochondrial electron transport, NADH to ubiquinone	7	1.5E-06	NDUFA4, NDUFV1, NDUFV2, DLD, NDUFA13, NDUFS2, NDUFA12	19.2
Annotation Cluster 6 Enrichment Score: 4.6				
mitochondrial proton-transporting ATP synthase	6	2.8E-07	ATP5D, USMG5, ATP5B, ATP5C1, ATP5A1, ATP5H	40.7
Annotation Cluster 7 Enrichment Score: 3.8				
Pyruvate	5	3.4E-06	DLD, PDHA1, PCK2, PDHB, PC	46.2
Glycolysis/Gluconeogenesis	4	5.0E-02	DLD, PDHA1, PCK2, PDHB	4.8
Annotation Cluster 8 Enrichment Score: 3.0				
protein import into mitochondrial matrix	4	2.5E-04	GRPEL1, TIMM17A, TOMM20, TIMM23B	31.6
~P-P-bond-hydrolysis-driven protein transmembrane transporter activity	3	1.5E-03	TIMM17A, TOMM20, TIMM23B	50.2

The Table reports the proteins down regulated in ns-ZrO_x or exclusively expressed on Glass (t-test $p \leq 0.05$). The column "Counts" indicates the number of genes present in each category. Functional grouping was based on $p \leq 0.05$ and at least three counts.

Table 2. *DAVID functional grouping of the mitochondrial proteins down regulated in ns-ZrO_x or exclusively expressed on Glass in the comparison ns-ZrO_x vs Glass. (Laboratory of prof. Tedeschi)*

Table 3

Classification		Gene ID	Protein name	
TCA Cycle		PDHB	Pyruvate dehydrogenase E1 component subunit beta, mitoch.	↓
		SUCLG1	Succinate-CoA ligase [ADP/GDP-forming] sub.alpha mitoch	↓
		OGDH	2-oxoglutarate dehydrogenase, mitochondrial	↓
		IDH3A	Isocitrate dehydrogenase [NAD] subunit alpha, mitochondrial	↓
		CS	Citrate synthase	↓
		IDH3B	Isocitrate dehydrogenase [NAD] subunit beta, mitochondrial	↓
		PDHA1	Pyruvate dehydr. E1 comp. sub, alpha, somatic form, mitoch.	↓
		MDH2	Malate dehydrogenase, mitochondrial	↓
		SDHA	Succinate dehydr. [ubiqu,] flavoprot. subunit, mitochondrial	↓
		SUCLG2	Succinate-CoA ligase [GDP-forming] subunit beta, mitochon.	↓
		FH	Fumarate hydratase, mitochondrial	↓
		MDH1	Malate dehydrogenase, cytoplasmic	↓
		ACLY	ATP citrate lyase	↓
		DLD	dihydrolipoamide dehydrogenase	↓
		IDH2	isocitrate dehydrogenase (NADP(+)) 2	↓
		IDH3G	isocitrate dehydrogenase (NAD(+)) 3 non-catalytic sub. gamma	↓
		OGDHL	oxoglutarate dehydrogenase like	↑
		PC	pyruvate carboxylase	↓
		PCK2	phosphoenolpyruvate carboxykinase 2, mitochondrial	↓
		SUCLA2	succinate-CoA ligase ADP-forming beta subunit	
Mitochondrial respiratory chain	complex I	NDUFB8	NADH dehydr.[ubiq.] 1 beta subcomplex subunit 8, mitoch.	↑
	complex I	SLC25A3	Phosphate carrier protein, mitochondrial	↑
	complex I	NDUFA12	NADH dehydr. [ubiquinone] 1 alpha subcomplex subunit 12	↓
	complex I	NDUFV2	NADH dehydr. [ubiquinone] flavoprotein 2, mitochondrial	↓
	complex I	NDUFA13	NADH dehydr. [ubiquinone] 1 alpha subcomplex subunit 13	↓
	complex I	NDUFS2	NADH dehydr. [ubiquinone] iron-sulfur protein 2, mitoch.	↓
	NADH:ubiq core subunit	NDUFS8	NADH:ubiquinone oxidoreductase core subunit S8	↑
		NDUFV1	NADH:ubiquinone oxidoreductase core subunit V1	↓
	NADH:ubiq. supernumerary subunits	NDUFB4	NADH:ubiquinone oxidoreductase subunit B4	↑
		NDUFS4	NADH:ubiquinone oxidoreductase subunit S4	↑
	complex II	SDHA	Succinate dehydr. [ubiquinone] flavoprotein subunit, mitoch	↓
	complex III	UQCRQ	Cytochrome b-c1 complex subunit 8	↓
	complex IV	COA3	Cytochrome c oxidase assembly factor 3 homolog, mitocho.	↓
	complex IV	COX6B1	Cytochrome c oxidase subunit 6B1	↓
	complex IV	NFUFA4	Cytochrome c oxidase subunit NDUFA4	↑
	complex IV	NDUFA4	Cytochrome c oxidase subunit NDUFA4	↓
	complex IV	MT-CO2	mitochondrially encoded cytochrome c oxidase II	↓
	complex V	ATP5B	ATP synthase subunit beta, mitochondrial	↓
	complex V	ATP5C1	ATP synthase subunit gamma, mitochondrial	↓
	complex V	ATP5A1	ATP synthase subunit alpha, mitochondrial	↓
	complex V	ATP5D	ATP synthase subunit delta, mitochondrial	↓
	Transporter IN	SLC25A5	ADP/ATP translocase 2	↓

*All the proteins down regulated in cells grown on ns-ZrO_x or exclusively expressed in Glass are listed in **Supplementary Table S2**. **Table 3** reports only the proteins of **Supplementary Table S2** that are described as involved in TCA cycle and the complex of the aerobic respiratory.*

Table 3. *List of all the mitochondrial proteins differentially regulated in the comparison ns-ZrO_x vs Glass that are involved in TCA cycle and the complex of the aerobic respiratory chain. (Laboratory of prof. Tedeschi)*

6. References

Aamodt, K.I., and Powers, A.C. (2017). Signals in the pancreatic islet microenvironment influence β-cell proliferation. Diabetes Obes Metab *19 Suppl 1*, 124–136.

Alberio, T., Pieroni, L., Ronci, M., Banfi, C., Bongarzone, I., Bottoni, P., Brioschi, M., Caterino, M., Chinello, C., Cormio, A., et al. (2017). Toward the Standardization of Mitochondrial Proteomics: The Italian Mitochondrial Human Proteome Project Initiative. J Proteome Res *16*, 4319–4329.

Alymatiri, C.M., Kouskoura, M.G., and Markopoulou, C.K. (2015). Decoding the signal response of steroids in electrospray ionization mode (ESI-MS). Anal. Methods *7*, 10433–10444.

American Diabetes Association (2014). Diagnosis and Classification of Diabetes Mellitus. Diabetes Care *37*, S81–S90.

Anesti, V., and Scorrano, L. (2006). The relationship between mitochondrial shape and function and the cytoskeleton. Biochim. Biophys. Acta *1757*, 692–699.

Aragona, M., Panciera, T., Manfrin, A., Giulitti, S., Michielin, F., Elvassore, N., Dupont, S., and Piccolo, S. (2013). A mechanical checkpoint controls multicellular growth through YAP/TAZ regulation by actin-processing factors. Cell *154*, 1047–1059.

Ardestani, A., Lupse, B., and Maedler, K. (2018). Hippo Signaling: Key Emerging Pathway in Cellular and Whole-Body Metabolism. Trends Endocrinol Metab *29*, 492–509.

Argentati, C., Morena, F., Tortorella, I., Bazzucchi, M., Porcellati, S., Emiliani, C., and Martino, S. (2019). Insight into Mechanobiology: How Stem Cells Feel Mechanical Forces and Orchestrate Biological Functions. IJMS *20*, 5337.

Asfari, M., Janjic, D., Meda, P., Li, G., Halban, P.A., and Wollheim, C.B. (1992). Establishment of 2-mercaptoethanol-dependent differentiated insulin-secreting cell lines. Endocrinology *130*, 167–178.

Ashburner, M., Ball, C.A., Blake, J.A., Botstein, D., Butler, H., Cherry, J.M., Davis, A.P., Dolinski, K., Dwight, S.S., Eppig, J.T., et al. (2000). Gene ontology: tool for the unification of biology. The Gene Ontology Consortium. Nature Genetics *25*, 25–29.

Assmann, A., Hinault, C., and Kulkarni, R.N. (2009). Growth factor control of pancreatic islet regeneration and function. Pediatr Diabetes *10*, 14–32.

Atchison, N.A., Fan, W., Papas, K.K., Hering, B.J., Tsapatsis, M., and Kokkoli, E. (2010). Binding of the fibronectin-mimetic peptide, PR_b, to alpha5beta1 on pig islet cells increases fibronectin production and facilitates internalization of PR_b functionalized liposomes. Langmuir *26*, 14081–14088.

Ballinger, W.F., and Lacy, P.E. (1972). Transplantation of intact pancreatic islets in rats. Surgery *72*, 175–186.

Ban, T., Ishihara, T., Kohno, H., Saita, S., Ichimura, A., Maenaka, K., Oka, T., Mihara, K., and Ishihara, N. (2017). Molecular basis of selective mitochondrial fusion by heterotypic action between OPA1 and cardiolipin. Nat Cell Biol *19*, 856–863.

Bartel, D.P. (2009). MicroRNAs: target recognition and regulatory functions. Cell *136*, 215–233.

Bartolák-Suki, E., Imsirovic, J., Nishibori, Y., Krishnan, R., and Suki, B. (2017). Regulation of Mitochondrial Structure and Dynamics by the Cytoskeleton and Mechanical Factors. Int J Mol Sci *18*.

Beattie, G.M., Rubin, J.S., Mally, M.I., Otonkoski, T., and Hayek, A. (1996). Regulation of proliferation and differentiation of human fetal pancreatic islet cells by extracellular matrix, hepatocyte growth factor, and cell-cell contact. Diabetes *45*, 1223–1228.

Ben-Othman, N., Vieira, A., Courtney, M., Record, F., Gjernes, E., Avolio, F., Hadzic, B., Druelle, N., Napolitano, T., Navarro-Sanz, S., et al. (2017). Long-Term GABA Administration Induces Alpha Cell-Mediated Beta-like Cell Neogenesis. Cell *168*, 73-85.e11.

Bettinger, C.J., Langer, R., and Borenstein, J.T. (2009). Engineering Substrate Topography at the Micro- and Nanoscale to Control Cell Function. Angew. Chem. Int. Ed. *48*, 5406–5415.

Boeri, L., Albani, D., Raimondi, M.T., and Jacchetti, E. (2019). Mechanical regulation of nucleocytoplasmic translocation in mesenchymal stem cells: characterization and methods for investigation. Biophys Rev *11*, 817–831.

Boland, B.B., Rhodes, C.J., and Grimsby, J.S. (2017). The dynamic plasticity of insulin production in β-cells. Mol Metab *6*, 958–973.

Bongiorno, G., Lenardi, C., Ducati, C., Agostino, R.G., Caruso, T., Amati, M., Blomqvist, M., Barborini, E., Piseri, P., La Rosa, S., et al. (2005). Nanocrystalline Metal/Carbon Composites Produced by Supersonic Cluster Beam Deposition. J. Nanosci. Nanotech. *5*, 1072–1080.

Bonner-Weir, S. (1988). Morphological evidence for pancreatic polarity of beta-cell within islets of Langerhans. Diabetes *37*, 616–621.

Borghi, F., Sogne, E., Lenardi, C., Podestà, A., Merlini, M., Ducati, C., and Milani, P. (2016). Cluster-assembled cubic zirconia films with tunable and stable nanoscale morphology against thermal annealing. Journal of Applied Physics *120*, 055302.

Borghi, F., Scaparra, B., Paternoster, C., Milani, P., and Podestà, A. (2018). Electrostatic Double-Layer Interaction at the Surface of Rough Cluster-Assembled Films: The Case of Nanostructured Zirconia. Langmuir *34*, 10230–10242.

Bouzid, T., Kim, E., Riehl, B.D., Esfahani, A.M., Rosenbohm, J., Yang, R., Duan, B., and Lim, J.Y. (2019). The LINC complex, mechanotransduction, and mesenchymal stem cell function and fate. J Biol Eng *13*, 68.

Brafman, D.A. (2013). Constructing stem cell microenvironments using bioengineering approaches. Physiol. Genomics *45*, 1123–1135.

Brammer, K.S., Choi, C., Frandsen, C.J., Oh, S., and Jin, S. (2011). Hydrophobic nanopillars initiate mesenchymal stem cell aggregation and osteo-differentiation. Acta Biomater *7*, 683–690.

Brandt, T., Cavellini, L., Kühlbrandt, W., and Cohen, M.M. (2016). A mitofusin-dependent docking ring complex triggers mitochondrial fusion in vitro. ELife *5*, e14618.

Brissova, M., Shostak, A., Shiota, M., Wiebe, P.O., Poffenberger, G., Kantz, J., Chen, Z., Carr, C., Jerome, W.G., Chen, J., et al. (2006). Pancreatic Islet Production of Vascular Endothelial Growth Factor-A Is Essential for Islet Vascularization, Revascularization, and Function. Diabetes *55*, 2974–2985.

Brunicardi, F.C., Stagner, J., Bonner-Weir, S., Wayland, H., Kleinman, R., Livingston, E., Guth, P., Menger, M., McCuskey, R., Intaglietta, M., et al. (1996). Microcirculation of the islets of Langerhans. Long Beach Veterans Administration Regional Medical Education Center Symposium. Diabetes *45*, 385–392.

Bushati, N., and Cohen, S.M. (2007). microRNA functions. Annu Rev Cell Dev Biol *23*, 175–205.

Butler, A.E., Janson, J., Bonner-Weir, S., Ritzel, R., Rizza, R.A., and Butler, P.C. (2003). Beta-cell deficit and increased beta-cell apoptosis in humans with type 2 diabetes. Diabetes *52*, 102–110.

Cahalan, S.M., Lukacs, V., Ranade, S.S., Chien, S., Bandell, M., and Patapoutian, A. (2015). Piezo1 links mechanical forces to red blood cell volume. Elife *4*.

Cano, D.A., Sekine, S., and Hebrok, M. (2006). Primary cilia deletion in pancreatic epithelial cells results in cyst formation and pancreatitis. Gastroenterology *131*, 1856–1869.

Cao, H., Xie, Y., and Chen, X. (2015). Type 2 diabetes diminishes the benefits of dietary antioxidants: Evidence from the different free radical scavenging potential. Food Chem *186*, 106–112.

Carolina Solis-Herrera, Curtis Triplitt, Charles Reasner, Ralph A DeFronzo, and Eugenio Cersosimo (2018). Classification of Diabetes Mellitus.

Cavelti-Weder, C., Zumsteg, A., Li, W., and Zhou, Q. (2017). Reprogramming of Pancreatic Acinar Cells to Functional Beta Cells by In Vivo Transduction of a Polycistronic Construct Containing Pdx1, Ngn3, MafA in Mice. Current Protocols in Stem Cell Biology *40*.

Cebola, I., Rodríguez-Seguí, S.A., Cho, C.H.-H., Bessa, J., Rovira, M., Luengo, M., Chhatriwala, M., Berry, A., Ponsa-Cobas, J., Maestro, M.A., et al. (2015). TEAD and YAP regulate the enhancer network of human embryonic pancreatic progenitors. Nat. Cell Biol. *17*, 615–626.

Chakrabarti, R., Ji, W.-K., Stan, R.V., de Juan Sanz, J., Ryan, T.A., and Higgs, H.N. (2018). INF2-mediated actin polymerization at the ER stimulates mitochondrial calcium uptake, inner membrane constriction, and division. Journal of Cell Biology *217*, 251–268.

Chakravarthy, H., Gu, X., Enge, M., Dai, X., Wang, Y., Damond, N., Downie, C., Liu, K., Wang, J., Xing, Y., et al. (2017). Converting Adult Pancreatic Islet α Cells into β Cells by Targeting Both Dnmt1 and Arx. Cell Metab *25*, 622–634.

Chalfie, M. (2009). Neurosensory mechanotransduction. Nat Rev Mol Cell Biol *10*, 44–52.

Chambliss, A.B., Khatau, S.B., Erdenberger, N., Robinson, D.K., Hodzic, D., Longmore, G.D., and Wirtz, D. (2013). The LINC-anchored actin cap connects the extracellular milieu to the nucleus for ultrafast mechanotransduction. Sci Rep *3*, 1087.

Chen, H., Gu, X., Liu, Y., Wang, J., Wirt, S.E., Bottino, R., Schorle, H., Sage, J., and Kim, S.K. (2011). PDGF signalling controls age-dependent proliferation in pancreatic β-cells. Nature *478*, 349–355.

Chen, W., Villa-Diaz, L.G., Sun, Y., Weng, S., Kim, J.K., Lam, R.H.W., Han, L., Fan, R., Krebsbach, P.H., and Fu, J. (2012). Nanotopography influences adhesion, spreading, and self-renewal of human embryonic stem cells. ACS Nano *6*, 4094–4103.

Chin, G.S., Lee, S., Hsu, M., Liu, W., Kim, W.J., Levinson, H., and Longaker, M.T. (2001). Discoidin domain receptors and their ligand, collagen, are temporally regulated in fetal rat fibroblasts in vitro. Plast. Reconstr. Surg. *107*, 769–776.

Cho, B., Cho, H.M., Jo, Y., Kim, H.D., Song, M., Moon, C., Kim, H., Kim, K., Sesaki, H., Rhyu, I.J., et al. (2017). Constriction of the mitochondrial inner compartment is a priming event for mitochondrial division. Nat Commun *8*, 15754.

Cho, N.H., Shaw, J.E., Karuranga, S., Huang, Y., da Rocha Fernandes, J.D., Ohlrogge, A.W., and Malanda, B. (2018). IDF Diabetes Atlas: Global estimates of diabetes prevalence for 2017 and projections for 2045. Diabetes Research and Clinical Practice *138*, 271–281.

Christopherson, G.T., Song, H., and Mao, H.-Q. (2009). The influence of fiber diameter of electrospun substrates on neural stem cell differentiation and proliferation. Biomaterials *30*, 556–564.

Ciobanasu, C., Wang, H., Henriot, V., Mathieu, C., Fente, A., Csillag, S., Vigouroux, C., Faivre, B., and Le Clainche, C. (2018). Integrin-bound talin head inhibits actin filament barbed-end elongation. J. Biol. Chem. *293*, 2586–2596.

Cirulli, V., Beattie, G.M., Klier, G., Ellisman, M., Ricordi, C., Quaranta, V., Frasier, F., Ishii, J.K., Hayek, A., and Salomon, D.R. (2000). Expression and function of alpha(v)beta(3) and alpha(v)beta(5) integrins in the developing pancreas: roles in the adhesion and migration of putative endocrine progenitor cells. J. Cell Biol. *150*, 1445–1460.

Clark, K., Middelbeek, J., and van Leeuwen, F.N. (2008). Interplay between TRP channels and the cytoskeleton in health and disease. Eur. J. Cell Biol. *87*, 631–640.

Clayton, H.W., Osipovich, A.B., Stancill, J.S., Schneider, J.D., Vianna, P.G., Shanks, C.M., Yuan, W., Gu, G., Manduchi, E., Stoeckert, C.J., et al. (2016). Pancreatic Inflammation Redirects Acinar to β Cell Reprogramming. Cell Reports *17*, 2028–2041.

ClinicalTrials.gov (2013). US National Library of Medidicine.

ClinicalTrials.gov (2014). US National Library of Medidicine.

ClinicalTrials.gov (2016). US National Library of Medidicine.

ClinicalTrials.gov (2016b). US National Library of Medidicine.

ClinicalTrials.gov (2016c). US National Library of Medidicine.

Cogliati, S., Enriquez, J.A., and Scorrano, L. (2016). Mitochondrial Cristae: Where Beauty Meets Functionality. Trends Biochem Sci *41*, 261–273.

Cohen, D.J., St Martin, L., Christensen, L.L., Bloom, R.D., and Sung, R.S. (2006). Kidney and pancreas transplantation in the United States, 1995-2004. Am J Transplant *6*, 1153–1169.

Collombat, P., Xu, X., Ravassard, P., Sosa-Pineda, B., Dussaud, S., Billestrup, N., Madsen, O.D., Serup, P., Heimberg, H., and Mansouri, A. (2009). The Ectopic Expression of Pax4 in the Mouse Pancreas Converts Progenitor Cells into α and Subsequently β Cells. Cell *138*, 449–462.

Colsoul, B., Vennekens, R., and Nilius, B. (2011). Transient receptor potential cation channels in pancreatic β cells. Rev. Physiol. Biochem. Pharmacol. *161*, 87–110.

Cortelli, P., Terlizzi, R., Capellari, S., and Benarroch, E. (2012). Nuclear lamins: functions and clinical implications. Neurology *79*, 1726–1731.

Crisp, M., Liu, Q., Roux, K., Rattner, J.B., Shanahan, C., Burke, B., Stahl, P.D., and Hodzic, D. (2006). Coupling of the nucleus and cytoplasm: role of the LINC complex. J. Cell Biol. *172*, 41–53.

Csordás, G., Várnai, P., Golenár, T., Roy, S., Purkins, G., Schneider, T.G., Balla, T., and Hajnóczky, G. (2010). Imaging Interorganelle Contacts and Local Calcium Dynamics at the ER-Mitochondrial Interface. Molecular Cell *39*, 121–132.

Cumaoğlu, A., Rackova, L., Stefek, M., Kartal, M., Maechler, P., and Karasu, C. (2011). Effects of olive leaf polyphenols against H_2O_2 toxicity in insulin secreting β-cells. Acta Biochim. Pol. *58*, 45–50.

Cummins, E.P., Berra, E., Comerford, K.M., Ginouves, A., Fitzgerald, K.T., Seeballuck, F., Godson, C., Nielsen, J.E., Moynagh, P., Pouyssegur, J., et al. (2006). Prolyl hydroxylase-1 negatively regulates I B kinase-beta, giving insight into hypoxia-induced NF B activity. Proceedings of the National Academy of Sciences *103*, 18154–18159.

Curtis, A.S., and Varde, M. (1964). CONTROL OF CELL BEHAVIOR: TOPOLOGICAL FACTORS. J. Natl. Cancer Inst. *33*, 15–26.

Dahl, K.N., Ribeiro, A.J.S., and Lammerding, J. (2008). Nuclear shape, mechanics, and mechanotransduction. Circ. Res. *102*, 1307–1318.

Dalby, M.J., Gadegaard, N., Tare, R., Andar, A., Riehle, M.O., Herzyk, P., Wilkinson, C.D.W., and Oreffo, R.O.C. (2007). The control of human mesenchymal cell differentiation using nanoscale symmetry and disorder. Nature Mater *6*, 997–1003.

Dalby, M.J., Gadegaard, N., and Oreffo, R.O.C. (2014). Harnessing nanotopography and integrin-matrix interactions to influence stem cell fate. Nat Mater *13*, 558–569.

D'Angelo, M., Benedetti, E., Tupone, M.G., Catanesi, M., Castelli, V., Antonosante, A., and Cimini, A. (2019). The Role of Stiffness in Cell Reprogramming: A Potential Role for Biomaterials in Inducing Tissue Regeneration. Cells *8*, 1036.

D'Angelo, A., Godeau, A.L., and Solon, J. (2019). A New Player in Tissue Mechanics: MicroRNA Control of Mechanical Homeostasis. Developmental Cell *48*, 596–598.

Da Silva Xavier, G., Loder, M.K., McDonald, A., Tarasov, A.I., Carzaniga, R., Kronenberger, K., Barg, S., and Rutter, G.A. (2009). TCF7L2 regulates late events in insulin secretion from pancreatic islet beta-cells. Diabetes *58*, 894–905.

Dass, C. (2007). Fundamentals of Contemporary Mass Spectrometry (Hoboken, NJ, USA: John Wiley & Sons, Inc.).

Del Rio, A., Perez-Jimenez, R., Liu, R., Roca-Cusachs, P., Fernandez, J.M., and Sheetz, M.P. (2009). Stretching single talin rod molecules activates vinculin binding. Science *323*, 638–641.

Desai, T., and Shea, L.D. (2017). Advances in islet encapsulation technologies. Nat Rev Drug Discov *16*, 338–350.

Di Cairano, E.S., Davalli, A.M., Perego, L., Sala, S., Sacchi, V.F., La Rosa, S., Finzi, G., Placidi, C., Capella, C., Conti, P., et al. (2011). The Glial Glutamate Transporter 1 (GLT1) Is Expressed by Pancreatic β-Cells and Prevents Glutamate-induced β-Cell Death. J. Biol. Chem. *286*, 14007–14018.

Di Cairano, E.S., Moretti, S., Marciani, P., Sacchi, V.F., Castagna, M., Davalli, A., Folli, F., and Perego, C. (2016). Neurotransmitters and Neuropeptides: New Players in the Control of Islet of Langerhans' Cell Mass and Function. J. Cell. Physiol. *231*, 756–767.

Di Cio, S., and Gautrot, J.E. (2016). Cell sensing of physical properties at the nanoscale: Mechanisms and control of cell adhesion and phenotype. Acta Biomaterialia *30*, 26–48.

Diaferia, G.R., Jimenez-Caliani, A.J., Ranjitkar, P., Yang, W., Hardiman, G., Rhodes, C.J., Crisa, L., and Cirulli, V. (2013). 1 integrin is a crucial regulator of pancreatic -cell expansion. Development *140*, 3360–3372.

DiIorio, P., Rittenhouse, A.R., Bortell, R., and Jurczyk, A. (2014). Role of cilia in normal pancreas function and in diseased states: ROLE OF CILIA IN PANCREAS. Birth Defects Research Part C: Embryo Today: Reviews *102*, 126–138.

DiMeglio, L.A., Evans-Molina, C., and Oram, R.A. (2018). Type 1 diabetes. The Lancet *391*, 2449–2462.

Discher, D.E., Janmey, P., and Wang, Y.-L. (2005). Tissue cells feel and respond to the stiffness of their substrate. Science *310*, 1139–1143.

Dittmer, T.A., and Misteli, T. (2011). The lamin protein family. Genome Biol *12*, 222.

Donnaloja, F., Jacchetti, E., Soncini, M., and Raimondi, M.T. (2019). Mechanosensing at the Nuclear Envelope by Nuclear Pore Complex Stretch Activation and Its Effect in Physiology and Pathology. Front. Physiol. *10*, 896.

Donnaloja, F., Carnevali, F., Jacchetti, E., and Raimondi, M.T. (2020). Lamin A/C Mechanotransduction in Laminopathies. Cells *9*, 1306.

Donnelly, H., Salmeron-Sanchez, M., and Dalby, M.J. (2018). Designing stem cell niches for differentiation and self-renewal. J R Soc Interface *15*.

Doyle, A.D., and Yamada, K.M. (2016). Mechanosensing via cell-matrix adhesions in 3D microenvironments. Experimental Cell Research *343*, 60–66.

DuFort, C.C., Paszek, M.J., and Weaver, V.M. (2011). Balancing forces: architectural control of mechanotransduction. Nat Rev Mol Cell Biol *12*, 308–319.

Dunn, S.L., and Olmedo, M.L. (2016). Mechanotransduction: Relevance to Physical Therapist Practice-Understanding Our Ability to Affect Genetic Expression Through Mechanical Forces. Phys Ther *96*, 712–721.

Dupont, S. (2016). Role of YAP/TAZ in cell-matrix adhesion-mediated signalling and mechanotransduction. Experimental Cell Research *343*, 42–53.

Dupont, S., Morsut, L., Aragona, M., Enzo, E., Giulitti, S., Cordenonsi, M., Zanconato, F., Le Digabel, J., Forcato, M., Bicciato, S., et al. (2011). Role of YAP/TAZ in mechanotransduction. Nature *474*, 179–183.

Efrat, S., Linde, S., Kofod, H., Spector, D., Delannoy, M., Grant, S., Hanahan, D., and Baekkeskov, S. (1988). Beta-cell lines derived from transgenic mice expressing a hybrid insulin gene-oncogene. Proc. Natl. Acad. Sci. U.S.A. *85*, 9037–9041.

Eliasson, L. (2017). The small RNA miR-375 – a pancreatic islet abundant miRNA with multiple roles in endocrine beta cell function. Molecular and Cellular Endocrinology *456*, 95–101.

Eliasson, L., and Esguerra, J.L.S. (2020). MicroRNA Networks in Pancreatic Islet Cells: Normal Function and Type 2 Diabetes. Diabetes *69*, 804–812.

Eliasson, L., and Regazzi, R. (2020). Micro(RNA) Management and Mismanagement of the Islet. Journal of Molecular Biology *432*, 1419–1428.

Elosegui-Artola, A., Andreu, I., Beedle, A.E.M., Lezamiz, A., Uroz, M., Kosmalska, A.J., Oria, R., Kechagia, J.Z., Rico-Lastres, P., Le Roux, A.-L., et al. (2017). Force Triggers YAP Nuclear Entry by Regulating Transport across Nuclear Pores. Cell *171*, 1397-1410.e14.

Engler, A.J., Sen, S., Sweeney, H.L., and Discher, D.E. (2006). Matrix elasticity directs stem cell lineage specification. Cell *126*, 677–689.

Enzo, E., Santinon, G., Pocaterra, A., Aragona, M., Bresolin, S., Forcato, M., Grifoni, D., Pession, A., Zanconato, F., Guzzo, G., et al. (2015). Aerobic glycolysis tunes YAP / TAZ transcriptional activity. EMBO J *34*, 1349–1370.

Ernkvist, M., Aase, K., Ukomadu, C., Wohlschlegel, J., Blackman, R., Veitonmäki, N., Bratt, A., Dutta, A., and Holmgren, L. (2006). p130-Angiomotin associates to actin and controls endothelial cell shape: p130-Angiomotin controls cell shape. FEBS Journal *273*, 2000–2011.

Esguerra, J.L.S., Nagao, M., Ofori, J.K., Wendt, A., and Eliasson, L. (2018). MicroRNAs in islet hormone secretion. Diabetes Obes Metab *20 Suppl 2*, 11–19.

Fabregat, A., Sidiropoulos, K., Garapati, P., Gillespie, M., Hausmann, K., Haw, R., Jassal, B., Jupe, S., Korninger, F., McKay, S., et al. (2016). The Reactome pathway Knowledgebase. Nucleic Acids Research *44*, D481-487.

Feng, Q., and Kornmann, B. (2018). Mechanical forces on cellular organelles. J. Cell. Sci. *131*.

Fenn, J., Mann, M., Meng, C., Wong, S., and Whitehouse, C. (1989). Electrospray ionization for mass spectrometry of large biomolecules. Science *246*, 64–71.

Fernández-Díaz, C.M., Merino, B., López-Acosta, J.F., Cidad, P., de la Fuente, M.A., Lobatón, C.D., Moreno, A., Leissring, M.A., Perdomo, G., and Cózar-Castellano, I. (2019). Pancreatic β-cell-specific deletion of insulin-degrading enzyme leads to dysregulated insulin secretion and β-cell functional immaturity. American Journal of Physiology-Endocrinology and Metabolism *317*, E805–E819.

Fish, K.N. (2009). Total Internal Reflection Fluorescence (TIRF) Microscopy. Current Protocols in Cytometry *50*.

Folli, F., La Rosa, S., Finzi, G., Davalli, A.M., Galli, A., Dick, E.J., Perego, C., and Mendoza, R.G. (2018). Pancreatic islet of Langerhans' cytoarchitecture and ultrastructure in normal glucose tolerance and in type 2 diabetes mellitus. Diabetes Obes Metab *20 Suppl 2*, 137–144.

Fong, G.-H., and Takeda, K. (2008). Role and regulation of prolyl hydroxylase domain proteins. Cell Death Differ *15*, 635–641.

Fraker, C.A., Ricordi, C., Inverardi, L., and Domínguez-Bendala, J. (2009). Oxygen: a master regulator of pancreatic development? Biology of the Cell *101*, 431–440.

Frantz, C., Stewart, K.M., and Weaver, V.M. (2010). The extracellular matrix at a glance. Journal of Cell Science *123*, 4195–4200.

Gagné, V., Moreau, J., Plourde, M., Lapointe, M., Lord, M., Gagnon, É., and Fernandes, M.J.G. (2009). Human angiomotin-like 1 associates with an angiomotin protein complex through its coiled-coil domain and induces the remodeling of the actin cytoskeleton. Cell Motil. Cytoskeleton *66*, 754–768.

Galli, A., Maffioli, E., Sogne, E., Moretti, S., Di Cairano, E.S., Negri, A., Nonnis, S., Norata, G.D., Bonacina, F., Borghi, F., et al. (2018). Cluster-assembled zirconia substrates promote long-term differentiation and functioning of human islets of Langerhans. Sci Rep *8*, 9979.

Galli, A., Algerta, M., Marciani, P., Schulte, C., Lenardi, C., Milani, P., Maffioli, E., Tedeschi, G., and Perego, C. (2020). Shaping Pancreatic β-Cell Differentiation and Functioning: The Influence of Mechanotransduction. Cells *9*.

Gamble, A., Pepper, A.R., Bruni, A., and Shapiro, A.M.J. (2018). The journey of islet cell transplantation and future development. Islets *10*, 80–94.

Garcia, A., Rodriguez Matas, J.F., and Raimondi, M.T. (2016). Modeling of the mechano-chemical behaviour of the nuclear pore complex: current research and perspectives. Integr Biol (Camb) *8*, 1011–1021.

Geiger, B., Bershadsky, A., Pankov, R., and Yamada, K.M. (2001). Transmembrane crosstalk between the extracellular matrix--cytoskeleton crosstalk. Nat. Rev. Mol. Cell Biol. *2*, 793–805.

Geiger, B., Spatz, J.P., and Bershadsky, A.D. (2009). Environmental sensing through focal adhesions. Nat. Rev. Mol. Cell Biol. *10*, 21–33.

Gene Ontology Consortium (2015). Gene Ontology Consortium: going forward. Nucleic Acids Research *43*, D1049-1056.

George, N.M., Day, C.E., Boerner, B.P., Johnson, R.L., and Sarvetnick, N.E. (2012). Hippo signaling regulates pancreas development through inactivation of Yap. Mol. Cell. Biol. *32*, 5116–5128.

Gerdes, J.M., Christou-Savina, S., Xiong, Y., Moede, T., Moruzzi, N., Karlsson-Edlund, P., Leibiger, B., Leibiger, I.B., Östenson, C.-G., Beales, P.L., et al. (2014). Ciliary dysfunction impairs beta-cell insulin secretion and promotes development of type 2 diabetes in rodents. Nat Commun *5*, 5308.

Giacomello, M., and Pellegrini, L. (2016). The coming of age of the mitochondria–ER contact: a matter of thickness. Cell Death Differ *23*, 1417–1427.

Gingras, A.R., Ziegler, W.H., Frank, R., Barsukov, I.L., Roberts, G.C.K., Critchley, D.R., and Emsley, J. (2005). Mapping and consensus sequence identification for multiple vinculin binding sites within the talin rod. J. Biol. Chem. *280*, 37217–37224.

Gingras, A.R., Ziegler, W.H., Bobkov, A.A., Joyce, M.G., Fasci, D., Himmel, M., Rothemund, S., Ritter, A., Grossmann, J.G., Patel, B., et al. (2009). Structural determinants of integrin binding to the talin rod. J. Biol. Chem. *284*, 8866–8876.

Gökerküçük, E.B., Tramier, M., and Bertolin, G. (2020). Imaging Mitochondrial Functions: From Fluorescent Dyes to Genetically-Encoded Sensors. Genes *11*, 125.

Golji, J., and Mofrad, M.R.K. (2014). The talin dimer structure orientation is mechanically regulated. Biophys. J. *107*, 1802–1809.

Gottardi, C.J., Arpin, M., Fanning, A.S., and Louvard, D. (1996). The junction-associated protein, zonula occludens-1, localizes to the nucleus before the maturation and during the remodeling of cell-cell contacts. Proc. Natl. Acad. Sci. U.S.A. *93*, 10779–10784.

Granot, Z., Swisa, A., Magenheim, J., Stolovich-Rain, M., Fujimoto, W., Manduchi, E., Miki, T., Lennerz, J.K., Stoeckert, C.J., Meyuhas, O., et al. (2009). LKB1 regulates pancreatic beta cell size, polarity, and function. Cell Metab. *10*, 296–308.

Groth, C.G., Korsgren, O., Tibell, A., Tollemar, J., Möller, E., Bolinder, J., Ostman, J., Reinholt, F.P., Hellerström, C., and Andersson, A. (1994). Transplantation of porcine fetal pancreas to diabetic patients. Lancet *344*, 1402–1404.

Gu, Y. (2018). The nuclear pore complex: a strategic platform for regulating cell signaling. New Phytol *219*, 25–30.

Gu, Y., and Gu, C. (2014). Physiological and Pathological Functions of Mechanosensitive Ion Channels. Mol Neurobiol *50*, 339–347.

Guay, C., and Regazzi, R. (2013). Circulating microRNAs as novel biomarkers for diabetes mellitus. Nat Rev Endocrinol *9*, 513–521.

Guilak, F., Tedrow, J.R., and Burgkart, R. (2000). Viscoelastic properties of the cell nucleus. Biochem. Biophys. Res. Commun. *269*, 781–786.

Guilak, F., Cohen, D.M., Estes, B.T., Gimble, J.M., Liedtke, W., and Chen, C.S. (2009). Control of stem cell fate by physical interactions with the extracellular matrix. Cell Stem Cell *5*, 17–26.

Gumbiner, B. (1990). Generation and maintenance of epithelial cell polarity. Curr. Opin. Cell Biol. *2*, 881–887.

Guney, M.A., Petersen, C.P., Boustani, A., Duncan, M.R., Gunasekaran, U., Menon, R., Warfield, C., Grotendorst, G.R., Means, A.L., Economides, A.N., et al. (2011). Connective tissue growth factor acts within both endothelial cells and beta cells to promote proliferation of developing beta cells. Proc. Natl. Acad. Sci. U.S.A. *108*, 15242–15247.

Guney, M.A., Lorberbaum, D.S., and Sussel, L. (2020). Pancreatic β cell regeneration: To β or not to β. Curr Opin Physiol *14*, 13–20.

Gunton, J.E., Kulkarni, R.N., Yim, S., Okada, T., Hawthorne, W.J., Tseng, Y.-H., Roberson, R.S., Ricordi, C., O'Connell, P.J., Gonzalez, F.J., et al. (2005). Loss of ARNT/HIF1beta mediates altered gene expression and pancreatic-islet dysfunction in human type 2 diabetes. Cell *122*, 337–349.

Halder, G., Dupont, S., and Piccolo, S. (2012). Transduction of mechanical and cytoskeletal cues by YAP and TAZ. Nat. Rev. Mol. Cell Biol. *13*, 591–600.

Harris, A.R., Jreij, P., and Fletcher, D.A. (2018). Mechanotransduction by the Actin Cytoskeleton: Converting Mechanical Stimuli into Biochemical Signals. Annu. Rev. Biophys. *47*, 617–631.

Hartman, C.D., Isenberg, B.C., Chua, S.G., and Wong, J.Y. (2016). Vascular smooth muscle cell durotaxis depends on extracellular matrix composition. Proc Natl Acad Sci USA *113*, 11190–11195.

Hayakawa, K., Tatsumi, H., and Sokabe, M. (2011). Actin filaments function as a tension sensor by tension-dependent binding of cofilin to the filament. J. Cell Biol. *195*, 721–727.

Hayes, H.L., Moss, L.G., Schisler, J.C., Haldeman, J.M., Zhang, Z., Rosenberg, P.B., Newgard, C.B., and Hohmeier, H.E. (2013). Pdx-1 activates islet α- and β-cell proliferation via a mechanism regulated by transient receptor potential cation channels 3 and 6 and extracellular signal-regulated kinases 1 and 2. Mol. Cell. Biol. *33*, 4017–4029.

Hepler, P.K. (2016). The Cytoskeleton and Its Regulation by Calcium and Protons. Plant Physiol *170*, 3–22.

Herum, K.M., Lunde, I.G., McCulloch, A.D., and Christensen, G. (2017). The Soft- and Hard-Heartedness of Cardiac Fibroblasts: Mechanotransduction Signaling Pathways in Fibrosis of the Heart. J Clin Med *6*.

Hogrebe, N.J., Reinhardt, J.W., and Gooch, K.J. (2017). Biomaterial microarchitecture: a potent regulator of individual cell behavior and multicellular organization. J Biomed Mater Res A *105*, 640–661.

Hollenbeck, P.J., and Saxton, W.M. (2005). The axonal transport of mitochondria. J Cell Sci *118*, 5411–5419.

Hong, S., Troyanovsky, R.B., and Troyanovsky, S.M. (2013). Binding to F-actin guides cadherin cluster assembly, stability, and movement. J. Cell Biol. *201*, 131–143.

Hrvatin, S., O'Donnell, C.W., Deng, F., Millman, J.R., Pagliuca, F.W., DiIorio, P., Rezania, A., Gifford, D.K., and Melton, D.A. (2014). Differentiated human stem cells resemble fetal, not adult, β cells. Proc. Natl. Acad. Sci. U.S.A. *111*, 3038–3043.

Hu, J.K.-H., Du, W., Shelton, S.J., Oldham, M.C., DiPersio, C.M., and Klein, O.D. (2017). An FAK-YAP-mTOR Signaling Axis Regulates Stem Cell-Based Tissue Renewal in Mice. Cell Stem Cell *21*, 91-106.e6.

Huang, D.W., Sherman, B.T., and Lempicki, R.A. (2009). Bioinformatics enrichment tools: paths toward the comprehensive functional analysis of large gene lists. Nucleic Acids Research *37*, 1–13.

Hughes, S.J., Clark, A., McShane, P., Contractor, H.H., Gray, D.W.R., and Johnson, P.R.V. (2006). Characterisation of collagen VI within the islet-exocrine interface of the human pancreas: implications for clinical islet isolation? Transplantation *81*, 423–426.

Humphrey, J.D., Dufresne, E.R., and Schwartz, M.A. (2014). Mechanotransduction and extracellular matrix homeostasis. Nat Rev Mol Cell Biol *15*, 802–812.

Humphries, J.D., Byron, A., and Humphries, M.J. (2006). Integrin ligands at a glance. J. Cell. Sci. *119*, 3901–3903.

Hutagalung, A.H., and Novick, P.J. (2011). Role of Rab GTPases in membrane traffic and cell physiology. Physiol Rev *91*, 119–149.

Huynen, M.A., Snel, B., von Mering, C., and Bork, P. (2003). Function prediction and protein networks. Current Opinion in Cell Biology *15*, 191–198.

Hynes, R.O., and Naba, A. (2012). Overview of the matrisome--an inventory of extracellular matrix constituents and functions. Cold Spring Harb Perspect Biol *4*, a004903.

Ingber, D.E. (1993). Cellular tensegrity: defining new rules of biological design that govern the cytoskeleton. J Cell Sci *104 (Pt 3)*, 613–627.

Ingber, D.E. (2006). Cellular mechanotransduction: putting all the pieces together again. The FASEB Journal *20*, 811–827.

Iozzo, R.V., and Schaefer, L. (2015). Proteoglycan form and function: A comprehensive nomenclature of proteoglycans. Matrix Biology *42*, 11–55.

Jaalouk, D.E., and Lammerding, J. (2009). Mechanotransduction gone awry. Nat. Rev. Mol. Cell Biol. *10*, 63–73.

Janoštiak, R., Pataki, A.C., Brábek, J., and Rösel, D. (2014a). Mechanosensors in integrin signaling: the emerging role of p130Cas. Eur. J. Cell Biol. *93*, 445–454.

Janoštiak, R., Brábek, J., Auernheimer, V., Tatárová, Z., Lautscham, L.A., Dey, T., Gemperle, J., Merkel, R., Goldmann, W.H., Fabry, B., et al. (2014b). CAS directly interacts with vinculin to control mechanosensing and focal adhesion dynamics. Cell Mol Life Sci *71*, 727–744.

Jansen, K.A., Atherton, P., and Ballestrem, C. (2017). Mechanotransduction at the cell-matrix interface. Seminars in Cell & Developmental Biology *71*, 75–83.

Jawahar, A.P., Narayanan, S., Loganathan, G., Pradeep, J., Vitale, G.C., Jones, C.M., Hughes, M.G., Williams, S.K., and Balamurugan, A.N. (2019). Ductal Cell Reprogramming to Insulin-Producing Beta-Like Cells as a Potential Beta Cell Replacement Source for Chronic Pancreatitis. Curr Stem Cell Res Ther *14*, 65–74.

Jiang, F.X., Cram, D.S., DeAizpurua, H.J., and Harrison, L.C. (1999). Laminin-1 promotes differentiation of fetal mouse pancreatic beta-cells. Diabetes *48*, 722–730.

Jiang, F.-X., Naselli, G., and Harrison, L.C. (2002). Distinct distribution of laminin and its integrin receptors in the pancreas. J. Histochem. Cytochem. *50*, 1625–1632.

Jiao, X., Xu, X., Fang, Y., Zhang, H., Liang, M., Teng, J., and Ding, X. (2017). miR-21 contributes to renal protection by targeting prolyl hydroxylase domain protein 2 in delayed ischaemic preconditioning: miR-21 targets PHD2. Nephrology *22*, 366–373.

Johansson, K.A., Dursun, U., Jordan, N., Gu, G., Beermann, F., Gradwohl, G., and Grapin-Botton, A. (2007). Temporal control of neurogenin3 activity in pancreas progenitors reveals competence windows for the generation of different endocrine cell types. Dev. Cell *12*, 457–465.

Kadrmas, J.L., and Beckerle, M.C. (2004). The LIM domain: from the cytoskeleton to the nucleus. Nat. Rev. Mol. Cell Biol. *5*, 920–931.

Kaido, T., Yebra, M., Cirulli, V., and Montgomery, A.M. (2004). Regulation of human beta-cell adhesion, motility, and insulin secretion by collagen IV and its receptor alpha1beta1. J. Biol. Chem. *279*, 53762–53769.

Kanchanawong, P., Shtengel, G., Pasapera, A.M., Ramko, E.B., Davidson, M.W., Hess, H.F., and Waterman, C.M. (2010). Nanoscale architecture of integrin-based cell adhesions. Nature *468*, 580–584.

Kanehisa, M., Goto, S., Sato, Y., Kawashima, M., Furumichi, M., and Tanabe, M. (2014). Data, information, knowledge and principle: back to metabolism in KEGG. Nucleic Acids Research *42*, D199-205.

Kebarle, P. (2000). A brief overview of the present status of the mechanisms involved in electrospray mass spectrometry. Journal of Mass Spectrometry: JMS *35*, 804–817.

Kim, D.-H., and Wirtz, D. (2015). Cytoskeletal tension induces the polarized architecture of the nucleus. Biomaterials *48*, 161–172.

Kim, D.-H., Khatau, S.B., Feng, Y., Walcott, S., Sun, S.X., Longmore, G.D., and Wirtz, D. (2012). Actin cap associated focal adhesions and their distinct role in cellular mechanosensing. Sci Rep *2*, 555.

Kim, J.H., Park, B.G., Kim, S.-K., Lee, D.-H., Lee, G.G., Kim, D.-H., Choi, B.-O., Lee, K.B., and Kim, J.-H. (2019). Nanotopographical regulation of pancreatic islet-like cluster formation from human pluripotent stem cells using a gradient-pattern chip. Acta Biomater *95*, 337–347.

Kirby, T.J., and Lammerding, J. (2018). Emerging views of the nucleus as a cellular mechanosensor. Nat Cell Biol *20*, 373–381.

Klugbauer, N., Dai, S., Specht, V., Lacinová, L., Marais, E., Bohn, G., and Hofmann, F. (2000). A family of γ-like calcium channel subunits. FEBS Letters *470*, 189–197.

Klymiuk, N., Aigner, B., Brem, G., and Wolf, E. (2010). Genetic modification of pigs as organ donors for xenotransplantation. Mol Reprod Dev *77*, 209–221.

Kumagai-Braesch, M., Jacobson, S., Mori, H., Jia, X., Takahashi, T., Wernerson, A., Flodström-Tullberg, M., and Tibell, A. (2013). The TheraCyte™ device protects against islet allograft rejection in immunized hosts. Cell Transplant *22*, 1137–1146.

Kumazawa, A., Katoh, H., Nonaka, D., Watanabe, T., Saotome, M., Urushida, T., Satoh, H., and Hayashi, H. (2014). Microtubule disorganization affects the mitochondrial permeability transition pore in cardiac myocytes. Circ J *78*, 1206–1215.

Kung, C. (2005). A possible unifying principle for mechanosensation. Nature *436*, 647–654.

Kusakabe, T., Motoki, K., and Hori, K. (1997). Mode of interactions of human aldolase isozymes with cytoskeletons. Arch Biochem Biophys *344*, 184–193.

Ladoux, B., and Mège, R.-M. (2017). Mechanobiology of collective cell behaviours. Nature Reviews Molecular Cell Biology *18*, 743–757.

Lammert, E., and Thorn, P. (2019). The Role of the Islet Niche on Beta Cell Structure and Function. J. Mol. Biol.

LaPierre, M.P., and Stoffel, M. (2017). MicroRNAs as stress regulators in pancreatic beta cells and diabetes. Molecular Metabolism *6*, 1010–1023.

Lavieu, G., Dunlop, M.H., Lerich, A., Zheng, H., Bottanelli, F., and Rothman, J.E. (2014). The Golgi ribbon structure facilitates anterograde transport of large cargoes. MBoC *25*, 3028–3036.

Leckband, D.E., and de Rooij, J. (2014). Cadherin adhesion and mechanotransduction. Annu. Rev. Cell Dev. Biol. *30*, 291–315.

Leite, A.R., Corrêa-Giannella, M.L., Dagli, M.L.Z., Fortes, M.A.Z., Vegas, V.M.T., and Giannella-Neto, D. (2007). Fibronectin and laminin induce expression of islet cell markers in hepatic oval cells in culture. Cell Tissue Res *327*, 529–537.

Li, J., Hou, B., Tumova, S., Muraki, K., Bruns, A., Ludlow, M.J., Sedo, A., Hyman, A.J., McKeown, L., Young, R.S., et al. (2014a). Piezo1 integration of vascular architecture with physiological force. Nature *515*, 279–282.

Li, L., Eyckmans, J., and Chen, C.S. (2017). Designer biomaterials for mechanobiology. Nature Mater *16*, 1164–1168.

Li, Q., Kumar, A., Makhija, E., and Shivashankar, G.V. (2014b). The regulation of dynamic mechanical coupling between actin cytoskeleton and nucleus by matrix geometry. Biomaterials *35*, 961–969.

Liesa, M., and Shirihai, O.S. (2013). Mitochondrial dynamics in the regulation of nutrient utilization and energy expenditure. Cell Metab. *17*, 491–506.

Lin, D., and Hoelz, A. (2016). Infographic: The Nuclear Pore Complex.

Lin, H.-Y., Tsai, C.-C., Chen, L.-L., Chiou, S.-H., Wang, Y.-J., and Hung, S.-C. (2010). Fibronectin and laminin promote differentiation of human mesenchymal stem cells into insulin producing cells through activating Akt and ERK. J Biomed Sci *17*, 56.

Liuwantara, D., Elliot, M., Smith, M.W., Yam, A.O., Walters, S.N., Marino, E., McShea, A., and Grey, S.T. (2006). Nuclear Factor-κB Regulates β-Cell Death: A Critical Role for A20 in β-Cell Protection. Diabetes *55*, 2491–2501.

Llacua, L.A., Faas, M.M., and de Vos, P. (2018). Extracellular matrix molecules and their potential contribution to the function of transplanted pancreatic islets. Diabetologia *61*, 1261–1272.

Lodh, S., O'Hare, E.A., and Zaghloul, N.A. (2014). Primary cilia in pancreatic development and disease: Primary Cilia In Pancreatic Development and Disease. Birth Defects Research Part C: Embryo Today: Reviews *102*, 139–158.

Lombardi, M.L., and Lammerding, J. (2011). Keeping the LINC: the importance of nucleocytoskeletal coupling in intracellular force transmission and cellular function. Biochem. Soc. Trans. *39*, 1729–1734.

Lombardo, C., Perrone, V.G., Amorese, G., Vistoli, F., Baronti, W., Marchetti, P., and Boggi, U. (2017). Update on pancreatic transplantation on the management of diabetes. Minerva Med. *108*, 405–418.

Losón, O.C., Song, Z., Chen, H., and Chan, D.C. (2013). Fis1, Mff, MiD49, and MiD51 mediate Drp1 recruitment in mitochondrial fission. MBoC *24*, 659–667.

MacDonald, P.E. (2011). TRP-ing down the path to insulin secretion. Diabetes *60*, 28–29.

Maechler, P., and Wollheim, C.B. (2001). Mitochondrial function in normal and diabetic beta-cells. Nature *414*, 807–812.

Maffioli, E., Nonnis, S., Angioni, R., Santagata, F., Calì, B., Zanotti, L., Negri, A., Viola, A., and Tedeschi, G. (2017). Proteomic analysis of the secretome of human bone marrow-derived mesenchymal stem cells primed by pro-inflammatory cytokines. J Proteomics *166*, 115–126.

Maffioli, E., Galli, A., Nonnis, S., Marku, A., Negri, A., Piazzoni, C., Milani, P., Lenardi, C., Perego, C., and Tedeschi, G. (2020). Proteomic analysis reveals a mitochondrial remodeling of βTC3 cells in response to nanotopography.

Martens, G.A. (2015). Species-Related Differences in the Proteome of Rat and Human Pancreatic Beta Cells. Journal of Diabetes Research *2015*, 1–11.

Martino, F., Perestrelo, A.R., Vinarský, V., Pagliari, S., and Forte, G. (2018). Cellular Mechanotransduction: From Tension to Function. Front Physiol *9*, 824.

Matsuoka, T.-A., Kawashima, S., Miyatsuka, T., Sasaki, S., Shimo, N., Katakami, N., Kawamori, D., Takebe, S., Herrera, P.L., Kaneto, H., et al. (2017). Mafa Enables Pdx1 to Effectively Convert Pancreatic Islet Progenitors and Committed Islet α-Cells Into β-Cells In Vivo. Diabetes *66*, 1293–1300.

McGee, K.M., Vartiainen, M.K., Khaw, P.T., Treisman, R., and Bailly, M. (2011). Nuclear transport of the serum response factor coactivator MRTF-A is downregulated at tensional homeostasis. EMBO Rep *12*, 963–970.

Méjat, A., and Misteli, T. (2010). LINC complexes in health and disease. Nucleus *1*, 40–52.

Metzen, E., Stiehl, D.P., Doege, K., Marxsen, J.H., Hellwig-Bürgel, T., and Jelkmann, W. (2005). Regulation of the prolyl hydroxylase domain protein 2 (phd2/egln-1) gene: identification of a functional hypoxia-responsive element. Biochemical Journal *387*, 711–717.

Mi, H., Huang, X., Muruganujan, A., Tang, H., Mills, C., Kang, D., and Thomas, P.D. (2017). PANTHER version 11: expanded annotation data from Gene Ontology and Reactome pathways, and data analysis tool enhancements. Nucleic Acids Res *45*, D183–D189.

Migliorini, E., Grenci, G., Ban, J., Pozzato, A., Tormen, M., Lazzarino, M., Torre, V., and Ruaro, M.E. (2011). Acceleration of neuronal precursors differentiation induced by substrate nanotopography. Biotechnol. Bioeng. *108*, 2736–2746.

Milloud, R., Destaing, O., de Mets, R., Bourrin-Reynard, I., Oddou, C., Delon, A., Wang, I., Albigès-Rizo, C., and Balland, M. (2017). αvβ3 integrins negatively regulate cellular forces by phosphorylation of its distal NPXY site. Biol. Cell *109*, 127–137.

Miralles, F., Posern, G., Zaromytidou, A.-I., and Treisman, R. (2003). Actin dynamics control SRF activity by regulation of its coactivator MAL. Cell *113*, 329–342.

Miroshnikova, Y.A., Nava, M.M., and Wickström, S.A. (2017). Emerging roles of mechanical forces in chromatin regulation. J Cell Sci *130*, 2243–2250.

Mo, J.-S., Meng, Z., Kim, Y.C., Park, H.W., Hansen, C.G., Kim, S., Lim, D.-S., and Guan, K.-L. (2015). Cellular energy stress induces AMPK-mediated regulation of YAP and the Hippo pathway. Nat Cell Biol *17*, 500–510.

Molina, A.J.A., Wikstrom, J.D., Stiles, L., Las, G., Mohamed, H., Elorza, A., Walzer, G., Twig, G., Katz, S., Corkey, B.E., et al. (2009). Mitochondrial networking protects beta-cells from nutrient-induced apoptosis. Diabetes *58*, 2303–2315.

Moro, A., Driscoll, T.P., Boraas, L.C., Armero, W., Kasper, D.M., Baeyens, N., Jouy, C., Mallikarjun, V., Swift, J., Ahn, S.J., et al. (2019). MicroRNA-dependent regulation of biomechanical genes establishes tissue stiffness homeostasis. Nat Cell Biol *21*, 348–358.

Mouw, J.K., Ou, G., and Weaver, V.M. (2014). Extracellular matrix assembly: a multiscale deconstruction. Nat Rev Mol Cell Biol *15*, 771–785.

Munger, B.L. (1958). A light and electron microscopic study of cellular differentiation in the pancreatic islets of the mouse. Am J Anat *103*, 275–311.

Murtaugh, L.C. (2006). Pancreas and beta-cell development: from the actual to the possible. Development *134*, 427–438.

Nair, G.G., Liu, J.S., Russ, H.A., Tran, S., Saxton, M.S., Chen, R., Juang, C., Li, M.-L., Nguyen, V.Q., Giacometti, S., et al. (2019). Recapitulating endocrine cell clustering in culture promotes maturation of human stem-cell-derived β cells. Nat Cell Biol *21*, 263–274.

Najarian, J.S., Sutherland, D.E., Matas, A.J., Steffes, M.W., Simmons, R.L., and Goetz, F.C. (1977). Human islet transplantation: a preliminary report. Transplant Proc *9*, 233–236.

Naon, D., and Scorrano, L. (2014). At the right distance: ER-mitochondria juxtaposition in cell life and death. Biochim Biophys Acta *1843*, 2184–2194.

Nava, M.M., Raimondi, M.T., and Pietrabissa, R. (2012). Controlling self-renewal and differentiation of stem cells via mechanical cues. J Biomed Biotechnol *2012*, 797410.

Nguyen, A.T., Sathe, S.R., and Yim, E.K.F. (2016). From nano to micro: topographical scale and its impact on cell adhesion, morphology and contact guidance. J Phys Condens Matter *28*, 183001.

Niessen, W.M.A. (2006). Liquid chromatography--mass spectrometry (Boca Raton: CRC/Taylor & Francis).

Nogales, E. (2000). Structural insights into microtubule function. Annu Rev Biochem *69*, 277–302.

Nourse, J.L., and Pathak, M.M. (2017). How cells channel their stress: Interplay between Piezo1 and the cytoskeleton. Semin. Cell Dev. Biol. *71*, 3–12.

Nyitray, C.E., Chavez, M.G., and Desai, T.A. (2014). Compliant 3D Microenvironment Improves β-Cell Cluster Insulin Expression Through Mechanosensing and β-Catenin Signaling. Tissue Engineering Part A *20*, 1888–1895.

Oh, S., Brammer, K.S., Li, Y.S.J., Teng, D., Engler, A.J., Chien, S., and Jin, S. (2009). Stem cell fate dictated solely by altered nanotube dimension. Proceedings of the National Academy of Sciences *106*, 2130–2135.

Ohgushi, M., Minaguchi, M., and Sasai, Y. (2015). Rho-Signaling-Directed YAP/TAZ Activity Underlies the Long-Term Survival and Expansion of Human Embryonic Stem Cells. Cell Stem Cell *17*, 448–461.

Oka, T., and Sudol, M. (2009). Nuclear localization and pro-apoptotic signaling of YAP2 require intact PDZ-binding motif. Genes Cells *14*, 607–615.

Olson, E.N., and Nordheim, A. (2010). Linking actin dynamics and gene transcription to drive cellular motile functions. Nat Rev Mol Cell Biol *11*, 353–365.

Onesto, V., Cancedda, L., Coluccio, M.L., Nanni, M., Pesce, M., Malara, N., Cesarelli, M., Di Fabrizio, E., Amato, F., and Gentile, F. (2017). Nano-topography Enhances Communication in Neural Cells Networks. Sci Rep *7*, 9841.

Onesto, V., Villani, M., Narducci, R., Malara, N., Imbrogno, A., Allione, M., Costa, N., Coppedè, N., Zappettini, A., Cannistraci, C.V., et al. (2019). Cortical-like mini-columns of neuronal cells on zinc oxide nanowire surfaces. Sci Rep *9*, 4021.

Orr, A.W., Helmke, B.P., Blackman, B.R., and Schwartz, M.A. (2006). Mechanisms of mechanotransduction. Dev Cell *10*, 11–20.

Osipovich, A.B., and Magnuson, M.A. (2018). Alpha to Beta Cell Reprogramming: Stepping toward a New Treatment for Diabetes. Cell Stem Cell *22*, 12–13.

Otonkoski, T., Banerjee, M., Korsgren, O., Thornell, L.-E., and Virtanen, I. (2008). Unique basement membrane structure of human pancreatic islets: implications for beta-cell growth and differentiation. Diabetes Obes Metab *10 Suppl 4*, 119–127.

Pagliuca, F.W., Millman, J.R., Gürtler, M., Segel, M., Van Dervort, A., Ryu, J.H., Peterson, Q.P., Greiner, D., and Melton, D.A. (2014). Generation of functional human pancreatic β cells in vitro. Cell *159*, 428–439.

Palmer, C.S., Osellame, L.D., Laine, D., Koutsopoulos, O.S., Frazier, A.E., and Ryan, M.T. (2011). MiD49 and MiD51, new components of the mitochondrial fission machinery. EMBO Rep *12*, 565–573.

Pankov, R., and Yamada, K.M. (2002). Fibronectin at a glance. J Cell Sci *115*, 3861–3863.

Papas, K.K., Avgoustiniatos, E.S., and Suszynski, T.M. (2016). Effect of oxygen supply on the size of implantable islet-containing encapsulation devices. Panminerva Med *58*, 72–77.

Park, J.S., Burckhardt, C.J., Lazcano, R., Solis, L.M., Isogai, T., Li, L., Chen, C.S., Gao, B., Minna, J.D., Bachoo, R., et al. (2020). Mechanical regulation of glycolysis via cytoskeleton architecture. Nature *578*, 621–626.

Park, K.-S., Wiederkehr, A., Kirkpatrick, C., Mattenberger, Y., Martinou, J.-C., Marchetti, P., Demaurex, N., and Wollheim, C.B. (2008). Selective actions of mitochondrial fission/fusion genes on metabolism-secretion coupling in insulin-releasing cells. J Biol Chem *283*, 33347–33356.

Pasqualini, F.S., Nesmith, A.P., Horton, R.E., Sheehy, S.P., and Parker, K.K. (2016). Mechanotransduction and Metabolism in Cardiomyocyte Microdomains. BioMed Research International *2016*, 1–17.

Pedraza, E., Coronel, M.M., Fraker, C.A., Ricordi, C., and Stabler, C.L. (2012). Preventing hypoxia-induced cell death in beta cells and islets via hydrolytically activated, oxygen-generating biomaterials. Proceedings of the National Academy of Sciences *109*, 4245–4250.

Pelham, R.J., and Wang, Y. l (1997). Cell locomotion and focal adhesions are regulated by substrate flexibility. Proc. Natl. Acad. Sci. U.S.A. *94*, 13661–13665.

Pellegrini, S., Cantarelli, E., Sordi, V., Nano, R., and Piemonti, L. (2016). The state of the art of islet transplantation and cell therapy in type 1 diabetes. Acta Diabetol *53*, 683–691.

Peloso, A., Citro, A., Zoro, T., Cobianchi, L., Kahler-Quesada, A., Bianchi, C.M., Andres, A., Berishvili, E., Piemonti, L., Berney, T., et al. (2018). Regenerative Medicine and Diabetes: Targeting the Extracellular Matrix Beyond the Stem Cell Approach and Encapsulation Technology. Front Endocrinol (Lausanne) *9*, 445.

Pendergrass, W., Wolf, N., and Poot, M. (2004). Efficacy of MitoTracker Green and CMXrosamine to measure changes in mitochondrial membrane potentials in living cells and tissues. Cytometry A *61*, 162–169.

Pepper, A.R., Bruni, A., and Shapiro, A.M.J. (2018). Clinical islet transplantation: is the future finally now? Curr Opin Organ Transplant *23*, 428–439.

Peric-Hupkes, D., Meuleman, W., Pagie, L., Bruggeman, S.W.M., Solovei, I., Brugman, W., Gräf, S., Flicek, P., Kerkhoven, R.M., van Lohuizen, M., et al. (2010). Molecular maps of the reorganization of genome-nuclear lamina interactions during differentiation. Mol Cell *38*, 603–613.

Phillip, J.M., Aifuwa, I., Walston, J., and Wirtz, D. (2015). The Mechanobiology of Aging. Annu. Rev. Biomed. Eng. *17*, 113–141.

Piccolo, S., Dupont, S., and Cordenonsi, M. (2014). The biology of YAP/TAZ: hippo signaling and beyond. Physiol. Rev. *94*, 1287–1312.

Piseri, P., Podestà, A., Barborini, E., and Milani, P. (2001). Production and characterization of highly intense and collimated cluster beams by inertial focusing in supersonic expansions. Review of Scientific Instruments *72*, 2261–2267.

Pitt, J.J. (2009). Principles and applications of liquid chromatography-mass spectrometry in clinical biochemistry. The Clinical Biochemist. Reviews *30*, 19–34.

Pittala, S., Levy, I., De, S., Kumar Pandey, S., Melnikov, N., Hyman, T., and Shoshan-Barmatz, V. (2020). The VDAC1-based R-Tf-D-LP4 Peptide as a Potential Treatment for Diabetes Mellitus. Cells *9*, 481.

Polte, T.R., and Hanks, S.K. (1995). Interaction between focal adhesion kinase and Crk-associated tyrosine kinase substrate p130Cas. Proc Natl Acad Sci U S A *92*, 10678–10682.

Poot, M., Zhang, Y.Z., Krämer, J.A., Wells, K.S., Jones, L.J., Hanzel, D.K., Lugade, A.G., Singer, V.L., and Haugland, R.P. (1996). Analysis of mitochondrial morphology and function with novel fixable fluorescent stains. J Histochem Cytochem *44*, 1363–1372.

Poteser, M., Graziani, A., Eder, P., Yates, A., Mächler, H., Romanin, C., and Groschner, K. (2008). Identification of a rare subset of adipose tissue-resident progenitor cells, which express CD133 and TRPC3 as a VEGF-regulated Ca2+ entry channel. FEBS Lett *582*, 2696–2702.

Poy, M.N., Eliasson, L., Krutzfeldt, J., Kuwajima, S., Ma, X., Macdonald, P.E., Pfeffer, S., Tuschl, T., Rajewsky, N., Rorsman, P., et al. (2004). A pancreatic islet-specific microRNA regulates insulin secretion. Nature *432*, 226–230.

Praetorius, H.A., and Spring, K.R. (2003). The renal cell primary cilium functions as a flow sensor. Curr Opin Nephrol Hypertens *12*, 517–520.

Puliafito, A., Hufnagel, L., Neveu, P., Streichan, S., Sigal, A., Fygenson, D.K., and Shraiman, B.I. (2012). Collective and single cell behavior in epithelial contact inhibition. Proceedings of the National Academy of Sciences *109*, 739–744.

Quaegebeur, A., Segura, I., Schmieder, R., Verdegem, D., Decimo, I., Bifari, F., Dresselaers, T., Eelen, G., Ghosh, D., Davidson, S.M., et al. (2016). Deletion or Inhibition of the Oxygen Sensor PHD1 Protects against Ischemic Stroke via Reprogramming of Neuronal Metabolism. Cell Metab *23*, 280–291.

Rackham, C.L., Vargas, A.E., Hawkes, R.G., Amisten, S., Persaud, S.J., Austin, A.L.F., King, A.J.F., and Jones, P.M. (2015). Annexin A1 is a key modulator of Mesenchymal Stromal Cell mediated improvements in islet function. Diabetes db150990.

Ranade, S.S., Qiu, Z., Woo, S.-H., Hur, S.S., Murthy, S.E., Cahalan, S.M., Xu, J., Mathur, J., Bandell, M., Coste, B., et al. (2014). Piezo1, a mechanically activated ion channel, is required for vascular development in mice. Proc Natl Acad Sci U S A *111*, 10347–10352.

Ranade, S.S., Syeda, R., and Patapoutian, A. (2015). Mechanically Activated Ion Channels. Neuron *87*, 1162–1179.

Regard, J.B., Kataoka, H., Cano, D.A., Camerer, E., Yin, L., Zheng, Y.-W., Scanlan, T.S., Hebrok, M., and Coughlin, S.R. (2007). Probing cell type–specific functions of Gi in vivo identifies GPCR regulators of insulin secretion. J. Clin. Invest. JCI32994.

Rezania, A., Bruin, J.E., Arora, P., Rubin, A., Batushansky, I., Asadi, A., O'Dwyer, S., Quiskamp, N., Mojibian, M., Albrecht, T., et al. (2014a). Reversal of diabetes with insulin-producing cells derived in vitro from human pluripotent stem cells. Nat. Biotechnol. *32*, 1121–1133.

Ricard-Blum, S. (2011). The collagen family. Cold Spring Harb Perspect Biol *3*, a004978.

Ricordi, C., Lacy, P.E., Finke, E.H., Olack, B.J., and Scharp, D.W. (1988). Automated method for isolation of human pancreatic islets. Diabetes *37*, 413–420.

Rieusset, J. (2011). Mitochondria and endoplasmic reticulum: mitochondria-endoplasmic reticulum interplay in type 2 diabetes pathophysiology. Int J Biochem Cell Biol *43*, 1257–1262.

Robin, J.D., and Magdinier, F. (2016). Physiological and Pathological Aging Affects Chromatin Dynamics, Structure and Function at the Nuclear Edge. Front Genet *7*, 153.

Rodriguez-Diaz, R., Speier, S., Molano, R.D., Formoso, A., Gans, I., Abdulreda, M.H., Cabrera, O., Molina, J., Fachado, A., Ricordi, C., et al. (2012). Noninvasive in vivo model demonstrating the effects of autonomic innervation on pancreatic islet function. Proceedings of the National Academy of Sciences *109*, 21456–21461.

Roggli, E., Britan, A., Gattesco, S., Lin-Marq, N., Abderrahmani, A., Meda, P., and Regazzi, R. (2010). Involvement of microRNAs in the cytotoxic effects exerted by proinflammatory cytokines on pancreatic beta-cells. Diabetes *59*, 978–986.

Rostovtseva, T.K., Sheldon, K.L., Hassanzadeh, E., Monge, C., Saks, V., Bezrukov, S.M., and Sackett, D.L. (2008). Tubulin binding blocks mitochondrial voltage-dependent anion channel and regulates respiration. Proc Natl Acad Sci U S A *105*, 18746–18751.

Rozario, T., and DeSimone, D.W. (2010). The extracellular matrix in development and morphogenesis: a dynamic view. Dev Biol *341*, 126–140.

Rutter, G.A., and Hodson, D.J. (2015). Beta cell connectivity in pancreatic islets: a type 2 diabetes target? Cell. Mol. Life Sci. *72*, 453–467.

Rutter, G.A., Hodson, D.J., Chabosseau, P., Haythorne, E., Pullen, T.J., and Leclerc, I. (2017). Local and regional control of calcium dynamics in the pancreatic islet. Diabetes Obes Metab *19 Suppl 1*, 30–41.

Saha, K., Keung, A.J., Irwin, E.F., Li, Y., Little, L., Schaffer, D.V., and Healy, K.E. (2008). Substrate Modulus Directs Neural Stem Cell Behavior. Biophysical Journal *95*, 4426–4438.

Salvatori, M., Katari, R., Patel, T., Peloso, A., Mugweru, J., Owusu, K., and Orlando, G. (2014). Extracellular Matrix Scaffold Technology for Bioartificial Pancreas Engineering: State of the Art and Future Challenges. Journal of Diabetes Science and Technology *8*, 159–169.

Samoylenko, A.A., Tepliuk, N.N., Obolenskaya, M.Yu., and Kietzmann, T. (2007). Oxygen as a regulator of serine dehydratase (SerDH) gene expression. Biopolym. Cell *23*, 391–397.

Schaefer, L. (2014). Proteoglycans, key regulators of cell–matrix dynamics. Matrix Biology *35*, 1–2.

Schofield, R. (1978). The relationship between the spleen colony-forming cell and the haemopoietic stem cell. Blood Cells *4*, 7–25.

Schulte, C., Rodighiero, S., Cappelluti, M.A., Puricelli, L., Maffioli, E., Borghi, F., Negri, A., Sogne, E., Galluzzi, M., Piazzoni, C., et al. (2016). Conversion of nanoscale topographical information of cluster-assembled zirconia surfaces into mechanotransductive events promotes neuronal differentiation. J Nanobiotechnol *14*, 18.

Schulte, C., Podestà, A., Lenardi, C., Tedeschi, G., and Milani, P. (2017). Quantitative Control of Protein and Cell Interaction with Nanostructured Surfaces by Cluster Assembling. Acc. Chem. Res. *50*, 231–239.

Shapiro, A.M.J., Lakey, J.R.T., Ryan, E.A., Korbutt, G.S., Toth, E., Warnock, G.L., Kneteman, N.M., and Rajotte, R.V. (2000). Islet Transplantation in Seven Patients with Type 1 Diabetes Mellitus Using a Glucocorticoid-Free Immunosuppressive Regimen. New England Journal of Medicine *343*, 230–238.

Shapiro, A.M.J., Ricordi, C., Hering, B.J., Auchincloss, H., Lindblad, R., Robertson, R.P., Secchi, A., Brendel, M.D., Berney, T., Brennan, D.C., et al. (2006). International trial of the Edmonton protocol for islet transplantation. N Engl J Med *355*, 1318–1330.

Shapiro, A.M.J., Pokrywczynska, M., and Ricordi, C. (2017). Clinical pancreatic islet transplantation. Nat Rev Endocrinol *13*, 268–277.

Shekaran, A., and Garcia, A.J. (2011). Nanoscale engineering of extracellular matrix-mimetic bioadhesive surfaces and implants for tissue engineering. Biochimica et Biophysica Acta (BBA) - General Subjects *1810*, 350–360.

Shen, B., Delaney, M.K., and Du, X. (2012). Inside-out, outside-in, and inside–outside-in: G protein signaling in integrin-mediated cell adhesion, spreading, and retraction. Current Opinion in Cell Biology *24*, 600–606.

Shivashankar, G.V. (2011). Mechanosignaling to the cell nucleus and gene regulation. Annu Rev Biophys *40*, 361–378.

Shukla, G.C., Singh, J., and Barik, S. (2011). MicroRNAs: Processing, Maturation, Target Recognition and Regulatory Functions. Mol Cell Pharmacol *3*, 83–92.

Singh, A.V., Ferri, M., Tamplenizza, M., Borghi, F., Divitini, G., Ducati, C., Lenardi, C., Piazzoni, C., Merlini, M., Podestà, A., et al. (2012). Bottom-up engineering of the surface roughness of nanostructured cubic zirconia to control cell adhesion. Nanotechnology *23*, 475101.

Skelin, M., Rupnik, M., and Cencic, A. (2010). Pancreatic beta cell lines and their applications in diabetes mellitus research. ALTEX *27*, 105–113.

Smith, A.C., and Robinson, A.J. (2016). MitoMiner v3.1, an update on the mitochondrial proteomics database. Nucleic Acids Res *44*, D1258-1261.

Solmaz, S.R., Blobel, G., and Melcak, I. (2013). Ring cycle for dilating and constricting the nuclear pore. Proceedings of the National Academy of Sciences *110*, 5858–5863.

Sosa, B.A., Rothballer, A., Kutay, U., and Schwartz, T.U. (2012). LINC Complexes Form by Binding of Three KASH Peptides to Domain Interfaces of Trimeric SUN Proteins. Cell *149*, 1035–1047.

Stagner, J., Mokshagundam, S., Wyler, K., Samols, E., Rilo, H., Stagner, M., Parthasarathy, L., and Parthasarathy, R. (2004). Beta-cell sparing in transplanted islets by vascular endothelial growth factor. Transplant. Proc. *36*, 1178–1180.

Stanborough, T., Niederhauser, J., Koch, B., Bergler, H., and Pertschy, B. (2014). Ribosomal protein S3 interacts with the NF-κB inhibitor IκBα. FEBS Letters *588*, 659–664.

Stefani, G., and Slack, F.J. (2008). Small non-coding RNAs in animal development. Nat Rev Mol Cell Biol *9*, 219–230.

Stendahl, J.C., Kaufman, D.B., and Stupp, S.I. (2009). Extracellular matrix in pancreatic islets: relevance to scaffold design and transplantation. Cell Transplant *18*, 1–12.

Stewart, C.L., Roux, K.J., and Burke, B. (2007). Blurring the boundary: the nuclear envelope extends its reach. Science *318*, 1408–1412.

Stiles, L., and Shirihai, O.S. (2012). Mitochondrial dynamics and morphology in beta-cells. Best Pract. Res. Clin. Endocrinol. Metab. *26*, 725–738.

Sun, Z., Guo, S.S., and Fässler, R. (2016). Integrin-mediated mechanotransduction. Journal of Cell Biology *215*, 445–456.

Swift, J., Ivanovska, I.L., Buxboim, A., Harada, T., Dingal, P.C.D.P., Pinter, J., Pajerowski, J.D., Spinler, K.R., Shin, J.-W., Tewari, M., et al. (2013). Nuclear lamin-A scales with tissue stiffness and enhances matrix-directed differentiation. Science *341*, 1240104.

Szklarczyk, D., Franceschini, A., Wyder, S., Forslund, K., Heller, D., Huerta-Cepas, J., Simonovic, M., Roth, A., Santos, A., Tsafou, K.P., et al. (2015). STRING v10: protein-protein interaction networks, integrated over the tree of life. Nucleic Acids Research *43*, D447-452.

Tai, Y., Feng, S., Du, W., and Wang, Y. (2009). Functional roles of TRPC channels in the developing brain. Pflugers Arch - Eur J Physiol *458*, 283–289.

Takamoto, I., Kubota, N., Nakaya, K., Kumagai, K., Hashimoto, S., Kubota, T., Inoue, M., Kajiwara, E., Katsuyama, H., Obata, A., et al. (2014). TCF7L2 in mouse pancreatic beta cells plays a crucial role in glucose homeostasis by regulating beta cell mass. Diabetologia *57*, 542–553.

Talchai, C., Xuan, S., Lin, H.V., Sussel, L., and Accili, D. (2012). Pancreatic β cell dedifferentiation as a mechanism of diabetic β cell failure. Cell *150*, 1223–1234.

Taniguchi, K., Wu, L.-W., Grivennikov, S.I., de Jong, P.R., Lian, I., Yu, F.-X., Wang, K., Ho, S.B., Boland, B.S., Chang, J.T., et al. (2015). A gp130-Src-YAP module links inflammation to epithelial regeneration. Nature *519*, 57–62.

Tao, J., Zhu, M., Wang, H., Afelik, S., Vasievich, M.P., Chen, X.-W., Zhu, G., Jensen, J., Ginsburg, D., and Zhang, B. (2012). SEC23B is required for the maintenance of murine professional secretory tissues. Proceedings of the National Academy of Sciences *109*, E2001–E2009.

Tedeschi, G., Pagliato, L., Negroni, M., Montorfano, G., Corsetto, P., Nonnis, S., Negri, A., and Rizzo, A.M. (2011). Protein pattern of Xenopus laevis embryos grown in simulated microgravity. Cell Biol Int *35*, 249–258.

Thorel, F., Népote, V., Avril, I., Kohno, K., Desgraz, R., Chera, S., and Herrera, P.L. (2010). Conversion of adult pancreatic α-cells to β-cells after extreme β-cell loss. Nature *464*, 1149–1154.

Tilokani, L., Nagashima, S., Paupe, V., and Prudent, J. (2018). Mitochondrial dynamics: overview of molecular mechanisms. Essays in Biochemistry *62*, 341–360.

Torre, C.A.L. de la, Blanco, J.E., Silva, J.T., Paschoalin, V.M.F., and Conte Júnior, C.A. (2015). Chromatographic detection of nitrofurans in foods of animal origin. Arq. Inst. Biol. *82*.

Townsend, S.E., and Gannon, M. (2019). Extracellular Matrix-Associated Factors Play Critical Roles in Regulating Pancreatic β-Cell Proliferation and Survival. Endocrinology *160*, 1885–1894.

Tremmel, D.M., and Odorico, J.S. (2018). Rebuilding a better home for transplanted islets. Organogenesis *14*, 163–168.

Tubbs, E., and Rieusset, J. (2017). Metabolic signaling functions of ER–mitochondria contact sites: role in metabolic diseases. Journal of Molecular Endocrinology *58*, R87–R106.

Uhler, C., and Shivashankar, G.V. (2017). Regulation of genome organization and gene expression by nuclear mechanotransduction. Nature Reviews Molecular Cell Biology *18*, 717–727.

Vaithilingam, V., and Tuch, B.E. (2011). Islet Transplantation and Encapsulation: An Update on Recent Developments. Rev Diabet Stud *8*, 51–67.

Valencia, A., and Pazos, F. (2002). Computational methods for the prediction of protein interactions. Current Opinion in Structural Biology *12*, 368–373.

Valente, A.J., Maddalena, L.A., Robb, E.L., Moradi, F., and Stuart, J.A. (2017). A simple ImageJ macro tool for analyzing mitochondrial network morphology in mammalian cell culture. Acta Histochem *119*, 315–326.

Vallese, F., Barazzuol, L., Maso, L., Brini, M., and Calì, T. (2020). ER-Mitochondria Calcium Transfer, Organelle Contacts and Neurodegenerative Diseases. In Calcium Signaling, Md.S. Islam, ed. (Cham: Springer International Publishing), pp. 719–746.

Van Helvert, S., Storm, C., and Friedl, P. (2018). Mechanoreciprocity in cell migration. Nat Cell Biol *20*, 8–20.

Varadi, A. (2004). Cytoplasmic dynein regulates the subcellular distribution of mitochondria by controlling the recruitment of the fission factor dynamin-related protein-1. Journal of Cell Science *117*, 4389–4400.

Vernocchi, V., Morselli, M.G., Varesi, S., Nonnis, S., Maffioli, E., Negri, A., Tedeschi, G., and Luvoni, G.C. (2014). Sperm ubiquitination in epididymal feline semen. Theriogenology *82*, 636–642.

Vining, K.H., and Mooney, D.J. (2017). Mechanical forces direct stem cell behaviour in development and regeneration. Nature Reviews Molecular Cell Biology *18*, 728–742.

Virtanen, I., Banerjee, M., Palgi, J., Korsgren, O., Lukinius, A., Thornell, L.-E., Kikkawa, Y., Sekiguchi, K., Hukkanen, M., Konttinen, Y.T., et al. (2008). Blood vessels of human islets of Langerhans are surrounded by a double basement membrane. Diabetologia *51*, 1181–1191.

Volkers, L., Mechioukhi, Y., and Coste, B. (2015). Piezo channels: from structure to function. Pflugers Arch - Eur J Physiol *467*, 95–99.

Von Dassow, M., and Davidson, L.A. (2007). Variation and robustness of the mechanics of gastrulation: the role of tissue mechanical properties during morphogenesis. Birth Defects Res C Embryo Today *81*, 253–269.

Waanders, L.F., Chwalek, K., Monetti, M., Kumar, C., Lammert, E., and Mann, M. (2009). Quantitative proteomic analysis of single pancreatic islets. PNAS *106*, 18902–18907.

Wada, K.-I., Itoga, K., Okano, T., Yonemura, S., and Sasaki, H. (2011). Hippo pathway regulation by cell morphology and stress fibers. Development *138*, 3907–3914.

Wang, N., Tytell, J.D., and Ingber, D.E. (2009). Mechanotransduction at a distance: mechanically coupling the extracellular matrix with the nucleus. Nat. Rev. Mol. Cell Biol. *10*, 75–82.

Webb, D.J., and Brown, C.M. (2013). Epi-fluorescence microscopy. Methods Mol Biol *931*, 29–59.

Weber, L.M., Hayda, K.N., Haskins, K., and Anseth, K.S. (2007). The effects of cell-matrix interactions on encapsulated beta-cell function within hydrogels functionalized with matrix-derived adhesive peptides. Biomaterials *28*, 3004–3011.

Wegner, K., Piseri, P., Tafreshi, H.V., and Milani, P. (2006). Cluster beam deposition: a tool for nanoscale science and technology. J. Phys. D: Appl. Phys. *39*, R439–R459.

Wei, F., Yang, S., and Wang, S. (2018). MicroRNAs: a critical regulator under mechanical force. Histol Histopathol *33*, 335–342.

Wente, S.R., and Rout, M.P. (2010). The nuclear pore complex and nuclear transport. Cold Spring Harb Perspect Biol *2*, a000562.

Wheeldon, I., Farhadi, A., Bick, A.G., Jabbari, E., and Khademhosseini, A. (2011). Nanoscale tissue engineering: spatial control over cell-materials interactions. Nanotechnology *22*, 212001.

Wilson, K.L., and Foisner, R. (2010). Lamin-binding Proteins. Cold Spring Harbor Perspectives in Biology *2*, a000554–a000554.

Winzell, M.S., and Ahrén, B. (2007). G-protein-coupled receptors and islet function—Implications for treatment of type 2 diabetes. Pharmacology & Therapeutics *116*, 437–448.

Wittkowske, C., Reilly, G.C., Lacroix, D., and Perrault, C.M. (2016). In Vitro Bone Cell Models: Impact of Fluid Shear Stress on Bone Formation. Front Bioeng Biotechnol *4*, 87.

Wong, Y.C., Kim, S., Peng, W., and Krainc, D. (2019). Regulation and Function of Mitochondria-Lysosome Membrane Contact Sites in Cellular Homeostasis. Trends Cell Biol *29*, 500–513.

Wozniak, M.A., and Chen, C.S. (2009). Mechanotransduction in development: a growing role for contractility. Nat Rev Mol Cell Biol *10*, 34–43.

Wu, J., Lewis, A.H., and Grandl, J. (2017). Touch, Tension, and Transduction – The Function and Regulation of Piezo Ion Channels. Trends in Biochemical Sciences *42*, 57–71.

Wu, J., Ding, J., Yang, J., Guo, X., and Zheng, Y. (2018). MicroRNA Roles in the Nuclear Factor Kappa B Signaling Pathway in Cancer. Front. Immunol. *9*, 546.

Wu, Y., Kanchanawong, P., and Zaidel-Bar, R. (2015). Actin-delimited adhesion-independent clustering of E-cadherin forms the nanoscale building blocks of adherens junctions. Dev Cell *32*, 139–154.

Xiao, X., Gaffar, I., Guo, P., Wiersch, J., Fischbach, S., Peirish, L., Song, Z., El-Gohary, Y., Prasadan, K., Shiota, C., et al. (2014). M2 macrophages promote beta-cell proliferation by up-regulation of SMAD7. Proceedings of the National Academy of Sciences *111*, E1211–E1220.

Xiao, X., Guo, P., Shiota, C., Zhang, T., Coudriet, G.M., Fischbach, S., Prasadan, K., Fusco, J., Ramachandran, S., Witkowski, P., et al. (2018). Endogenous Reprogramming of Alpha Cells into Beta Cells, Induced by Viral Gene Therapy, Reverses Autoimmune Diabetes. Cell Stem Cell *22*, 78-90.e4.

Yang, Y., Wang, K., Gu, X., and Leong, K.W. (2017). Biophysical Regulation of Cell Behavior—Cross Talk between Substrate Stiffness and Nanotopography. Engineering *3*, 36–54.

Ye, J., Fan, J., Venneti, S., Wan, Y.-W., Pawel, B.R., Zhang, J., Finley, L.W.S., Lu, C., Lindsten, T., Cross, J.R., et al. (2014). Serine catabolism regulates mitochondrial redox control during hypoxia. Cancer Discov *4*, 1406–1417.

Yoshigi, M., Hoffman, L.M., Jensen, C.C., Yost, H.J., and Beckerle, M.C. (2005). Mechanical force mobilizes zyxin from focal adhesions to actin filaments and regulates cytoskeletal reinforcement. J Cell Biol *171*, 209–215.

Zhang, E., Mohammed Al-Amily, I., Mohammed, S., Luan, C., Asplund, O., Ahmed, M., Ye, Y., Ben-Hail, D., Soni, A., Vishnu, N., et al. (2019a). Preserving Insulin Secretion in Diabetes by Inhibiting VDAC1 Overexpression and Surface Translocation in β Cells. Cell Metabolism *29*, 64-77.e6.

Zhang, Z., Hu, Y., Xu, N., Zhou, W., Yang, L., Chen, R., Yang, R., Sun, J., and Chen, H. (2019b). A New Way for Beta Cell Neogenesis: Transdifferentiation from Alpha Cells Induced by Glucagon-Like Peptide 1. Journal of Diabetes Research *2019*, 1–11.

Zhao, B., Wei, X., Li, W., Udan, R.S., Yang, Q., Kim, J., Xie, J., Ikenoue, T., Yu, J., Li, L., et al. (2007). Inactivation of YAP oncoprotein by the Hippo pathway is involved in cell contact inhibition and tissue growth control. Genes & Development *21*, 2747–2761.

Zhou, D.W., Lee, T.T., Weng, S., Fu, J., and García, A.J. (2017). Effects of substrate stiffness and actomyosin contractility on coupling between force transmission and vinculin-paxillin recruitment at single focal adhesions. Mol. Biol. Cell *28*, 1901–1911.